ESR-Dosimetry in Thermal and Epithermal Neutron Fields for Application in Boron Neutron Capture Therapy

Dissertation

zur Erlangung des akademischen Grades
„Doktor der Naturwissenschaften”

im Promotionsfach Chemie

am Fachbereich Chemie, Pharmazie und Geowissenschaften
der Johannes Gutenberg-Universität Mainz

Tobias Schmitz
geb. in Bonn

Mainz, 2016

1. Berichterstatter: [redacted]
2. Berichterstatter: [redacted]

Tag der mündlichen Prüfung:

Die vorliegende Arbeit wurde in der Zeit von November 2010 bis August 2015 am Institut für Kernchemie der Johannes Gutenberg-Universität Mainz unter der Anleitung von [redacted] erstellt.
Ich versichere gemäß § 10 Abs. 3d der Promotionsordnung vom 24.07.2007 des Fachbereichs 09 der Johannes Gutenberg-Universität Mainz, die vorliegende Arbeit selbst angefertigt und als Hilfsmittel ausschließlich die im Literaturverzeichnis und die in den Anhängen genannten Quellen verwendet zu haben.

Mainz, den 22.01.2016

By way of illustration [of the destructive power of X-rays]
let us recall that nearly all pioneers in the medical X-ray laboratories
in the United States died of cancer induced by the burns.
The Washington Post, 1945

Contents

Acronyms

ATM	amorphous track model
BC	before Christ
BNCT	Boron Neutron Capture Therapy
BPA	boronophenylalanine
BSH	mercaptoundecahydro-closo-dodecaborate
CERN	Conseil Européen pour la Recherche Nucléaire
CPE	charged particle equilibrium
CSDA	continuous slowing-down approximation
CT	x-ray computer tomography
EBRT	external beam radiotherapy
FNT	Fast Neutron Therapy
FWHM	full width at half maximum
GB-10	decahydrodecaborat
HP-Ge	high-purity germanium
IC	ionisation chamber
IT	isomeric transition
IMRT	intensity modulated radiotherapy
LET	linear energy transfer
LINAC	linear accelerator
MC	Monte Carlo
MRI	magnetic resonance imaging
MWd	megawatt days
NPL	National Physical Laboratory
NTCP	normal tissue control probability
PE	polyethylene
PET	positron emission tomography
PMMA	polymethyl-methacrylate
PTB	Physikalisch-Technische Bundesanstalt
PTS	pneumatic transfer system
RBE	relative biological effectiveness
RE	relative effectiveness
REQ	radiation equilibrium
RIT	radioisotope therapy
TC	tumour control
TCP	tumour control probability
TLD	thermoluminescent dosimeters
TP	treatment planning
Z	atomic number
ZfKD	German Centre for Cancer Registry Data

Figures

Tables

List of publications

T. Schmitz, M. Blaickner, C. Schütz, N. Wiehl, J.V. Kratz, N. Bassler, M.H. Holzscheiter, H. Palmans, P. Sharpe, G. Otto, and G. Hampel, Dose calculation in biological samples in a mixed neutron-gamma field at the TRIGA reactor of the University of Mainz, *Acta Oncologica* 49, 1165-1169 (2010).

T. Schmitz, K. Appelman, P. Kudejova , J.V. Kratz, R. Moss, G. Otto, and G. Hampel, Determination of boron concentration in blood and tissue samples from patients with liver metastases of colorectal carcinoma using Prompt Gamma Ray Activation Analysis (PGAA), *Applied Radiation and Isotopes* **69**, 936-941 (2011).

T. Schmitz, M. Blaickner, M. Ziegner, N. Bassler, C. Gunewald, J.V. Kratz, C. Schütz, P. Langguth, P. Sharpe, H. Palmans, M.H. Holzscheiter, G. Otto, and G. Hampel, Dose determination using alanine detectors in a mixed neutron and gamma field for boron neutron capture therapy of liver malignancies, *Acta Oncologica* **50**, 817-822 (2011).

T. Schmitz, N. Bassler, M. Blaickner, M. Ziegner, M.C. Hsiao, Y.H. Liu, H. Koivunoro, I. Auterinen, T. Serén, P. Kotiluoto, H. Palmans, P. Sharpe, P. Langguth, and G. Hampel, The alanine detector in BNCT dosimetry: Dose response in thermal and epithermal neutron fields, *Medical Physics* **42**, 400-412 (2015).

G. Hampel, C. Grunewald, J.V. Kratz, T. Schmitz, C. Schütz, S. Werner, K. Appelman, R. Moss, M. Blaickner, T. Nawroth, G. Otto, and H. Schmidberger, Medical and Radiobiological Applications at the Research Reactor TRIGA Mainz, *Proceedings of the 14th International Topical Meeting on Research Reactor Fuel Management* (RRFM) 2010.

C.L. Schütz, C. Brochhausen, G. Hampel, D. Iffland, B. Kuczewski, G. Otto, T. Schmitz, C. Stieghorst, and J.V. Kratz, Intercomparison of inductively coupled plasma mass spectrometry, quantitative neutron capture radiography, and prompt gamma activation analysis for the determination of boron in biological samples. *Analytical and Bioanalytical Chemistry* **404**, 1887-1895 (2012).

H. Koivunoro, T. Schmitz, E. Hippeläinen, Y-H. Liu, T. Serén, P. Kotiluoto, I. Auterinen, and S. Savolainen, The FiR 1 photon beam model adjustment according to in-air spectrum measurements with the Mg(Ar) ionization chamber, *Applied Radiation and Isotopes* **88**, 134-138 (2014).

M. Ziegner, T. Schmitz, R. Khan, M. Blaickner, H. Palmans, P. Sharpe, G. Hampel, and H. Böck, Confirmation of a realistic reactor model for BNCT dosimetry at the TRIGA Mainz, *Medical Phyics* **41**, 111706 (2014).

M. Marrale, T. Schmitz, S. Gallo, G. Hampel, A. Longo, S.Panzeca, and L. Tranchina, Comparison of EPR response of alanine and Gd_2O_3-alanine dosimeters exposed to TRIGA Mainz reactor, *Applied Radiation and Isotopes* **106**, 116-120 (2015).

Abstract

Dosimetry is essential for every form of radiotherapy. In Boron Neutron Capture Therapy (BNCT) mixed neutron and gamma fields have to be considered. Dose is deposited in different neutron interactions with elements in the penetrated tissue and by gamma particles, which are always part of a neutron field. The therapeutic dose in BNCT is deposited by densely ionising particles, originating from the fragmentation of the isotope boron-10 after capture of a thermal neutron. Despite being investigated for decades, dosimetry in neutron beams or fields for BNCT remains complex, due to the variety in type and energy of the secondary particles. Today usually ionisation chambers combined with metal foils are used. The applied techniques require extensive effort and are time consuming, while the resulting uncertainties remain high. Consequently, the investigation of more effective techniques or alternative dosimeters is an important field of research. In this work the possibilities of ESR-dosimeters in those fields have been investigated.

Certain materials, such as alanine, generate stable radicals upon irradiation. Using Electron Spin Resonance (ESR) spectrometry the amount of radicals, which is proportional to absorbed dose, can be quantified. Different ESR detector materials have been irradiated in the thermal neutron field of the research reactor TRIGA research reactor in Mainz, Germany, with five setups, generating different secondary particle spectra. Further irradiations have been conducted in two epithermal neutron beams. The detector response, however, strongly depends on the dose depositing particle type and energy. It is hence necessary to accompany measurements by computational modelling and simulation. In this work the Monte Carlo code FLUKA was used to calculate absorbed doses and dose components. The relative effectiveness (RE), linking absorbed dose and detector response, has been calculated using amorphous track models. For the simulation, detailed models of the irradiation facilities are mandatory. Therefore, also the validation of an enhanced model of the TRIGA Mainz is presented in this work.

For all experiments carried out, the measured dose response of the detectors has been evaluated and compared to model predictions. Five materials (alanine, ammonium, calcium, lithium formate, and calcium carbonate) were found suitable for a dosimeter set for the characterisation of thermal and epithermal BNCT neutron fields. Each of these detectors reveals a different behaviour and dose composition. RE-factors have been calculated for each dose component, accounting for its dependence on particle type and energy. Agreement within 5% between model and measurement has been achieved for most irradiated detectors. The irradiation of the ESR detectors can, hence, be a helpful tool in field characterisation and model validation. It could be shown that in some areas ESR detectors are superior to the currently predominant ionisation chambers. How far both types of detectors can be complementary or even synergistic will have to be part of future research.

Zusammenfassung

Die Dosimetrie ist ein essentieller Bestandteil aller Radiotherapien. Für die Bor-Neutroneneinfangtherapie (BNCT) müssen gemischte Neutronen-Gamma-Felder untersucht werden. Hierbei wird Dosis durch verschiedene Wechselwirkungen der Neutronen mit Elementen des bestrahlten Gewebes und durch Gammaquanten, die in jedem Neutronenfeld enthalten sind, deponiert. Die therapeutische Dosis wird in der BNCT durch ionisierende Partikel erzeugt, welche durch die Fragmentierung des Isotops Bor-10 nach Neutroneneinfang entstehen. Durch die große Vielfalt der sekundären Teilchen bleibt die Dosimetrie in BNCT-Neutronenfeldern auch nach Jahrzehnten der Forschung herausfordernd. Heute werden standardmäßig Ionisationskammern und Metallfolien genutzt. Die damit verbunden Techniken sind arbeits- und zeitaufwändig und zum Teil mit erheblichen Unsicherheiten verbunden. Die Forschung an effektiveren Techniken oder alternativen Dosimetern ist deshalb ein wichtiges Forschungsfeld. In dieser Arbeit wurde die Möglichkeit der Anwendung von ESR-Dosimetern untersucht.

Bestimmte Materialien, wie zum Beispiel Alanine, generieren bei Bestrahlung stabile Radikale. Mittels Elektronenspinresonanz- (ESR) Spektrometrie kann die Menge der Radikale, die proportional zur Dosis ist, quantifiziert werden. Verschiedene ESR-Detektormaterialien wurden im thermischen Neutronenfeld des TRIGA Forschungsreaktors in Mainz, Deutschland, in fünf Versuchsaufbauten, die verschiedene Sekundärpartikel erzeugen, untersucht. Weitere Bestrahlungen wurden in zwei epithermischen Neutronenstrahlen durchgeführt. Das Antwortverhalten eines solchen Detektors hängt jedoch auch stark von Art und Energie der Strahlung ab. Es ist deshalb unerlässlich die Messungen durch Modellierung und Simulation nachzuvollziehen. In dieser Arbeit wurde der Monte Carlo Code FLUKA genutzt, um absorbierte Dosis und Dosiskomponenten zu berechnen. Die Relative Effektivität (RE), die absorbierte Dosis und Detektorantwort verknüpft, wurde mittels Ionenspur-Struktur-Modellen bestimmt. Dazu sind detaillierte Modelle der jeweiligen Bestrahlungseinrichtung nötig. In einem ersten Schritt wurde deshalb das verbesserte Model des TRIGA Mainz validiert.

Die gemessene Dosisantwort der Detektoren in den verschiedenen Experimenten wurde mit den Modelvorhersagen verglichen. Fünf Materialien (Alanin, Ammonium-, Calcium- und Lithiumformiat sowie Calciumcarbonat) bilden einen Satz Dosimeter, mit dem sich thermische und epithermische Neutronenfelder in der BNCT charakterisieren lassen. Die Detektoren zeigen dabei ein unterschiedliches Antwortverhalten besonders hinsichtlich der Dosiskomponenten. RE-Faktoren wurden für jede Dosiskomponente in Abhängigkeit von Teilchentyp und -energie berechnet. Für die meisten Detektoren wichen gemessenes und berechnetes Ergebnis weniger als 5% voneinander ab. ESR-Detektoren können daher ein hilfreiches Werkzeug zur Charakterisierung und Model-Validierung sein. In bestimmten Bereichen sind sie den bisher verwendeten Ionisationskammern überlegen.

1. Introduction

In the 45th of 48 cases, known from an antique papyrus, the Egyptian scribe, priest, architect, astronomer and magician Imhotep might be the first human who described cancer, about the year 2625 BC. He advises his readers:

„If you examine (a case) having bulging masses on (the) breast and you find that they have spread over his breast; if you place your hand upon (the) breast (and) find them to be cool, there being no fever at all therein when you hand feels him; they have no granulations, contain no fluid, give rise to no liquid discharge, yet they feel protuberant to your touch you say concerning him: 'This is a case of bulging masses I have to contend with' … Bulging masses of the breast mean the existence of swelling on the breast, large, spreading, and hard; touching them is like touching a ball of wrappings, or they may be compared with unripe hemat fruit, which is hard and cool to the touch."

Inspiring for his period, he describes lesions not as occult phenomena, but as disease and injuries, each including an anatomic glossary, diagnosis, summary and prognosis. However regarding the 'treatment' of case 45 he only gives one sentence: *"There is none."* [Mukherjee, 2010].

What is called cancer, also referred to as malign tumours, is a collective term for a class of disease, characterized by abnormal cell growth and the potential to spread, through blood and lymph systems, in other organs or parts of the body. Tumours occurring at distant sites, different from the original site, are called metastases.

Cancer tended to be sidelined for centuries, but after the suppression of other disease, such as tuberculosis, and the rise of life expectancy, it became one of the most prevalent causes of death in most countries and especially in the industrialised world [Ferlay et al., 2013]. The German Centre for Cancer Registry Data (ZfKD) estimates that in 2010 about 220.000 persons died from cancer in Germany and that about 470.000 cases were newly diagnosed. 54% of the cases of death were men, lung, colorectum and prostate were the most frequent cancer sites. Among women, representing 46% of the cases, breast, lung and colorectum were the most frequent sites [ZfKD, 2014].

ZfKD observed an increase in the incident rate during the last decades and predicts a continuation of this trend, due to the demographic change and the ongoing gain in life expectation [ZfKD, 2014]. Compared to Imohotep today oncology has impressive options in the treatment of cancer. But still diagnosis is shocking and in many cases with only poor chances of cure. Instead of searching for a panacea, modern oncology goes towards a personalised therapy, looking for and combining optimal treatments for each patient. Boron Neutron Capture Therapy (BNCT), a form of radiotherapy, has the potential to be a rewarding component in the treatment of several types of cancer.

This Thesis deals with a fundamental aspect for both development and application of BNCT-related treatment protocols: An improved theoretical and practical approach for dosimetry in complex radiation fields. Therefore first an introduction into radiotherapy and BNCT is given, before dosimetry and related issues will be addressed.

1.1 Radiotherapy

Already in January 1896, less than 60 days after Wilhelm Conrad Röntgen discovered X-rays, Emil Grubbé conducted the first clinical radiotherapy in Chicago, United States. With his treatment of an advanced breast cancer the field of radiation oncology was born. In the following years and decades mechanisms of the interaction of radiation with matter were explored parallely to ongoing advances in clinical application [Bernier et al., 2004]. Today radiotherapy is, together with surgery and chemotherapy, one of the most common treatment options for malignant tumours. It has been estimated that more than half of all patients suffering from cancer are receiving radiotherapy at least once at some stage during their treatment [Delaney et al., 2005].

The aim of radiotherapy is the concentration of a sufficient energy deposition, called dose, in the tumour and simultaneously sparing the surrounding tumour-free tissue to ultimately control or kill tumour cells. Most patients undergoing radiotherapy are treated with gamma ray photons. They are produced via

Bremsstrahlung resulting from the rapid deceleration of electrons, which were previously accelerated in a Linear Accelerator (LINAC). The dose deposition of photons in tissue is a function of depth with the maximum dose located close to the entrance of the photon beam into the tissue. To maximise the dose in a tumour, which is located at a position deeper than this maximum, it is irradiated from different directions. These directions are chosen in a way that the photon fields overlap in the tumour position. In addition, the intensity of the fields is modulated; in such a way that the dose distribution is matched with the shape of the tumour. This technique is called Intensity Modulated Radiotherapy (IMRT) and today state of the art [Staffurth, 2010]. Nonetheless, the application of IMRT remains difficult if the tumour has a complex shape or is located in immediate vicinity to radiosensitive organs. In these cases photon radiotherapy is often applied in combination with other treatment options, such as surgery or chemotherapy.

Due to the limitations of photon radiotherapy, alternatives using other types of ionising radiation are under investigation or already part of the clinical routine. Mostly they are aiming for an improvement of the tumour to tumour-free tissue dose ratio by a different depth dose profile. They can be distinguished by their Linear Energy Transfer (LET), the energy loss of a particle per distance travelled in a certain medium. Usually particles are separated in two groups, radiation with a high linear energy transfer (high LET radiation) and with a low linear energy transfer (low LET radiation). Some examples are summarised in table 1-1. Since LET is highly medium and energy dependant and in addition often changes with depth of penetration the given values should be seen as rough estimates.

Electrons have a very low penetration depth and therefore limited to the treatment of superficial tumours. Probably most prominent are proton and heavy ion therapy. In the table, carbon ions are shown as an example for heavy ions, but also others such as alpha-particles, neon or oxygen ions have been used or are part of recent research. LET is highly energy dependent; hence protons are listed in both categories in the table. While protons from nuclear reactions considered in this work are of comparably low energies, their LET is high, on the other side, protons used in radiotherapy are usually called low LET particles, due to their high energy. The basic advantage of these therapies is the different depth dose behaviour compared to photons. Protons and heavier ions have a finite range and an inverse dose profile with the maximum dose close to the end of their track in the so-called Bragg peak [Karger and Jäkel, 2007]. By the end of 2013 more than 120.000 patients had been treated with ion therapy; 15606 of them with ions heavier than protons [PTCOG, 2014].

Antiprotons or pions are forming a Bragg peak as well. In addition they deposit energy in the end of their track in an annihilation process. Pions have been clinically on used from 1974 to 1993 in three institutions in the world [Slater, 2006]. With antiprotons only basic research has been carried out so far [Bittner et al., 2014]. The utilisation of neutrons in radiotherapy is described in section 1.2.

Table 1-1. Examples for different high and low LET radiation suggest or applied in radiotherapy. [Bassler and Holzscheiter, 2009] [Herrmann and Baumann 1997]

	Typical incident energy (MeV)	***LET (keV/µm)***
low LET		
gamma ray	*1.25*	*0.3*
x-rays	*0.2*	*2.5*
electrons	*2.0*	*0.2*
protons	*115*	*0.7*
high LET		
protons	*2.0*	*17*
carbon ions	*270*	*13.5*
neutrons	*6.2*	*21*
antiprotons	*126*	*19**

** in the peak region*

Therapies named so far are forms of External Beam Radiotherapy (EBRT), ionising radiation is applied from outside the body. Instead it is also feasible to position or generate radiation inside the patient's body. A widely used example is Brachytherapy, where a sealed radiation source is surgically placed inside or near the targeted tumour area. The major contrast to EBRT is the missing penetration path and, hence, dose deposition in tumour-free tissue is avoided. Common isotopes are γ- or β^--emitter, such as ^{103}Pd, ^{106}Ru, ^{125}I, ^{131}Cs and ^{137}Cs. One of the most frequent treatment modalities is prostate cancer [Koukourakis et al., 2009].

In radioisotope therapy (RIT) a radioactive nuclide is administered, which has a higher uptake in tumour tissue than in tumour free tissue. Thus, RIT is a form of biological targeting. Most common is the use of iodine-131, a β^--emitter, which is specifically absorbed in the thyroid gland. Iodine therapy represents the simplest application of the tracer principle, since the sole iodine anion is used to treat specific types of thyroid cancer. The radioactive isotope can be also connected or inserted into a molecule, such as antibodies or other biologically active compounds, targeting specifically the sites of interest [Hoskin, 1986].

1.2 Boron Neutron Capture Therapy

1.2.1 Neutrons and their role in radiotherapy

Neutrons have a mass slightly higher than that of protons, but compared to them they are uncharged. Consequently they are referred to as indirectly ionizing radiation like photons. Due to these properties the neutron was discovered relatively late in 1932 by James Chadwick [Chadwick, 1932], twelve years after Ernest Rutherford postulated the possible existence of a neutral particle [Rutherford, 1920]. Neutrons are classified by their kinetic energy. There is no sharp distinction between the different classes; values varying from those presented here can be found in literature. Table 1-2 shows the common definition in neutron dosimetry. Although 0.025 eV is referred to as the typical thermal neutron energy, the term covers a wide energy range, whose upper limit is usually defined as the cadmium cut-off energy at 0.4 eV.

Table 1-2. Neutron energy classification.

Name	***Kinetic energy***	***Speed (m/s)***
Cold neutrons	*< 3.0 meV*	*$< 7.58 \times 10^2$*
Thermal neutrons	*3.0 meV – 0.4 eV*	*7.58×10^2 - 8.76×10^3*
Epithermal neutrons	*0.4 eV – 0.1 keV*	*8.76×10^3 - 1.38×10^5*
Fast neutrons	*> 0.1 keV*	*$> 1.38 \times 10^5$*

In most radiotherapies neutron are unwanted particles. Photo neutrons are generated by photon beams with high energies through interaction with high atomic number materials as tungsten or lead which are present in the accelerators used for IMRT [Thomas et al 2002,][Králík, and Turek, 2004]. Using either protons or heavier ions, neutrons are generated as secondary products. Their contribution to the total therapy dose is about 5 %, but since they carry no charge, the dose distribution is very different from ions. Due to their physically different behaviour they change the transversal dose profile and, hence, they are of interest in dosimetry for radiotherapy [Zacharatou Jarlskog and Paganetti, 2008].

But neutrons of different energies are also used for cancer therapy. Due to their properties as indirect ionising particles, the neutron depth dose profile is comparable to that of photons. Fast Neutron Therapy (FNT) uses neutrons with energies around 20 MeV. Their higher LET compared to photons has been found favourably for radiotherapy of certain disease patterns [Jones and Wambersie, 2007]. BNCT also includes irradiation with neutrons, but with substantially lower neutron energies in the thermal and epithermal range. However, neutrons in this context are not the direct, but rather indirect therapeutic agent. The present work was carried out in this context and therefore focuses on the dosimetry in low energy neutron fields.

1.2.2 Principles of BNCT

BNCT combines aspects of EBRT and RIT. It is biologically targeted and uses the effect of secondary particle radiation released inside the tumour cells. The idea was first proposed by Gordon Locher in 1936 [Locher, 1936], shortly after the discovery of a number of different nuclear reactions with neutrons, amongst others also the reaction of the isotope boron-10 (≈20% abundance in natural boron) [Slatkin, 1991]. If a neutron is absorbed by an atomic nucleus, forming a heavier nucleus, the reaction is called a neutron capture. In the case of boron-10 the reaction leads to fission of the short-lived nucleus boron-11, as shown in figure 1-1. An additional 478 keV photon is emitted prompt by lithium in 94% of all reactions $^{10}B(n,\alpha)^{7}Li$. Due to the relatively low energy in coincidence with the high LET, the resulting alpha and lithium particles have a limited range in the micrometre scale, corresponding to dimensions of human cells. If tumour cells are enriched with boron-10 and irradiated with neutrons, the formed particles have the chance to eliminate or seriously damage the cells.

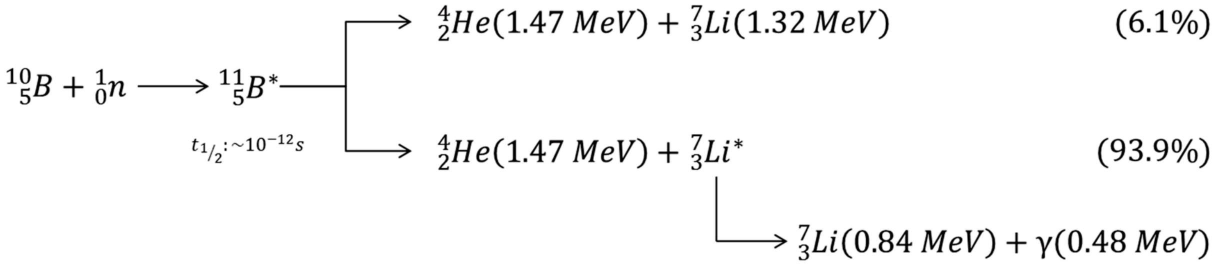

Figure 1-1. Neutron capture reaction of the boron-10 isotope.

Besides the generation of high LET particles, in the first place the nuclear reaction of boron-10 is practical for radiotherapy due to another reason. The isotope has one of the highest neutron capture cross sections in the periodic table. The cross section (σ) is a measure for the probability of the interaction between an incident neutron and a target nucleus to occur, given in barn ($1\ b = 10^{-28}\ m^2$). For neutrons they are often compared by their value for thermal neutrons (σ_{th}). Boron-10 has a thermal neutron capture cross section of 3840 barn.

Others neutron capture reactions have been investigated as well regarding possible application in radiation therapy. Probably most research has been carried out on the gadolinium isotope ^{157}Gd [Salt et al., 2004], which has a cross section of $\sigma_{th} = 2.59 \times 10^5$ b, but generates, as a consequence of the different nuclear interaction, different secondary particles. So far boron-10 is the only isotope used clinically.

1.2.3 Short history of clinical application and boron compounds

The clinical outcome of BNCT highly depends on the boron concentration in the tumour cells and the enrichment factor towards the tumour free tissue. Hence the boron carrier, which is delivering the target atoms to the tumour, plays a fundamental role.

First clinical trials, carried out in the United States in early 1950s on malignant brain tumours, used boron-10 enriched borax and sodium pentaborat, later also 4-

carboxylphenyl boronic acid and disodium decahydrodecaborat (GB-10). The outcome was similar to conventional therapies at that time, although in part severe side effects were observed. The results did not meet the expectations for several reasons, the most prominent being the lack of any selectivity of the applied boron compounds for tumour tissue and the rudimentary treatment planning available at that time. The poor results lead to the temporarily cessation of clinical application [Slatkin, 1991].

A new stage in the development of BNCT was reached with the synthesis of disodium mercaptoundecahydro-closo-dodecaborate $Na_2B_{12}H_{11}SH$ (BSH) by Soloway and his co-workers [Soloway et al., 1967]. The compound, shown in figure 1-2 a), was brought to clinical application by Hiroshi Hatanaka one year later in Japan [Nakagawa and Hatanaka, 1997] and has since then been almost exclusively used for brain tumours. Although cell uptake of the molecule has been proven for several brain tumour cells, the uptake mechanism remains unclear. Some studies support the hypothesis that transport is not only by passive diffusion, but also endocytosis [Neumann et al., 2002]. Until 1995, patients were treated at various Japanese research reactors in thermal neutron fields. Because of the limited penetration depth of thermal neutrons, it was an option to perform the irradiation intraoperatively by directly exposing the brain with skin reflected and the bone flap raised [Nakagawa and Hatanaka, 1997].

During this time also the second boron compound clinically used today was established. In 1987 Yutaka Mishima introduced p-boronophenylalanine (BPA) as a boron carrier for the treatment of malign melanoma [Mishima et al., 1989]. Even though the hypothesis leading to this approach could not be confirmed, his work was an important step for the application of BNCT to non-brain tumours. The BPA molecule, shown in figure 1-2 b), was already synthesised in 1950s [Snyder et al., 1958] and needs to be administered as fructose or mannitol complex for water solubility. Compared to BSH the BPA has selectivity for specific malignant cells; usually enrichment rates of tumour to tumour-free tissue of 3:1 are observed [Yoshimoto et al, 2013]. Due to the inhomogeneity of most tumours the BPA concentration in different parts can show huge differences [Schütz et al., 2011].

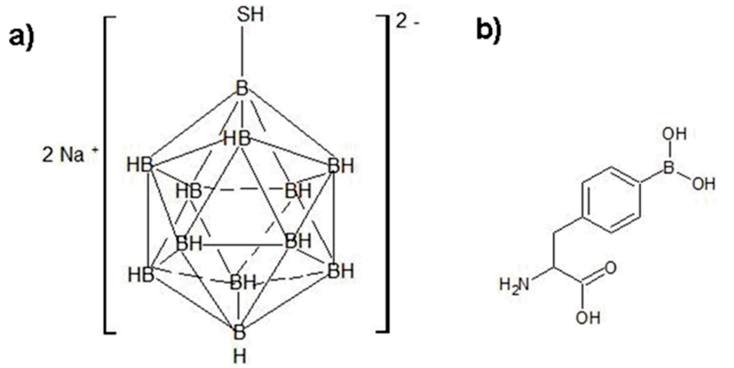

Figure 1-2. Clinically used boron compounds: a) BSH; b) BPA.

Although since the introduction of BPA no new boron carriers reached the stage of clinical application, BNCT has made important progress since then in other fields. In the 1990s especially the possibilities of computation grew and enabled great advance in treatment planning and spectral tailoring. Calculation and simulations, for example using Monte Carlo (MC) codes, lead to the design of completely new BNCT facilities. Instead of the old thermal beams, now predominately epithermal beams were used. The neutron energy was adjusted in a way that the neutrons were moderated to thermal energies along their flight path whilst penetrating the surrounding tumour-free tissue. The beam design was furthermore improved to minimise the omnipresent photon dose in neutron beams, and the fast neutron fraction in the spectrum. In most facilities this was achieved by a combination of different shielding layers, containing on the one hand light elements for moderation and heavy elements as photon shields. At the FiR 1 research reactor in Espoo, Finland, for example Fluental™ was developed as moderating element, mostly containing aluminium and fluoride. After 63 cm of Fluental™ the design is completed by a 9 cm layer of bismuth followed by a collimator also made out of bismuth and in addition a lithium polymer, which is in part enriched with lithium-6 [Serén et al., 2001].

In principal all clinical research and patient trials used research reactors as neutron sources. But these facilities are affiliated with several disadvantages. They are quite high in maintaining and running costs, with extensive requirements for the staff, and often it is not possible to use them continually around the year or to switch them easily on and off, but maybe most important is the in many cases long distance to the hospital and therewith associated difficult accessibility. During the last ten years therefore the development of accelerator based neutron sources was expedited. Accelerators are a prominent feature in hospitals for years, and hence, there is already a long-term experience. Build in Kyoto, Japan, the first facility is treating single patients since 2012. Further projects in Japan, Argentina or Europe are still under construction [Kreiner et al., 2014]. A more detailed description of the technique can be found in section 1.4.1 As a consequence of the physical parameters of this process an additional advantage is higher efficiency and reduction of the fast neutron contamination in the beam.

Despite of all progress many questions towards an understood therapy, tapping the full potential, are unsolved. BNCT, as it is practised today, already showed its possible benefits in various clinical trials. In 15 centres worldwide patients have been treated with numerous types of cancer.

1.2.4 Recent clinical application of BNCT

Comprehensive summaries of past and current clinical trials have been given recently by Moss [Moss, 2014] and Barth [Barth et al., 2012]. During the past 15 years application was limited to single European countries, such as Sweden, Finland, and The Netherlands and Japan. In other countries such as Argentina or Israel, small patient cohorts were treated or first clinical trials are ongoing as in Taiwan. Until today, cancer treated with BNCT can be divided into two groups, brain and non-brain tumours. Brain tumours are the historic target of BNCT, but still found rewarding since alternative therapies are rare. The overwhelming majority is focussed on Glioblastoma multiforme, a very aggressive, highly malignant tumour, infiltrating the normal brain tissue and therefore nearly impossible to be completely removed surgically. Because of the heterogeneity of the tumour tissue, after the surgical debulking a combination of chemotherapy and radiotherapy is applied regularly, leading to a mean survival time of 14.6 month. In spite of the extensive therapy recurrence is prevalent about seven months later [ABTA, 2012]. BNCT was applied on recurrent as well as newly diagnosed Glioblastoma multiforme, as exclusive treatment or in combination with others. In all cases since the end of the 1990s, epithermal beams have been used, but while in Europe with few exceptions BPA only was used, in Japan it was mostly co-administered with BSH or BSH was used alone. Mean survival times reach from seven months in a Finnish trial [Kankaanranta et al., 2011] to almost 30 months in a Japanese trial [Matsuda et al., 2009]. Evaluation and comparison of the results to standard therapy is difficult, since in many cases patient selection is unclear and therapy protocols were often changed. Besides Glioblastoma multiforme also other brain tumours such as intracranial metastatic melanoma, anaplastic astrocytoma, malignant meningioma, mesenchymal chondrosarcoma, and anaplastic oligoastrocytoma were treated, but mostly with very limited patient numbers or in single case studies only [Barth et al., 2012].

Connected to the introduction of BPA as boron pharmaceutical, malign melanoma were the first non-brain tumours, treated with BNCT, in the late 1980s [Mishima et al., 1989]. Since then these tumours have been treated in several studies in Japan [Fukuda et al., 2003; Morita et al. 2006], and also Argentina [Menendéz et al., 2009]. Mostly inoperable or advanced disease having bad prognosis were irradiated. Encouraging results have been reported in some cases even considered curative. Different to brain tumours, with non-brain tumours almost solely BPA alone was used.

In 2001 Kato et al. [Kato et al., 2004] treated the first tumour out of the class of Head and Neck tumours. Until today more than 100 patients were enrolled in Japan and Finland [Kato et al., 2009; Kankaanranta et al., 2012]. Most tumours were squamous cell carcinoma, other types were adenocystic carcinoma, urothelial cell carcinoma, myofibroblastic sarcoma, mucoepidermoid carcinoma, and salivary gland carcinoma. In almost all cases tumours were recurrent and had previously been resected and treated with radiotherapy and chemotherapy or combinations of all three. In addition most patients did not have any treatment options left, and treatment was only palliative. A majority of more than 70% of patients responded to the therapy, with in most studies more than 40% of complete response, meaning complete remission of the tumour. Altogether this leads to a prolongation in mean survival times [Barth et al., 2012].

Besides occasional improvements in mean survival time, BNCT offers an increase in quality of life for most patients. Different to photon radiotherapy it is in almost all cases limited to two or three fractions and has with exceptions no serious side effects, as for example chemotherapy. A further effect might be with head and neck patients. If such tumours are surgically resected often substantial parts of head or face are impaired. Especially for recurrent cases reconstruction is difficult or even not feasible. For these patients BNCT dramatically increases quality of life, when surgery can be avoided, even if the treatment is only palliative [Haapaniemi et al., 2014].

1.3 Basics of dosimetry

1.3.1 Treatment planning and the need for dosimetry

In 1901 J.E. Gilman, Senior Professor at a Medical College in Chigago described radiotherapy with the following words: "I believe this treatment is an absolute cure for all form of cancer. I do not know what its limitations are…" [New York Times, 1901] But enthusiasm was lessened soon, once the pioneers of radiotherapy became conscious that radiation cures cancer, but also has the ability to generate it. Most of them died from cancer themselves. Emil Grubbe, the first to apply radiotherapy, died in 1960 after 92 successive surgical amputations and tumour resections, due to various malign tumours [Obituary, 1960].

The aim of radiotherapy, the complete extinction of tumour cells at the end of the treatment, is called tumour control (TC), often expressed as tumour control probability (TCP). TCP rises with increasing dose to target volume. But as described before, during radiotherapy dose is also deposited in the normal tissue. Thereby when dose to tumour is increasing, also dose to surrounding tissue does. As a consequence, the likelihood of side effects or cancer induced by the treatment, expressed as normal tissue complication probability (NTCP), is ascending, too. The relation between these probabilities is often shown in dose response curves, as schematically drawn in figure 1-3. Treatment planning and exact dosimetry are needed to ensure the balance between these dimensions.

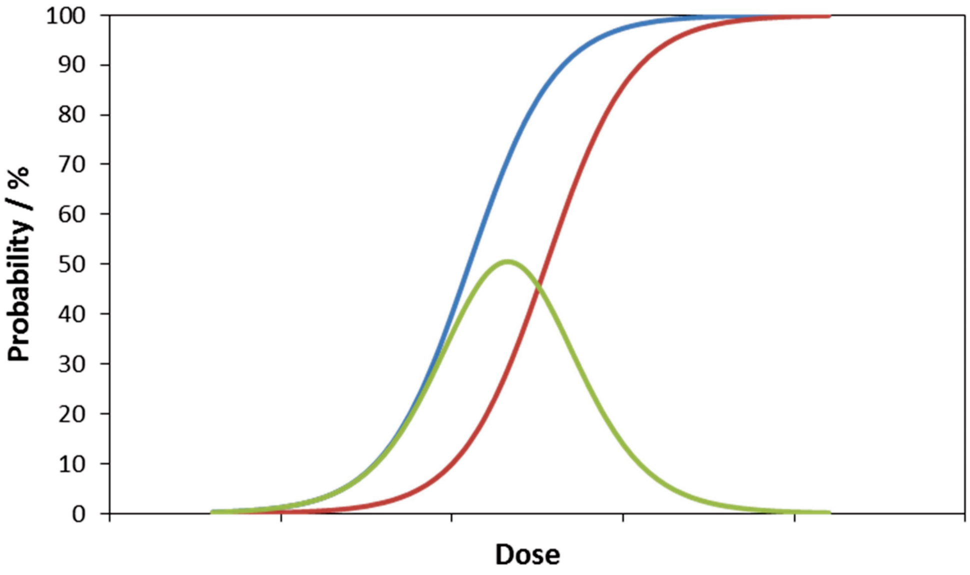

Figure 1-3. Schematic draw of a dose response curve. TCP is shown in blue, NTCP in red, green curve represents the probability of tumour control without side effects.

Today the need for an accurate beam delivery is quantified by models and clinical observations. As indicated by the slope of the curves in figure 1-3 a small change in dose can have big impact on the probability and thereby on the clinical outcome. It has been calculated that a change of 5% in dose deposited may lead to a change of 10% to 20% in TCP and 20% to 30% in NTCP [Papanikolaou et al., 2004]. Consistent with this Brahme [Brahme, 1984] stated that uncertainty in TCP through dose delivery should desirably by lower than 7%. Regarding head and neck tumours in the special case of larynx cancer it has been estimated from clinical data that a dose too low by 5% leads to a reduction of TCP by about 15%, while a dose too high by 5% increases the probability for side effects [Chappell and Fowler, 1994].

To ensure the correct dose delivery a detailed Treatment Planning (TP) is crucial. Modern techniques are computer based and require medical imaging. X-ray computer tomography (CT) and magnetic resonance imaging (MRI) are common techniques to identify the tumour, thus the target volume, and the surrounding tissue morphology. From these images TP programs are forming virtual patient models, in which geometrical, radiological and dosimetric aspects are brought to

an optimised solution. In case of EBRT this involves the selection of the particle (if miscellaneous are available), the choice of an appropriate particle energy and the arrangement and combination of different radiation fields.
Especially for the latter points, extensive knowledge about the treatment beam is necessary. A particle beam, no matter whether consisting of photons, charged particles or neutrons, needs to be exactly characterised in its energy spectrum, geometrical dimensions and angular distributions. Depending on the type of particle, this requires complex measurements and modelling.

In the following sections first essential interaction of radiation with matter and basic concepts of dosimetry are introduced before common detectors in neutron dosimetry are described.

1.3.2 Interactions of radiation with matter

As already indicated above, radiation can be divided into two groups directly and indirectly ionising radiation. Neutrons and photons are indirectly ionising particles as they are neutral and create secondary charged particles, which then deposit energy within the target matter. Charged particles, such as protons or heavier ions, coulomb interact with matter, hence they are called directly ionising particles. While photons and neutrons lose their energy in relatively few large events, charged particles do so in many small collisions, losing their energy gradually.
Accordingly this section has three subsections, one each for photons, charged particles and neutrons, and follows the book of Attix [Attix, 1986]. Explanations are limited to the relevant energy range in radiotherapy and the present work.

1.3.2.1 Photon interaction in matter

In the considered energy range, four interactions are responsible for the energy deposition of photons. In all cases the deposition occurs through secondary particles, mainly electrons, which are generated in these interactions.

Compton effect

In low Z media such as water, tissue or air the Compton effect is dominating from about 20 keV to 30 MeV, gradually narrowing with increasing Z. During the process a photon is scattering by an electron bound to an atomic nucleus. The photon transfers energy and momentum to the electron, so that it is ejected. The remaining photon is deflected with reduced energy. The distribution of kinetic energy given to the electron is almost flat from zero to the maximum electron energy, where a higher concentration occurs. The difference between the initial photon energy and the maximum energy of the ejected electron approaches 0.25 MeV for large photon energies.

Photoelectric effect

While the Compton effect dominates in low Z media, the photoelectric effect occurs especially at high Z and low energies. In the process an incident photon interacts with a tightly bound electron of the inner shell of an atom. The photon gives the kinetic energy completely to the electron, which is ejected. In turn the photon is totally absorbed and ceases to exist. While on the one hand the photon needs to have at least the potential energy with which the electron is bound to the atomic nucleus, on the other hand the interaction is more likely the smaller the initial photon energy is. The remaining vacancy in the inner shell of the atom, where the electron was ejected, is promptly filled by another electron from a less tightly bound shell. The excess in potential energy is disposed in two processes. Especially with K- and L-shell vacancies the transition is accompanied by the emission of a fluorescence x-ray. Alternatively energy can by disposed in the Auger effect, leading to the emission of several electrons from outer shells.

Pair production

Similar to the photo effect also pair production is an absorption process. The interaction requires the presence of a Coulomb force field, usually near an atomic nucleus, but also with lower probability in the field of an atomic electron. In both cases the photon disappears and gives rise to an electron and a positron. If the process occurs in the field of an atomic electron also the electron itself is emitted, for which reason the process then is called triplet production. The minimum photon energy of 1.022 MeV respectively 2.044 MeV (in the case of triplet production) is required. Excess energy of the photon is transferred into kinetic energy of the remaining particles. The probability for the interaction increases with photon energy and Z.

Photonuclear interactions

Photons, exceeding energies of a few MeV, can enter and excite atomic nuclei, which then emit protons or neutrons. These (γ,p)- or (γ,n)-reactions are photonuclear interactions. Since their relative contribution to the energy deposition is usually less than 5% of that due to pair production, they are often neglected in dosimetry. However due to their long range especially neutrons in clinical photon beams are of interest. They can change the spatial dose distribution in the patient and cause activation in the machine.

The attenuation of photons in matter can be described by Lambert Beer´s law. The intensity I at a certain depth x depends on the initial intensity I_0 and the attenuation coefficient μ, as shown in equation (1). The attenuation coefficient divided by the density ρ of the material gives the mass attenuation coefficient μ/ρ, which is more often used, since it is similar for many materials. The total mass attenuation coefficient can be written for photon interactions according to equation (2). Thereby τ/ρ is the contribution of the photoelectric effect, σ/ρ that of the Compton effect, and κ/ρ that of pair production. σ_R/ρ refers to the contribution of Rayleigh scattering. Since this type of interaction is elastic, deposits no energy, and deflects photons only though small angles, it needs to be considered only in narrow beams.

$$I = I_0 e^{-\mu x} \tag{1}$$

$$\frac{\mu}{\rho} = \frac{\tau}{\rho} + \frac{\sigma}{\rho} + \frac{\kappa}{\rho} + \frac{\sigma_R}{\rho} \tag{2}$$

The mass energy transfer coefficient μ_{tr}/ρ is a related quantity and sums the amount of energy transferred, due to the described interactions. Reduced by the fraction of radiation losses (bremsstrahlung, annihilation) the mass energy transfer coefficient becomes the mass energy absorption coefficient μ_{en}/ρ.

1.3.2.2 Charged particle interaction in matter

Charged particles are surrounded by their Coulomb electric force fields. While for a photon or neutron it is possible to pass through matter without any interaction at all, a charged particle interacts with electrons or nuclei of almost any atoms it passes. But while the neutral particles lose energy in one or only few big fractions, charged particles transfer only minute portions of their incident energy in every individual interaction. The process of gradually loss of kinetic energy is often described in the Continuous Slowing-Down Approximation (CSDA). Explanations of the complex processes, which are the basis of the slow-down, were foregone, since they are not relevant for the present work.

The average negative energy loss dE of a particle passing the distance dl is called stopping force S, illustrated in equation (3). The mass stopping force is the stopping force divided by the materials density ρ. The stopping force can be written as the sum of energy losses due to three interactions, as shown in equation (4). The electronic stopping force takes account of the interactions with electrons in the material and is dominating over a wide energy range. Energy transferred this way causes excitation or ionisation of the target atom. The electronic stopping force is commonly expressed in an equation, which is referred to as Bethe-Bloch formula. The nuclear stopping force is important especially at low energies, around or below 25 keV/u. Energy loss is mainly due to elastic scattering, which is (using some assumptions) handled with classical binary elastic scattering theory. In contrast radiative energy loss is relevant only for high energies above 106 MeV/u, where pair creation and Bremsstrahlung occur in heavy materials.

$$S = \frac{dE}{dl} \tag{3}$$

$$S = \left(\frac{dE}{dx}\right)_{elec} + \left(\frac{dE}{dx}\right)_{nucl} + \left(\frac{dE}{dx}\right)_{radiat} \tag{4}$$

From the known stopping force the range of a charged particle can be calculated as shown in equation (5) as integral over energy (from initial energy $\mathrm{E_0}$ to $\mathrm{E=0}$) of the inverse stopping force. Since no changes in the rate of energy loss are considered the range is referred to as CSDA-range $\mathrm{R_{CSDA}}$. However, distinction has to be made towards penetration depth and projected range. All three concepts are schematically illustrated in figure 1-4.

$$R_{CSDA} = \int_{E=0}^{E_0} \frac{1}{S(E)} dE \tag{5}$$

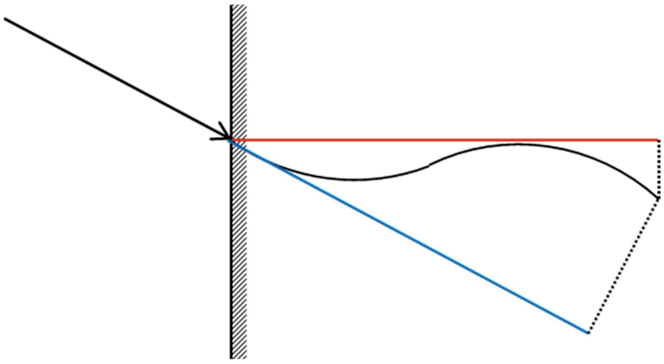

Figure 1-4. Schematic drawing of the three range concepts: R_{CSDA} is shown as black curve, penetration depth and projected range are indicated red and blue, respectively.

1.3.2.3 Neutron interaction in matter

Like photons neutrons are assigned to the group of indirect ionising radiation, but while secondary particles generated by photons are predominately electrons, the secondary particles due to neutrons exhibit a greater variety. In the considered energy range, from thermal to fast energies of about 20 MeV, two processes are mainly responsible for their production: Neutron capture and neutron scattering. Similar to photons the attenuation of neutrons can be described by exponential functions, as shown in equation (6). Thereby σ_t is the total cross section, which is a sum out of neutron scattering and neutron capture cross sections, N describes the number of target atoms, while l is the considered penetration depth.

$$I = I_0 e^{-\sigma_t N l} \tag{6}$$

Neutron Capture

Neutron capture reactions occur mainly with thermal neutrons and were already introduced with the example of the boron-10 reaction. They can be classified and compared by their thermal neutron capture cross section, which can range from less than a thousandth part of one barn to several thousand barn, as in the case of boron-10. If an element needs to be considered for dosimetry, hence, depends on the cross section as well as on the relative amount of the element in the irradiated material. Nuclear reactions can be also classified by the amount of energy, which is released by the reaction, the so-called Q value. It can be calculated according to equation (7), out of the rest masses m of the initial (index i) and final (index f) nuclei. A positive Q value indicates an exothermic reaction, while a negative Q value indicates an endothermic reaction. The boron-10 neutron capture has a Q value of 2.79 MeV and is exothermic. Endothermic reactions have an energy threshold, usually requiring neutron energies above this threshold.

$$Q = \left(m_i - m_f\right)c^2 \tag{7}$$

As mentioned before, the cross section is a measure of the probability for a certain reaction to occur, and often given as the thermal cross section. However, the value depends strongly on the energy of the neutron. Figure 1-5 gives the cross section of the neutron capture of boron-10 and gold-197 as a function of neutron energy. The thermal neutron capture cross section is only one point in this curve at 2.5 x 10^{-8} MeV. The curves in the figure as well as most curves for exothermic reactions exhibit two different parts. The first part is linear, as can be seen in the low energy region in figure 1-5. It is followed by the resonance part, also visible in the figure, but rather prevalent in the curve of gold-197 than with the boron-10.
The linear part is, as indicated by equation (8), inversely proportional to the speed of incoming neutron $\mathrm{v_n}$. Most neutron capture cross sections are therefore parallel in this part.

$$\sigma_n \sim \frac{1}{v_n} \tag{8}$$

This correlation is disturbed when the sum of neutron energy and the Q value of the formation reaction equal an excitation energy of the formed nucleus. At this point the transition between the target nucleus and the product is more likely and hence the cross section shows resonance. As the density of excitation states, the distance of resonances is decreasing with increasing energy. The width of such resonance is a function of the lifetime of the excitation state.

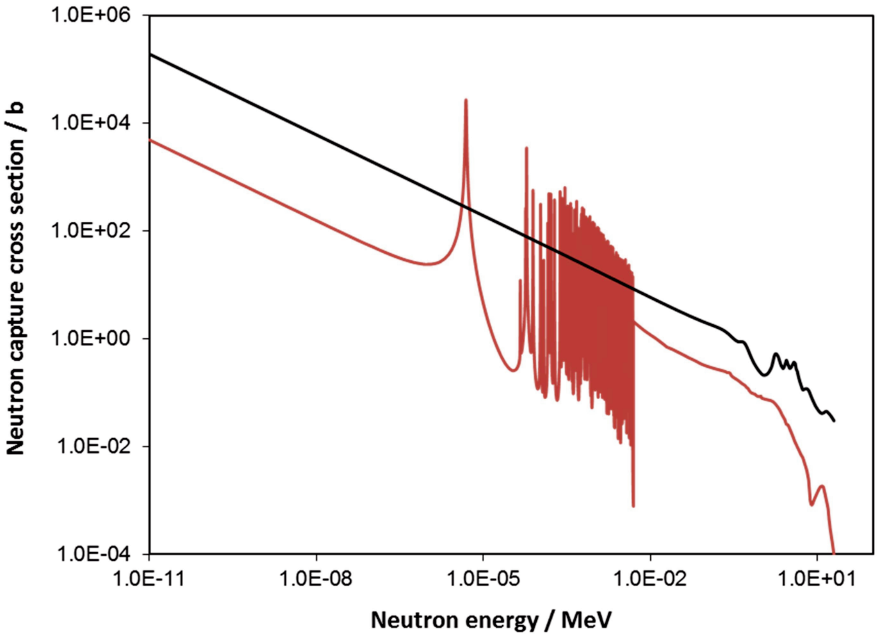

Figure 1-5. Neutron capture cross section as a function of neutron energy for boron-10 (black) and gold-197 (red). [ENDF]

In compounds the macroscopic cross section, defined according to equation (9), can be used to quantify the amount of interaction. In a certain material i the macroscopic cross section $\Sigma\mathrm{i}$ is given as the sum of contributions of each element x contained in it. Therefore the elemental microscopic cross sections $\sigma_{\mathrm{th}}^{\mathrm{x}}$ are multiplied by the number of atoms per volume $(\mathrm{N}\rho)_{\mathrm{x}}$. The resulting dimension of the macroscopic cross section is cm^{-1}.

$$\Sigma_i = \sum_x (N\rho)_x \sigma_{th}^x \tag{9}$$

Neutron scattering

Due to their energy and the corresponding low cross sections, epithermal or fast neutrons deposit energy predominantly by scattering processes. Similar to the neutron capture reactions scattering cross sections can give information about the probability of such processes. Assuming isotropic scattering in the centre of mass system, the average energy transferred $\overline{\mathrm{E}_{\mathrm{a}}^{\mathrm{tr}}}$ by elastic scattering to a nucleus is approximately given by equation (10). Here $\mathrm{M_n}$ refers to the neutron Mass, $\mathrm{M_a}$ to the mass of the target nucleus, and $\mathrm{E_n}$ to the neutron energy prior scattering. The more similar masses of neutron and nucleus are the more of the incident energy is transferred. For example in the case of hydrogen, scattering gives $\overline{E_H^{tr}} = 0.500\ E_n$, while scattering with oxygen gives $\overline{E_O^{tr}} = 0.083\,E_n$. In the case of light nuclei a sufficient amount of energy is transferred, so that the nucleus becomes recoiling.

$$\overline{E_a^{tr}} = E_n \frac{2M_a M_n}{(M_a+M_n)^2} \tag{10}$$

1.3.3 Basic concepts and quantities

Consecutive to the introduction of basic interactions of radiation with matter, the following section is dedicated to the basic concepts and quantities of dosimetry. Thereby explanations are focussed on problems addresses in this thesis.

Radiation dosimetry is in its original sense the determination of absorbed dose deposited by ionising radiation. A detector with the ability to measure absorbed dose is referenced to as dosimeter. However, also the measurement of related quantities is called dosimetry.

1.3.3.1 Particle Fluence and Flux

At a certain point the particle fluence ϕ is given as the number of particles N passing an infinitesimal small sphere with cross section da around this point. Fluence is usually expressed in units of cm^{-2}, the definition is shown in equation (11). The particle fluence rate is called particle flux φ and defined in equation (12), with the time interval dt, in units of cm^{-2}s^{-1}. Planar fluence is the number of particles crossing a plane. Due to the angle dependence of this definition, it only equals the definition in equation (11) when the radiation crosses the plane perpendicular.

$$\phi = \frac{dN}{da} \tag{11}$$

$$\varphi = \frac{d\phi}{dt} \tag{12}$$

Instead of the particle fluence, photons are often described by their energy fluence. However, the quantity is defined analogue to particle fluence. As shown in equation (13), in place of the number of particles, the value of the total energy R, they are carrying, is used.

$$\psi = \frac{dR}{da} \tag{13}$$

1.3.3.2 Kerma

The term kerma K is the acronym for *Kinetic energy released in matter* and only relevant for indirectly ionising radiation. It is defined as the energy transferred ϵ_{tr} in a certain volume V with mass dm, as shown in equation (14). Thereby only the kinetic energy transferred to the first generation of secondary particles is included. Kerma is expressed in units of J/kg or Gy. Transferred energy can be expressed according to equation (15), as the difference between radiant energy of uncharged particles entering V ($(R_{in})_u$) and radiant energy of uncharged particles leaving V ($(R_{out})_u^{nonr}$), plus the net energy derived from rest mass in V ($\sum Q$). The upper index nonr indicates that the radiant energy originating from radiative losses of kinetic energy of charged particles (such as Bremsstrahlung) is excluded.

$$K = \frac{d\epsilon_{tr}}{dm} \tag{14}$$

$$\epsilon_{tr} = (R_{in})_u - (R_{out})_u^{nonr} + \sum Q \tag{15}$$

In a photon field the kerma at a certain point is given, as defined in equation (16), as function of the energy fluence and mass energy transfer coefficient, which in turn is a function of photon energy and the elemental composition.

$$K = \int_{E=0}^{E_{max}} \psi'(E) * \left(\frac{\mu_{tr}}{\rho}\right)_{E,Z} dE \tag{16}$$

Since neutrons are commonly described by particle fluence or flux instead of energy fluence, for consistency a quantity called kerma factor $\mathrm{F_n}$ is defined as shown in equation (17). $\mathrm{F_n}$ is depending on the material and neutron energy E, and usually tabulated. Examples are shown in figure 1-6. It connects to K according to equation (18).

$$(F_n)_{E,Z} = \left(\frac{\mu_{tr}}{\rho}\right)_{E,Z} * E \tag{17}$$

$$K = \int_{E=0}^{E_{max}} \phi'(E) * (F_n)_{E,Z} dE \tag{18}$$

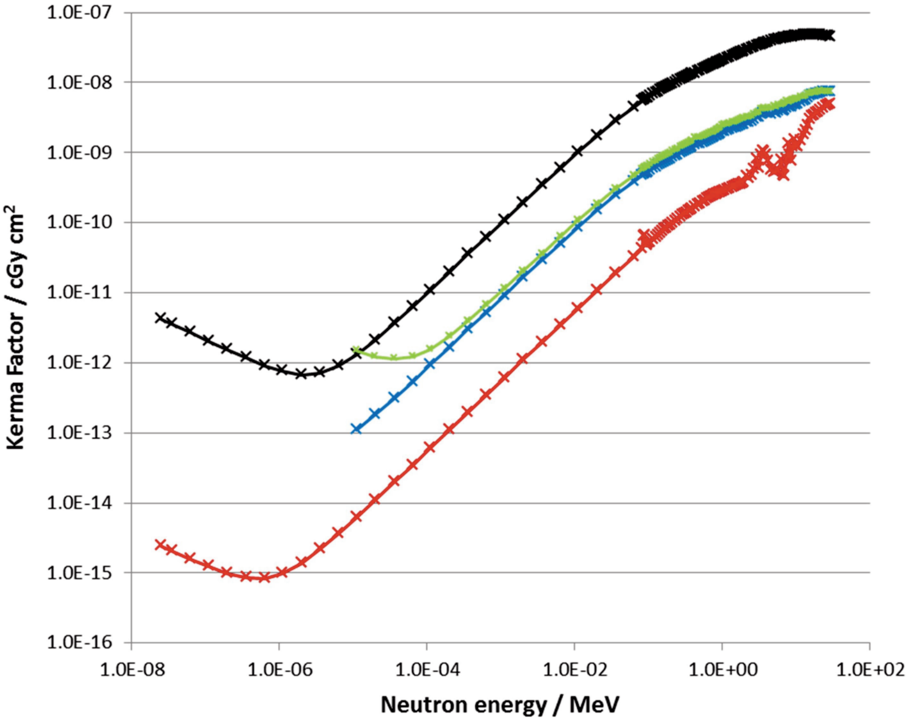

Figure 1-6. Exemplary neutron kerma factors $\mathrm{F_n}$ *for hydrogen (black), carbon (red), PMMA (blue), and ICRU muscle tissue (green).* [Caswell et al., 1980]

Kerma can be divided in two parts, collision kerma K_c and radiative kerma K_r. The first includes energy transferred by Coulomb force interactions with atomic electrons of the absorbing material, resulting ionisation and excitation. Thereby energy is deposited in or close to the particle track. Radiative kerma includes energy transferred by interactions with the Coulomb force field of atoms in the absorbing material, resulting in the production of x-rays or photons, which carry energy in bigger distance to the particle track (R_u^r). In the case of neutrons the radiative kerma is considered to be vanishingly small, so that kerma equals collision kerma. The transferred energy, contributing to K_c, is defined as net energy transferred ϵ_{tr}^n (equations (19) and (20)).

$$K_c = \frac{d\epsilon_{tr}^n}{dm} \tag{19}$$

$$\epsilon_{tr}^n = (R_{in})_u - (R_{out})_u^{nonr} - R_u^r + \sum Q = \epsilon_{tr} - R_u^r \tag{20}$$

1.3.3.3 Absorbed dose

Absorbed dose D is defined as energy imparted ϵ per mass by charged as well as uncharged particles in a volume V, according to equation (21). Dimension and units of absorbed dose are the same as for Kerma. Imparted energy is the sum of all energy deposited by energy depositing events and can be written according to equation (22). Thereby quantities are analogue to equation (15), additionally including the difference radiant energy of charged particles entering and leaving V $((R_{in})_c - (R_{out})_c)$.

$$D = \frac{d\epsilon}{dm} \tag{21}$$

$$\epsilon = (R_{in})_u - (R_{out})_u + (R_{in})_c - (R_{out})_c + \sum Q \tag{22}$$

Whenever comparing values of absorbed dose it is important to know the media for which the dose has been calculated. In radiotherapy values are often given as dose to water, since most reference phantoms are water filled. Dose to tissue, however, can vary from the dose to water, depending on the distribution of primary and secondary dose depositing particles. Especially regarding neutrons with the elemental composition also the cross sections, and hence secondary particle types and quantities, change significantly.

1.3.3.4 Linear energy transfer - LET

LET has been roughly introduced in chapter 1.1, but needs to be described more specific. Equation (23) gives the general definition of LET. According to ICRU report no.60 [ICRU Report 60, 1998] LET_Δ is the amount of energy lost by a particle in a material dE, due to secondary electrons with an energy less than Δ, over a distance dx. Without an upper energy limit LET_∞ numerically equals the electronic stopping force S_{elec}.

$$LET_\Delta = \frac{dE}{dx} \tag{23}$$

However, this definition is not meaningful for mixed radiation fields of particles with different energies or of different particle types. In these cases LET is defined as averaged LET, whereas it can be either dose averaged (index DA) or track length averaged (index TA). Both alternatives are shown in equations (24) and (25). Here $\phi_{\mathrm{i,E}}$ denotes the fluence of the particle i with kinetic energy E and the belonging stopping force $\left.\frac{\mathrm{dE}}{\mathrm{dx}}\right|_{\mathrm{i,E}}$.

$$LET_{DA} = \frac{\sum_{i,E} \Phi_{i,E} \left(\left. \frac{dE}{dx} \right|_{i,E} \right)^2}{\sum_{i,E} \Phi_{i,E} \left. \frac{dE}{dx} \right|_{i,E}} \tag{24}$$

$$LET_{TA} = \frac{\sum_{i,E} \Phi_{i,E} \left. \frac{dE}{dx} \right|_{i,E}}{\sum_{i,E} \Phi_{i,E}} \tag{25}$$

If not indicated differently in the present work the dose averaged LET is used for fields composed of different particles or particles of different energies.

1.3.3.5 Relative biological effectiveness - RBE

To describe the effect of ionising radiation on biological systems the term of absorbed dose is deceptive. RBE is introduced to weight radiation regarding its effectiveness. Although it is of little relevance for this work RBE is briefly described for completeness and due to its analogy to a quantity introduced later, called relative effectiveness.

Irradiation with two different types of particles, but with the same absorbed dose, may lead to a different effect (i.e. cell survival, necrosis) in a biological system. To allow a comparison of different types of radiation the concept of RBE uses ^{60}Co-gamma rays as reference according to equation (26). Dose $\mathrm{D_x}$ of a considered radiation x, and the ^{60}Co dose $\mathrm{D}_{^{60}\mathrm{Co}}$ are chosen in a way, that they have the same biological effect on the material

$$RBE = \left. \frac{D_{^{60}Co}}{D_x} \right|_{-} \tag{26}$$

In this context two points need to be considered. Although RBE is often described as a function of averaged LET [Wilkens and Oelfke, 2004; Sørensen et al., 2011], also regarding FNT [Pihet et al., 1990], there is no strict connection or correlation between RBE and LET [Kraft et al., 1992]. Furthermore the actual value of the RBE depends strongly on the chosen biological endpoint and the whole concept is seen critical also towards its validity in BNCT [González and Santa Cruz, 2012].

1.3.3.6 Charged particle and radiation equilibria

The presence of Radiation Equilibrium (REQ) enables equalisation of absorbed dose D and net rest mass converted to energy $\overline{\Sigma \mathrm{Q}}$, while in Charged Particle Equilibrium (CPE) absorbed dose equals the collision kerma $\mathrm{K_c}$. Both concepts therefore are important to relate basic quantities in radiation physics.

REQ exists in a certain volume v included in a larger volume V, if density and atomic composition of the medium are homogenous, the radioactive source is uniformly distributed and there are no external electric or magnetic fields present, perturbing charged particle paths. The volume V needs to be large enough, so that the maximum distance of penetration of any emitted ray and following, secondary particles is less than the minimum distance of v to the boundaries of V. As a consequence for each type and energy of a ray entering v, another identical ray leaves. According to equation (22) this means $(R_{in})_u = (R_{out})_u$ and $(R_{in})_c = (R_{out})_c$, hence equation (21) describing energy imparted becomes equation (27).

$$\epsilon = \sum Q \qquad (27)$$

Practical importance has the concept of REQ for example in dosimetric considerations for nuclear medicine and radiobiology, where radioactive tracers are introduced into the human body for diagnostic, analytical or therapeutic purposes.

For the case of external fields of indirect ionising radiation the concept of CPE is of greater importance. Requirements for the presence of CPE are similar to those of REQ. Again a Volume V is considered, in which density and composition of the penetrated medium are homogeneous. The field of indirect ionising radiation needs to be uniform through the medium and only negligibly attenuated during the passage through the medium. External magnetic and electric fields can be present if they are homogeneous. Due to these requirements secondary charged particles are generated homogenously through the medium. But particles are not emitted isotropically, as in the case of radioactive sources. However this anisotropy is homogenous through the considered volume, and hence conditions are sufficient to produce CPE in the smaller volume v. As a result $(R_{in})_c = (R_{out})_c$, and in addition $(R_{out})_u = (R_{out})_u^{nonr} - R_u^r$, in the case that v is small enough to allow photons, contained in the radiative loss, to escape. Consequently equations (20) and (22) are equal and give equation (28).

$$D = K = \Phi F_n \qquad (28)$$

1.4 Neutron dosimetry

1.4.1 Neutron sources

Types of neutron sources are numerous and chosen specifically for each application. In the present work three different research reactors were used, for which reason the discussion of neutron sources is focussed on them.

In nuclear reactors neutron production is based on fission of heavy element isotopes, such as uranium-235, which is the most common fissionable material, or plutonium-239. Other materials are possible, but less often used. The fission isotope captures a neutron, forming, in the case of uranium-235, the highly excited uranium-236, which then undergoes fission. The neutron capture cross section shows the typical energy dependence, for which reason fission occurs predominantly with thermal neutrons. Under emission of prompt neutrons and gamma rays (timescale: 10^{-14} s – 10^{-15} s) the two fission fragments turn two primary fission products. Due to the excess of neutrons these nuclei undergo β^--decay and emit further gamma rays, converting to secondary fission products. The β^--decay chain is continued until stable isotopes are formed. When the total energy released in such decay exceeds the binding energy of the last neutron in the daughter nucleus, this nucleus eventually emits neutrons, promptly after the decay. Such neutrons occur with the half-life of the $\beta\beta$ –-decay, seconds or minutes after the fission. In contrast to the prompt neutrons they are called β-delayed neutrons, and represent about 1% of the total neutron number.

Table 1-3. Energy balance of nuclear fission of uranium-235. [Weinberg and Wigner, 1958]

Energy or radiation type	***Mean energy / MeV***
Kinetic energy of the fission fragments	*167*
Kinetic energy of prompt neutrons	*5*
Energy of prompt gamma rays	*6*
Electrons from β^--decay of fission products	*8*
Electron antineutrino from β^--decay of fission products	*12*
Gamma rays from fission products	*6*
Total energy per fission	*204*

The total energy released during fission is distributed between the different processes as shown in table 1-3. The kinetic energies of the prompt neutrons are distributed on average between 2.7 neutrons. The mean energy of emitted neutrons is about 2 MeV, while 0.7 MeV is the most probable emission energy. 99.8% of all neutrons have energies below 10 MeV. For the continuation of the nuclear chain reaction these fast neutrons need to be moderated to thermal energies to undergo the next fission. In most research reactors the moderation is assured using either light or heavy water.

As mentioned before in BNCT also accelerators are used for neutron production. Their advantages have been already discussed in section 1.2.3., mechanism is still outstanding. In accelerators neutrons are produced in nuclear reactions, mostly induced by protons. The endothermic reactions ^{7}Li(p,n)^{7}Be and ^{9}Be(p,n)^{9}B are favourable due to parameters as cross section, energy threshold (defining the minimum proton energy), and kinematics of the emitted neutrons. As discussed above during fission neutrons emitted have average energies around 2 MeV. In (p,n)-reactions neutrons can be generated with a sufficient production rate below 1 MeV, requiring much less moderation to reach the epithermal energy range. Therefore, the process is more efficient and reduces the fast neutron contamination in the beam.

Outside BNCT radioactive neutron sources are common. They can be based on different decay modes. Instead of induced fission, like in a nuclear reactor, the spontaneous fission of the isotope californium-252 can be used, also providing neutrons with average energy of 2 MeV. Besides several types of Be(α,n) sources are available. As alpha emitter polonium-210, plutonium-239, americium-241, and radium-226 are employed. With 4 MeV though average emission energy is higher compared to other sources. Also the neutron yield is quite low with about one neutron per 10^4 alpha particles. Less common are sources based on photonuclear reactions or spallation.

1.4.2 Requirements in neutron dosimetry

Neutrons interact in diverse manner with material or tissue. The observed effect per unit of absorbed dose strongly depends on the neutron energy. This way the problem of neutron dosimetry is also a problem of neutron spectrometry. Furthermore, in all sources described, the emitted neutrons are accompanied by gamma rays, originating not only from the process of neutron generation, but also from activation of structure and shielding materials. Neutron fields are hence mixed fields. Due to the different biological effectiveness of these primary source particles, it is necessary to separate the absorbed dose deposited by each of them. Analogously also the absorbed doses of secondary particles from neutron interactions (described in section 1.3.2.3) need to be separated. The total neutron dose absorbed by a material is therefore the sum of several dose components. Each dose component includes the absorbed dose of a certain type of particle or interaction.

Since a single detector is not capable to quantify all dose components usually several detectors are combined. In the ideal case each dosimeter is sensitive towards a certain particle species or energy and completely insensitive towards the others. However, since most dosimeters are not that specific interpretation of the dosimeter reading, the so-called response, requires knowledge of the response function towards the particle species of interest. Response functions specify precision and accuracy of the dosimeter, as well as detectable dose range and rate, signal stability, and of course energy dependence. Because dosimeters commonly used in neutron dosimetry are not absolute, great effort is necessary to determine response functions and to calibrate the dosimeter for a specific radiation field.

1.4.3 Common neutron dosimeters

The types of dosimeters used in neutron dosimetry are manifold. In addition every type exists in numerous variations. The following subsections are confined to those dosimeters with relevance to this work and are only a brief introduction.

1.4.3.1 Ionisation chambers

The detection of an ionisation chamber (IC) is based on the ionisation of matter by radiation. Applying an electric field, the charge created can be measured at the electrodes. To quantify the energy deposited, the irradiated volume, the mean energy per ionisation in this volume, and the efficiency of the collection of charge have to be known.

ICs are the most widely used dosimeters in radiotherapy. Although it is possible to use them as absolute dosimeters, this is usually not practicable outside national standard laboratories. In most cases it is preferred to work with chambers having a calibration traceable to such laboratory. Detectors are available in a large variety of designs. In BNCT neutron fields almost exclusively gas-filled, cylindrical cavity ICs are used. They are capable of a great variety of designs and can be made relatively small to enable measurements inside a phantom. On the one hand the needed continuous power supply is a disadvantage, on the other hand the real time measurement is an advantage compared to passive detectors.

The design of such chambers is usually simple. The high voltage is applied to the chamber wall, serving as one electrode. The other electrode is a rod, positioned central in the cylindrical cavity, connected to the electrometer, where the detector signal is read. The cavity is continuously flushed with a gas. Gas type and wall material need to be chosen regarding the dose component of interest. For example with a carbon graphite chamber flushed with argon the neutron sensitivity is quite low, while the majority of the signal is generated by photons.

1.4.3.2 Activation foils

Activation foils are used for neutron spectrometry. The result of the measurement is therefore not a dose but a flux, fluence or the energy distribution of both. The method is based on the irradiation of different metal foils with neutrons and the determination of their activation afterwards. The present text mainly follows the elaboration of Nigg [Nigg, 2012].

The response function of each activation foil is given by their energy dependant cross section. Some materials are primarily sensitive towards thermal neutrons. This is the especially the case when there are no significant resonances in the cross section. Otherwise if there are major resonances the detector foil is sensitive particularly at the energy of the resonance. An example for such an element is gold (see red line in figure 1-5). Gold has a broad resonance at 5 eV. The relative sensitivity at this point can be even increased if the thermal neutrons are shielded. A common shielding material is cadmium, often used in form of little capsules, providing a layer of about 1 mm cadmium in each direction. Mainly the isotope cadmium-113 is responsible for the effect as obvious from the cross section indicated in figure 1-7 by the black line. By passaging through a layer of cadmium neutrons with energies smaller than 0.4 eV are absorbed, while those with higher energy most likely pass the shielding.

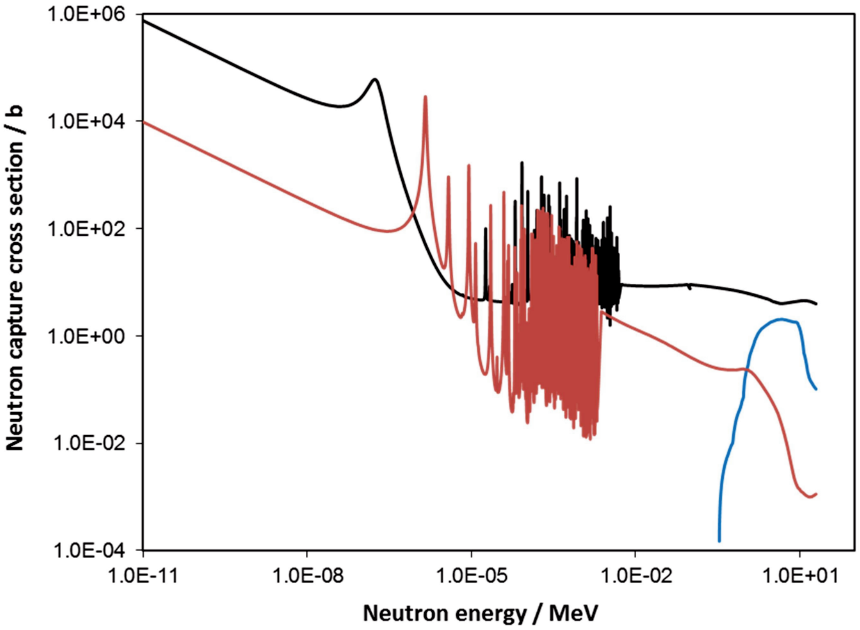

Figure 1-7. Total neutron capture cross section for cadmium-113 (black line), (n,γ)-cross section for In-115 (red line) and inelastic scatter cross section for In 115 (blue line), all as a function of energy [ENDF].

Also shown in the figure is the cross section of the (n,γ)-reaction of Indium-115 (red line). It is very similar to the one of gold, having a broad resonance at 1 eV. Most of the resonances are in the epithermal or lower fast energy range. To gain sensitivity above 10 keV therefore endothermic reactions with an energy threshold are taken. One example is shown in figure 1-7 by the blue line. Neutrons with energy above 340 keV have the ability to interact with indium-115 in a competing process via inelastic scattering. During this process the isotope is exited from its ground state to the isomeric state indium-115m. It has a half-life of 4.49 hours and returns to the ground state by emission of a 336 keV gamma ray.

When choosing elements and isotopes for neutron spectrometry several requirements need to be fulfilled. The isotope of interest should be in adequate amount inside the foil. For a good resolution in gamma spectrometry lines below 100 keV should be avoided. For sufficient gamma ray yield, the abundance of the observed line should be high, paired with a feasible cross section. In addition the half-life of the produced isotope should be neither to short, to have enough time for the measurement, nor to long, since then also the gamma ray yield declines and the foil cannot be re-used for a longer time. Foils can be used alone to measure an integral flux or combined, to conduct neutron spectrometry. In this case foils are chosen such way, that resonances and regions of favourable sensitivity are distributed over the whole energy range of interest.

The analysis afterwards is performed using algorithms. In the following a few mathematical details are given. The response or activation rate R of a foil is given as the product of the microscopic cross section $\sigma_{\mathrm{d}}(\mathrm{E})$ of the observed interaction and the neutron flux $\phi_{\mathrm{d}}(\mathrm{E})$, both as a function of energy. Equation (29) illustrates this relation. However in this form the equation is not sufficient. The neutron flux at the detector position is perturbed by the foil, especially in combination with shielding. To correct this the equation is modified as shown in equation (30), through the extension with the unperturbed flux at the sample position $\phi(\mathrm{E})$. Since the quotient in equation (30) is only a flux ratio it can be replaced by the self-shielding function $P_d(E)$, as shown in equation (31).

$$R = \int_0^\infty \sigma_d(E)\phi_d(E)dE \tag{29}$$

$$R = \int_0^\infty \sigma_d(E)\frac{\phi_d(E)}{\phi(E)}\phi(E)dE \tag{30}$$

$$R = \int_0^\infty \sigma_d(E)P_d(E)\phi(E)dE \tag{31}$$

The determination of a neutron spectrum is usually done in energy bins, with group fluxes Φ_j in intervals with EL_j and EH_j as lower and upper energy limits, as defined in equation (32). For simplification the activation constant a_{ij} is introduced as given in equation (33). Thereby the index i differentiates between foils and interactions, limits are the same as in equation (32).

$$\Phi_j = \int_{EL_j}^{EH_j} \phi(E) dE \tag{32}$$

$$a_{ij} = \frac{\int_{EL_j}^{EH_j} \sigma_d^i(E) P_d^i(E) \phi(E) dE}{\int_{EL_j}^{EH_j} \phi(E) dE} \tag{33}$$

In consequence equation (31) can be written as the summation shown in equation (34). NG gives the number of energy groups, indicated by index j. NF gives the number of interactions. Combining variations of equation (34) for all available activation responses leads to the system of equations shown in matrix form in (35) or in the short form in (36).

$$R_i = \sum_{j=1}^{NG} a_{ij} \Phi_j \tag{34}$$

$$\begin{bmatrix} a_{11} & a_{12} & a_{13} & \dots & a_1 \\ a_{21} & a_{22} & a_{23} & \cdots & a_{2NG} \\ a_{31} & a_{32} & a_{33} & \cdots & a_{3NG} \\ \vdots & \vdots & \vdots & & \vdots \\ a_{NF1} & a_{NF2} & a_{NF3} & \dots & a_{NFNG} \end{bmatrix} \begin{bmatrix} \Phi_1 \\ \Phi_2 \\ \Phi_3 \\ \vdots \\ \Phi_{NG} \end{bmatrix} = \begin{bmatrix} R_1 \\ R_2 \\ R_3 \\ \vdots \\ R_{NF} \end{bmatrix} \tag{35}$$

$$[A][\Phi] = [R] \tag{36}$$

Three possible relations between NF the number of energy intervals and NG the number of detector responses need to be considered. If NG equals NF the matrix [A] is square, provided that the rows are linearly independent, matix (35) can be solved by any standard solution method. Linearly independence implies that the response functions are sufficiently different and the responses are measured with adequate precision. In practise this case is reached when quantities as the cadmium ratio are determined. For the cadmium ratio two gold foils are measured, inside and without cadmium, resulting in the thermal neutron flux and the epithermal/fast neutron flux. Also other ratios of the same foil material with and without cadmium can be determined. They can be used to compare different research reactors.

Assumed that NF is bigger than NG the problem is over-determined and the excess information can be used to in a linear least square procedure. The third possibility is the under-determination of the system when NF is smaller than NG. In this case there is no unique solution for the problem and extra information is required. A popular option is the use of a priori neutron spectrum, in combination with algorithms, which iterate the matrix (35) to the most probable solution. This way a more detailed energy distribution can be gained, than with the other methods, but the result is strongly depending on the priori spectrum and also the iteration method, why they have to be chosen carefully. However, the third case is the method of choice during most applications, since sufficient information for advanced utilisation, as for example dosimetry, is gained.

1.4.3.3 Further detectors relevant in BNCT dosimetry

Although the two detector types mentioned are mainly used in BNCT, Nigg [Nigg, 2012] names several other types which were adapted for BNCT.

Among gas-filled detectors besides ICs also proton recoil spectrometers, fission chambers, BF_3 and ^3He detectors are equipped. The two later types are used because of the large cross sections of boron-10 and helium-3 for emission of charged particles after neutron capture. In appropriate gas the energy of these particles is detected analogue as in ICs, although detectors are operated as proportional counters. They are used for beam monitoring or simple flux measurements, but do not provide further information about the incident neutron. Proton recoil detectors are regularly filled with hydrogen gas at pressures of a few atmospheres and also operated as proportional counters. Using a multichannel analyser a proton recoil spectrum is detected, which can be unfolded into a neutron spectrum. Depending on the fissionable isotope, fission chambers can have selectivity for fast neutrons, thermal neutrons, or both. Neutrons entering the chamber have the ability to initiate a fission process. The subsequent fragments cause ionisation in the gas, i.e. argon; resulting charge is collected. Regularly fission chambers are used for beam monitoring.

Thermoluminescent dosimeters (TLD) are important in general in neutron dosimetry. They are made out of materials capable of storing energy, i.e. deposited during irradiation, which is released during later heating as luminescence. Detectors based on lithium fluoride have most applications in BNCT. As electron and hole trapping centres, so-called activators, the material contains manganese or titanium. By using enriched lithium-6 (TLD-600) the neutron sensitivity can be enhanced, while when using lithium-7 (TLD-700) the dosimeter is nearly insensitive towards neutrons. Using natural lithium the detector is called TLD-100.

Gel detectors, also called Fricke dosimeters, are read-out by optical absorption or magnetic resonance imaging. The tissue-equivalent gels contain ferrous ions (Fe^{2+}) which are oxidised to ferric ions (Fe^{3+}) during irradiation. Detectors are capable of two- and three-dimensional dosimetry, depending on the shape of the gel.

1.5 ESR dosimetry

Ionising radiation has in certain materials the ability to form stable radicals. These radicals can be read-out by Electron Spin Resonance (ESR) spectrometry, also referred to as Electron Paramagnetic Resonance (EPR) spectrometry. Since in this work nearly exclusively carbon centred radicals are examined, the denotation ESR is preferred. Using calibration the amount of radicals in such material can be correlated to a dose response. In this chapter first ESR spectrometry is briefly introduced, before the details of ESR dosimetry are given on the example of alanine, the best known ESR detector.

1.5.1 ESR spectrometry

A comprehensive description of ESR spectrometry, including consideration of quantum mechanics and related effects, can be found in the books of Atherton [Atherton, 1993] and Gerson and Huber [Gerson and Huber, 2003], while here only the basic mechanism is described, as necessary for the understanding of

ESR dosimetry and the present work.

The detection mechanism of ESR spectrometry is based on the Zeeman effect. Every electron has a spin with spin quantum number $s = +\frac{1}{2}$ and a magnetic moment, leading to a secondary spin quantum number $m_s = \pm\frac{1}{2}$. The belonging energy states are generally degenerated, but can be separated for example in an external magnetic field. Then the electron spin can be orientated parallel to the magnetic field ($m_s = +\frac{1}{2} \triangleq |\alpha\rangle$) or antiparallel ($m_s = -\frac{1}{2} \triangleq |\beta\rangle$). The energy of each state is given according to equation (37), with the Landé factor g_e, having a value of 2.0023 for the free electron, the Bohr magneton μ_B, and the field strength of the external magnetic field B_0. The difference between both states is hence given by equation (38), which depends linearly on the magnetic field strength, and leads to a separation of energy levels as shown in figure 1-8.

$$E_{\alpha/\beta} = m_s g_e \mu_B B_0 \tag{37}$$

$$\Delta E = E_\alpha - E_\beta = g_e \mu_B B_0 \tag{38}$$

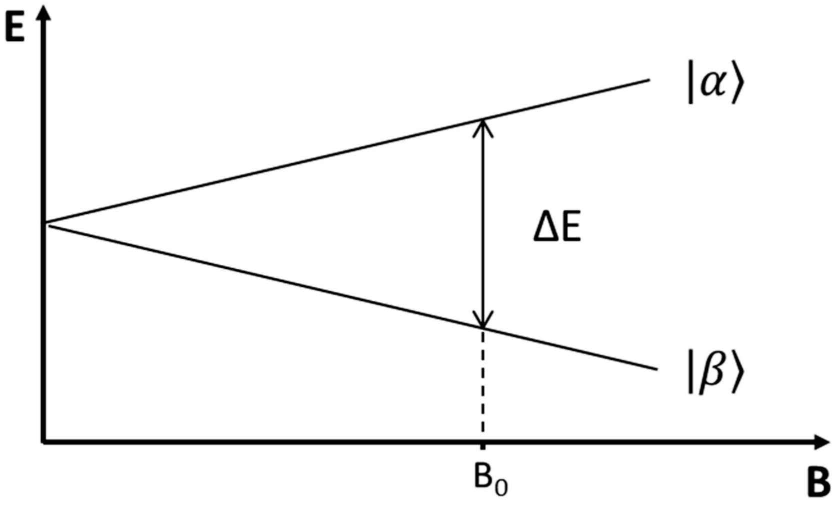

Figure 1-8. Zeeman splitting of electron spin states as a function an external magnetic field with field strength B.

In material with multiple electrons orientating in the magnetic field the distribution of spins between the two states is given by the Boltzmann equation (39). Thereby n is the population of either state, k the Boltzmann constant, and T the temperature in kelvin. Given a thermal equilibrium the lower spin state is populated more than the upper spin state. If an electromagnetic wave fulfils the resonance condition, shown in equation (40), hence, overall a fraction of electrons is lifted to the upper state and parts of the electromagnetic wave are absorbed. The amount of absorption is measured and can be correlated to the number of electron spin centres. Usually the absorption spectrum is displayed as first derivative as shown in the example in figure 1-9. Frequencies needed for resonance are in the microwave energy range. Due to practicability in most ESR spectrometers the frequency of the electromagnetic wave is kept constant, while the magnetic field strength is varied.

$$\frac{n_\alpha}{n_\beta} = \qquad \frac{\Delta E}{kT}\Big) \tag{39}$$

$$\Delta E = g_e \mu_B B_0 = h\nu \tag{40}$$

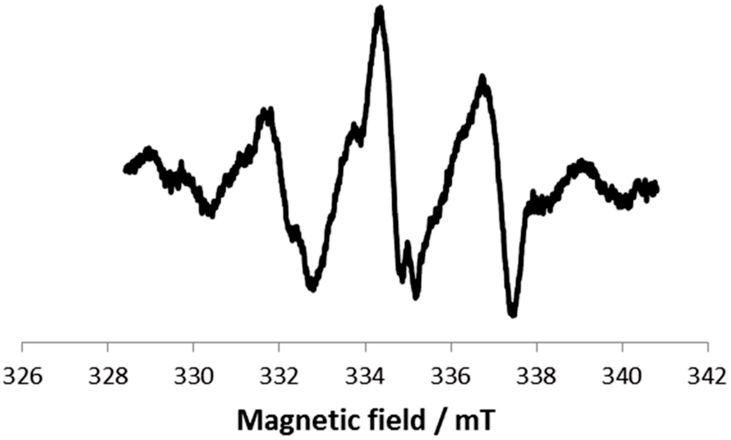

Figure 1-9. Exemplary ESR spectrum of alanine irradiated with neutrons.

The peak in ESR spectra might be split as in the example due to the so-called hyperfine interaction. It occurs between the radical and the magnetic moments of surrounding atomic nuclei. The line width ΔB depends on the lifetime Δt of the spin states. According to equation (41) Δt is a function of spin-lattice relaxation time T_1 and the spin-spin relaxation time T_2. The spin-lattice relaxation tends to restore the thermal equilibrium by energy transfer to the lattice, after it was perturbed by the electromagnetic wave. In organic molecules usually large T_1 values are found. Spin-spin relaxation occurs through mutual spin flips, due to dipolar and exchange interactions. In organic radicals T_2 is usually much shorter compared to T_1 and therefore dominates the line width. Exchange interactions are most likely with overlapping orbitals, hence with increasing spin density T_2 decreases and the line width increases.

$$\Delta B \sim \frac{1}{\Delta t} = \frac{1}{T_1} + \frac{1}{T_2} \tag{41}$$

1.5.2 The alanine dosimeter

Alanine is a chiral amino acid and for dosimetric purposes used as L-α-alanine (molecule shown in figure 1-10 a)). The detector has been first mentioned by Bradshaw [Bradshaw et al., 1962] and is commercially used for photon dosimetry today. However, it has been also used in extensive studies with protons, particles heavier than protons, neutrons, and even antiprotons [Bassler et al., 2009].

1.5.2.1 The alanine radical and ESR spectrum

As most organic substances alanine contains an even number of electrons, which are centred at the atoms or located between them, forming covalent bonds. However, the sum of all magnetic moments of the electrons is zero and hence the substance is diamagnetic and not ESR active.

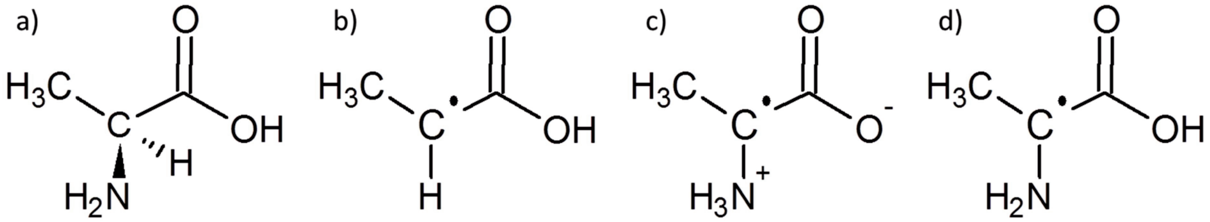

Figure 1-10. Molecule structures of a) L-α-alanine, b) to d) alanine radicals after irradiation

Ionising radiation has the ability to break the bonding between two atoms, resulting in two unpaired electrons, detectable by ESR spectroscopy. These unpaired electrons are called free radicals and commonly known for their short life time. In solutions life time is usually in the sub-second range, but in a rigid molecular surrounding, as present in most crystal lattices it can be much longer. The radicals formed in L-α-alanine can be seen as almost stable. As a measure for the amount of radicals figure 1-11 shows the fading of the ESR signal for different beam qualities. Under normal laboratory storing conditions regarding temperature and humidity, a decrease is only observed for high doses deposited by particle radiation. Thereby fading is increasing with particle mass and decreasing with particle energy. Among the four proton energies fading is biggest with the lowest energy [Hansen and Olsen, 1989]. Besides particle mass and energy fading is a strong function of absorbed dose. While with 0.5 MGy deposited by 16 MeV protons a decrease of 16 % has been observed 4000 h post irradiation, it is only 3% for a dose of 10 kGy [Hansen et al., 1987]. More recently with carbon ions no fading was observed until 660 h after irradiation at doses below 100 Gy [Herrmann et al, 2011].

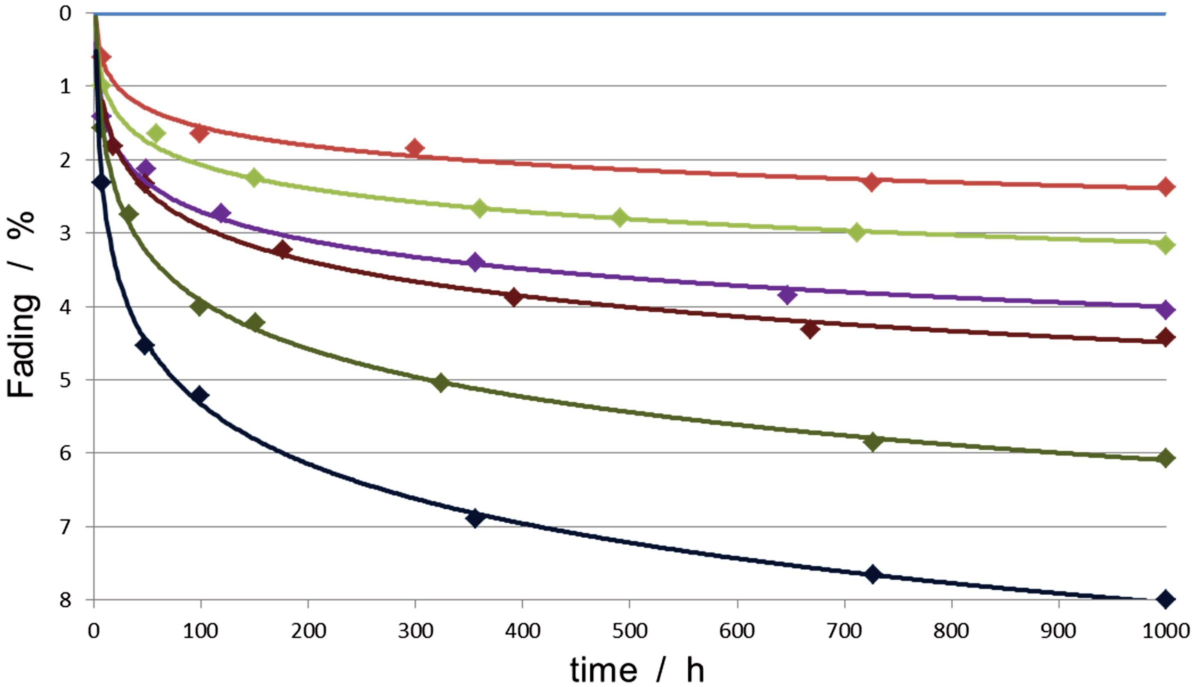

Figure 1-11. Fading of the alanine ESR signal for ^{60}Co gamma rays and 10 MeV electrons (blue), 16 MeV protons (red), 6 MeV protons (green), 3 MeV protons (purple), 1 MeV protons (dark red), 15.2 MeV/u ^{48}Ca ions (dark green) and ^{16}O ions (dark blue). [Hansen and Olsen, 1989]

The exact process of radical formation in the crystals remains unclear, but the molecules in figure 1-10 b) to d) have been identified to account for the biggest fraction among the radicals generated. The spectrum is dominated by the radical in part b), which accounts for about 60% of the signal. However, fractions might vary with the radiation quality [Malinen et al., 2003]. The typical first derivative L-α-alanine spectrum was already presented in figure 1-9, as recorded after irradiation in a neutron field within this work. Due to hyperfine coupling with the nuclear magnetic moment of hydrogen atoms in the molecule, the spectrum has multiple lines instead of one single line.

For the quantitative analysis of the ESR spectra several options are possible. Since the form of the spectrum in figure 1-9 shows only very little abbreviations during irradiation with different LET the spin concentration is proportional to the peak-to-peak amplitude. The more general approach, the determination of the area below the absorption curve, is more intricate and less used in dosimetry.

The evaluation can be carried out either absolute or relative. The absolute spin concentration can be gained through knowledge about the paramagnetic susceptibility. However, this is not practicable, since the necessary data is difficult to obtain. Consequently the absolute spin concentration is more often determined using primary standards, for which the number of unpaired spins is determined by an alternative method, or using secondary standards, which themselves are referring to primary standards, but having a better long term stability compared to those. However, due to numerous experimental parameters influencing the measurement, overall uncertainties with either of the standards may amount to up to 50%.

In most literature as well as in the present work therefore only relative measurements, working with standard samples, are carried out. These samples (compare section 1.5.2.2) can be chosen to have identical properties and dimensions, thereby reducing the influence of experimental parameters dramatically. Further simplification is made by using dosimetric quantities for their calibration. Overall uncertainties down to a few percent are achievable.

1.5.2.2 Dosimetric Properties

In today’s practise simply microcrystalline alanine powder, compressed to pellets, is used, often mixed with a binder such as paraffin or polymers like polyvinylpyrrolidone. The binder enables easier handling, since the compressed pellets are less brittle. The dimensions of the dosimeter can be reduced to cylinders in the millimetre range. Therefore their positioning in phantoms or any experimental setup is simple, perturbing the field only very little. In this context also the “tissue equivalence” needs to be mentioned. Alanine as an organic material contains the same elements as tissue, and has with 1.42 g/cm³ also a similar density. Therefore the alanine detector is considered tissue equivalent. However, neutron interactions rely on very few interactions with certain isotopes, hence the validity of the equivalence is shortened, due to the different element concentrations.

Typical dose response curves of alanine are shown in figure 1-12, as a function of absorbed dose in Gy against the corresponding ESR signal (arbitrary units). The curves and data points have been extracted from the publication of Hansen and Olsen [Hansen and Olsen, 1985]. Most conspicuous is the large range of linear correlation between absorbed dose and ESR signal, which is reaching up to several thousand Gy. At high doses the curves show saturation. For heavier ions also a decrease after the point of saturation has been observed, but is not shown in the figure. The curves plotted in figure 1-12 are following the assumption, which considers alanine a one-hit-detector and is further discussed in section 1.6.2.1.

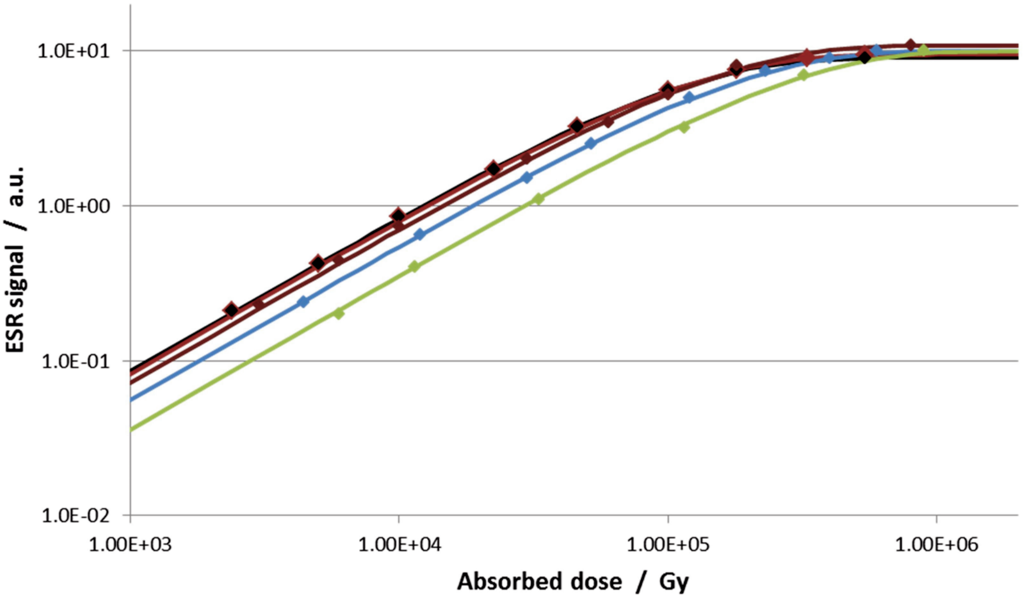

Figure 1-12. Dose response curves for alanine irradiated with ^{60}Co gamma rays (black), 6 MeV protons (dark red), 16 MeV protons (ligh red), 20 MeV alpha particles (blue), and 21 MeV ^{7}Li ions (green) [Hansen and Olsen, 1985]. Curves were fitted using equation (46) in section 1.6.2.2.

While in figure 1-12 the black curve of the ^{60}Co gamma rays and the light red curve of the 16 MeV protons are almost identical until saturation, the curves of the lower energy protons with 6 MeV, the alpha particles and the lithium ions deviate from them. Though they are all parallel in the linear section indicates that the radical yield of those particle species is lower. In general it can be stated, that the radical yield is particle and energy dependant.

For calibration pellets are irradiated in a known calibration field, to a certain dose response, which is then compared to the signal from pellets in the investigated field. Calibration is typically done in photon fields. The response of photons shows only little dependence on the photon energy. Figure 1-13 a), using data from Waldeland [Waldeland et al., 2010a], shows that the response function approaches 1.0 above 100 keV. The two functions shown are both relative towards ^{60}Co gamma rays. The black dots represent the relative photon response of the indicated energy in terms of dose to alanine, while the red dots show the relative response in terms of dose to water, which is in addition a function of the ratio in the mass energy absorption coefficient (shown in figure 1-13 b)) between alanine and water. For higher energies the response curve remains very close to unity [Anton et al., 2008]. These findings are also supported by earlier publications [Bermann et al., 1971][Regulla and Deffner, 1982].

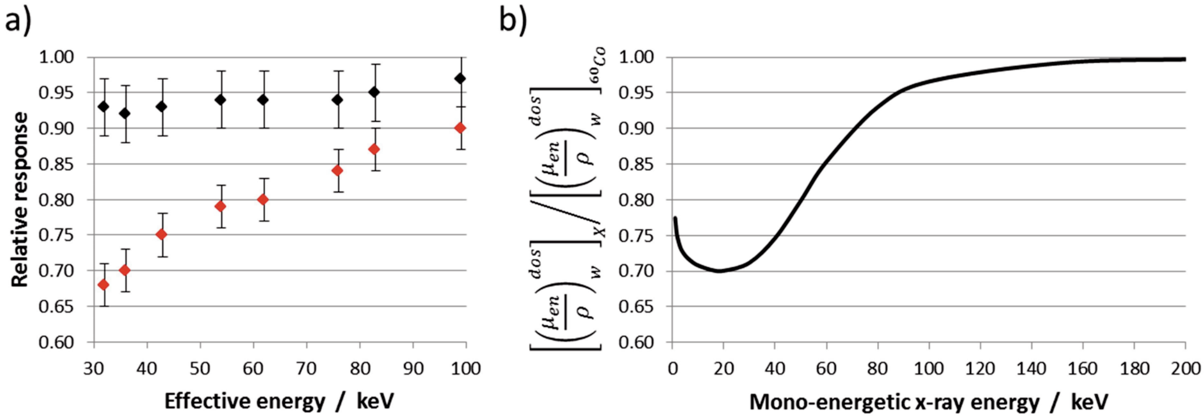

Figure 1-13. a) Alanine response towards low photon energies normalised to ^{60}Co gamma rays in terms of dose to alanine (black dots) and dose to water (red dots) b) Theoretical mass energy absorption coefficient ratio of alanine and water for mono-energetic photon energies relative to ^{60}Co gamma rays [Waldeland et al., 2010a][NIST].

To account for the different radical yields obvious from figure 1-12 in charged particle fields or mixed neutron and photon fields two approaches can be considered. In the easiest case particles are calibrated in a field with the same or very similar parameters compared to the investigated field. However, this is neither practicable nor possible in most cases. The energy of a charged particle is changing rapidly and in mixed fields, as occurring with neutrons, it is impossible to calibrate for each combination of particles occurring somewhere in the field. Due to the different properties regarding attenuation and interaction, the characteristics of the field are a strong function of the irradiated setup. Any attempt to calibrate in comparable fields therefore leads to a strong increase in calibration uncertainties. In this work all calibration has been done in photon fields. To account for the differences in radical yield the relative effectiveness (RE) is used, which is putting the detector responses in relation.

1.5.2.3 Relative Effectiveness

The concept of RE is widely used and has been also matter of many theoretical considerations, as will be shown in detail in section 1.6.2. Two different definitions are common, but often not distinguished in publications. Figure 1-14 illustrates both. The black respectively grey curves represent a draft of the dose response curves in figure 1-12. The reference or photon response is shown in black, while response in an arbitrary field Z is shown in grey. A certain absorbed dose D_Z, given to the detector by the field Z, leads to a certain ESR signal $S_Z(D_Z)$. During read-out with the reference this signal will be correlated to a lower dose D_{ref}, which is referred to as detector response or dose response. This correlation, shown in the figure in red colour, is the basis of the iso-response definition of the RE given in equation (42). Alternatively the received signal $S_Z(D_Z)$ can be related to the reference signal at the same absorbed dose $S_{ref}(D_Z)$, indicated in blue in figure 1-14. This way the relation, expressed in equation (43), is called iso-dose definition of the RE.

$$RE\ \_ \qquad = \left.\frac{D_{ref}}{D_Z}\right|_{\_} \tag{42}$$

$$RE\ \_ \qquad = \left.\frac{S_Z(D_Z)}{S_{ref}(D_Z)}\right|_{\_} \tag{43}$$

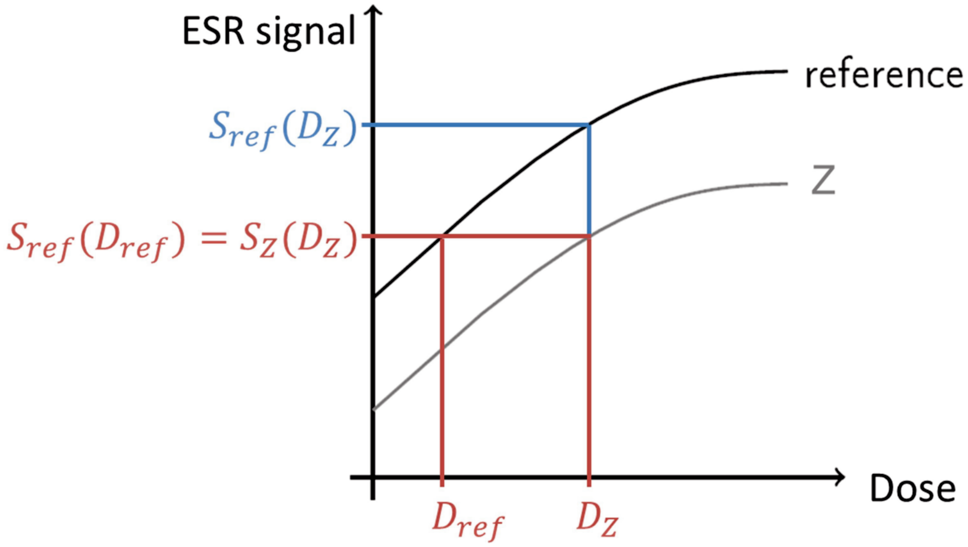

Figure 1-14. Illustration of the two common definitions of RE. Compare also equations (42) and (43).

Under certain conditions the values of both definitions might have the same numerical value, but there can be no general statement. However, both definitions are commonly used. The iso-dose correlation has been for example used by Waligorski during his investigations on the neuron response [Waligorski et al., 1989]. It might be preferable if dosimeters are irradiated by different beam qualities to a defined dose and compared afterwards. For dosimetric purposes, as described in this work, the iso-response formulation is much more practicable, since after the determination of the dose response D_{ref} with known RE – the value of the absorbed dose D_Z can be calculated. This is not possible using the iso-dose definition. Therefore through this work solely the iso-reponse definition of equation (42) is applied.

The relative response is highest toward photon irradiation. In theory RE is therefore always less or equal to unity. RE does not change with increasing dose until saturation begins, as figure 1-15 illustrates. It can be seen that with either definition of the RE several thousand Gray have to be reached until the value varies. The increase above 1.0 is a result of the non-uniform ESR signals at saturation.

The concept of RE is widely accepted as a valid method to transform detector readings in arbitrary fields into absorbed dose. The determinations of the energy dependant values is therefore one central issue in alanine respectively ESR-detector research.

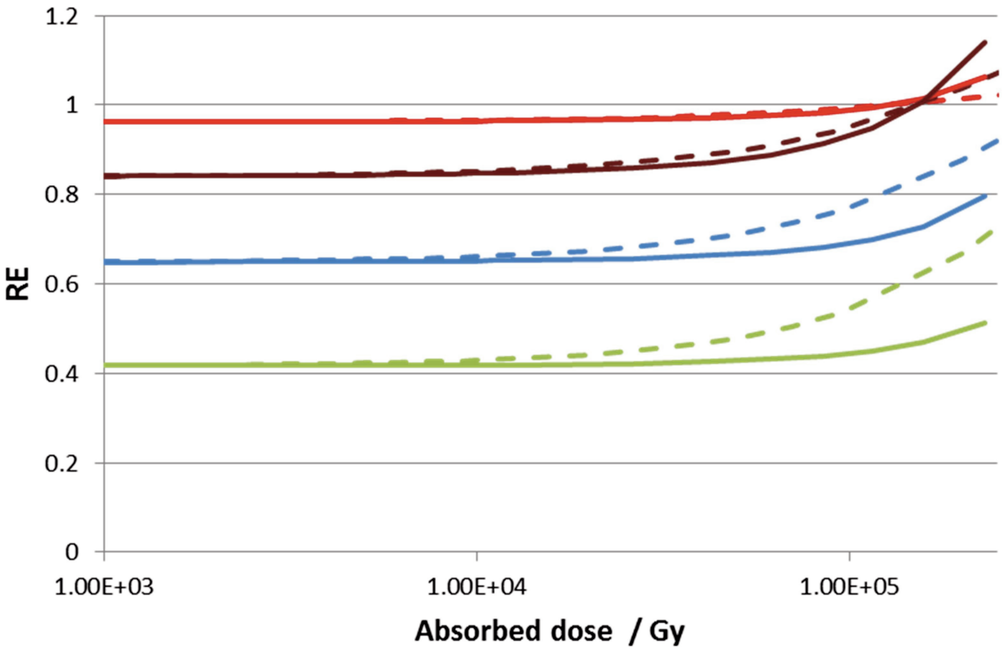

Figure 1-15. Values of $RE_{iso\text{-}response}$ (solid lines) and $RE_{iso\text{-}dose}$ (dashed lines) according to the data from figure 1-12 (6 MeV protons - dark red, 16 MeV protons - light red, 20 MeV alpha particles - blue, and 21 MeV ^{7}Li ions - green).

1.5.2.4 Investigations in charged particles beams

In common it is not possible to differentiate high or low LET irradiation on the basis of the ESR spectrum of alanine. Hansen and Olsen stated that the formation of radicals is independent of how the energy is deposited [Hansen and Olsen, 1985]. However Ciesielski and Wielopolski described variations at the non-central peaks of the spectrum, [Ciesielski and Wielopolski, 1994]. These findings might be explained by a change in the ratio of generated radical species or changes in the environment around these radicals, due to damages to the crystal lattice. The observed deviations though are minor and mostly relevant at higher doses in the saturation region of the dose response.

More relevant are deviations in the fading characteristics, as already shown in figure 1-11, although they are also only occurring at high doses. Fading is a result of radical recombination, which is occurring more often at high radical concentrations as present at high absorbed doses and close to particle tracks of high LET radiation.

Already in the initial paper of Bradshaw et al. [Bradshaw et al., 1962] the alanine response towards protons is described. Although a value of the RE is not mentioned, it can be calculated form the presented data. Waligórski et al. [Waligórski et al., 1989] summarised early findings towards the response in charged particles in their publication in 1989, further investigations took place since then. Figure 1-16 shows available RE data for different proton energies, legend is given in table 1-4. Where values were not given in text, methods described by Waligórski et al. [Waligórski et al., 1989] have been employed for extraction from figures. When possible, values were transferred into iso-response formulation of RE. The indicated proton energies refer to the proton energy inside the pellet and therefore are not mandatory equal to the initial proton energy. It can be seen in the figure that RE is increasing with proton energy towards unity, which is reached at about 20 MeV particle energy. No data is available for energies lower than 1 MeV. The big deviation at certain energies between the values in different works might be explained by different experimental setups. In addition especially in the early publications the actual proton energy inside the alanine pellet is not always specified, and might be lower as indicated in the figure. A table with all values is given in the appendix A.

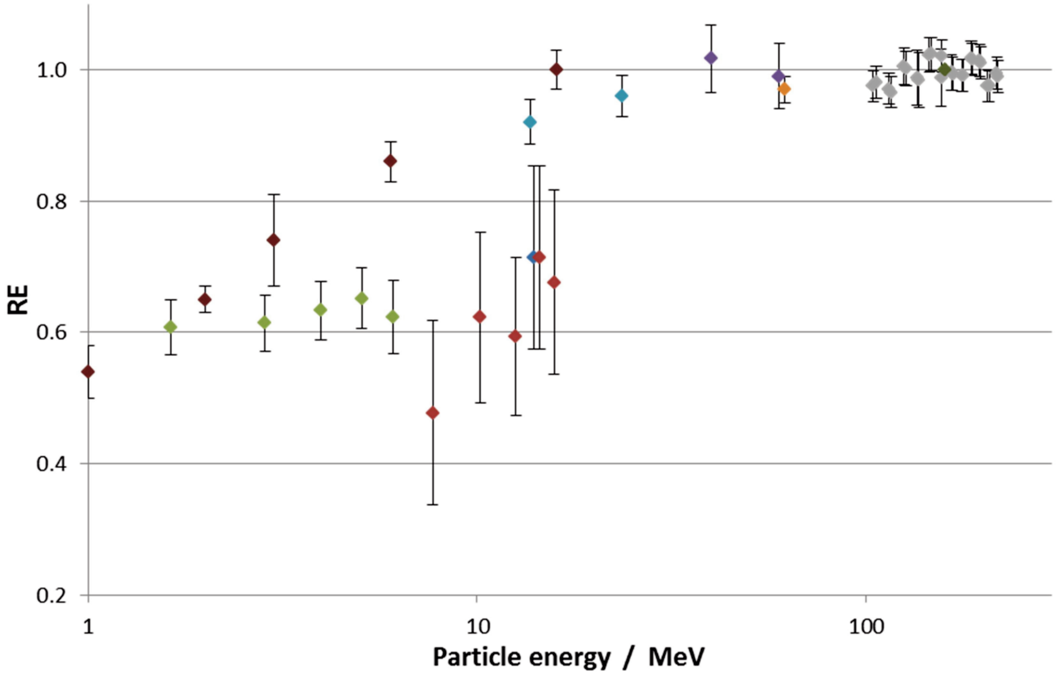

Figure 1-16. RE values measured for protons of different energies. Data taken form publications in table 1-4 (a – blue, b – red, d – dark green, f – dark red, g – purple, h – light blue, i – orange, j – light green, k - grey).

Table 1-4. Legend of figures 1-16 and 1-17.

Label	Reference
a	Bradshaw et al. [Bradshaw et al., 1962]
b	Ebert et al. [Ebert et al., 1965]
c	Henriksen [Henriksen, 1966]
d	Bermann [Bermann, 1978]
e	Hansen and Olsen [Hansen and Olsen, 1985]
f	Olsen and Hansen [Olsen and Hansen, 1990]
g	Cuttone et al. [Cuttone et al., 1999]
h	Bartolotta et al. [Bartolotta et al., 1999]
i	Onori et al. [Onori et al., 1999]
j	Fattibene et al. [Fattibene et al., 2002]
k	Herrmann [Herrmann, 2012]

Similar behaviour has been observed for the RE of particles heavier than protons. A collection of references and values can also be found in appendix A. For reasons of better visibility only a few series of different ions from this data are plotted in figure 1-17. Again particle energies inside the detectors are indicated. Similar to protons values are approaching unity with increasing particle energy. This is especially visible with the data for alpha particles, shown in blue, and the values for carbon ions, shown in orange. Furthermore at a fixed energy per nucleon of the irradiating particle with increasing mass the RE value is decreasing. One example for this observation is the series of Henriksen at 10.4 MeV/u, indicated in the figure by diamonds. While for alpha particles with an energy of 10.4 MeV/u his data lead to a RE of 0.99, for boron-11 extraction gave 0.61. The biggest mass in his series had argon-40, for which a RE of 0.31 could be cextracted [Henriksen, 1966].

Several attempts have been made to model the alanine detector response towards charged particles. Besides approaches based on microdosimetric considerations [Olko, 1999, Olko, 2002] and fit functions using LET weighted effective energy as a parameter [Palmans, 2003], mostly Amorphous Track Models (ATM) were employed. First proposed and applied to alanine by Katz in 1978 [Katz, 1978], theory was varied and enlarged by Hansen and Olsen [Hansen and Olsen, 1984], Waligórski et al. [Waligórski et al., 1989] and Ohno et al. [Ohno et al., 2001]. Since in this work the theory of Hansen and Olsen is adapted, ATMs are further described in section 1.6.2.

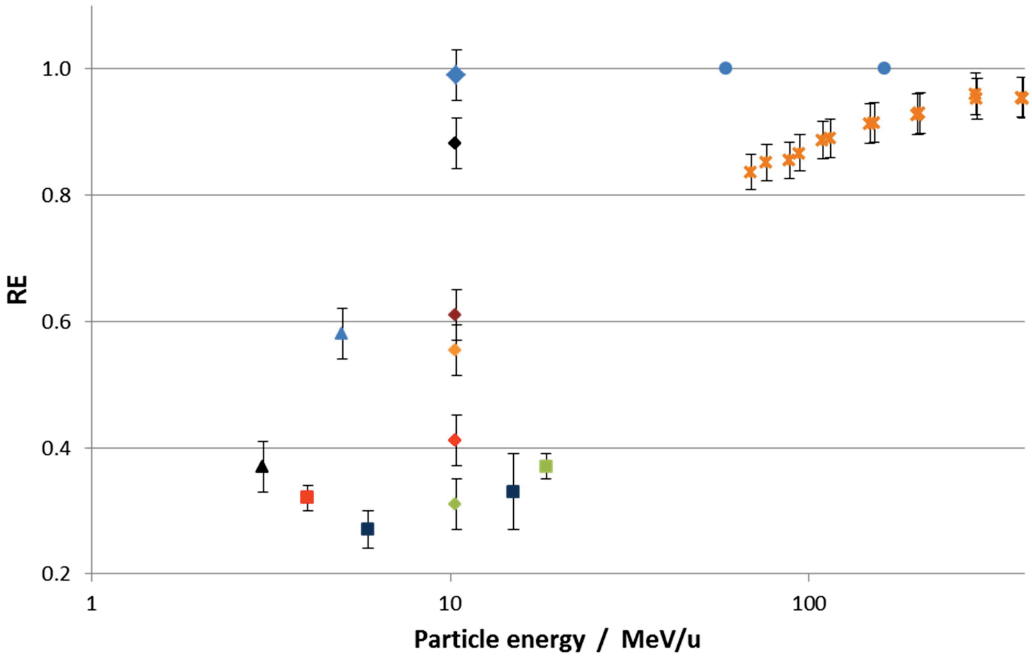

Figure 1-17. RE values measured various ions of different energies (^{4}He – blue, ^{7}Li – black, ^{11}B – dark red, ^{12}C – orange, ^{16}O – red, ^{40}Ar – green, ^{238}U – dark blue). Data taken form publications in table 1-4 (c – diamonds, d- circles, e – triangles, f – squares, k - crosses).

1.5.2.5 Investigations in neutron fields

Compared to the numerous investigations in charged particles beams, investigations in neutron fields are few. Early studies on the response of neutrons have been made by Bermann et al. [Bermann et al., 1971] in the early 1970s, using 3 MeV and 14 MeV neutrons, mainly reporting the influence of condition and composition of the used alanine and a possible binder. Later Bermann also studied the influence of neutron energy on the RE [Bermann, 1978]. He carried out experiments in eight facilities, using fields with seven different neutron spectra. His results showed a decreasing RE with decreasing neutron energy. As can be seen in table 1-5 at 20 MeV he reported an RE of 0.83 ± 0.08 respectively 0.82 ± 0.09, decreasing to 0.4 ± 0.1 for a neutron spectrum with fluence averaged energy of 1.5 MeV. This trend is similar to those of charged particles, although even with very fast neutrons unity is not reached. For neutrons in the epithermal range indeed Bermann found, different to charged particles, increasing values. Later investigations as for example summarised in the publications of Waligórski et al. [Waligórski et al., 1989], Hansen et al. [Hansen et al., 1989], Schraube et al. [Schraube et al., 1989], or more recently by D'Errico et al. [D'Errico et al., 1996], or Trompier et al. [Trompier et al., 2004], confirmed the trend regarding fast neutron energies, while epithermal and thermal energies were not examined. Figure 1-18 and table 1-5 illustrate their RE values. Differences might be due to different pellet compositions, containing different kinds and amounts of binder, differences in the neutron spectrum not obvious from the averaged energy or also due to the chosen RE definition, which is not consistently reported. In addition most of the values are in some way corrected, i.e. in most experiments the response fraction by the photon contamination of the field was previously determined and subtracted afterwards.

Since also with neutrons radicals are generated either by gamma rays, electrons or charged particles, no significant change in the shape of the ESR signal of alanine has been observed compared to irradiation with photons [Hansen et al., 1989].

Additionally figure 1-18 includes two approaches to model the neutron response. Both have in common that they are based on ATM and try to evaluate the neutron response by the calculation of the RE of the secondary charged particles. The solid line represents a model proposed by Waligórski et al. [Waligórski et al., 1989]. Their attempt includes the determination of a "radiation equivalent". They determined a particle with Z = 1.5 and a mass of 3.0 u to yield the same RE as a neutron of the same energy (in MeV/u). For this particle the RE was calculated employing an ATM. The curve in figure 1-18 reaches a minimum at 0.06 MeV and indicates an increase for lower energies. For higher energies the model predicts an increase consistent with the experimental data. Alternatively in their paper they describe the calculation of RE values for the experiments at 7.5 MeV neutron energy by Simmons and Bewley (label b) and for the two experiments at 14.0 MeV neutron energy by Bermann (label a) and by Katsumura (label d). They combined calculated spectra of the secondary charged particles for mono-energetic neutrons with the neutron spectra of the experiments. Based on the RE for charged particles, calculated by their ATM, they got neutron RE values for each facility. In all three cases their calculation underestimates the measured results. For the 7.5 MeV neutrons Simmons and Bewley measured 0.65 ± 0.05, the calculation gave

0.61, which is an underestimation of 6%. In the 14.0 MeV experiments 0.74 ± 0.12 and 0.76 ± 0.02 were measured, while the calculation gave 0.62 in both cases, an underestimation of 16 % respectively 18 %. This attempt is not indicated in the figure.

The model of Gerstenberg et al. [Gerstenberg et al., 1990] is similar to this also based on the evaluation of secondary charged particle spectra. He folded the RE of different charged particles (also calculated by an ATM), with their corresponding spectra in mono-energetic neutron beams. The result is shown as a dashed line in figure 1-18 and follows roughly the experimental results. Different to the model of Waligórski et al. the curve seems to reach a maximum RE around 7 MeV, and is slightly decreasing afterwards. In general the curve is less continuous, showing several local maxima and minima.

In mixed fields, especially in the presence of a strong photon component, the neutron fraction of the absorbed dose is often low and further reduced by the RE. Due to this in various publications alanine was considered to have an insufficient effectiveness towards neutrons [Galindo and Ureña-Nuñez, 1993, Marrale et al., 2007]. To enlarge the fraction deposited by neutrons a common idea is to mix alanine with neutron sensitive materials in order to increase the macroscopic cross section of the material, and therefore the number of secondary charged particles. Most work has been done on mixtures with boric acid [Galindo and Ureña-Nuñez, 1993, Ciesielski and Wielopolski, 1995, Marrale et al., 2007]. The resulting charged particles have a low range in the micrometre scale and hence deposit dose very locally. The change in dose response is consequently not only a function of the amount of boron in the pellet, but also of the grain size in which the boric acid is present. An enhancement in the ESR signal was found, but understanding remained qualitatively, since modelling of the material is difficult. Therefore a more promising approach could be the use of gadolinium oxide, since the secondary charged particles have a much bigger range. Such mixtures have been especially investigated by the group of Marrale, also within the cooperation in the present work. Results are discussed later in detail (section 3.2.3 and 3.2.4) [Marrale et al., 2007, 2013, 2014, and 2015].

Table 1-5. RE values of the alanine detector for different neutron energies sorted by year of publication. The given mean neutron energy is averaged by fluence. At the SILENE reactor fission neutrons were used, the noted 2.0 MeV are estimated. Given uncertainties are included.

Neutron source	Mean energy	RE	Reference	Label
EL3 reactor, CEA Saclay, France	0.2 keV	1.00 ± 0.03	Bermann, 1978	a
Naiade reactor, Fontenay aux Roses, France	0.1 MeV	0.57 ± 0.3		
Oak Ridge reactor, Oak Ridge, United States	1.5 MeV	0.4 ± 0.1		
CALIBAN reactor, Valduc, France	2.0 MeV	0.54 ± 0.1		
VdG accelerator, CTU, Prague, Czech Republic	14.0 MeV	0.74 ± 0.12		
Accelerator, Naval Res. Lab, Washington, United States	15.0 MeV	0.76 ± 0.08		
TAMVEC accelerator, Texas, United States	20.0 MeV	0.83 ± 0.08		
Accelerator, Catholic Univ., Louvain, Belgium	20.0 MeV	0.82 ± 0.09		
LINAC, Hammersmith Hospital, London, UK	7.5 MeV	0.65 ± 0.05	Simmons and Bewley, 1976*	b
Fusion Neutron Source, JAERI, Japan	14.0 MeV	0.72 ± 0.03	Ikezoe et al., 1984**	c
Yayoi reactor, Univ. of Tokyo, Tokyo, Japan	0.9 MeV	0.42 ± 0.03	Katsumura et al., 1986*	d
Accelerator, JAERI, Japan	14.0 MeV	0.76 ± 0.02		
U-120 Cyclotron, INP, Cracow, Poland	5.6 MeV	0.6 ± 0.05	Waligórski et al., 1981, 1987*	e
U-120 Cyclotron, INP, Cracow, Poland	5.6 MeV	0.63 ± 0.04 0.62 ± 0.03	Hansen et al., 1989	f
LINAC, Hammersmith Hospital, London, UK	550 keV 1.8 MeV 5.0 MeV 15.0 MeV	0.38 ± 0.04 0.42 ± 0.01 0.60 ± 0.04 0.65 ± 0.08	Schraube et al., 1989	g
SILENE reactor, Valduc, France	2.0 MeV	0.42	D’Errico et al., 1996	h
SILENE reactor, Valduc, France	2.0 MeV	0.42	Trompier et al., 2004	i

* extracted from Waligórski et al. [Waligorski et al., 1989]

** extracted from Schraube et al [Schraube et al., 1989]

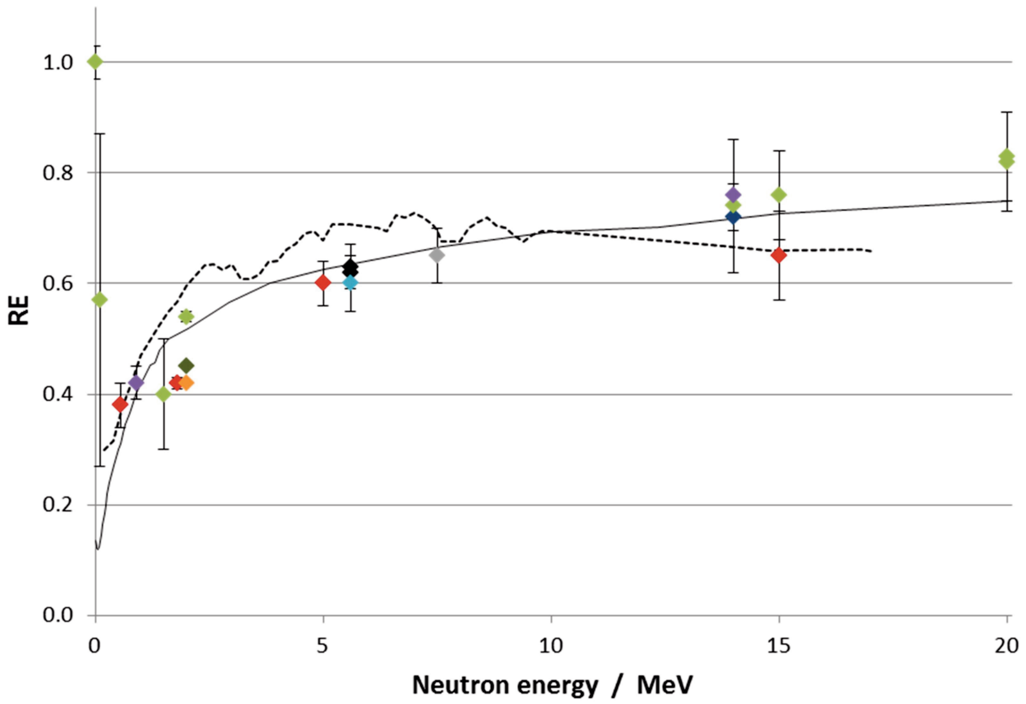

Figure 1-18. Measured and calculated RE values for different neutron energies as shown in Table 1-5. The diamonds represent measured data (a – light green, b – grey, c – dark blue, d – puple, e- light blue, f - black, g – red, h – dark green, i – orange). The solid line represents the modelled RE due to Waligórski [Waligórski et al., 1989], while the dashed line represents the modelled data of Gerstenberg [Gerstenberg et al., 1990].

1.5.3 Other detector materials

Already in the early stage of ESR dosimetry various substances were investigated regarding their dosimetric properties. Henriksen, who studied the influence of various particle types on the alanine response, also examined other amino acids as glycine, the tri-peptide reduced glutathione, trypsine, a serine protease, cytosine, a nucleobase, and the nucleosides cytidine and guanosine [Henriksen, 1966].

Later especially substances found in nature have been of big interest, such as calcites or apatites. Studies were carried out for dating and retrospective dosimetry [Lyons, 1996; Schramm and Rossi, 1996]. Connected are experiments conducted with in-vivo substances such as bone or tooth enamel [Stuglik and

Sadlo, 1996; Onori et al., 1996, Fattibene and Callens, 2010]. They were mainly carried out to investigate possibilities of dosimetry after radiation exposure (emergency dosimetry) or to identify irradiated material, such as food [Dodd et al., 1985]. Although the radical $\bullet CO_2^-$ was often considered the dominant species in all of these samples, Callens and co-workers collected several other radical species [Callens et al., 1998].

More recently possibilities for application of ESR dosimetry in radiation therapy were investigated, and a big variety of materials were tested. Although many of them had promising features none of them was found superior to the alanine. In addition also data describing properties and especially the relative effectiveness is fewer. Lithium formate might be the detector with the second broadest knowledge and is discussed detailed later in this work (compare chapter 3.3 and subsection 4.2.2.2). Further materials are often related to these structures. Most promising results were found on simple molecules such as other formates [Malinen et al, 2004; Gustaffson et al, 2004; Lund et al, 2005], tartrates [Ollsson et al., 2004], amino acids [Bartolotta et al., 1999], and dithionates [Lund et al., 2005; Baran et al., 2006]. Also collections of various materials can be found in literature [Lund et al., 2002; Borgonove et al., 2007].

1.6 Modelling

In order to understand a radiation detector the modelling of the response is a central issue. In this chapter first Monte Carlo (MC) Codes are introduced, a frequently used tool to simulate radiation fields. In the second section ATMs are described, which have been already mentioned as common models to evaluate ESR detectors. Both are central elements of the present work.

1.6.1 Monte Carlo Codes

MC simulations are a stochastic technique, based on the execution of a large number of identical random experiments. This way probability theory is used to solve problems numerically, which are impractically to solve analytical. A fundament is thereby the “law of big numbers”, stating, that the relative incidence of a random result approaches the probability of this result, if the basing random experiment is carried out repeatedly. In particular for radiation transport codes this usually means that a chosen particle is moving through a programmed geometry, undergoing possible interactions, with assigned probabilities. Such way of a particle in a code, called “history”, is exemplary illustrated in figure 1-19 for a neutron.

Today these simulations are carried out with the help of computers or computer clusters, in order to generate extensive numbers of random events. Furthermore MC codes are designed for certain applications or research areas. For selected problems therefore only certain codes are applicable. In transport codes for example only certain particle species or types of interactions are treated, maybe also the energy range is limited or the possibilities of programming in geometry.

In the present work two codes were used, namely MCNP and FLUKA. Other codes such as GEANT4, PHITS or ECGnrc or PENELOPE, which are also commonly used in literature, were not part of this work.

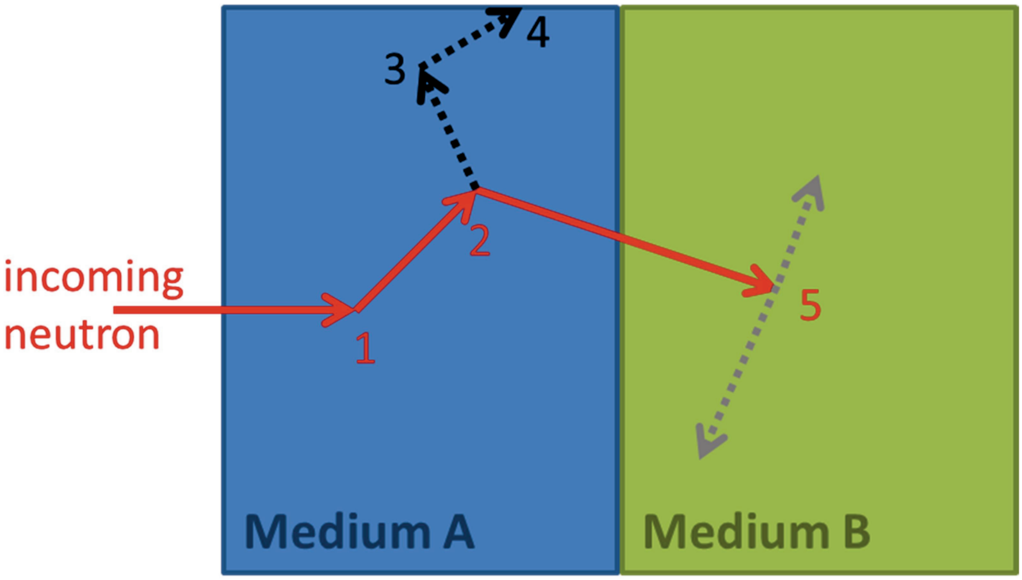

Figure 1-19. Illustration of an exemplary particle history in a MC transport code. An incoming neutron (red arrows) is transported through two media (blue and green) and undergoes several interactions including neutron scattering (1), neutron scattering with photon production (2), and neutron capture (5). The secondary particles produced might be also transported; the photon (black arrows) undergoes photon scattering (3) and leaves the system (4); two particles are emitted following the neutron capture (grey arrows).

MCNP [X-5 Monte Carlo Team, 2003, Pelowitz, 2008] is the abbreviation for Monte Carlo N-Particle Transport Code and programmed for the transport of neutral particles, in particular neutrons and photons. Eventually produced charged particles are not transported, effects related to them are calculated differently. MCNP is the common code for neutron problems and in BNCT research, and primarily used for criticality calculations. The code is developed since the 1950 in the Los Alamos National Laboratory. The extended MCNP version, called MCNPX, enables additionally the transport of a variety of charged particles.

FLKUA [Ferrari et al., 2005, Battistoni et al, 2007] is a multi-purpose transport code, enabling simulation of hadron- hadron interactions of more than 60 particles, including photons and electrons, up to energies of 10.000 TeV. The code has been developed at CERN (Conseil Européen pour la Recherche Nucléaire) and been continuously expanded since then. Originally the code was aiming to simulate particle accelerators and high energy physics problems, but until today many programs have been added to enable application in other research fields. Since 2008 FLUKA includes also extended models to transport neutrons below energies of 20 MeV.

1.6.2 Amorphous Track Models

Amorphous Track Models (ATM) are used to predict the response of different systems towards irradiation with ions. The basis of ATMs dates back to 1967, when Butts and Katz developed a model to predict RBEs of heavy ions on enzymes and viruses [Butts and Katz, 1967].

The path of an ion through matter is called track or trajectory. The phenomenological approach of Butts and Katz to explain the effects of ions on their path is based on two main assumptions. First they assume that the dose around a particle track can be described by a continuous, averaged, radial profile. This might not be valid for a single ion, but it is for a large sum of ions. The electrons generated by ions on their path are called δ-electrons or δ-rays. Indeed they deposit the majority of their dose very close to the track of the incident particle. Only few electrons have energies allowing them to deposit energy in further distance to the track. In the case of protons with a kinetic energy from 1

MeV to 100 MeV already in a 10 nm distance to the particle track the energy deposition is lower by two orders of magnitude [Waligórski et al., 1986].

According to the second assumption, energy, deposited by secondary electrons, has the same local effect, regardless of the origin of the electron. This means that the effect of particle radiation can be derived from the effect of photon radiation. A requirement of this assumption is the similarity of the energy spectrum of secondary electrons of different kinds of particles or that the effect is not influenced by the kinetic energy of the electron.

According to these assumptions differences in the macroscopic response of a detector towards the same dose, deposited by different kinds of radiation, are the result of differences in the microscopic dose distribution. While photons are considered to ionise matter homogeneously, ions deposit dose close to their trajectory, and hence inhomogenously. This way ATMs enable to predict the response function of a detector towards heavy ions relative to the response towards photons.

Butts and Katz build their ATM on target theory, which is shortly introduced next. Hansen and Olsen in turn extended the theory by Butts and Katz. Both theories are used in the present work and therefore also described in this section.

1.6.2.1 Target theory

Originally target theory was formulated for biological systems. The summary shown here is taken from the corresponding chapter in the book of Dertinger and Jung [Dertinger and Jung, 1969]. According to target theory a medium consists of sensitive elements or substructures with volume v, which are embedded in a passive matrix. An energy deposition inside v is called hit. After a certain amount of hits of a minimum energy the sensitive element is deactivated. Theory postulates the hits to follow a Poisson distribution. Therefore the probability for a certain number of hits n is defined as shown in equation (44). Here vD is the mean number of hits in v, with dose D given in hits per volume.

$$P(n) = \frac{(vD)^n exp(- \quad)}{n!} \tag{44}$$

If n hits are needed for deactivation, all elements receiving not more than n-1 hits stay activated. To gain the corresponding fraction of deactivated elements

$\mathrm{N(D)/N_0}$ hence the sum of elements which received 0,1,2 … n-1 hits needs to be subtracted from unity (equation (45)).

$$\frac{N(D)}{N_0} = 1 - \exp(-vD)\sum_{k=0}^{n-1}\frac{(vD)^k}{k!} \tag{45}$$

If the number of deactivated cells can be determined the system can be used as a detector. In the case that one hit deactivates the element equation (45) becomes equation (46). A detector fulfilling this special case is called one-hit-detector.

$$\frac{N(D)}{N_0} = 1 - \exp(-vD) \tag{46}$$

Equation (46) was used to plot the curves in figure 1-12. Alanine is commonly treated as one-hit detector. Of great practical value is the dose $\mathrm{D_{37}}$, at which 37% of elements stay activated, while 63% are inactivated. The value can for example be determined from experimental data. Due to equation (47) it is obvious that $\mathrm{D_{37}}$ is the reciprocal value of v as shown in equation (48). Furthermore $\mathrm{D_{37}}$ enables the calculation of a radius $\mathrm{a_0}$ of the sensitive elements, assuming that they are spherical. The correlation is shown in equation (49), where ξ denotes the mean energy per hit and ρ the density of the material.

$$\frac{N(D_{37})}{N_0} = 1 - \exp(-1) \approx 0.63 \tag{47}$$

$$v = \frac{1}{D_{37}} \tag{48}$$

$$a_0 = \sqrt[3]{\frac{3}{4\pi}\frac{1}{\rho}\frac{1}{D_{37}}\xi} \tag{49}$$

1.6.2.2. Track structure theory

Track structure theory has been developed by Butts and Katz [Butts and Katz, 1967] in the 1960s on the basis of target theory to explain the behaviour of dry enzymes and viruses. Thereby they treated them, as required for target theory, as consisting of targets or sensitive elements embedded in a passive matrix. Regarding the response they only considered one-hit-processes. Build on the two assumptions of ATMs, which have been described earlier, they examined the energy deposition or hits in coaxial cylindrical shells about the ions path. For each shell the resulting effect was then determined from the effect of gamma rays. Figure 1-20 illustrates the examination. The length of a shell T is chosen sufficiently small, so that the speed of the ion is nearly constant over T. The shell has a radius x and a thickness dx.

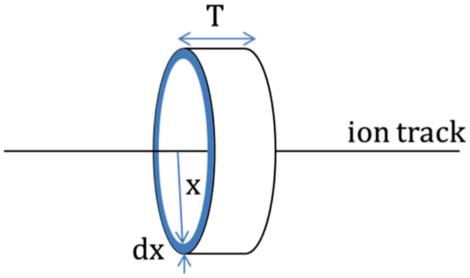

Figure 1-20. Illustration of the coaxial shell around an ion track

The dose $D_\delta$deposited by δ-rays is uniform over the shell. Therefore the number of hits inside the shell $d\mathfrak{R}$ is given by the product shown in equation (50). Here the term $(T2\pi x dx)$ represents the volume of the cylinder shell, N_0 denotes the number of targets per volume, and the term in squared brackets the hit probability from equations (44) and (46), incorporating equation (48). The dose D_{37}^{γ} is here explicit the D_{37} of gamma rays. The total number of hits inside a cylinder $\mathfrak{R}$ is calculated by integrating equation (50) over all x. Equation (51) gives the inactivation cross section σ, which is calculated by dividing the total number of hits $\mathfrak{R}$ by the total amount of targets per area $N_0 T$.

$$d\mathfrak{R} = (T2\pi x dx)N_0\left[1 - \exp\left(-D_\delta/D_{37}^{\gamma}\right)\right] \qquad (50)$$

$$\sigma = \frac{\mathfrak{R}}{N_0 T} = 2\pi \int_0^x x dx\left[1 - \exp\left(-D_\delta(x)/D_{37}^{\gamma}\right)\right] \qquad (51)$$

The δ-ray dose $D_\delta(x)$ deposited in a shell as a function of radial distance can be calculated with the number of electrons n passing the shell and the energy that they deposited For the following considerations two basic assumptions are made, electrons are ejected normally ($=90°$) to the ion trajectory and targets are treated as point targets. To evaluate the number of electrons passing a shell Butts and

Katz started from the cross section σ_w for the emission of a δ-electron with kinetic energy in the interval $[w, w + dw]$. To gain an expression they used the solution of the Kepler problem, with the central force being the Coulomb force, as shown in equation (52).

$$\sigma_w = \frac{2\pi e^4}{m_e c^2}\left(\frac{Z_{eff}}{\beta}\right)^2 \frac{dw}{w^2} \tag{52}$$

Here m_e denotes the electron mass, e the elementary charge, Z_{eff} the effective charge of the ion, and β its speed relative to the speed of light. Multiplied with the electron density of the material N_e equation (52) becomes an expression for dn, the number of electrons emitted in the energy interval $[w, w + dw]$. Integrating over all possible energies leads to equation (53), the number of electrons passing through a shell $n[w(x), w_{max}]$. Thereby $w(x)$ and w_{max} indicate the interval of possible energies. The maximal energy w_{max} is given by equation (54), representing a classical central hit between ion and electron.

$$n[w(x), w_{max}] = \frac{2\pi N_e e^4}{m_e c^2}\left(\frac{Z_{eff}}{\beta}\right)^2 \int_{w(x)}^{w_{max}} \frac{dw}{w^2} = \frac{2\pi N_e e^4}{m_e c^2}\left(\frac{Z_{eff}}{\beta}\right)^2 \left[\frac{1}{w(x)} - \frac{1}{w_{max}}\right] \tag{53}$$

$$w_{max} = 2 m_e c^2 \frac{\beta^2}{1-\beta^2} \tag{54}$$

The integration minimum $w(x)$ is the minimum energy needed, to reach the shell with radius x. In track structure theory the correlation between range and energy is made by equation (55), with the empirical parameters k and α. The latter was found to be one by Butts and Katz in the first publication [Butts and Katz, 1967], later different values were obtained. Analogue to equation (55) the energy dw, deposited while travelling distance dx inside a shell, can be written according to equation (56).

$$x = k w^{\alpha} \tag{55}$$

$$dw = (k^{-1} dx)^{\alpha^{-1}} \tag{56}$$

Combining equations (53) and (55) leads to the energy deposited in a shell. Butts and Katz only showed the solution for an α of one [Butts and Katz, 1967], a more general expression can be found in the work of Hansen [Hansen, 1984]. Division by the shells mass results in equation (57), the δ-ray dose $\mathrm{D}_\delta(\mathrm{x})$ per unit track length.

$$D_\delta(x,\beta,Z_{eff}) = \frac{N_e e^4}{m_e c^2}\left(\frac{Z_{eff}}{\beta}\right)^2 \frac{1}{\rho}\frac{1}{\alpha}\frac{1}{x}\left(1-\frac{x}{x_{max}}\right)^{\alpha^{-1}} \qquad (57)$$

To expand the considerations from point targets to extended targets Katz and co-workers made several simplifications. Targets were assumed to be cylindrical with radius a_0 and orientated parallel to the ion trajectory. The average δ-ray dose in to such geometry is given by equation (58) and illustrated in figure 1-21. In general a convolution of the target shape and the belonging δ-ray dose distribution has to be made [Katz et al., 1972].

$$\bar{D}_\delta(x,\beta,Z_{eff},a_0) = \frac{1}{\pi a_0}\int_{x_0-a_0}^{x_0+a_0} D_\delta(x,\beta,Z_{eff})2\varphi x dx \qquad (58)$$

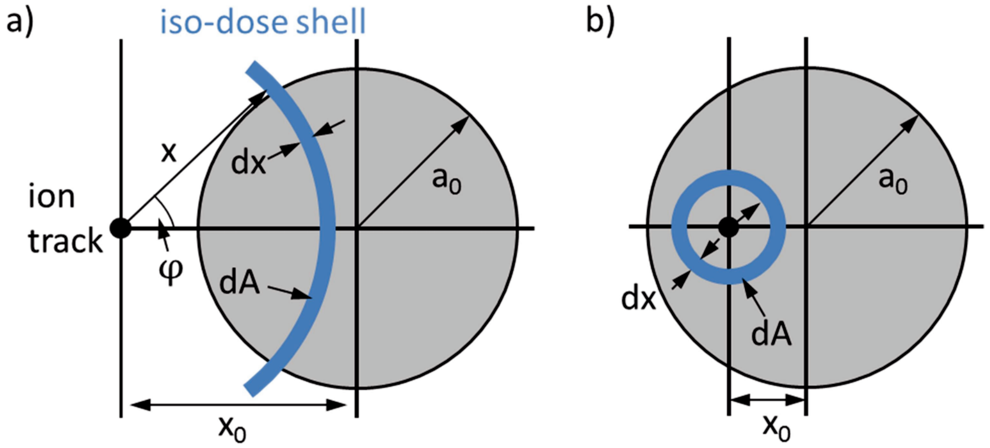

Figure 1-21. Illustration of the considerations towards δ-ray dose in an extended target. (Adapted from [Hansen, 1984][Herrmann, 2012]).

Also in later works Butts and Katz are not distinguishing between RBE and RE. Both are treated as shown in equation (59) as ratio of sensitivities κ towards radiations i and j. In the case of a one-hit-detector and the use of gamma-rays as reference RE can be calculated as indicated in equation (60).

$$RE_{i,j} = \frac{\kappa_i}{\kappa_j} \tag{59}$$

$$RE_{i,\gamma} = D_{37}^{\gamma} \sigma_i \left(\frac{S}{\rho}\right)^{-1} \tag{60}$$

Recalling considerations towards RE in section 1.5.2.3, equations (42) and (43) can be re-written for one-hit detectors according to track structure theory as shown in equations (61) to (65). According to equation (46) the observed dose response from different kinds of radiation differs only in the characteristic dose D_{37}. Substituting equation (42) therefore leads to equation (65).

$$RE\ \_ \qquad = \left.\frac{S_Z(D_Z)}{S_{ref}(D_Z)}\right|_{\_} \tag{43}$$

$$RE\ \_ \qquad = \frac{S_0^Z[1- \quad (-D_Z/D_{37}^Z)]}{S_0^{ref}\left[1- \quad \left(-D_Z/D_{37}^{ref}\right)\right]} \tag{61}$$

$$RE\ \_ \qquad \approx \frac{S_0^Z}{S_0^{ref}} \frac{D_{37}^{ref}}{D_{37}^Z}\text{, for } D_Z \ll D_{37} \tag{62}$$

Here S_0^Z and S_0^{ref} are the saturation signals for each kind of radiation. However, since the number of sensitive elements is identical for different kinds of radiation, also the saturation signals should be identical, but as can be seen in figure 1-12 that is the case only approximately.

$$RE\ \_ \qquad = \left.\frac{D_{ref}}{D_Z}\right|_{\_} \tag{42}$$

$$RE\ \_ \qquad = \frac{-D_{37}^{ref}\, ln\left[1-\frac{S_Z(D)}{S_0^{ref}}\right]}{D_Z} \tag{63}$$

$$RE\ \_ \qquad = \frac{-D_{37}^{ref}}{D_Z}\, ln\left[1-\frac{S_0^Z}{S_0^{ref}}(1-exp(-D_Z/D_{37}^Z)\right] \tag{64}$$

$$RE\ \_ \qquad = \frac{-D_{37}^{ref}}{D_Z}\text{, for } S_0^Z = S_0^{ref} \tag{65}$$

Comparing equations (62) and (65) shows that, for small values of $\mathrm{D_Z}$, RE values with either definition should yield the same numerical value. For higher $\mathrm{D_Z}$ RE_{-} approaches $\mathrm{S_Z(D_Z)}$, finally becoming unity, while RE_{-} stays constant. In the case of unequal saturation signals $\mathrm{RE_{iso-dose}}$ still approaches $\mathrm{S_Z(D_Z)}$ and unity, but reduced by the ratio of the saturation signals. In the case of the iso-response definition RE is decreasing for high values if $\mathrm{S_0^Z} < \mathrm{S_0^{ref}}$ and becomes undefined if $\mathrm{S_0^Z} > \mathrm{S_0^{ref}}$.

1.6.2.3. The Hansen and Olsen model

Hansen and Olsen adapted the track structure theory for dye film and alanine detectors. Thereby they made several modifications [Hansen, 1984, Hansen and Olsen, 1984]. Most relevant is the introduction of a core dose $\mathrm{D_{core}}$ close to the ion trajectory. The chosen radial dose distribution as indicated in equation (66) is differing from those described in equation (57). The specification became necessary, when Hansen and Olsen noticed that the dose in the core around the ion track is underestimated by track structure theory. For infinitesimal short cylinder length dT equation (57) should be equal with the stopping force. The observed underestimation might be a result of the missing integration of the electron binding energies or the negligence of interactions between ion and the nuclei of the material. The core dose was calculated according to equation (67), as a function of the stopping power. Such the total energy deposited equals the stopping power, all energy not deposited at a distance above $\mathrm{a_0}$ is treated as core dose.

$$D(x) = \begin{cases} D_{core} & : \ r \leq a_0 \\ \overline{D}_\delta(x) & : \ a_0 < r < r_{max} \\ 0 & : \ r > r_{max} \end{cases} \tag{66}$$

$$D_{core} = \left(\frac{S}{\rho}\right) - 2\pi \int_{a_0}^{r_{max}} \overline{D}_\delta(r) r dr \tag{67}$$

Another change regarding the exponent α being unequal to one, has been attributed above. Furthermore a better estimation for the calculation of the effective charge was introduced.

Later Hansen and Olsen also added a model for signal stability [Hansen and

Olsen, 1989], basing on empirical data on signal fading. The inactivation cross section in equation (51) was augmented by a polynomial as a function of absorbed dose and time. However, since this specific part of the model has not been used in this work, it is not further described here.

1.7 Dosimetry in BNCT

After the description of principles and techniques, which are essential for the present work, this introduction is concluded with the description of the common dosimetric methods in BNCT as used today in clinical practise. The basic concepts, described by Rogus et al. in 1994 [Rogus et al., 1994], are still valid today, and varied only in details. This text therefore follows their description throughout most of this chapter.

In BNCT in general four dose components are distinguished, which have in part been mentioned before in this introduction. Reactions or interactions not mentioned among them are of negligible importance due to either low cross sections or minor energy deposition. Below the four components are listed with the causative nuclear interaction, the corresponding thermal neutron cross section, a rough weight fraction of the target atom in tissue and some complementary remarks.

- Boron dose D_B:

  $^{10}B(n,\alpha)\ ^{7}Li \qquad \sigma_{th} = 3838\ b \qquad \approx 10^{-4}\ \%_{wt}\ in\ tissue$

  The boron dose is the therapeutic dose in BNCT, and deposited due to the capture reaction of boron-10. The resulting alpha and lithium particles have a high LET and a low range in the micrometre scale. The boron dose is hence deposited locally and, besides the neutron fluence, a strong function of the local boron concentration. The given weight fraction in tissue indicates the boron amount during therapy. However the variations in the boron concentration between different kinds of tissue are substantial.
- Proton dose D_P:

  $^{14}N(n,p)^{14}C \qquad \sigma_{th} = 1.82\ b \qquad 3\ \%_{wt}\ in\ tissue$

  The proton dose, also referenced to as nitrogen dose, is deposited by the recoiling carbon-14 nucleus, but mainly by the 560 keV proton. Due to its energy the range of the proton is also on the micrometre scale. But since the nitrogen distribution in tissue is quite homogenous the proton dose is primarily a function of the neutron fluence.

- Photon dose D_γ:

  $^1H(n,\gamma)\ ^2H \qquad \sigma_{th} = 0.333\ b \qquad 10\ \%_{wt}\ in\ tissue$

  The photon dose is dominated by the indicated neutron capture of hydrogen. In addition photons can originate from neutron interactions of other elements such as carbon or oxygen, but due to a lower cross section they are of little relevance. Furthermore the component also includes the dose from photons not generated in the patient body, but for example in the reactor core or in structure materials. This so-called photon contamination is usually quite low by the design of the irradiation facilities.

- Fast neutron dose D_N:

  $^1H(n,n')\ ^1H \qquad 10\ \%_{wt}\ in\ tissue$

  While the other three dose components are mainly a result of thermal neutron interactions, the fast neutron dose is, as the name suggest, deposited by fast or epithermal neutrons in scattering processes. Due to the similar mass of neutrons and protons, so-called “recoiling protons” can result from the $^1H(n,n')^1H$ interaction. The proton energy depends on the incident neutron energy and the scattering process. Also here, the dose due to the hydrogen interaction is dominating. Dose from scattering on carbon, oxygen or other elements is negligible.

The total absorbed dose in BNCT D_{total} is written according to equation (68) as the sum of the four components. An example for the depth dose curves of all four components is given in figure 1-22 with data extracted from the review of Coderre and Morris, calculated for the epithermal beam of the Brookhaven Medical Research Reactor [Coderre and Morris, 1999]. Due to the diversity of the dose depositing particles also the depth dose behavior of the components is diverse. Boron dose and proton dose show a similar course, since here both are mainly a function of the thermal neutron flux (the boron-10 concentration is assumed constant). Both components exhibit an increase at low depth, due to moderation of the predominately epithermal neutrons. Also due to moderation, the fast neutron dose shows a continuous decrease.

$$D_{total} = D_B + D_P + D_\gamma + D_N \tag{68}$$

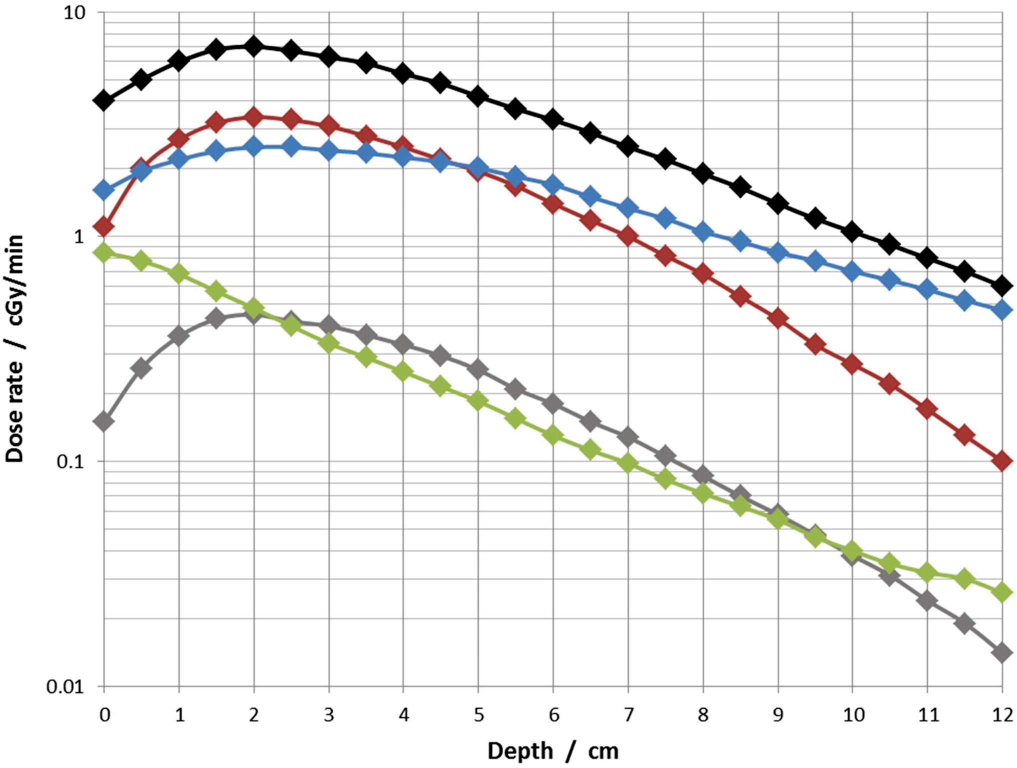

Figure 1-22. Calculated components of absorbed dose of the epithermal neutron beam at the Brookhaven Medical Research Reactor along the beam axis as a function of depth in tissue; including total dose (black), boron dose (red), nitrogen dose (grey), photon dose (blue), and fast neutron dose (green). For the calculation of the boron dose concentration was estimated to 13 ppm of boron-10. [Coderre and Morris, 1999]

The different particles have different biological effects, and hence absorbed dose alone is of little significance for evaluation the therapeutic prospects. Therefore the weighed total dose $\mathrm{D_{w,total}}$ in determined, for which each component is multiplied by a weighing factor, as shown in equation (69). By the weighing factors absorbed dose is converted to photon-equivalent dose. In common the concept of RBE is used for the weighting. Merely for the boron dose instead a compound biological effectiveness (CBE) factor is used. The CBE factor depends on the tissue type and boron compound, since both are influencing the local boron-10 concentration. To distinguish absorbed dose and weighed dose, the latter is often given in the unit Gy_w. Weighting factors need to be determined experimentally for each irradiation field separately. Further information on the importance and determination of weighing factors can be found elsewhere [Coderre and Morris, 1999; Hopewell et al., 2012].

$$D_{w,total} = w_B D_B + w_P D_P + w_\gamma D_\gamma + w_N D_N \tag{69}$$

The curves in figure 1-22 are calculation results; but of course it is also necessary to determine them experimentally. Photon and fast neutron dose are measured using dual ionization chambers, boron and proton dose are determined via kerma factors and neutron flux measurements. Details of these techniques are given in the next two sections.

1.7.1 Photon and fast neutron dose

Both doses are determined in combination using the dual ionization chamber technique in appropriate phantoms. Thereby one ionization chamber is having a very low sensitivity towards neutrons, as for example a carbon graphite chamber flushed with carbon dioxide or a magnesium chamber flushed with argon gas. A second chamber is made out of tissue equivalent plastic and flushed with a tissue equivalent gas, measuring photon and neutron dose. Wall material is for example made out of A-150 plastic, a possible gas consist of 64.4 % methane, 32.4 % carbon dioxide, and 3.2 % nitrogen gas by partial pressure. Wall thickness of both chambers is chosen so that CPE and TCPE is provided for particles of interest. However with manageable wall thickness particle equilibrium is not provided for photons of energies higher than approximately 1 MeV. The following uncertainty is estimated to be several percent, especially at the surface of a phantom or free in air.

Measurements are made in reference phantoms. Geometry and material composition of the phantom have a large impact on the propagation of neutrons and photons. To achieve propagation comparable to the one in tissue the hydrogen content is most important. On the one hand the hydrogen is an effective neutron moderator, and on the other hand hydrogen is mainly responsible for two dose components. For dosimetry under reference conditions the use of a water phantom with simple geometrical shape is recommended by ICRU [ICRU Report 45, 1989]. However, to simulate the treatment situation during BNCT more closely, also other shapes and phantom compositions should be used [Munck af Rosenschöld, 2012]. Common alternative materials are PMMA, or tissue equivalent plastics and liquids [Seppälä et al., 1999, Raaijmakers et al., 2000].

The conversion of the measured currents of the ICs into the two dose components involves calibration of the chambers in a reference field, calculation of the neutron to gamma sensitivity ratios, and various other parameters.

In addition several corrections have to be applied to the measured current. The number of corrections is varying, mandatory are corrections towards temperature and pressure. Further corrections might be applied to account for incomplete charge collection after ion recombination, the polarity effect, the influence of the electrometer (if different to the one used for calibration), the gas flow rate (if different to the one used during calibration), the beam intensity, and the wall effect. Detailed information on each correction can be found in literature [Rogus et al., 1994, Rogers et al., 2005, Lin et al., 2011].

In addition the fraction of the measured current, which is generated by thermal neutrons $\dot{Q}_{\phi}$, needs to be subtracted. The sensitivity of the tissue equivalent chamber is naturally higher, since the chamber contains nitrogen, but also the neutron insensitive chamber shows a thermal neutron response. Equation (70) is used to calculate the thermal neutron current, thereby ϕ_{th} the thermal neutron flux and f_{ϕ} is the thermal neutron sensitivity, which is in common calculated using the MC method.

$$\dot{Q}_{\phi} = f_{\phi}\phi_{th} \tag{70}$$

The equations for the response of the two chambers are given according to equations (71) and (72).

$$\dot{Q}_{TE} = A_{TE}\dot{D}_{\gamma} + B_{TE}\dot{D}_{N} \qquad \textit{(70)}$$

$$\dot{Q}_{CG} = A_{CG}\dot{D}_{\gamma} + B_{CG}\dot{D}_{N} \qquad (71)$$

Thereby index TE indicates the tissue equivalent chamber and CG the carbon graphite chamber, $\dot{\mathrm{Q}}$ is the corrected current, A the response per unit of absorbed dose in the tissue of interest from photons, and B the analogue from neutrons. $\dot{\mathrm{D}}_{\mathrm{N}}$ and $\dot{\mathrm{D}}_{\gamma}$ are the dose rates to the corresponding dose components. Since the sensitivities of both chambers are different, equations (71) and (72) can be solved. Results are given in equations (73) and (74).

$$\dot{D}_{\gamma} = \frac{B_{TE}\dot{Q}_{CG} - B_{CG}\dot{Q}_{TE}}{B_{TE}A_{CG} - B_{CG}A_{TE}} \qquad (73)$$

$$\dot{D}_{N} = \frac{A_{TE}\dot{Q}_{CG} - A_{CG}\dot{Q}_{TE}}{A_{TE}B_{CG} - A_{CG}B_{TE}} \qquad (74)$$

The ratio $\mathrm{B/A}$ of a dosimeter is called neutron to gamma sensitivity ratio. Values of A might be determined by a standard laboratory via exposure calibration. Since during this measurement chambers are necessarily open, an additional air to gas correction factor is needed. Finally the exposure calibration has to be converted into a dose in tissue constant. Thereby the value of the constant varies for different tissues, such as brain, muscle or others [Rogus et al., 1994]. Alternatively the sensitivities can be determined through calibration in water in different characterised photon beams. The dose weighted mean energies of these beams are then used in an interpolation of the sensitivity towards the energy of interest [Kosunen et al., 1999].

The value of neutron sensitivity of the tissue equivalent chamber B_{TE} depends on the neutron spectrum. A detailed calculation of the energy dependence is given by Jansen [Jansen et al., 1997]. For the combination of these values, necessary to calculate B_{TE}, for a certain neutron spectrum Lin and co-workers suggested equation (75) [Lin et al., 2011]. The energy dependant values $\mathrm{B}_{\mathrm{i,TE}}$ are weighted by the neutron spectrum (expressed as function $\phi(E)$ or in intervals ϕ_i) and the Kerma K, either as function of energy $K(E)$ or energy intervals K_{i}. Here K_{n} is the neutron kerma calculated from the neutron spectra.

$$B_{TE} = \frac{\int_E \; B_{i,TE}(E)K(E)\phi(E)deE}{\int_E \; K(E)\phi(E)deE} \cong \frac{\sum_i B_{i,TE}K_i\phi_i}{K_n} \tag{75}$$

The neutron sensitivity of the carbon graphite or magnesium walled chamber is quite low, but also a function of neutron energy. Values can be found in literature, which need to be adjusted to the actual neutron spectrum [Waterman et al., 1979], in some studies the value is also set to zero [Kosunen et al., 1999]. Due to changes in the neutron spectrum depending on the material of the phantom and the position inside the phantom values of the sensitivities are varying and need to be adjusted for every measurement position.

The estimated uncertainties for the dose determination in a phantom using the dual chamber technique are ± 9% for the photon dose and ± 17% for the fast neutron dose. Comparing to the requirements formulated earlier in section 1.3.1 these uncertainties appear to be quite high.

1.7.2 Boron and proton dose

The boron and proton doses are calculated using the kerma factor method, described in section 1.3.3.6. Thereby dose is calculated using equation (28), although the necessary CPE will not exist near biological inhomogeneities, such as between different kinds of tissue and for boron-10, since it is not uniformly distributed. Several assumptions, which are made to cope with this, are contributing to uncertainties of the resulting dose components. For the boron dose in addition the boron concentration in different compartments, such as tumour, blood, and other surrounding tissues (for example muscle, brain, etc.) is determined. Usually the blood boron concentration of the patient is measured several times during and after the boron infusion. Using kinetic models these boron blood concentrations are converted to the desired tissue concentrations [Macey et al., 2001, Ryynänen et al., 2002]. A collection of methods for boron determination can be found in the review of Wittig et al. [Wittig et al., 2008].

Kerma factors are tabulated for various elements, compounds, and biological tissues as a function of neutron energy, as described and shown in section 1.3.3.2. For a neutron spectrum equation (18) has to be applied. Determination of neutron flux and neutron spectrum is described in section 1.4.3.2. In this context the previously mentioned cadmium ratio is an often used simple parameter, indicating the neutron spectrum.

2. Motivation and Aim

Boron Neutron Capture Therapy combines characteristics of External Beam Radiotherapy and Radionuclide Therapy. Neutrons are generated by nuclear reactors or accelerators; their beam is moderated, filtered and shaped, before it penetrates the patient. Dose though is predominately deposited by secondary particles and hence not only a function of the neutron fluence, but also of the local element concentrations. BNCT takes advantage of the fact that the interactions of neutrons with tissue are few and dose is comparatively low. Thus it is possible to steer the dose deposition by the distribution of the high cross section isotope boron-10. In an ideal case no boron-10 is located in the tumour-free tissue and the dose deposited remains on a low level. In the tumour the boron concentration is maximised. Consequentially dose is higher by magnitudes there. However, present practise is far from such ideal case. Between tumour and tumour-free tissue rarely ratios above 4:1 are reached, whereby significant amounts of boron are in the tumour-free tissue. The development of new boron pharmaceuticals is hence a central issue in BNCT. Another big issue is radiobiology: The search for the mode of action of boron pharmaceuticals and, in general, the understanding of underlying processes and mechanisms of neutrons interacting in tissue. Both issues are not addressed in this work. In the end, however, for patient therapy all information available is combined in individual treatment planning. The irradiation setting is deduced from neutron field characteristics, radiobiological models and the patient data, including imaging results for example from CT or PET screenings.

The final goal is the deposition of a definite dose to the tumour and a definite dose to the tumour-free tissue. As pointed out, under- as well as overestimation of dose of only a few percent has influence on the clinical outcome. The basis of the whole process is, hence, dosimetry, the measurement of absorbed dose, field characterisation and monitoring. To generate, validate, and control models which are underlying treatment planning protocols dosimeters are a mandatory tool. Consequently a dosimeter has to comply with various requirements. It of course needs to be accurate and precise. Fortunately it shows linearity in response without any dose rate or directional dependence. It should provide spatial resolution, depending on the radiation field, accessibility to the dose range of interest, and sensitivity to the present particle types and energies. Additionally a "good" dosimeter offers convenience regarding handling, read-out, and expenditure of time.

The central proposition of this thesis is that ESR dosimeters fulfil these requirements in BNCT neutron fields.

Neutron dosimetry remains difficult. Rather than by neutrons, dose is deposited by secondary particles, which are generated in a great variety. This is a problem not only in BNCT, but also in industry, emergency dosimetry, and especially aerospace industry. Airline staff has among radiation exposed person groups by far the highest exposure. Depending on many parameters about 30% of their effective dose is related to neutrons. However, the biggest demand is in radiation therapy. Whether with IMRT or EBRT, neutrons occur as unwished particles. In BNCT dosimetry is solved by a combination of activation foil spectrometry, beam monitoring and dual ionisation chambers. Especially the chambers require high amounts of work, especially for installation and maintenance. Uncertainties though remain high. Therefore research has been consistently conducted on the development of dosimetry systems. The research area is broad and indicates the lack of sufficient solutions. Worldwide research groups are working on improvements of the dual ionisation chamber technique, or adaption of new systems to neutron fields, such as radiochromic film, Fricke dosimeters, scintillators, or several kinds of neutron spectrometers.

This work investigates the possibilities of ESR dosimetry. As presented in the introduction, alanine and other ESR dosimeter materials are capable of accurate and precise measurements. It has been shown that their response behaviour is linear in the complete dose range important for radiotherapy. Thereby response is not varying with dose rate or direction of the incident particles. Due to its size dosimeters provide spatial resolution. As shown, tests were conducted with various particle types and energies, also in the context of radiotherapy. However, so far data on thermal and epithermal neutron fields is fragmentary. Also no data exists for charged particles in the energies as generated during neutron interactions. If ESR detectors are sufficiently sensitive to all particles and if their detector response can be completely understood is, hence, one question this work had to answer.

The final aim of this work was the compilation of a set of ESR detectors which is, in combination with auxiliary models, able to measure the total absorbed dose as well as all dose components in thermal and epithermal neutron fields.

Therefore, besides ESR detectors, amorphous track models play an important role in this work. For their use a detailed model of the irradiation facility is mandatory. In the next chapter first the validation of the model of the TRIGA research reactor in Mainz, where most experiments took place, is shown. Followed by a detailed study on the alanine detector, including experiments, conducted not only in the field of the TRIGA Mainz, but also in two epithermal neutron fields of BNCT facilities. Knowledge gained in these experiments has then been transferred to other ESR detector materials. The materials are based on organic molecules. Dose components are therefore analogue as in tissue. To simulate in addition the dose deposition during a BNCT treatment, a detector containing boron was considered favourable for the set. Different attempts were made to find a sufficient material. Except for two, these attempts will be only mentioned in passing. Experiments with gadolinium doped alanine were conducted in this context. However, ultimately lithium formate was found most auspicious as analogue of such detector, and is characterised in an own chapter. Besides alanine in total six more compounds were analysed in detail regarding their response in neutron fields and finally combined to a dosimeter set.

3. Experimental and results

3.1 Evaluation of the model of the research reactor TRIGA Mainz

In this chapter experiments and results of the evaluation of the model of the TRIGA research reactor in Mainz, Germany, are described. Due to great relevance also for the rest of the work, first the facility and recent modelling approaches, including the model used in this work, are introduced.

The reactor model of Ziegner et al. [Ziegner et al., 2014] was evaluated mainly using two types of experiments. This chapter includes the use of activation foils, in order to confirm the modelled neutron fluxes and energy spectra. Irradiations of alanine detectors were made to verify the dose predictions. Their detailed description can be found in section 3.2.1. An independent verification of the photon flux distribution or the photon energy spectra, as for example done at the FiR2 research reactor in Espoo, Finland* [Koivunoro et al., 2014], have not been carried out at the TRIGA Mainz, due to occurring experimental difficulties, which have been observed during preliminary tests and related experiments. Hence ionisation chambers were not used at the TRIGA Mainz within this work.

Furthermore, this chapter contains a section describing a system for online neutron monitoring, as necessary for example during animal experiments in the reactor or for any clinical application. The system is based on the use of a PIN-diode, combined with lithium fluoride converter foils.

While Ziegner employed the MC code MCNP (mainly version MCNP5), in this work calculations were carried out using the FLUKA code. The general applicability of this code in mixed neutron fields has been shown beforehand [Schmitz, 2010; Schmitz et al., 2011].

---

* carried out parallel with the alanine study described in section 3.2.2.

3.1.1 The research reactor TRIGA Mainz

3.1.1.1 Description of the facility

The TRIGA Mark II research reactor of the Johannes Gutenberg-University in Mainz is one of 43 active TRIGA reactors worldwide. TRIGA as an abbreviation stands for “Training, Research, Isotopes, General Atomics”, and denotes main functions and the manufacturer. The TRIGA Mainz has been operated since 1965 and has a maximum power of 100 kW_{th} during continuous operation. A schematic drawing is shown in figure 3-1. The supplement Mark II implies that the reactor is erected completely above ground. Detailed information about the dimensions of the reactor can be found in appendix B, a general description can be found also in literature [Eberhardt and Kronenberg, 2000; Hampel et al., 2009]

A special feature of all TRIGA reactors is inherent safety, based on the fuel element design. At present the research reactor in Mainz has 75 fuel elements, composed of $8\%_{wt}$* uranium (with an enrichment of 20% in uranium-235) and $92\%_{wt}$ zirconium hydride matrix. The matrix and in particular the hydrogen in the fuel elements is important for the neutron moderation of the reactor. The moderation ability of the zirconium hydride matrix is decreasing with increasing temperature, resulting in a prompt negative temperature coefficient of the fuel elements. Therefore, a nuclear meltdown is physically impossible. Before burn-up each element contained 36 g uranium-235. Due to the prompt negative temperature coefficient, besides continuous operation the reactor can be pulsed. During a pulse, reactor power up to 250 MW_{th} can be reached for a period of about 30 ms (FWHM**).

Besides the fuel elements the reactor core contains three control rods made of boron carbide (two) and boron graphite (one), each with an individual thickness, and graphite containing dummy elements, filling up empty positions. Irradiation samples can be positioned at four points in the core. The central experiment tube (CET), reaching vertically from the reactor platform, is located in the centre of the core. Three pneumatic transfer systems (PTS) are connected to laboratories and located in the margin of the core. In this work two of the PTS have been examined for comparison reasons regarding their neutron spectrum.

* $\%_{wt}$ – weight percent

** full width at half maximum

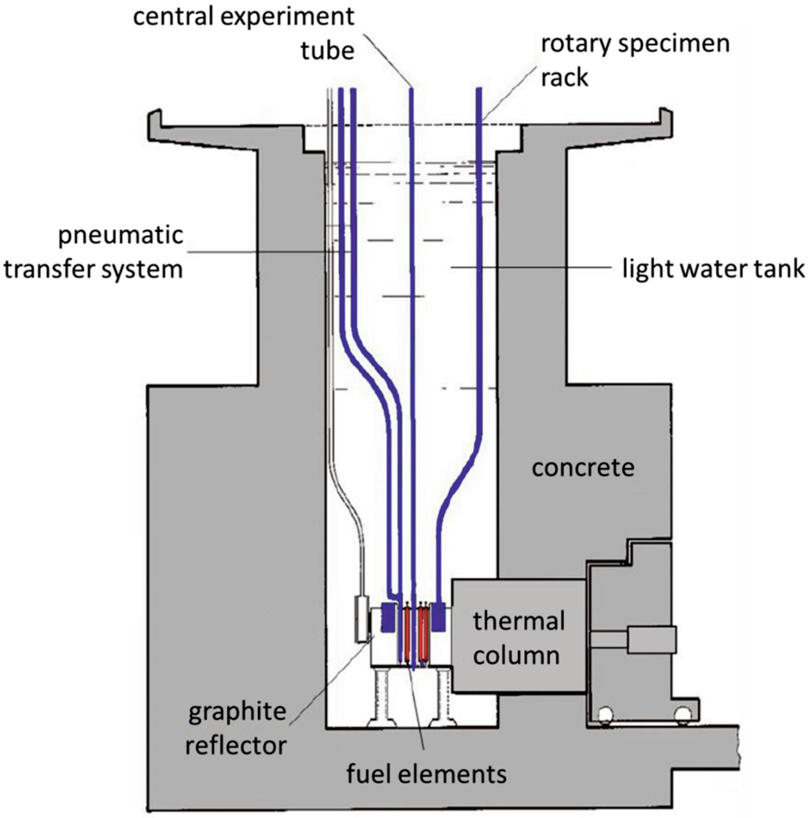

Figure 3-1. Lateral schema of the TRIGA Mainz, indicating the in-core irradiation positions with their access tubes and the thermal column.

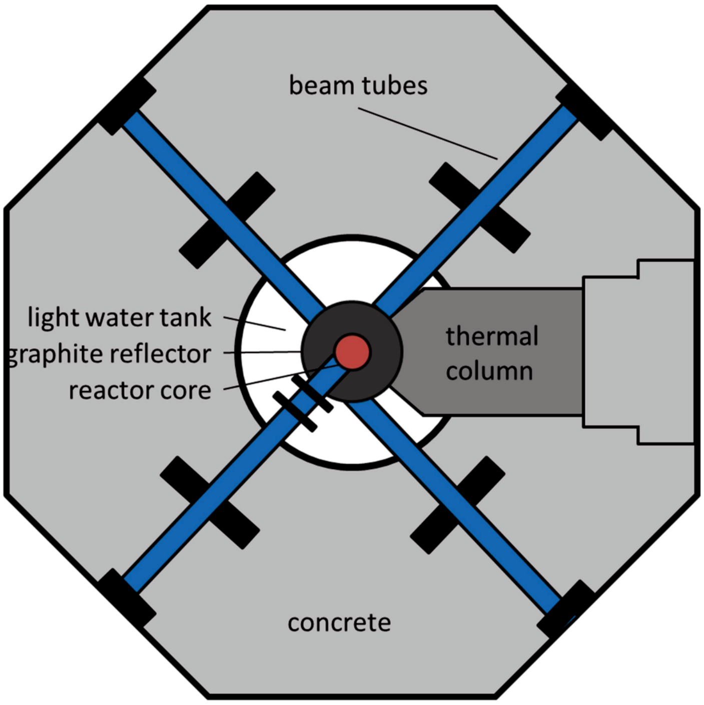

Figure 3-2. Horizontal schema of the TRIGA Mainz, indicating the four radial beam tubes and the thermal column.

The reactor core is surrounded by a rotary specimen rack and a graphite reflector. Including the reflector the core has a diameter of 109 cm. The surrounding light water tank has a diameter of 200 cm and a height of 625 cm, with 490 cm distance between core and reactor platform. Besides the so-called in-core irradiation positions, the TRIGA Mainz has four radial beam tubes and a thermal column, as illustrated in figure 3-2. In general, beam tubes end at the graphite reflector and point towards the centre of the core. Only one beam tube is penetrating the graphite reflector, and another beam tube approaches the core tangentially.

The most important experiment position for the work presented here is the thermal column. It is covered by 13 mm of aluminium and has a boral liner. The front part of the column is connected to the reactor core, and widens towards its cuboid main part. Cover and liner are interrupted at the front. The cuboid part has a length of 160 cm and a width and height of 120 cm. The column can be accessed from behind by opening a rolling concrete gate. The complete volume of the column is filled with graphite, hence providing an isotropic, predominantly thermal neutron field, giving the column its name. By removing graphite rods, selected channels can be opened in the column. Figure 3-3 shows the two configurations used in this work.

Both channels generated have a depth of 127 cm. The standard configuration providing a quadratic opening of 20 cm side length is indicated in blue. Examined from the back side the channel is located up-left from the centre, with the bottom right corner being in the centre. It is opened by removing four graphite plugs, each with a quadratic base of 10 cm side length. Their length is reduced compared to the channel depth, since in the reactor-near end of the channel a permanent photon shield is installed. The shield is made of bismuth and matches the quadratic cross section of the channel. It has a thickness of 5 cm and is equipped with a small handle at the bottom occupying another 2.5 cm. The handle is also made out of bismuth. The shield is shown in figure 3-3 c) in combination with a irradiation box, as usually utilised for experiments.

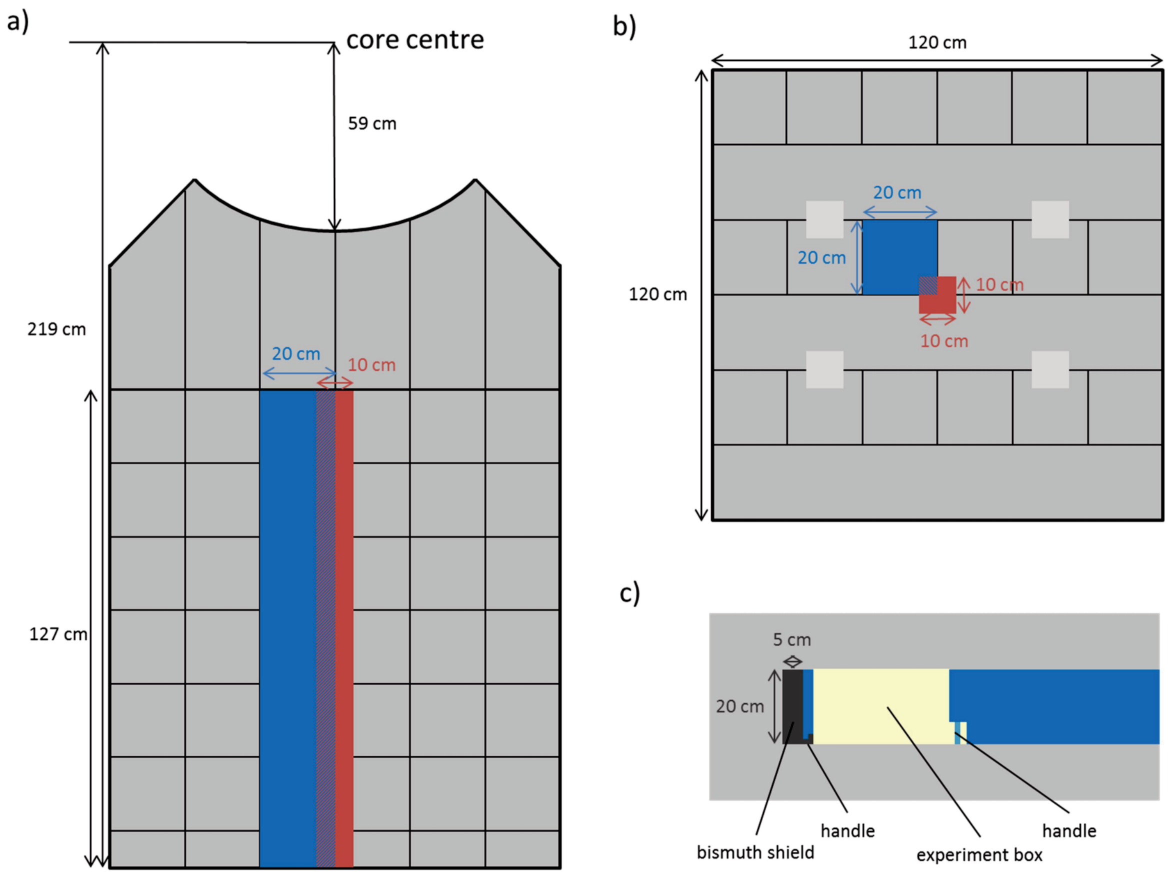

Figure 3-3. Schematic drawings of the two possible channels (blue and red) in the thermal column: a) top view; b) rear view, as seen with open gate; c) side view of the reactor-near end of the blue channel, equipped with bismuth shield and experiment box. Concrete gate, aluminium cover, and boral liner are not shown in the schema.

The second channel indicated in red in figure 3-3 is smaller (10 cm side length). But different to the blue channel it is located in the centre of the column, and therefore in line with the centre of the reactor core. As will be shown later, due to this fact the observed neutron field in the red channel is of better symmetry. Both channels are overlapping, hence the red channel is closed by an angular based plug, which is formed as indicated by the un-shaded red area in figure 3-3 b). To open the complete red channel, two of the overlying plugs of the blue channel have to be removed as well, with an edge of the photon shield still looming into the channel. To open the mere 10 × 10 cm^2 channel, the photon shield has to be removed and the blue channel has to be filled with one angular and three square based plugs.

Table 3-1 summarises the various irradiation positions. The thermal neutron flux given in the table represents nominal values, which should be considered as approximate values. In general it can be seen that those values are a function of distance to the core centre, where the highest flux is observed. The in-core facilities are made for small samples which have to be mandatorily in specific PE capsules. They are mainly used for activation experiments like neutron activation analysis. In contrast, the beam tubes are used for long term experiments in fundamental physics research. Example applications are high precision mass measurements or investigations with ultra-cold neutrons. The given value of the neutron flux has been measured at the tube exit.

Table 3-1. Irradiation positons in the TRIGA Mark II research reactor in Mainz.

Name	No.	Sample insertion	ϕ_{th} / cm^{-2}s^{-1}W^{-1}
Central experiment tube	1	Manually in sample capsules*	4×10^7
Pneumatic transfer system	3	In sample capsules* inserted by pneumatic transfer	2×10^7
Rotary specimen rack	40	Manually in sample capsules*	7×10^6
Radial beam tubes	4	Long term experiments inside and in front of the tubes	5×10^6 to 10^5
Thermal column	1	Manually in different channels	2×10^5 to 3×10^2

* Sample capsules are specific for each type, but in general cylindrical (about 2 cm in diameter and 10 cm in height) and made out of Polyethylene.

3.1.1.2 Models of the facility

Description here is focussed on the modelling of those parts of the reactor which are relevant for this work, especially the thermal column. All data shown is the result of previous work and studies done by cooperation partners.

The first extensive study has been carried out by B. Wortmann [Wortmann, 2008]. Results of her work have been used in an early phase of this work. However, when measurements differed from predictions of this model, a more sophisticated model was developed in cooperation with the Austrian Institute of Technology in Vienna, Austria [Ziegner et al., 2014]. The experimental verification is part of this work, and described in the following sections 3.1.3 and 3.2. All calculations in this thesis are solely based on this model.

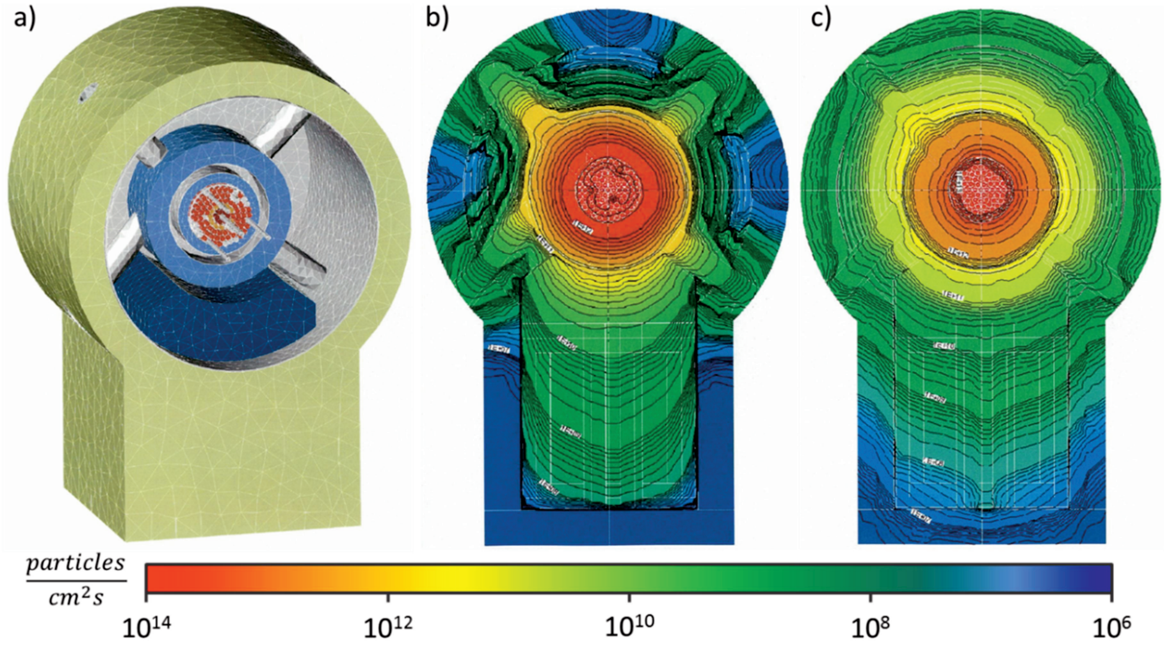

Figure 3-4. a) ATTILA tetrahedron model of the TRIGA Mainz; b) neutron flux of a horizontal cut through the centre of the reactor core; c) photon flux of a horizontal cut through the centre of the reactor core. Legend particles at 100 kW_{th} reactor power.

Wortmann primarily used the program ATTILA, which is no MC, but a deterministic program. The modelled geometry is rebuilt on the base of a net structure using tetrahedrons. For each element the Boltzmann transport equation is solved numerically. In figure 3-4 a) to c) a tetrahedron structure of the complete TRIGA and corresponding calculated results are shown. Wortmann evaluated her simulations mainly with gold activation foils and cadmium capsules. In addition, MCNP was used for comparison calculations. Regarding the neutron field, good agreement was achieved. Dose measurements, carried out at the same time, were accompanied with large uncertainties, derogating their significance. Parts b) and c) of the figure are consistent with the theoretical considerations. Neutrons and photons show an exponential decrease in flux with increasing distance from the core. Inside the core, especially the neutron flux simulation results in an inhomogeneous distribution. As already mentioned, the core is equipped not only with fuel elements, but also irradiation tubes, control rods and graphite dummy elements. In addition, every few years a new fuel element is added to the core, to compensate for burn-up. This might go along with rearrangement of elements in the core, hence fuel elements have different burn-up fractions depending on their time and position inside the core. Wortmann considered these points only with simplifications. Inside the thermal column also an exponential decrease is observed in the calculations for both particles. Through scattering on carbon the neutron flux is almost isotropic. The boral liner leads to a strong decrease of the neutron flux especially outside the thermal column, but also inside it. As a result the propagation of neutrons from the core to the column is not spherical, but lowered at the border of the column. As previously mentioned, the flux distribution is calculated to be asymmetric throughout a perpendicular plane in the 20×20 cm^2 channel. Both calculations shown have been carried out for the 10×10 cm^2 open channel, as visible particularly in figure 3-4 c).

To reduce calculation times in simulations it is acceptable to reduce the size of the simulated geometry. Instead of modelling the whole reactor site, only relevant parts are taken into consideration. A constructive choice is to restrict modelling to the graphite of the thermal column not even including the reactor core. The boral liner is chosen as border of the simulated geometry. Since only a marginal number of neutrons is entering the column through the liner, the overwhelming part of neutrons enters the column in the front, where the liner is interrupted. Consequently, Wortmann designed a plane, virtual source located perpendicular to the entrance of the thermal column, matching the geometrical cross section. The plane is located 63 cm from the centre of the reactor core, and is of quadratic shape with 116 cm side length. This plane was used by of the author of this work before [T. Schmitz, 2010] [T. Schmitz et al., 2010] [T. Schmitz et al., 2011]. Furthermore based on the data a feasibility study was carried out [Blaickner et al., 2012].

Due to larger relevance the development of the model created by Ziegner et al., it is described more in detail. The first step in the processes was a burn-up calculation, which was performed using the program ORIGEN2 [Croff, 1980]. Since the program did not contain a TRIGA library for reaction cross sections and fission product yields, based on previous studies [Khan et al., 2010, Mele et al., 1990], the library for pressurized water reactors was selected. For each of the 76 fuel elements the burn-up was calculated separately. The material inventory was obtained from General Atomics. For all fuel elements present in the core, an average value of the initial inventory was used. The fuel irradiation history was reconstructed from the reactor operation logs from 1967 to 2010, including the evaluation of steady state operation and all pulses. Based on the number of megawatt days (MWd) each fuel element was assigned a burn-up number. Based on these numbers 11 groups were arranged, with 0.3 MWd to up to 3.4 MWd. Each group is characterised by the average burn-up number of the associated fuel elements and the group indicator, which is the fuel element with the burn-up number closest to the group average. From the material composition of the 11 group indicators the containment of the current core is approximated. Uncertainties in the calculation arose from the choice of libraries, but also due to the fact that ORIGEN2 neglects the time dependence of the neutron spectrum. However, Ziegner et al. recognised that these uncertainties might influence the calculated core composition, but argued that they are of only minor relevance for the later particle fluxes in the thermal column.

In a next step, the gained current core composition was implemented into a MCNP5 geometry of the TRIGA Mainz and criticality calculations were carried out. In such calculations, the effective multiplication factor in neutron production is determined. Therefore, embedded in the geometry, strength and energy spectra are accessible. During these particular calculations the neutrons and photons were propagated form the reactor core through the thermal column. Thereby neutrons of all possible energies were transported, while for photons cut-off energy of 1 keV existed and only particles with higher energies were transported.

Similar to the work of Wortmann subsequently a plane, virtual source was constructed. Equal energy bins were used as well as the same positon, perpendicular, 63 cm from the reactor core, matching the cross section of the thermal column. For the neutron source the identical size of 116 x 116 cm^2 was chosen, for the photon source a much bigger source was created with the size of 320 × 322 cm^2. This way the inclusion of scattered photons is ensured, since they are not limited by the boral liner, as neutrons are. Comparing the simplified, virtual source to the sophisticated, whole reactor source a good agreement could be demonstrated.

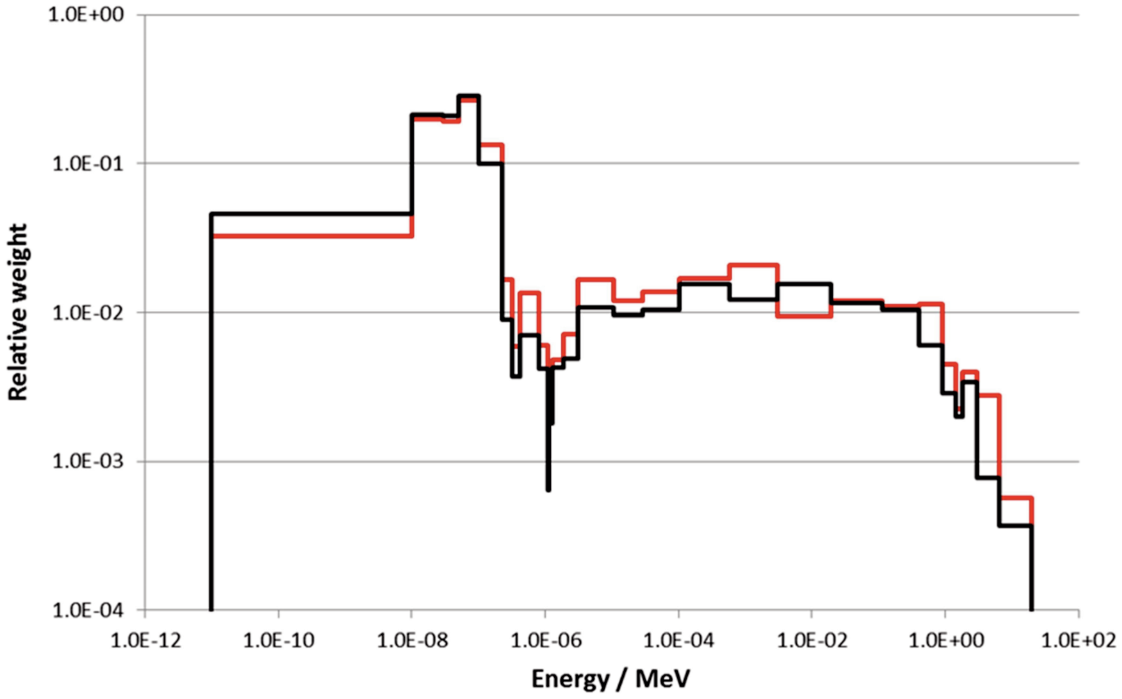

Figure 3-5. Neutron energy spectra obtained by Wortmann (red) and Ziegner (black) for the planar, virtual source of the thermal column. The area below the black curve is normalised to one, the red curve is adjusted according to the source strength ratio.

Compared to the Wortmann source, resulting energy spectra and source strength are different, as depicted in figures 3-5 and 3-6. In the new model, the neutron source has a strength of 7.79×10^{10} $cm^{-2}s^{-1}$ at a reactor power of 100 kW_{th}. Wortmann obtained a similar strength of 7.94×10^{10} $cm^{-2}s^{-1}$ under the same conditions. In contrast regarding photons a large difference was observed. With 5.73×10^{10} $cm^{-2}s^{-1}$ the new photon source strength of Ziegner et al. is much smaller compared to the Wortmann source strength, which is with a value of 2.54×10^{11} $cm^{-2}s^{-1}$ about a factor 4.4 stronger. For the relative values in each energy bin observations are similar. The shown values in figures 3-5 and 3-6 are normalised such way that the area below the new, black spectra accounts to one. The area below red curve, indicating the spectra of the older source, is adjusted according to the source strength ratio, and therefore in both cases bigger. The neutron spectra are very similar with only small differences, and so is the shape of the photon spectra. An exception is the bin of the low energy photons between 10 keV and 45 keV. Here, contrary to the other parts, the new spectrum has a higher value. For easier comparison of calculations by which these spectra were obtained, the lowest photon energy was adjusted from 1 keV to 10 keV, since this was the lower limit of the former model.

The differences are explained by Ziegner et al. with the shortcomings of ATTILA regarding photon transport, as for example discrete instead of continuous cross sections, and less sophisticated underlying models. According to them this should have a bigger impact on the final result, than the more detailed modelling of the core. As stated before, in this work solely the model of Ziegner et al. was used.

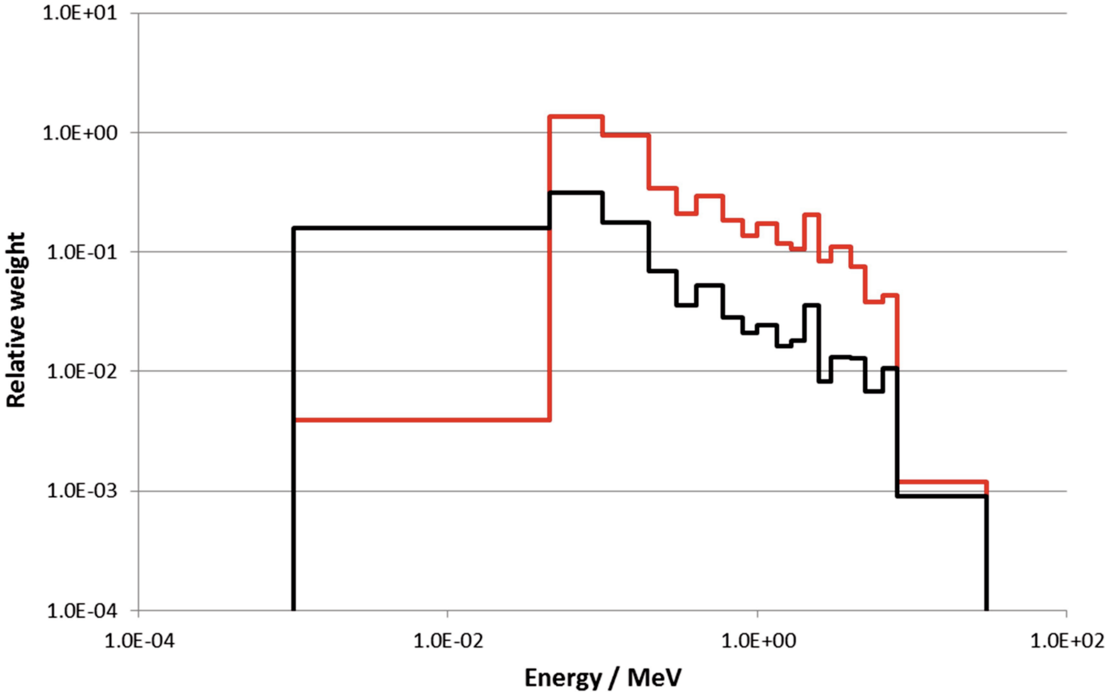

Figure 3-6. Photon energy spectra obtained by Wortmann (red) and Ziegner (black) for the planar, virtual source of the thermal column. The area below the black curve is normalised to one, the red curve is adjusted according to the source strength ratio.

3.1.2 Description of evaluation experiments and calculations

This section consists of two parts. In the first one solely the neutron distribution throughout the thermal column is investigated using gold foils only. Here also preparative tests and work is described, as mandatory for accurate measurements. In the second part other activation foil materials are introduced, which are then used for neutron spectrometry as described previously in subsection 1.4.3.2 of the introduction. Most measurements are accompanied by modelling for the purpose of evaluation.

3.1.2.1 Neutron flux distribution

The neutron flux distribution in the thermal column was examined by comparison of gold foil activation and calculations made with the MC code FLUKA. As described in subsection 1.4.3.2, the measured response of a foil is activation after irradiation. With respect to its parameters, gold foils are in many aspects almost ideal to serve as flux monitors. Gold-197 is the only stable isotope, and has hence an abundance of 100%. During neutron irradiation it reacts with a relatively high cross section of 98.7 barn to the isotope gold-198, which then subsequently decays to mercury-198, as demonstrated in equation (76). Due to the long half-life, extended activation measurements are possible, without any corrections regarding decay during the activation measurement. In the experiments activation analysis was done using a standard high-purity germanium (HPGe) gamma spectrometry system (Genie$_{\mathrm{TM}}$, Canberra Industries, Meriden, United States), measuring the gammas emitted during the decay of gold-198. The known gamma energies are depicted in table 3-2. From the table it is obvious that the 411.8 keV photopeak is most favourable due to its high branching ratio.

$$ {}^{197}_{79}Au \xrightarrow[]{\substack{- \\ \sigma_{th} = 98.7\ b}} {}^{198}_{79}Au \xrightarrow[]{\substack{\beta^{-} - \\ t_{1/2} = 2.}} {}^{198}_{80}Hg \tag{76} $$

Table 3-2. Gamma lines during the decay of gold-198

Gamma energy / keV	Branching ratio / %
0.99	1.27
68.89	0.76
70.82	1.38
80.20	0.48
82.50	0.12
411.8	**95.53**
675.9	0.83
1087.6	0.16

As shown in figure 3-5, the neutron spectrum within the thermal column of the TRIGA Mainz is dominated by thermal neutrons. For the study of the flux distribution the neutron flux is therefore simply calculated as thermal equivalent, ϕ_{th}, neglecting the neutron spectrum dependence of the cross section and applying the thermal neutron capture cross section, σ_{th}, according to equation (77). The measured activity is counted back by the spectrometer software to the activity at the end of the irradiation, A_0. The number of target atoms (gold atoms), N, is calculated via the foil mass; λ and $\mathrm{t}_{\mathrm{irr}}$ are the decay constant of gold-198 and the irradiation time of the foil during the experiment.

$$\phi_{th} = \frac{A_0}{N\sigma_{th}[1- \qquad (-\lambda t_{irr})]} \tag{77}$$

Preparation of the gold activation foils

Gold foil was obtained from Goodfellow, with a thickness of 12.5 µm. At this thickness, the self-shielding effect was expected to be rather low or even negligible. The foil was cut in pieces of 5 × 5 mm^2 and weighed. In total 87 foils were prepared, weighing between 4.2 µg and 7.2 µg, the average weight observed was 5.7 µg with a relative standard deviation of 0.7 µg. Uncertainty in weighing was 5%. Differences in weight might be explained by un-exact cutting and inhomogeneities in the foil thickness. After weighing foils were fixed with a numbered label in adhesive tape for easier handling. All foils were irradiated for test purposes to ensure purity, weighted mass, and homogeneity in thickness.

Operational constraints

Due to constructional constraints, all samples or experimental build-ups have to be inserted into the thermal column before irradiation at zero reactor power. This way all detectors observe not only the described irradiation time, but in addition the time in which the reactor is reaching the selected power. The reactor is operated manually. The time to reach the maximum power of 100 $\mathrm{kW}_{\mathrm{th}}$ is about 5 minutes and, respectively, shorter for lower reactor powers. The influences on the signal of an integral detector, as for example activation foils, were evaluated with the help of the recorder reading of the reactor power. The reading was integrated for the time of the raising of the reactor power and for the time during operation in steady state. For irradiations carried out in this work, irradiation times where chosen such way that the integral of the raising-time was at least less than 1% of the integral of the steady state time. Since the increase in reactor power is nearly exponential the time needed to reach the 1% ratio is relatively low. In the case of a reactor power of 100 kW_{th} the time needed in steady state mode is 10 minutes in a conservative estimation.

Gamma Spectrometry

The HPGe-spectrometer is surrounded by lead, to minimise the radiation background, and backed by copper, to shield the X-ray fluorescence of lead. The spectrometer itself contains a germanium crystal behind a beryllium window. In front of this window samples can be positioned in polymethyl-methacrylate (PMMA) elements, which are fixed in a PMMA holder. The distance between window and sample can be increased in steps of 2 cm by varying the position of the PMMA element within the holder (figure 3-7 a)).

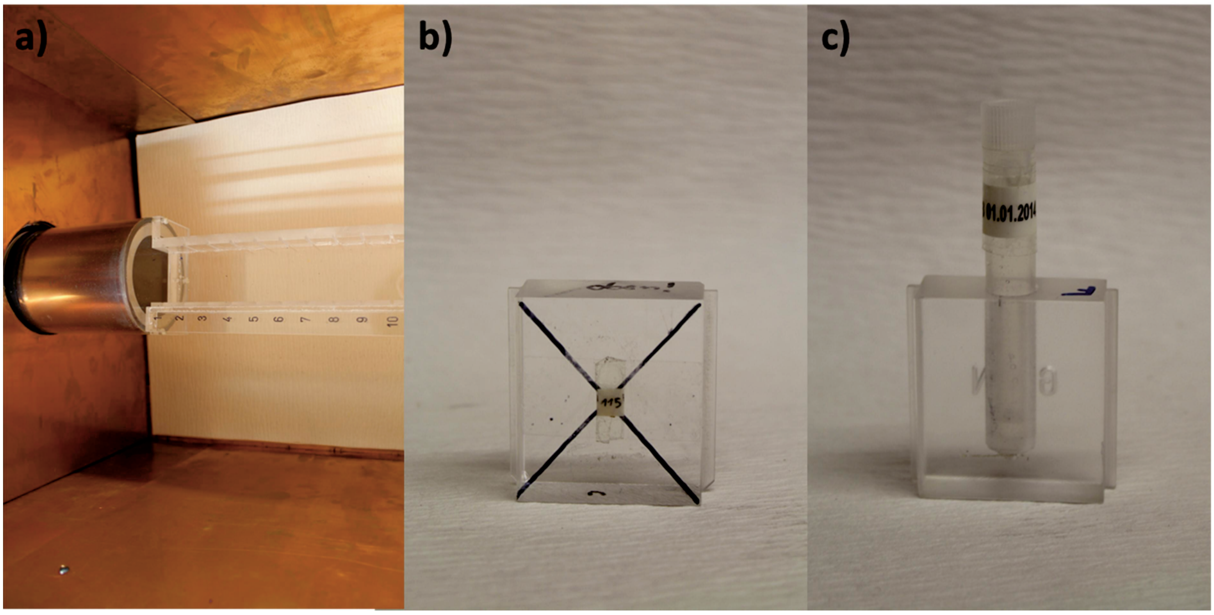

Figure 3-7. Photographs of a) detector head of the HPGe-spectrometer with the PMMA holder; b) exemplary gold foil fixed with adhesive tape on the corresponding PMMA element; c) capillary tube with liquid 500 µL-standard and corresponding PMMA element.

The HPGe-spectrometer needs to be calibrated in two ways. Since the foil composition is known, energy calibration has to be carried out for every single spectrum with the gamma lines from table 3-2. The also needed efficiency calibration is more complex. It is based on the measurement of a reference solution containing known amounts of various radioisotopes. At the research reactor TRIGA Mainz routinely the calibration solution QCY48, provided and certified by the Physikalisch-Technische Bundesanstalt (PTB) is used. The radionuclide composition of such QCY48 solution is itemised in table 3-3, including the major parameters of all nuclides (as an example, data of the latest 2014 standard are shown). The solution has to be replaced every one to two years, since the lines of some nuclides weaken significantly within this time period, as can be seen from the table by specific activity and half-life.

Table 3-3. Radionuclides in the 2014 OCY48 calibration solution according to the calibration sheet provided by PTB.

Gamma-Ray Energy / keV	Nuclide	Half-life	Branching ratio / %	Specific activity / Bq/g	Gamma rays / $s^{-1}g^{-1}$	Total uncertainty / %
60	**Am-241**	432.17 y ± 0.66 y	36.0	1760	633.6	3.1
88	**Cd-109**	462.6 d ± 0.7 d	3.63	24900	903.9	2.4
122	**Co-57**	271.79 d ± 0.09 d	85.6	562	481.1	2.3
166	**Ce-139**	137.640 d ± 0.023 d	79.9	810	647.2	2.3
279	**Hg-203**	46.59 d ± 0.013 d	81.5	1820	1483	2.3
392	**Sn-113**	115.09 d ± 0.04 d	64.9	1410	915.1	2.3
514	**Sr-85**	64.849 d ± 0.004 d	98.4	1740	1712	2.3
662	**Cs-137**	30.17 y ± 0.16 y	85.1	662	563.4	2.3
898	**Y-88**	106.630 d ± 0.025 d	94.0	2370	2228	2.3
1173	**Co-60**	5.272 y ± 0.001 y	99.86	1100	1098	2.3
1333	**Co-60**	5.272 y ± 0.0001 y	99.98	1100	1100	2.3
1836	**Y-88**	106.630 d ± 0.025 d	99.4	2370	2356	2.3

Usually from the calibration solution a 500 µL liquid aliquot is measured in a capillary tube, as regularly used for sample measurements (figure 3.7 c)). However, for efficiency calibration the geometry of the standard should as much as possible match the geometry of the sample. Therefore, in the case of activation foils, the cylindrical, liquid standard was found to be insufficient. To achieve better agreement a defined quantity of the reference solution was evaporated on three gold foils (50 µL for each foil, pipetted as 5×10 µL). The foils had identical lateral dimensions as the monitor foils. For uncertainty reduction the pipetted mass was weighed with an analytical balance for every single amount of 10 µL. Evaporation was assisted using an infrared lamp, positioned in about 10 cm distance from the foil, requiring approximately 1 min to evaporate 1 µL. After completeness the foil was sealed analogue to the gold foils. Verification of the calibration foils was done by comparison to the liquid 500 µL-standard in different distances. At an increased distance response should be equal, since influence of geometry is of less importance.

The time between irradiation and measurement of monitor foils was chosen in such way that the dead time of the detector was below 3%. The position inside the detector is a compromise between reducing the geometry influence and signal intensity. Usually a positon 6 cm (slot 4) from the detector window has been used. The measurement time was adjusted to reach statistical uncertainties below 1% for the determination of the peak area and hence the calculated activity of the foil, which is proportional. Standard measurement time was one hour.

Stack experiment

When passing through the activation, foil neutrons may be absorbed, leading to a decreasing neutron flux. The resulting activation, and therefore the calculated flux, is hence lower than the undisturbed flux. The relevance of this self-absorption or self-shielding effect is proportional to the target thickness. To scrutinise this effect, an experiment was carried out twice in which foils were stacked for irradiation. The irradiations were carried out in the 20 × 20 cm^2 channel, equipped with the bismuth shield and the standard irradiation box, shown in figure 3-3 c). The box is made of polyethylene (PE) with a width and height of 19.8 cm and a length of 33.0 cm. With a wall thickness of 1.5 cm the inside space has the dimensions of 30.0 × 16.8 × 16.8 cm^3. Inside the box a cubic PMMA phantom with a side length of 15.0 cm was used. It was positioned in the front on the left side, seen from the reactor core, where the highest flux is expected. On the front surface of the cube foils were fixed on nine positions within a square of 5 × 5 cm^2. In each position either a single foil or stacks of up to four were arranged. In total 20 foils were irradiated. Figure 3-8 illustrates the box, seen form above and the positioning of the foils. Foils were irradiated for 15 minutes at a reactor power of 1.0 kW_{th}.

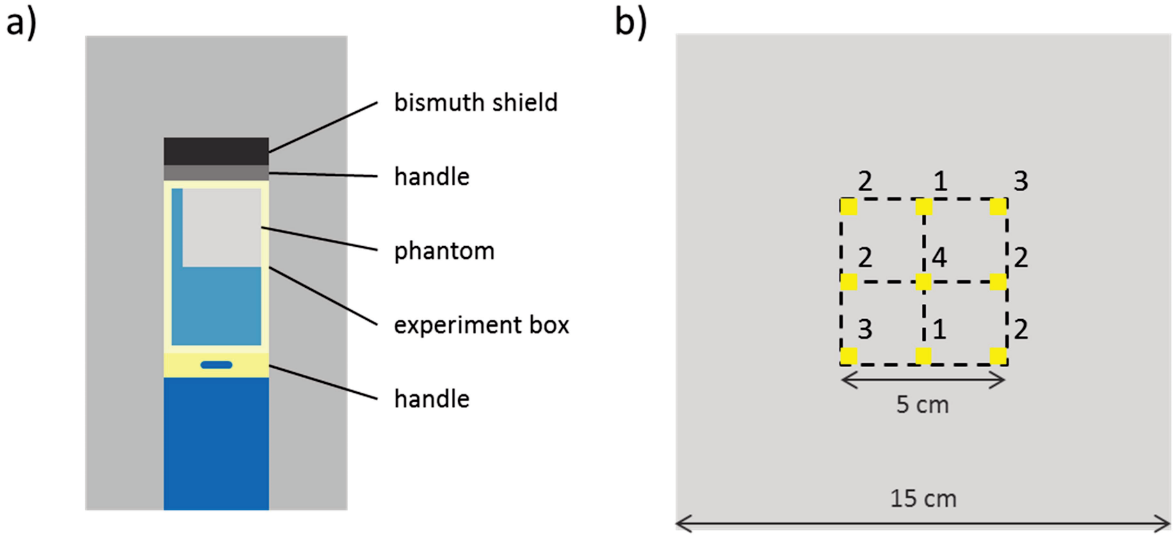

Figure 3-8. a) PE box including cubic phantom in the 20 x 20 cm^2 channel of the thermal column; b) Arrangement of foils on the front of the cubic phantom, as seen from the reactor core. Numbers indicate the stack size.

Free in air experiment

To examine the flux distribution over the whole depth of the thermal column foils were irradiated in the central 10 × 10 cm^2 channel in ten different positions. Two foils were fixed in every depth next to each other on a 3 mm thick, 5 × 5 cm^2 PMMA plate. The plates were fixed on a PE rod with a length of 118 cm and a diameter of 2.5 cm. The ten positons were distributed through the channel. In terms of distance to the reactor core all depths were between 99.6 cm and 208.3 cm. An exemplary part of the build-up can be seen in figure 3-9. Foils have been irradiated for 15 minutes at a reactor power of 1.0 kW_{th}.

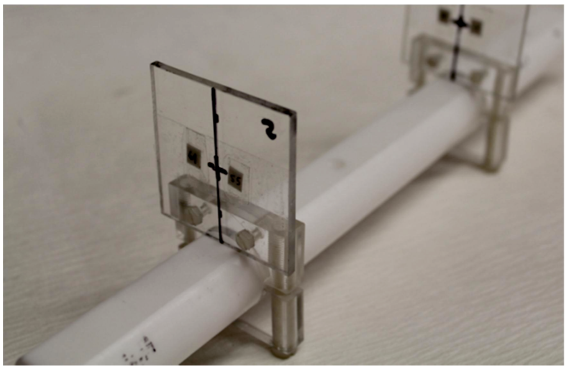

Figure 3-9. Photograph of a section of the PE rod with PMMA holder and two gold foils.

Phantom experiment

Analogue to the experimental setup in the pile experiment irradiations were carried out in the standard PE box in the 20 × 20 cm^2 channel. Also the positioning within the box was similar (front left side, seen from the reactor core). However a different, cuboid-shaped (10 × 10 × 23 cm^3) PMMA phantom was used. It was equipped with several cavities, which can be used for detectors or otherwise be filled with PMMA elements. On its central length axis the phantom has drill holes on both sides with a depth of 10.2 cm, leaving a gap of 2.6 cm in the middle (figure 3-10). In the first setup in both holes three foils where positioned on or in-between PMMA elements. Depths relative to the phantom front surface were 0.0, 5.2, 10.2, 12.8, 17.8, and 23 cm. As before the irradiation was carried out twice with 1.0 kW_{th} reactor power for 15 minutes.

In a second setup, which was also irradiated twice under the same conditions, nine foils were irradiated in each run. Three foils were fixed with tape on the left side, three inside, and three on the right side. Compared to the other experiments foils were arranged laterally, rotated by 90°. Measured from the front, foils were at depths of 5.0, 11.5, and 18 cm.

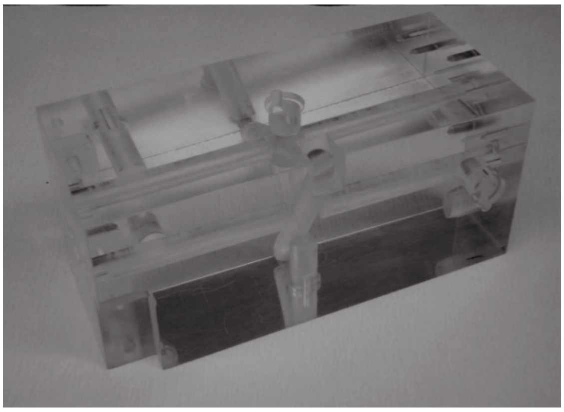

Figure 3-10. Photograph of the cuboid shaped PMMA phantom.

Uncertainties

Uncertainties for each foil are calculated based on equation (77). Regarding cross section and decay constant uncertainties are neglected. Irradiation time $\mathrm{t_{irr}}$ equals the operation time of the reactor, which is monitored by a stop watch. Related uncertainty is below 3 s, corresponding to 0.3% for 15 min irradiation time. More important is the uncertainty due to the raise of power in the starting time until the selected power is reached. Due to evaluation of recorder readings uncertainty was set to 1%. For the determination of the activity two sources of uncertainties have to be considered. The peak area is afflicted to a statistical uncertainty of below 1%, and the efficiency calibration prepared by combination of measurements with three, identical calibration foils is afflicted to an uncertainty of 3.8%. This value includes uncertainties regarding the fitting curves, the amount of radioisotopes evaporated on the foil, and the PTB solution. Combined uncertainties of the thermal equivalent fluxes are varying around 4.5%.

Calculations

Calculations have been carried out using the Monte Carlo code FLUKA. The source description of Ziegner et al. [Ziegner et al., 2014] was adapted for FLUKA with the help of a “source” user-routine, activated in FLUKA by the “SOURCE” card. The user routine samples energy and lateral position in the source for each emitted neutron, according to the model. Therefore, the routine was programmed with the necessary information about energy spectrum and lateral distribution.

The modelled geometry included mainly the graphite of the thermal column. Since in simulations for this chapter no photon simulations had been necessary, the surrounding concrete was not considered, due to the presence of the boral liner.

All parts of each experimental setup were modelled in detail, including the bismuth shield, PE- and PMMA-elements and the activation foils. Only the papery labels and the tape were neglected. Material data like composition and density were obtained from literature or manufacturer data sheets. The density of reactor graphite in the thermal column was determined by weighing of one of the removable plugs, since density of reactor-graphite can vary. Default settings for hadron therapy “HADROTHE” were used, with “USRBIN” scoring to calculate the neutron propagation in the thermal column. “USRTRACK” scoring was used to obtain neutron spectra for each foil. The angular dependence of neutrons was analysed using “USRBDX” cards. Results were multiplied with the given source strength without any further normalisation. The received neutron fluxes were weighted with corresponding calculated neutron spectra to gain the thermal neutron equivalent and enable comparison with the measured values.

Calculations were carried out until resulting statistical uncertainties in the “USRBIN” scoring were below 1%. In the “USRTRACK” scoring uncertainties associated to energy bins were in general below 3%. Only single values for bins in high energy regions above 10 keV are reaching up to 11%. In general with the “USRTRACK scoring uncertainties are higher for higher energies, since particle numbers per energy bin decrease. Uncertainties afflicted to the results of the “USRBDX” are in the maximum between 0.5% and 4%.

3.1.2.2 Neutron spectrometry

While for the determination of the flux distribution the simple thermal equivalent flux is sufficient, it is not for neutron spectrometry. Therefore the measured activities have been transformed into reaction rates according to equation (78), which is independent of the cross section.

$$R = \frac{A_0}{N[1- \qquad (-\lambda t_{irr})]} \tag{78}$$

Besides the gold foils, described in detail above, four more foil materials, i.e. copper, indium, manganese, and wolfram, were used. Regarding their parameters they are comparable to gold-197, some are shown in table 3-4.

Table 3-4. Isotope and interaction characteristics of the foil materials.

Isotope	Abundance	Interaction	Half-life	thermal cross section	Energy range of first resonance
^{55}Mn	100.0 %	(n,γ)	2.58 h	13.3 b	340 eV
^{63}Cu	69.15 %	(n,γ)	12.7 h	4.5 b	1 keV
^{115}In	95.71 %	(n,γ)	54 min	161 b	1 eV
		(n,n’)	1.78 h	2 b*	430 keV
^{186}W	28.43 %	(n,γ)	23.7 h	37.0 b	18 eV
^{197}Au	100.0 %	(n,γ)	2.69 d	98.7 b	5 eV

* threshold reaction, cross section at 4 MeV neutron energy (compare text)

Half of the isotopes have a natural abundance below 100%. The lowest abundance has wolfram-186, with a value of 28.43%. Considered interactions are mostly (n,γ)-reactions. Only indium-115 combines two different types of interactions, (n,γ) and (n,n’). The later leaves the core of the indium-115 isotope in a metastable state (indium-115m). Also the (n,γ)-reaction leads to a metastable state, but of the isotope indium-116. In both cases gamma-rays are emitted. Cross sections, given in the table, are thermal neutron capture cross sections, valid for a neutron energy of 0.025 eV. The (n,n’)-reaction is again an exception. The interaction has a threshold at neutron energy of 430 keV, reaching a maximum of 2 b at 4 MeV. Below the threshold, the reaction does not occur. The radioactive isotope decays in most cases in β^--mode, only copper-44 shows β^+-decay and indium-115m undergoes in 95% of the cases an isomeric transition (IT), while 5% also decay in β^--mode. Reactions are shown in equations (79) to (83).

$${}^{63}_{29}Cu \xrightarrow{\substack{- \\ \sigma_{th}= 4.5\ b}} {}^{64}_{29}Cu \xrightarrow{\substack{\beta^{+}-decay \\ t_{1/2}= 12.7\ h}} {}^{64}_{28}Ni \qquad (79)$$

$${}^{56}_{25}Mn \xrightarrow{\substack{- \\ \sigma_{th}= 13.3\ b}} {}^{56}_{25}Mn \xrightarrow{\substack{\beta^{-}- \\ t_{1/2}= 2.58\ h}} {}^{56}_{26}Fe \qquad (80)$$

$${}^{115}_{49}In \xrightarrow{\substack{- \\ \sigma_{th}= 161\ b}} {}^{116m}_{49}In \xrightarrow{\substack{\beta^{-}-decay \\ t_{1/2}= 54\ m}} {}^{116}_{50}Sn \qquad (81)$$

$${}^{115}_{49}In \xrightarrow{\substack{inel.-scat. \\ \sigma_{4\ MeV}= 2\ b}} {}^{115m}_{49}In \xrightarrow{\substack{IT \\ t_{1/2}= 4.49\ h}} {}^{115}_{49}In \qquad (82)$$

$${}^{186}_{74}W \xrightarrow{\substack{- \\ \sigma_{th}= 37.0\ b}} {}^{187}_{74}W \xrightarrow{\substack{\beta^{-}- \\ t_{1/2}= 23.7\ h}} {}^{187}_{75}Re \qquad (83)$$

The gamma energies used for analysis of the activated foils are given bold in table 3-5, those of gold-198 were given previously in table 3-2. In the case of copper-64 the emitted positron annihilates with an electron and emits annihilation radiation. By background measurements it was ensured that the observed peak at 511 keV is resulting solely from the emitted positrons and not from competing sources. In the spectrum of indium-116m three favourable lines can be found, which are combined for analysis.

Table 3-5. Gamma lines during the decay of activated isotopes.
Only branching ratios above 10% are shown, bold lines indicate used energies.

Isotope	Gamma energy / keV	Branching ratio / %
^{56}Mn	**846.6**	**99.0**
	1811.2	30.0
	2112.6	15.5
^{64}Cu	7.5	14
	511.0	**37**
^{115m}In	24.2	18.0
	336.3	**45.0**
^{116m}In	**417.0**	**30.0**
	818.8	17.0
	1097.1	**53.0**
	1293.4	**80.0**
	2112.0	16.0
^{187}W	61.1	12.8
	134.2	10.1
	479.5	26.6
	685.7	**32.0**

All foil materials were obtained from Goodfellow, with a thickness of 12.5 µm. The manganese foil was backed with non-removable polyester. Foils were cut, weighed and packed analogue to the gold foils. Numbers of foils per material and connected weight ranges are shown in table 3-6. Differences in weight might be explained by un-exact cutting and inhomogeneities in foil thickness. Uncertainty in weighing was again 5%, only with manganese foil uncertainty was increased to about 10%, due to the necessary subtraction of the weight of the polyester backing. All foils were irradiated for test purposes to ensure purity, weighed mass, and homogeneity in thickness. Irradiation prerequisites are analogue to those for the irradiations of gold foils. Different to experiments described before, neutron spectrometry experiments have been carried out not only in the thermal column, but also using in-core irradiation positions.

Table 3-6. Foil numbers and weights.

Isotope	**No. of foils**	**Weight / µg**			
		Average	**Std.dev.**	**Minimum**	**Maximum**
^{55}Mn	25	2.3	0.3	1.8	3.1
^{63}Cu	23	2.6	0.2	2.2	3.1
^{115}In	21	3.0	0.4	2.4	3.6
^{187}W	27	5.4	0.6	4.2	6.4

Experiments in the thermal column

Two different setups were irradiated in the thermal column of the TRIGA reactor. In the 10 × 10 cm^2 channel foils of each material were irradiated free in air on a PMMA plate. Plates have been described in the previous sub-section within the free in air experiment. One foil of each material has been irradiated simultaneously on the same plate in a distance of 99.6 cm to the centre of the core. In total four irradiations have been carried out. Two with foils covered in cadmium capsules and two with bare foils without any cover. Cadmium capsules used, were cylindrical with an diameter of 13.3 mm and a height of 2.8 mm. Inside space was also cylindrical with a radius of 10.3 mm and a height of 1.0 mm. Bare foils were irradiated 15 min at 2.0 kW$_{th}$, foils in capsules were irradiated 30 min at 100 kW$_{th}$. Duration and power were estimated from test irradiations to provide sufficient activation for convenient execution of foil measurements, but limited dose to the experimenter at the same time. Especially indium generates dose due to the short half-life and high cross section.

In a second experiment the cubic PMMA phantom (side length 15 cm) has been used in the standard PE box in the 20 x 20 cm^2 channel. In general, a similar irradiation setup, two times with and two times without cadmium, employing five foils at a time, had been chosen. Foils were positioned similarly to the foils in the pile experiment within the 5 × 5 cm^2 surface in the centre of the phantom forefront. Since in this setup also test irradiations were carried out, sufficient data were available to correct for the lateral shift in flux. Time and duration of each irradiation were chosen identical to the free in air experiment.

Experiments outside the thermal column

Experiments were carried out in two facilities of the PTS, located in the outward ring of the reactor core. In a first step preparing experiments investigated the flux height profile within the irradiation capsules using wire made of an aluminium-gold-alloy (containing $0.1124\%_{wt}$ gold). These curves, which can be found in appendix C, suggest foil positioning at a particular height within the capsules, to avoid the necessity of further correction due to changes in flux with height. Again foils were irradiated with and without cadmium. Two modes of irradiation have been tested. Five foils, one of each kind, were irradiated in stack and alternatively apart in five separate runs. Each irradiation was carried out twice with 100 kW_{th} reactor power for 57 s.

Calculations

Calculations have only been carried out for the thermal column, where the described model is valid. Unfolding of the TRIGA spectra was performed with the SAND algorithm [Griffin et al., 1994]. Necessary input consists of the obtained reaction rates and priori spectra for each position, which were obtained from FLUKA calculations. Simulations were build analogue to those described above. Spectra were obtained using “USRTRACK” scoring. Statistical uncertainties in the results were below 3% in all energy bins. The binning has been chosen identical in the MC code and the unfolding algorithm.

3.1.3 Results

As in the previous section, first preparative works will be described to ensure the accuracy of the later measurements. In a second step the neutron distribution measured with gold foils will be compared to the modelled distribution. In the last step the results of the neutron spectrometry will be shown. All modelling relies solely on the model by Ziegner and co-workers [Ziegner et al., 2014].

The efficiency calibration of the gamma spectrometer is of great relevance. Therefore, the evaluation of the prepared calibration foil is presented first, before describing the results of neutron flux and spectrometry experiments.
The supplier of the activation foils provides information on thickness, and a list of impurities. Especially in the case of the foil thickness, specifications of the deviation from the mean value remained uncertain. As a consequence all foils were test irradiated, since substantial variations in thickness would influence the self-absorption. However as a result of the test irradiations, also in comparison with later irradiations of the foils, it could be shown, that the foil response does not vary in excess of the statistical uncertainty.

3.1.3.1 Detector calibration

All three calibration foils have been evaluated as described in the previous section by comparison to the regular 500 µL standard. Efficiency curves can be found in appendix D. From these curves efficiencies for certain energies were extracted and plotted versus several distances towards the detector window. As an example, in figure 3-11 the efficiency as a function of distance is shown for an energy of 412 keV, which is equal to the energy of the main line in the activation spectrum of gold-197. As it can be seen in the photographs in figure 3-7, calibration foils are fixed on the PMMA element, while the 500 µL solution is placed inside the PMMA element in a drilling. Therefore foil and solution measured in the same holder position are corresponding to different distances in the figure. In the same position the foil is closer to the detector by 1 cm. Values of the solution, shown in black, decrease from an efficiency of 0.056 to 0.0023. Efficiencies of the three calibration foils were averaged, with relative standard deviation below 2%. Values decrease from 0.090 to 0.0024. Curves shown in the figure are fitted to measured data and proportional to $\frac{1}{r^2}$ (with r distance to the detector window). Already in a distance of about 4 cm curves and efficiencies are almost identical. At low distances the efficiency, and therefore number of gammas detected per emission, is higher with the foil. For energies different from 412 keV observations are similar. In the following experiments calibration was made using the prepared foils.

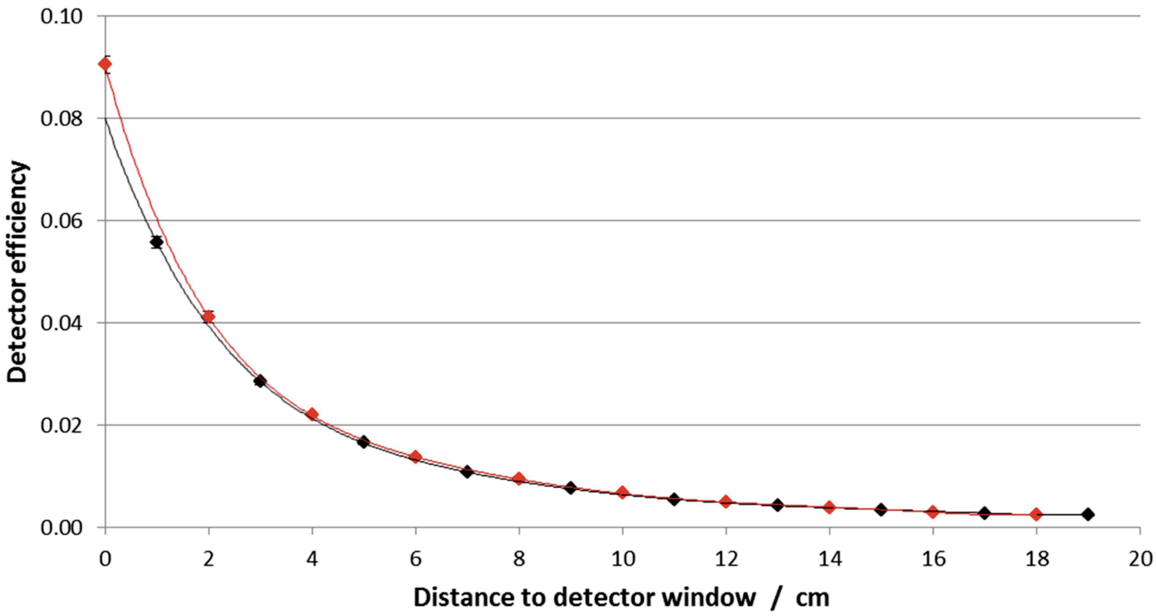

Figure 3-11. Efficiency of the gamma spectrometer as measured with the regular 500 µL calibration solution (black) and with the calibration foils (red) at 412 keV.

3.1.3.2 Neutron flux distribution in the thermal column

The 40 foils of the pile experiment were irradiated in two identical but separate experiments. For evaluation the measured thermal neutron equivalent flux was averaged for each position. The two values differed in the maximum by 3.1%, the average difference was 1.0 %. Two trends can be observed, one between the positions on the phantom and a second one within each pile.

The trend observed between the nine positions on the 5 × 5 cm^2 square is shown in figure 3-12. For the figure the results of all foils within one pile were averaged without further correction (i.e. regarding position within a pile, cf. second trend, next paragraph). Each position is identified by a lateral positon (left, middle, right), and a height (bottom, middle, top). As explained before the big channel is not located central in the thermal column, which is why the neutron flux distribution is not symmetric. A continuous trend can be observed in both directions. Towards the top the trend is larger, where within one lateral position an average decrease of 4.4% is observed, while values between left and right (in a certain height) differ on average by only 2.7%. From bottom/left to top/right flux decreases by 7.2%. For reasons of better visibility uncertainties are not shown in the diagram. As mentioned before single measurements had uncertainties of 4.5%, the standard deviation of single coordinates is on average 1.1%.

During the testing of all foils (regarding homogeneity etc.) identical setup with nine positions on the cubic phantom were chosen. Qualitatively and quantitatively the same trend has been observed in flux as presented here for the pile experiment. Hence these results were used for normalisation of later experiments.

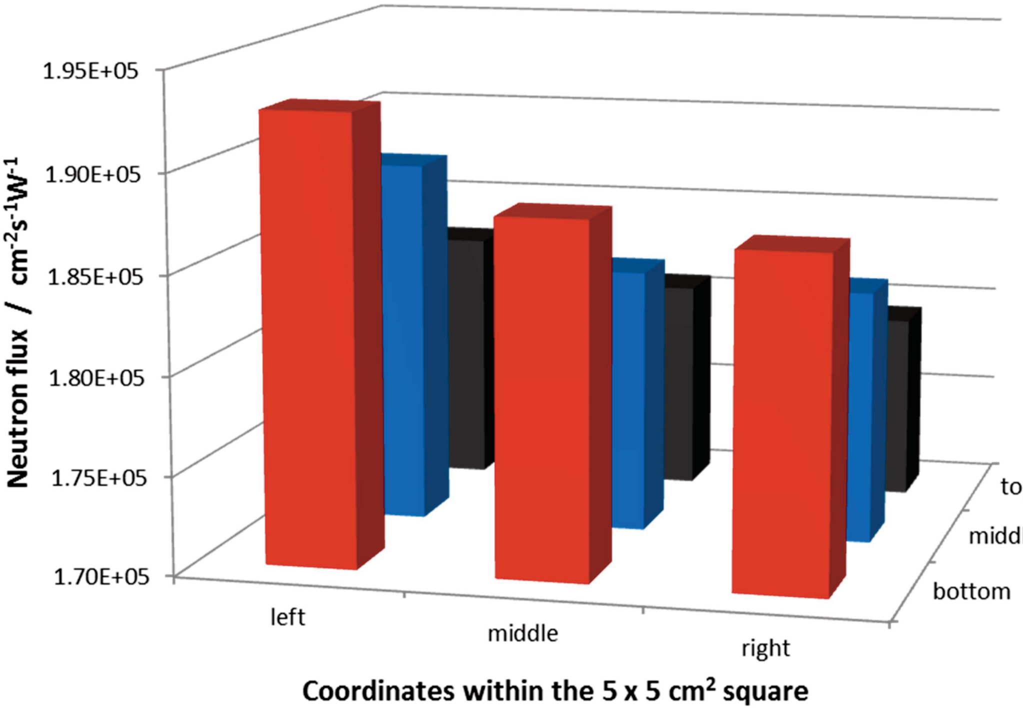

Figure 3-12. Thermal neutron equivalent flux as a function of position on the front surface of the cubic phantom within the 5 x 5 cm^2 square in coordinates as seen from the reactor core.

However, the general purpose of this experiment was the second trend, which can be observed within one stack. The highest flux is observed in the uppermost foil. Between two foils arranged directly behind each other in one pile the observed neutron flux decreases on average about 1.4%. Thereby no significant difference has been found when comparing change between first and second or second and third foil in a pile. Figure 3-13 shows the decrease as a function of foil position, thereby 1 indicates the uppermost foil. All values are shown relative to the uppermost foil of each pile. Uncertainties shown are as indicated in the previous section. Parts a) to c) of the figure indicate the top, middle and bottom row. The lateral position can be differentiated by the symbol. Piles top/middle and bottom/middle only consisted of a single foil, therefore they are not shown in the graphs. In total of 7 piles with more than one foil, two show an increase, five a decrease, whereby in the case with four foils the change is not continuous. Compared to the uncertainties change is not significant in all cases. The biggest decrease can be observed for the pile in top/left. From these results a self-shielding factor was extracted, which was applied to the following experiments, and is described in detail in the discussion.

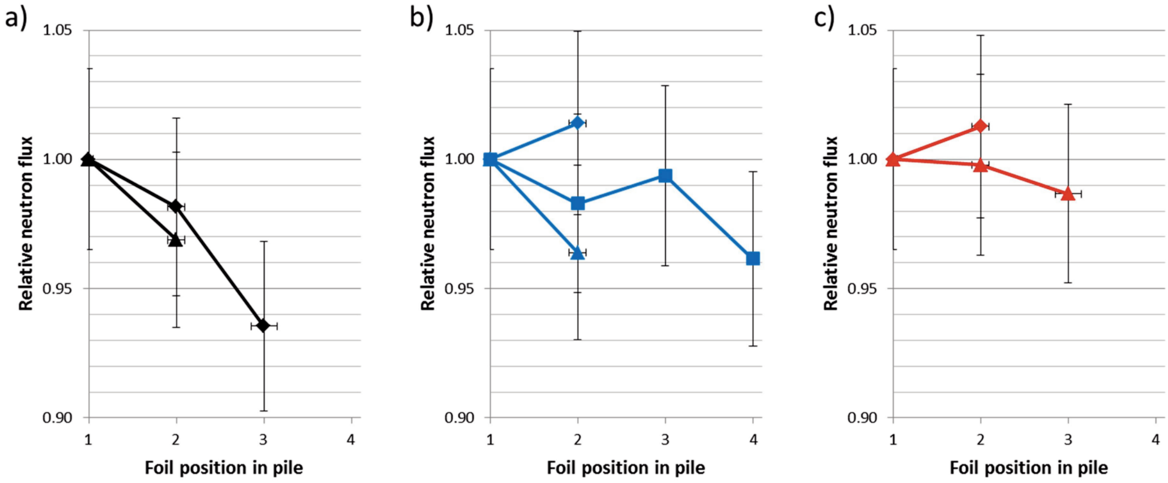

Figure 3-13. Relative thermal neutron equivalent flux as a function of position within a pile (piles with only one foil are not shown): a) top coordinates, b) middle coordinates, c) bottom coordinates. Lateral coordinates are differentiated by symbols: diamonds – left, squares – middle, triangles – right.

In the free in air experiment in the central, 10 x 10 cm^2 channel a pair of foils was irradiated in each of the ten depths. Between these foils the resulting thermal neutron equivalent flux differed less than 3% in all cases. Figure 3-14 shows the resulting average value for each position versus distance to the centre of the reactor core. Values are normalised with the reactor power, and therefore displayed in $cm^{-2}s^{-1}W^{-1}$. The measured values, illustrated in black, show an almost perfect exponential decrease. At the reactor near end of the channel a flux of $2.14 \pm 0.07 \times 10^5$ $cm^{-2}s^{-1}W^{-1}$ has been determined. The minimum flux at a distance of 208.3 cm was measured to be $3.99 \pm 0.14 \times 10^3$ $cm^{-2}s^{-1}W^{-1}$.

Calculation results are shown in the same figure indicated by red dots. The calculation follows the course of the measured results, starting form a neutron flux of $2.07 \pm 0.01 \times 10^5$ $cm^{-2}s^{-1}W^{-1}$ at 99.8 cm distance to the centre of the core and decreases to $4.01 \pm 0.03 \times 10^3$ $cm^{-2}s^{-1}W^{-1}$ in the biggest distance. The agreement between both data series is good. The biggest difference can be observed at second position where points deviate by 7%. The mean deviation is 3.5%. Thereby the applied correction with the neutron spectra, was of only very little relevance, due to the domination of neutron energies in the thermal region in the spectra. For illustration an exemplary, calculated neutron spectra for the gold foil is given in figure 3-15. It is obvious that the energy bins around the characteristic thermal energy 0.025 eV are dominating the spectrum.

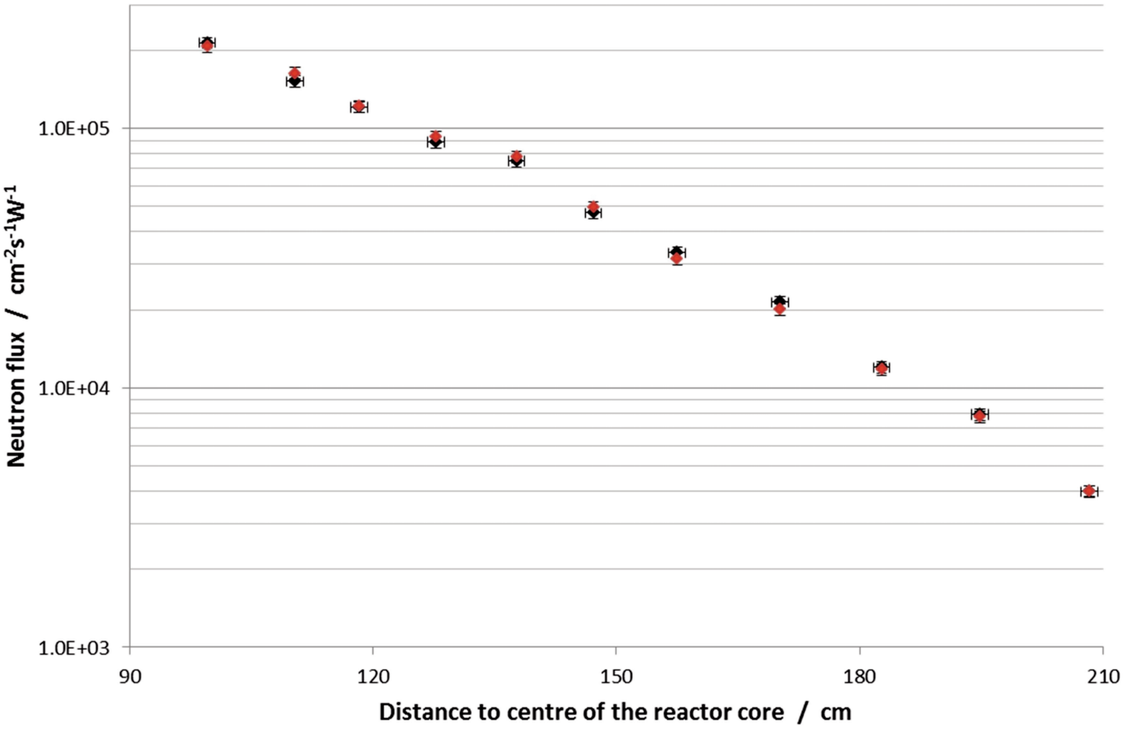

Figure 3-14. Thermal neutron equivalent flux as a function of depth in the central 10 x 10 cm^2 channel of the thermal column as measured using gold foil activation (black) and calculated with the FLUKA code (red).

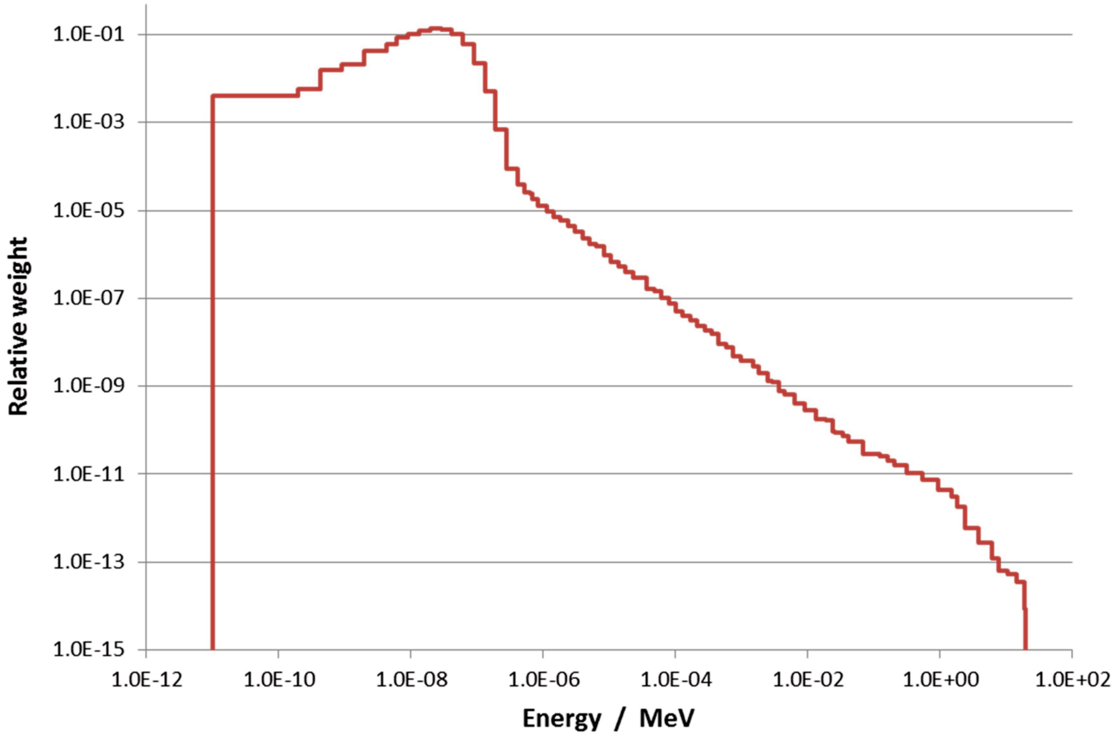

Figure 3-15. Calculated neutron spectra in the gold foil in 99.8 cm distance to the centre of the reactor core. Values are weighted with bin-width and normalised to one.

The result of the similar experiment carried out in the cuboid phantom is shown in figure 3-16. Each data point is the average value of the two separate runs. The mean difference between averaged foils was 1.5%. On the length axis of the phantom the flux is decreasing from $1.83 \pm 0.06 \times 10^5$ $cm^{-2}s^{-1}W^{-1}$ to $3.48 \pm 0.12 \times 10^4$ $cm^{-2}s^{-1}W^{-1}$ at a depth of 17.8 cm, before it slightly increases again, reaching $4.88 \pm 0.17 \times 10^4$ $cm^{-2}s^{-1}W^{-1}$ at the rear side of the phantom. In the figure dots are indicated in black.

The FLUKA calculation results are shown again as red dots in the figure and are in good agreement with the measured data. The first data point is slightly overestimated ($1.86 \pm 0.04 \times 10^5$ $cm^{-2}s^{-1}W^{-1}$) by 2.0%. The biggest difference can be found at the minimum of the curve, where $3.80 \pm 0.08 \times 10^4$ $cm^{-2}s^{-1}W^{-1}$ were calculated, the difference to the measured value is 8.5%. The mean difference observed between measurement and calculation is 2.7 %.

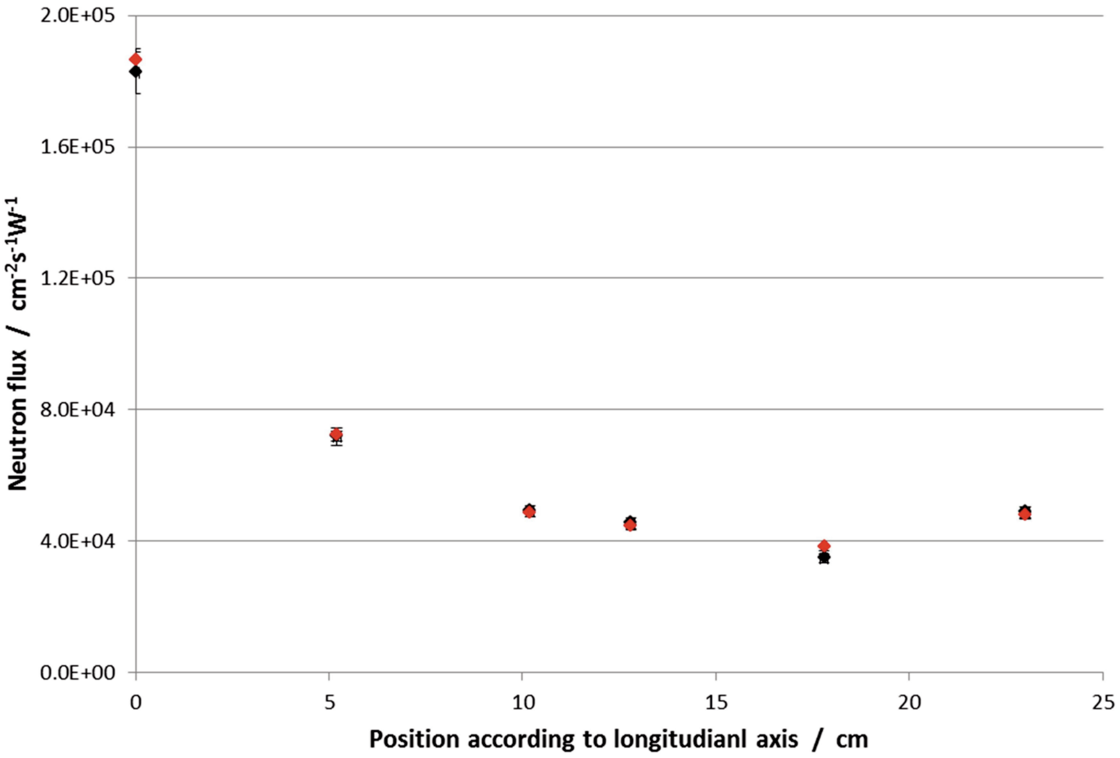

Figure 3-16. Thermal neutron equivalent flux as a function of depth in the cuboid shaped phantom, as measured using gold foil activation (black) and calculated using the FLUKA code (red).

The nine foils, oriented laterally, on the same phantom, lead to similar results, presented in figure 3-17. Instead of choosing positions according to length axis, results are shown for three lateral axes normally to the length axis. Points of each axis are connected by dashed lines for better visibility. Within each curve of three data points a minimum is reached. Comparing the three curves, a decrease in flux with increasing depth is observed, which quantitatively corresponds to the one shown in figure 3-16. On the left side of the phantom (position 0 cm, seen from the reactor core) the flux is higher in all cases, by at least 8% at the highest depth. At the lowest depth of 5 cm the difference is largest with 55%. A similar trend can be seen in figure 3-12.

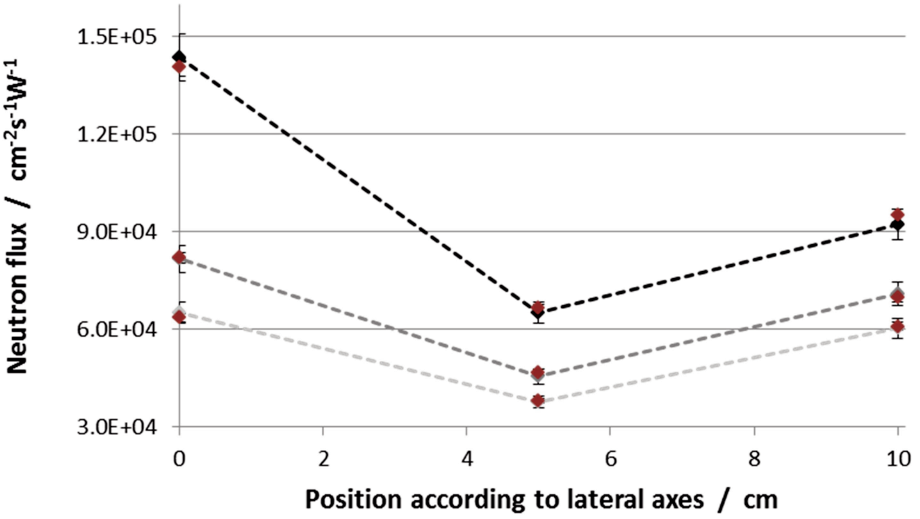

Figure 3-17. Thermal neutron equivalent flux as a function of the lateral position in the cuboid shaped phantom at three different depth (5.0 cm – black, 11.5 cm – dark grey, 17 cm – light grey) as measured using gold foil activation. Calculations with the FLUKA code are shown in red.

3.1.3.3 Neutron spectra of the TRIGA Mainz

In the second part of the work with activation foils five different materials were used. Foils were irradiated bare and inside cadmium capsules. In cadmium capsules the foils are sensitive towards neutron energies having resonances in cross section. To gain the thermal response, the resonance response is subtracted from the result of the bare foil. Therefore for each type of interaction a set of three reaction rates (equation (78)) was calculated: The total reaction rate, originating from the bare foil, the resonance reaction rate, resulting from the foil in cadmium, and the thermal reaction rate as a combination of both. The only exception is the (n,n')-reaction of indium-115, which does not occur with thermal neutrons. The obtained reaction rates are shown in appendix E for all facilities and positions investigated.

To gain information about the spectrum and to easily compare various facilities reaction rates are combined to spectral indices. In most cases they are defined as ratio of the resonance reaction rate of a certain material and the thermal reaction rate of gold. The prominent cadmium ratio though is defined as the ratio of the total gold reaction rate and the resonance gold reaction rate. Spectral indices are shown in figure 3-18. Due to the large difference of the absolute values, cadmium ratios are given extra in figure 3-19. Indices are ordered according to the energy of the first resonance in cross section of the upper value. In figure 3-18 a) values of the different facilities at the TRIGA are shown, while part b) compares values measured free in air in thermal fields of various reactors. Values for this comparison were taken from literature [Protti et al., 2012]. Indices reach from 0.74 to 8×10^{-8}.

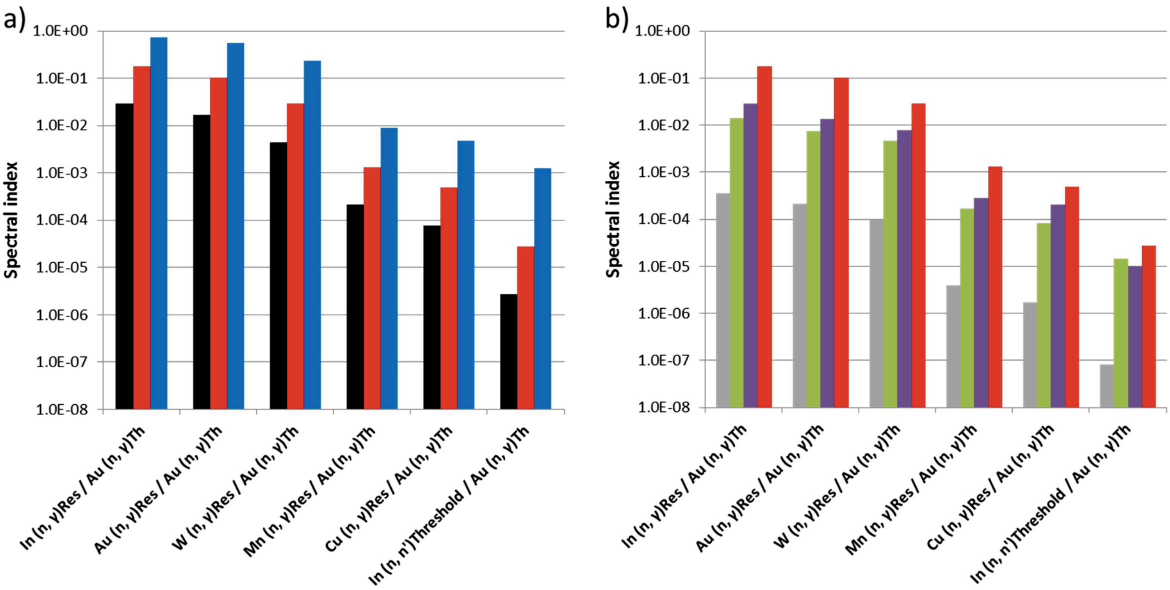

Figure 3-18. Spectral indices: a) TRIGA Mainz: Thermal column measured on phantom (black), Thermal column measured free in air (red), and inside PTS (blue); b) Comparison of various facilities: Argentinean research reactor RA-3 (grey), University of Missouri Research Reactor (MURR, green), TRIGA research reactor in Pavia (LENA, purple), TRIGA Mainz inside thermal column free in air (red). [Protti et al., 2012]

Two trends are visible in figure 3-18 a). For a certain interaction, spectral indices increase from those measured on phantom in the thermal column to those measured free in air in the thermal column, and are highest for the PTS. The two PTS facilities are not differentiated, since their values, as their flux profiles (appendix C), are in agreement within uncertainties. A second observation is the decrease in values with increasing energy of the first corresponding resonance. Especially for the two series measured in the thermal column, thereby the ratio between the two values stays almost constant. Analogue trends are visible in figure 3-18 b). For cadmium ratios, shown in figure 3-19, between facilities an inverse trend can be seen. Values are ranging from 1.77 for the PTS at the TRIGA

Mainz to >3000, which is the value given for the Argentinian research reactor RA-3.

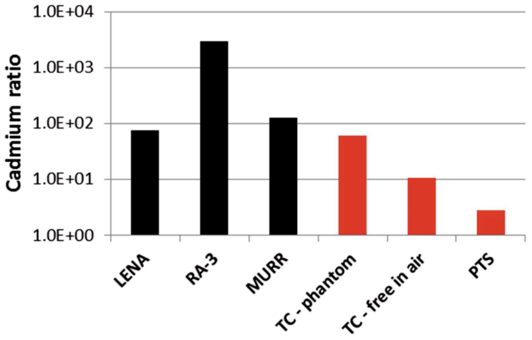

Figure 3-19. Cadmium ratios: Shown in black - TRIGA research reactor in Pavia (LENA), Argentinean research reactor RA-3, University of Missouri Research Reactor (MURR); Shown in red - three facilities of the TRIGA Mainz, thermal column (TC) on phantom and free in air, and inside PTS [Protti et al., 2012].

Finally the two series of reaction rates, which were gained in the thermal column, were used in an unfolding process with the SAND II algorithm. Thereby the algorithm identified the input spectra as a possible solution. Spectra were calculated by the FLUKA code for the exact build-up and are shown in figures 3-20 and 3-21. Identical energy bins as for the source definition were used. To test the result input spectra were varied by “hardening” or “softening”. In such process in spectra optionally fast or thermal energies are accentuated. Spectra are illustrated as dotted and dashed curves in figure 3-20. As an example the dashed line represents a “softening”, where parts of the neutrons from high energy bins were transferred to the thermal region. This way the changed input is implemented and processed by the algorithm as the original spectrum. However, also using these varied input spectra no significant difference in the result was observed after the iteration process. Comparison of the two spectra in figure 3-21 shows that the presence of the phantom leads to an increased moderation of neutrons towards thermal energies. The values of energy bins in the epithermal region are lowered. The corresponding increase in thermal energy bins is too small to be visible in the logarithmic plot. Analogue to the ratio between spectral indices also the ratio between energy bins in the epithermal region varies only slightly around a certain level.

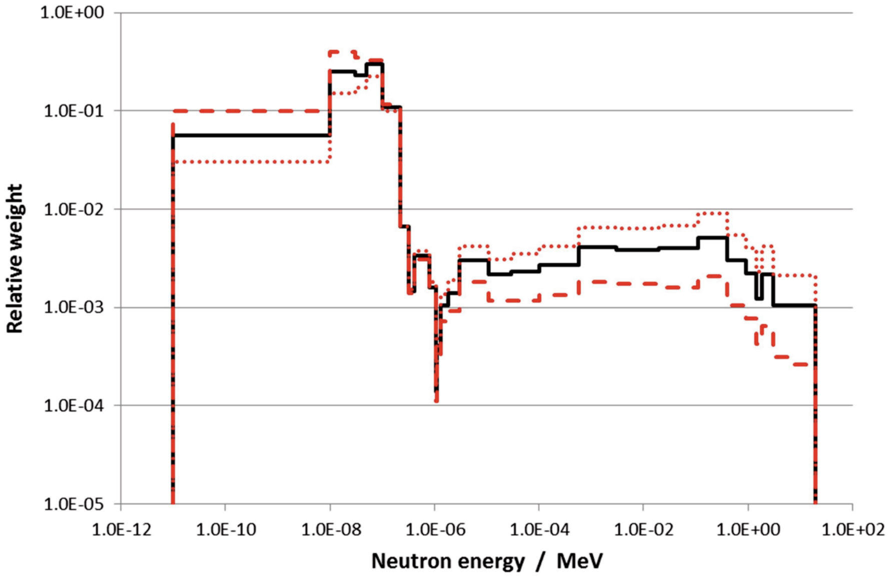

Figure 3-20. Calculated neutron spectrum of the free in air experiment (solid black line); alternative input spectra after hardening or softening are shown as dotted or dashed grey lines respectively.

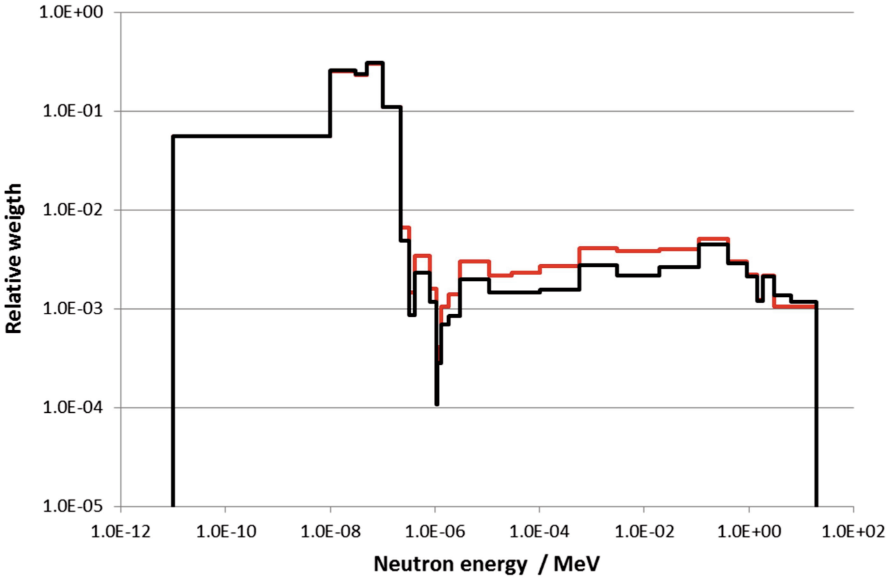

Figure 3-21. Calculated neutron spectra of the phantom experiment (black). For comparison the spectrum of the free in air experiment is also shown (grey)

3.1.4 Adaption of an online neutron monitoring system

During the clinical application of BNCT monitoring of the neutron field is mandatory in terms of quality assurance. Although at the TRIGA research reactor in Mainz no such treatment is planned, the irradiation for example of animals was considered several times. In the context of the activation foil measurements therefore also an online monitoring system was tested and adapted for possible future use in the thermal column. The following description includes solely final parameters and setup, and presents the corresponding results.

3.1.4.1 Description of the detection system

Since charged particles are way easier to detect, most neutron monitoring systems are based on some kind of particle conversion. Also the system, used in this work, was a combination of a silicon pin-diode and a conversion foil. In contrast to conventional (pn-) diodes in the pin-type p- and n-layer are separated by an un-doped intrinsic (i) layer. For particle detection such diode is reverse biased, so that it is not conducting. An entering particle generates electron-hole-pairs, creating a current. The original detectors were obtained from Silicon Sensor, Berlin, Germany, but then modified by the workshop of the Institute of Nuclear Chemistry. The detector had a surface size of 1 mm^2, was connected to a coaxial plug and fixed in an aluminium casing. The casing was designed with an open top, on which a converter foil could be fixed with a removable, screw-on type ring. A schema of the build-up of the detector is shown in figure 3-22. The shape of the casing was chosen cylindrical with a diameter of 2.0 cm and a height of 3.35 cm.

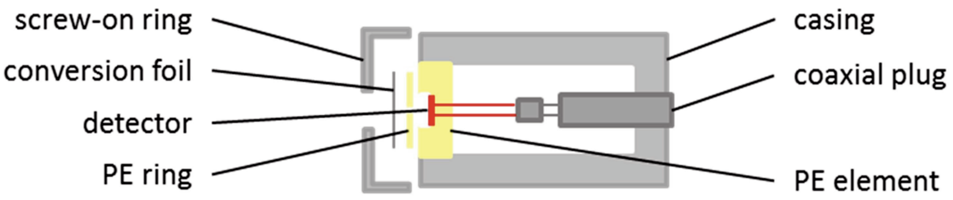

Figure 3-22. Schematic build-up of the detector, with the diode and connection shown in red.

For the converter foil lithium fluoride was evaporated and condensed onto aluminium foil with 0.1 mm thickness. In the final setup, adapted for the neutron fluxes present in the thermal column, foil with 42 µg/cm^2 of lithium fluoride was used, with lithium in natural isotope composition. The actual conversion occurs with the lithium isotope ^{6}Li, which has an abundance of 7.4% and a thermal neutron capture cross section of 940 b. As illustrated in equation (84), the reaction results in an alpha and a tritium particle, detectable by the pin-diode. The small detector in combination with the unenriched lithium led to an acceptable detector dead time, also at high fluxes as present with reactor powers of 100 kW$_{th}$.

$$^6_3Li + ^1_0n \longrightarrow ^4_2He(2.06\ MeV) + ^3_1H(2.73\ MeV) \qquad (84)$$

The detector was connected via a coaxial cable to a preamplifier. While the detector is inside the thermal column the preamplifier is located outside. The un-amplified signal is still relatively weak, which is why the length of the coaxial cable has a great influence on the signal-to-noise ratio. Therefore, a position of the detector at the reactor distant end was chosen, so that the cable length could be reduced to the thickness of the concrete gate. The electronic system is completed by the main amplifier, a multi channel analyser, the voltage supply and a PC. The detector is operated with a supply voltage of -20 V.

The final setup was tested with reactor powers of 1 kW$_{th}$, 10 kW$_{th}$, and 100 kW$_{th}$, whereby the experiment with the medium energy was carried out twice. Each irradiation was carried out for 30 minutes. During this time five spectra were recorded with the pin-diode, each with five minutes lifetime. Afterwards, spectra were averaged and evaluated by peak integration. Due to the peak shape, integration was made by summation of channel contents, accompanied by an underground correction.

Since the detector is also sensitive towards low energy gamma rays, it was placed in a bismuth block. The cuboid shaped block had a width and height of 5 cm and a length of 6 cm, with a central drill hole, fitting the detector. With the bismuth block the detector can be fixed at the rear end of the cuboid phantom (10 × 10 × 23 cm^3). Photographs of phantom, detector and bismuth block can be found in figure 3-23. As already mentioned, the phantom and detector were positioned at the rear end inside the column. The 20 × 20 cm^2 channel was used. Thereby the coaxial plug was positioned in contact with the forefront of the concrete gate. Only in the second run with 10 kW$_{th}$ reactor power a position 3.0 cm deeper in the channel was chosen, to gain an assessment of the influence of the boral liner, which is in this position near by the detector.

In order to create a situation as present during a possible, later application in the reactor near end of the channel an additional cubic phantom (15 × 15 × 15 cm^3) was inserted within the standard irradiation box. Both phantoms were equipped with gold foils at front and rear side. For analysis the measured fluxes are compared to the count rate of the pin-diode. For easier differentiation the phantom carrying the pin-diode will be called detector phantom, the other one front phantom.

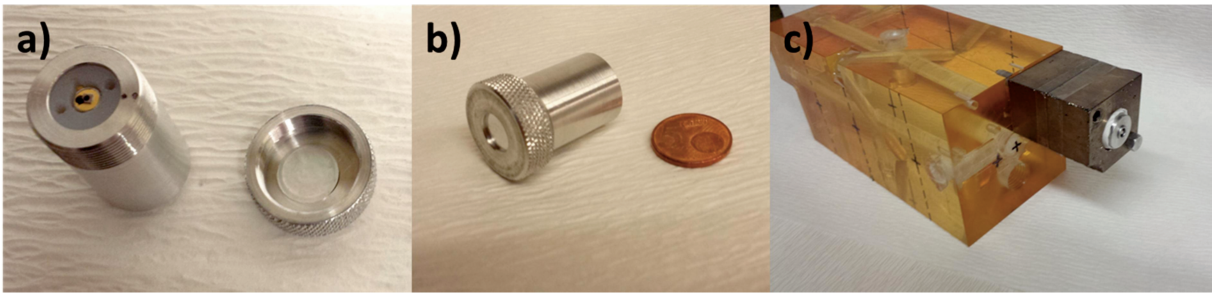

Figure 3-23. Photographs of a) diode within casing and screw-on type ring with conversion foil, b) casing with fixed ring, c) detector in bismuth shielding fixed on phantom rear side.

3.1.4.2 Results

Generally it can be stated, that during all irradiations of the pin-diode with the 42 $\mu g/cm^2$ lithium fluoride conversion foil no change in the response behaviour was observed, for example in terms of abrasion of the foil. In total during all experiments carried out, the combination of foil and detector was irradiated for about 300 kW_{th} h. As long as no substantial parts of the detection system are changed, for example the conversion foil or the cable for the unamplified signal, also a high reproducibility of spectra is given. Single spectra of certain reactor powers, which were averaged for evaluation, differed only within statistical uncertainties. Size, shape and position of peaks between spectra taken during the same irradiation did not change with time or duration, giving evidence of a good reproducibility. However, elongation of the coaxial cable, connecting diode and preamplifier, led to an extensive broadening of peaks.

A spectra recorded over five minutes during the 10 kW_{th} irradiation is shown in figure 3-24. Since the detector was not energy calibrated, the x-axis in the diagram is dimensionless. The relatively narrow peak at higher energies is generated by tritium particles. FLUKA simulations suggested that the ions mainly loose only about 0.1 MeV of their initial energy, before reaching the detector. The other peak is generated by the alpha particles. The energy of the peak maximum was simulated to be about 0.25 MeV smaller than the initial particle energy. Compared to the tritium peak, the peak area is smaller by about 45% in all spectra. Simulations showed that this is a result of increased scattering compared to the tritium, which in addition leads to a peak broadening. Both peaks have a connected smaller peak at lower energies, which is supposed to be also a result of scattering processes.

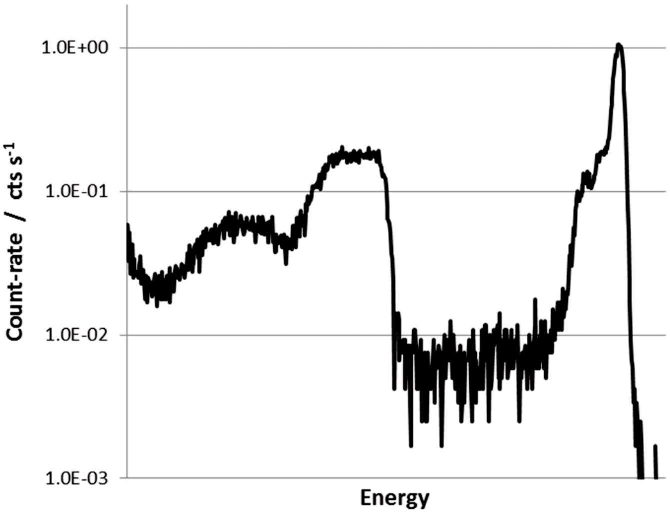

Figure 3-24. Exemplary spectra, as measured with the pin diode at 10 kW$_{th}$ *reactor power.*

To enable determination of absolute neutron fluxes, the count rate in the peak area of alpha and tritium particles needs to be calibrated. Gold foils were located close to the detector, but also distant from it at the high flux end of the thermal column on the front phantom. In part a) of figure 3-25 the linear correlation of count rate versus neutron flux is plotted for foils directly neighbouring the detector. Foils were located in the same longitudinal distance towards the reactor core as the converter foil of the detector. In the figure data for each particle type and their summation is shown. Between the two irradiations, carried out with 10 kW$_{th}$, a difference of 22% in the measured flux was observed, as a result of the slight difference in positioning. The corresponding data points are in identical colour but unfilled. Uncertainties are about 4% in flux and below 1% for the count rate. Due to the logarithmic scale error bars are too small to be visible. Part b) shows the ratio of the values from part a) as a function of reactor power. The value of counts per neutron remains constant during all irradiations. The points of data taken form the irradiation carried out with the detector 3.0 cm shifted, again shown as unfilled dots, are only slightly increased compared to the others. For the tritium data series points at 10 kW_{th} are almost exactly overlying. Deviations in the ratio between the four points of each series are within the calculated uncertainties, which are on average 4.8%. Smallest deviations can be observed with tritium.

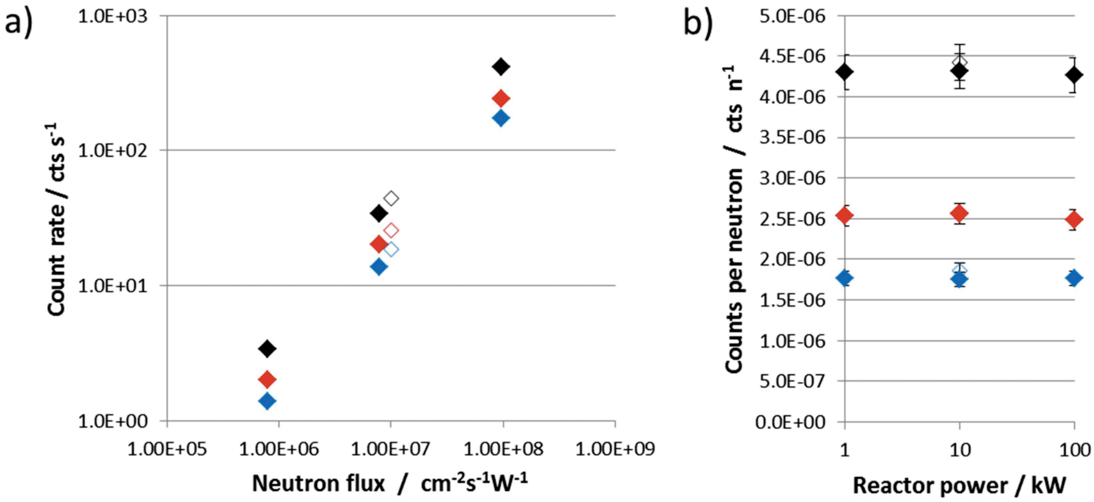

Figure 3-25. Correlation of neutron flux and detector count rate for identical longitudinal distance to the reactor core: a) Neutron flux as a function of count rate, and b) count rate flux ratio as a function of reactor power, as determined form the alpha peak (blue), tritium peak (red) and the summation (black).

Analogue diagrams for other gold foil positions are given in figures 3-26 to 3-28. While foils in the previous figure where located on the rear side of the detector phantom, foils of figure 3-26 were positioned at the front side. They had 26.0 cm longitudinal distance to the converter foil of the detector. Remaining figures show data for activation foils fixed on the front phantom. For foils on the rear side of the phantom longitudinal space to the converter foil was 98 cm, for those at the front side 113 cm. In the single run at 10 kW_{th}, during which the detector phantom was located 3.0 cm ahead, distances towards the front phantom are reduced by this value. Hence distances are 95 cm, respectively 110 cm.

The results for those positions, plotted analogue to figure 3-25, show a similar behaviour. Diagrams in parts a) show linear correlation between count rate and flux in all positions. However different to figure 3-25 the unfilled points of data taken with the detector positioned 3.0 cm more in front are not following the linear behaviour. The fact is even more obvious in parts b), where the unfilled data points are substantially increased. Data points of the other irradiations are on a constant level in each series as before. Considering the measured neutron fluxes on the detector phantom the shift of 3.0 cm has a bigger influence on the rear side, than on the front side. At the rear side flux and count rate change in similar manner, at the front side flux is less increased. The front phantom is not shifted at all, hence the longitudinal distances are decreased between filled and unfilled data points. Therefore in parts a) of figures 3-27 and 3-28 the measured neutron fluxes are identical within the uncertainties, since also the positioning is identical, while the count rate is increased by the shift of the detector phantom.

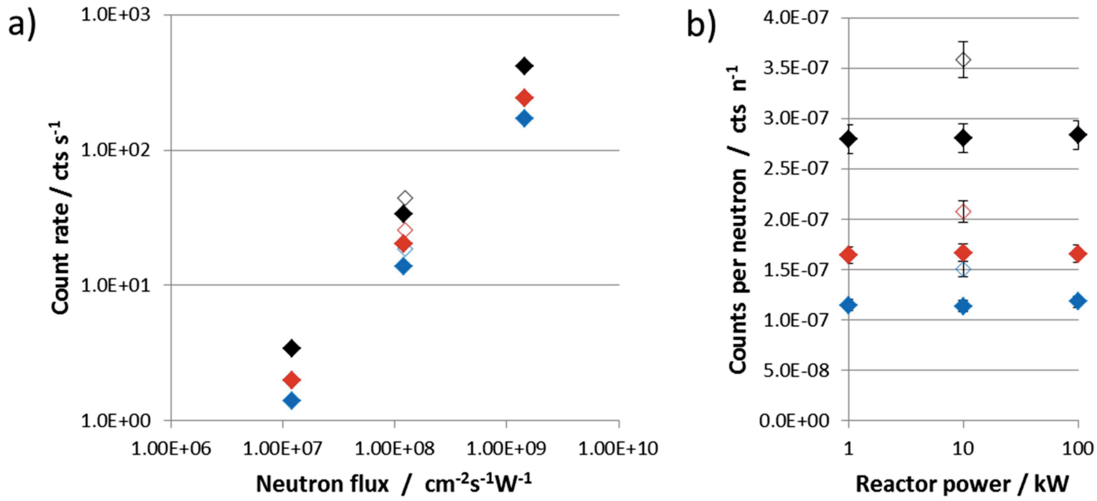

Figure 3-26. Correlation of neutron flux and detector count rate for a difference of 26.0 cm longitudinal distance to the reactor core: a) Neutron flux as a function of count rate, and b) count rate flux ratio as a function of reactor power, as determined form the alpha peak (blue), tritium peak (red) and the summation (black).

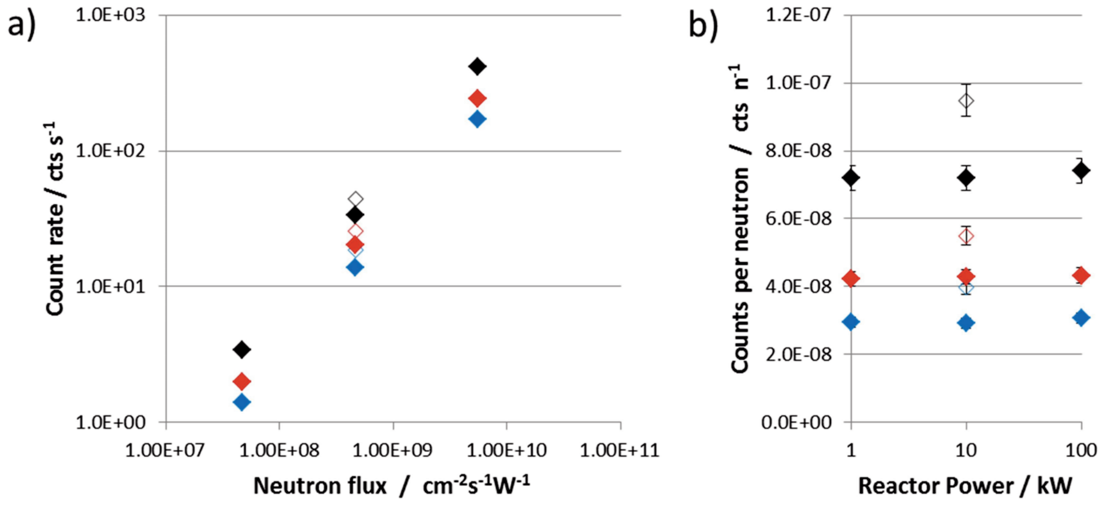

Figure 3-27. Correlation of neutron flux and detector count rate for a difference of 98.0 cm longitudinal distance to the reactor core: a) Neutron flux as a function of count rate, and b) count rate flux ratio as a function of reactor power, as determined form the alpha peak (blue), tritium peak (red) and the summation (black).

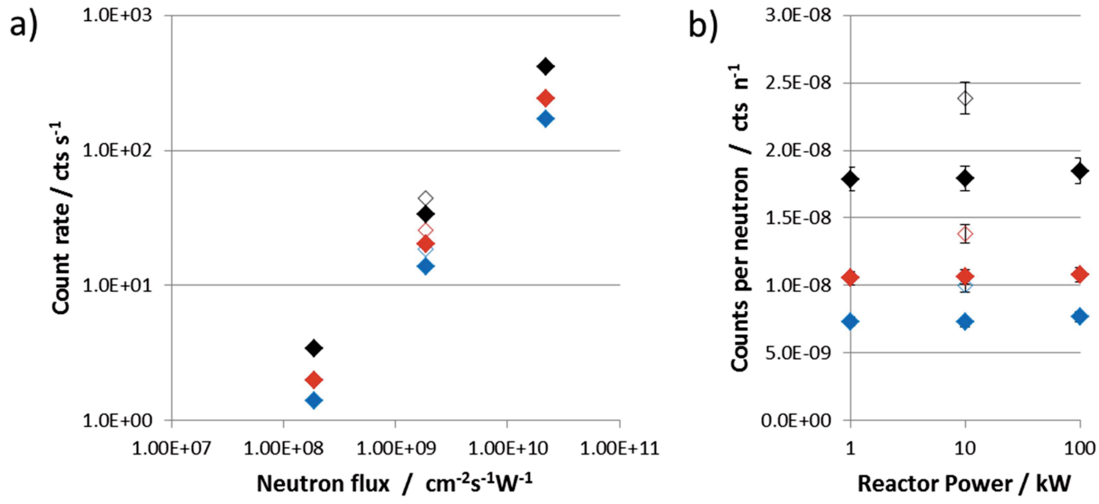

Figure 3-28. Correlation of neutron flux and detector count rate for a difference of 113.0 cm longitudinal distance to the reactor core: a) Neutron flux as a function of count rate, and b) count rate flux ratio as a function of reactor power, as determined form the alpha peak (blue), tritium peak (red) and the summation (black).

3.2 The alanine detector

The response of the alanine detector was investigated in predominately thermal and epithermal neutron fields. The general characteristics of the detector were examined in the thermal column of the TRIGA Mainz. The knowledge gained there, was applied in, from the dosimetric point of view, more complex, epithermal fields at the research reactors FiR 1 in Espoo, Finland, and THOR in HsinChu, Taiwan ROC.

An important part of the research concerns the determination of RE factors. The concept was introduced in chapter 1.5 and according to equation (42). For one-hit detectors like alanine the equation is valid for the total absorbed dose as well as for single dose components. Furthermore, the RE of the total field is the dose-weighted average of the $\mathrm{RE_i}$ of the components [Katz, 1993, Bassler et al., 2008]. In this study $\mathrm{D_{Alanine}}$ refers to the total absorbed dose, while photon, proton and fast neutron dose $(\mathrm{i} = \gamma,\ \mathrm{p},\ \mathrm{n})$ are considered as dose components. The alanine response, as read from the reference, $\mathrm{D_{ref}}$ can hence be written as the sum of dose components as shown in equation (85), each one multiplied with a specific RE factor. For a clear distinction in the following text, “dose” or “absorbed dose” refers to $\mathrm{D_{Alanine}}$, while “detector response” or “response” refers to $\mathrm{D_{ref}}$, which is the measured quantity.

$$D_{ref} = RE_{\gamma}D_{\gamma} + RE_{P}D_{P} + RE_{N}D_{N} \qquad (85)$$

$\mathrm{D_{Alanine}}$ and its components can be calculated by MC codes. In this work mainly the code FLUKA version 2011.2 has been used. For comparison MCNP (MCNP5/MCNPX 2.6.0) was employed. FLUKA is used since in addition to absorbed dose, the response $\mathrm{D_{ref}}$ can also be calculated. The $\mathrm{RE_i}$ are derived from the Hansen and Olsen model, which is implemented to the FLUKA code [Bassler et al., 2008], and was described earlier in this work in detail (section 1.6.2).

The main part of the alanine characterisation has been carried out in cooperation with the National Physical Laboratory (NPL) in Middlesex, United Kingdom. However, within other cooperations also alanine detectors were irradiated, enabling a small study on the influence of the binder. Binder is added to the dosimeters to ensure mechanical stability. In the first part of this chapter the NPL study for the thermal field of the TRIGA Mainz is presented, followed by the comparison, before finally the experiments in epithermal fields are described.

Besides in this chapter also experiments conducted with modified alanine pellets are shown. Irradiations were carried out also in the thermal field of the TRIGA. Alanine has fortunate dosimetric properties, but a higher sensitivity towards neutrons would be preferable, for example in fields with a minor neutron component. For enhancement gadolinium can be used as an additive. Gadolinium, and in particular the isotope ^{157}Gd, has the highest neutron capture cross section of all known elements. Pellets doped with natural gadolinium were tested at the TRIGA Mainz in cooperation with researchers from the University of Palermo, Italy [Marrale et al. 2008, 2014a and 2014b], to investigate the possibilities in modelling and prediction of the response of such detectors in neutron fields.

Parts of this work have been previously published [Schmitz et al., 2011 and 2015; Marrale et al, 2015].

3.2.1 Thermal neutron fields

3.2.1.1 Phantom and shielding study

The dosimeters have been obtained as pressed pellets, manufactured by Harwell Dosimeters Limited in Oxfordshire, United Kingdom. For read-out service by the NPL was used [Sharpe and Septhon, 1999]. The dosimeters consist of 90.9% microcrystalline L-α-alanine and 9.1% high melting point paraffin wax as a binding agent. Pellets are cylindrically shaped with slanted edges and a diameter of 5.0 mm, a height of ~2.2 mm, and a medium weight of 55 mg. Each pellet is exactly weighed before read-out and the corresponding ESR-signal is weighted by division. Read-out is performed with a Bruker X-band spectrometer and the reported dose is traceable to NPL's primary standard of absorbed dose to water in a ^{60}Co-gamma ray reference beam.

The relative uncertainty of the NPL read-out procedure is dose dependent and is indicated by the NPL to be between 2% and 3% (k = 2) in the observed dose range. This uncertainty has components for the calibration against the primary standard (~1.6%), and the reproducibly of the pellet read-out (2% at 5 Gy, decreasing to 0.6% at doses above 20 Gy).

All irradiations have been performed in the field of the thermal column of the TRIGA Mainz. A detailed description of the field can be found in the previous chapter 3.1. Five different experimental setups have been used. All of them were carried out in the 20 × 20 cm^2 channel in the column. The channel is equipped with a 5 cm thick bismuth shield. The most forward position behind the bismuth shield is located 98 cm from the centre of the reactor core. Inside the column four of the five experiments were placed in the standard PE-box, which is exactly fitting the channel cross section and has been described earlier for the activation foil experiments.

In the experimental setups three phantoms, made of PMMA, Teflon, and organic tissue, and two types of shielding, lead/bismuth, and boric acid, have been used. Figure 3-29 shows photographs of four of the five setups, solely without the organic tissue, which is shown in figure 3-30. In all three phantom experiments pellets were located on the central longitudinal axis, measuring a depth dose curve.

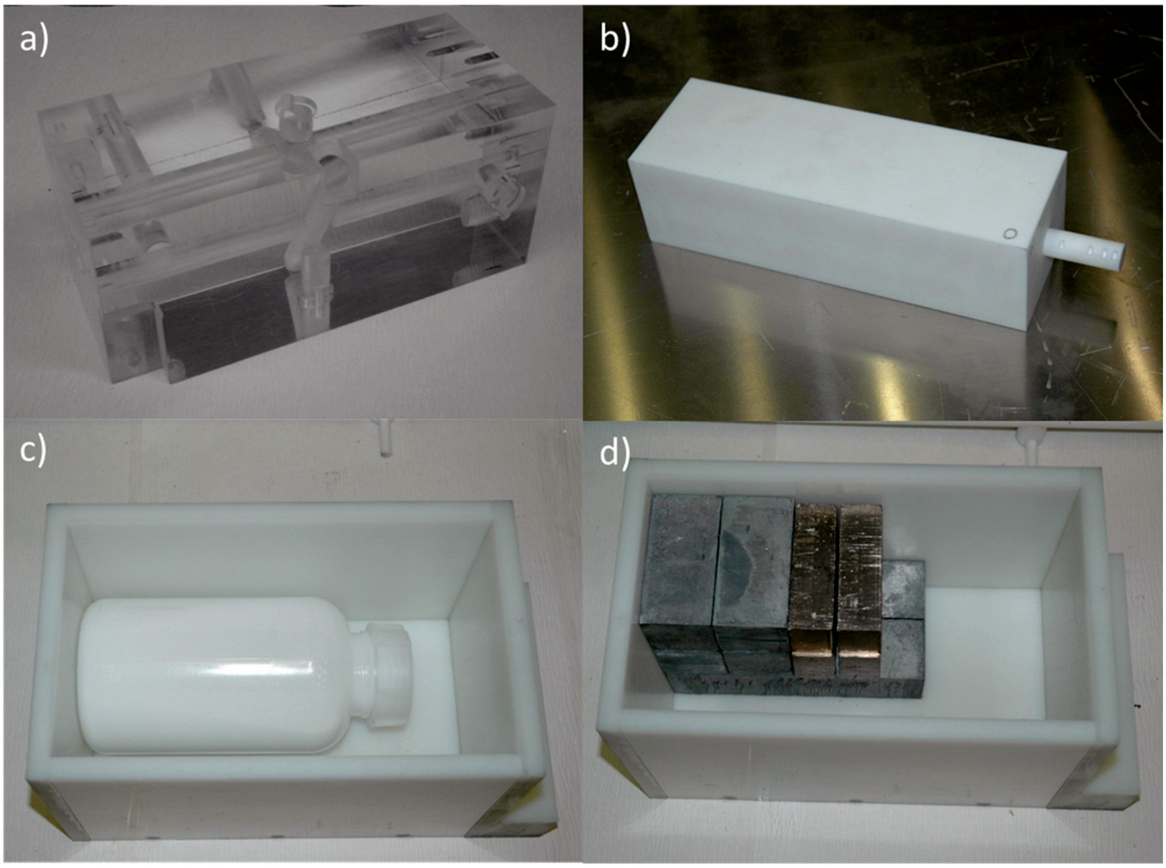

Figure 3-29. Phantoms and shielding at the TRIGA Mainz: a) PMMA phantom, b) Teflon phantom, c) boric acid neutron shield, d) lead and bismuth photon shield.

The PMMA phantom was the same as employed before with the activation foils. It is cuboid-shaped (10 × 10 × 23 cm^3) and has drilled holes with optional PMMA elements, where detectors can be inserted. Ten alanine pellets were arranged on the central length axis at different depth. At the forefront and the backside two gold foils where fixed to ensure the neutron fluence. The phantom was positioned on the left forefront inside the PE box. Irradiation parameters were selected to reach dose levels common in BNCT. In the case of the PMMA phantom irradiation for 13 minutes at a power of 100 kW_{th} has been chosen. The experiment was carried out twice.

Ten additional pellets have been irradiated in a cuboid-shaped Teflon phantom (8 × 10 × 30 cm^3). The phantom has a single drill hole on the longitudinal axis, which is filled with a Teflon rod with cavities, exactly suited for the alanine detectors. In contrast to PMMA Teflon contains only carbon and fluorine, but no hydrogen. To avoid the presence of unnecessary hydrogen the Teflon phantom was the only experiment inserted without the PE box. Due to this the foremost pellet is closer to the core than in the other experiments. Neutron fluence was monitored using two neutron foils, one on the front and one on the back of the phantom.

For the third phantom experiment carried out in organic tissue a resected lobe of a human liver was used. The setup was adopted from the Taormina project at the TRIGA Pavia, Italy [Zonta et al., 2006]. The resected specimen was obtained during a clinical trial, described in literature [Schmitz et al., 2010]. Sealed in PE foil, the pellets were sewed in lateral lamellas, cut along the longitudinal axis of the liver tissue. With each of the dosimeters also gold foils were sealed. Six alanine pellets have been positioned in the dissected liver lobe. Additional gold foils were positioned analogue to the other experiments at front and rear of the tissue. While in the other experiments pellets where exactly located on the central length axis this was not the case in the tissue. The lobe had no simple central length axis, due to its naturally not simple geometry. In addition little shifts occurred during the sewing in the soft material. Therefore, pellets differ up to 1.5 cm from the averaged axis through all pellets. As common in transplant surgery, the organ was packed in bags together with Histidine-Tryptophan-Ketoglutarate (HTK) preservation solution. The bag was placed in the PE box. But different to the PMMA phantom, the bag was located central in the front of the box. To ensure exact positioning of detectors and gold monitors the organ was stabilised using three PMMA elements at both sides and in the back of the lobe. Photographs of the lobe and preparing process can be found in figure 3-30.

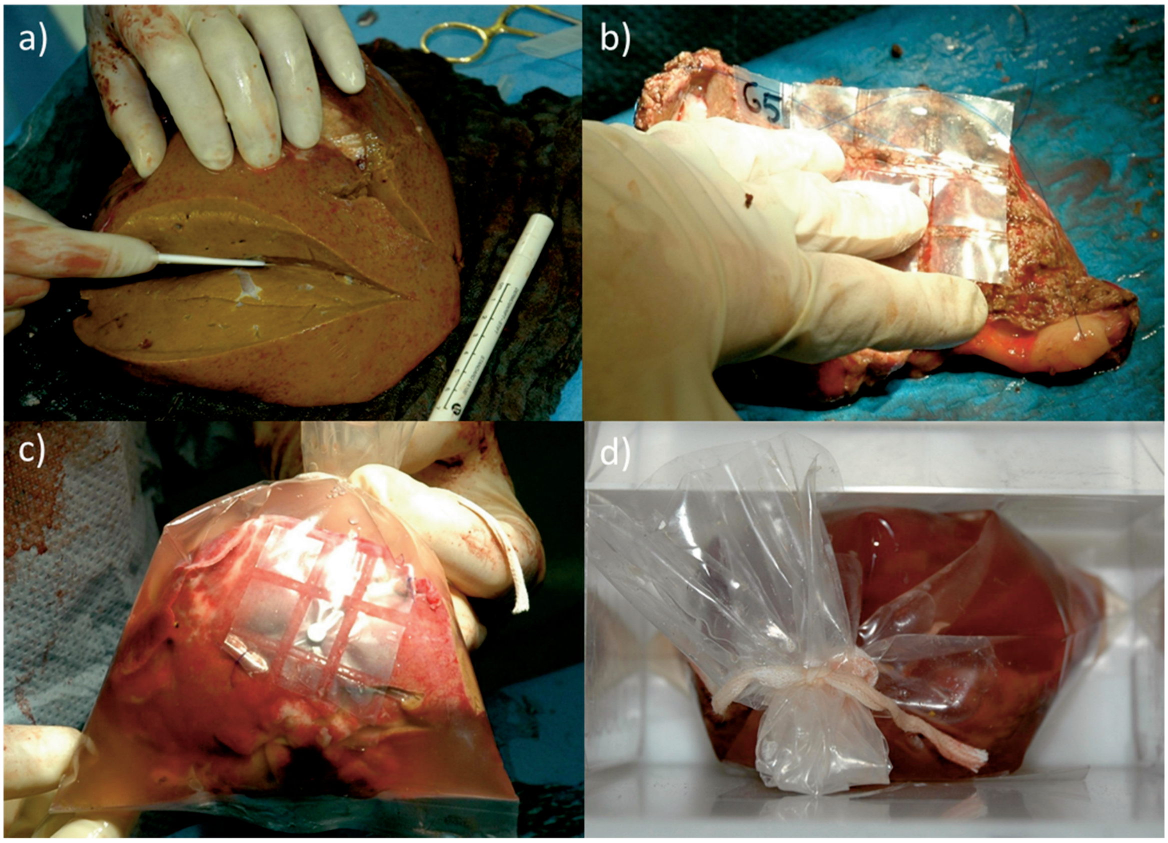

Figure 3-30. Photographs of the liver lobe: a) lamella cutting, b) sewing of PE foil packages containing detectors and activation foils, c) liver lobe packed with HTK solution, d) liver lobe in irradiation box with stabilising PMMA elements (left, right, and back).

In each of the two shielding experiments one primary particle species was suppressed. In both setups the particular particle flux was reduced in each pellet position by at least a factor of 100. The neutron shield was realised by a cylinder-like shape, filled with boric acid. In each direction the shield had a thickness of at least 5 cm, the distance from the most forefront pellet to the cylinder front was 15 cm. Within the boric acid four pellets were positioned in a PMMA tube. Neutron flux was measured using four activation foils, three inside the cylinder at the PMMA tube, and one on the front side of the cylinder.

Finally two pellets have been irradiated with photon shielding made of lead and bismuth. Simulations show that the photon field is much less isotropic. Hence shielding thickness to the front and back could be reduced compared to the neutron shield. In contrast to the other experiments the pellets were positioned without longitudinal difference at a 3 cm lateral distance. The amount of shielding that could be used was limited and therefore, to reduce weight and provide a minimal shielding of 99% of the photon dose, all detector positions had been chosen lateral to each other. Between them two gold foils were positioned. To the front the shielding had a thickness of 15 cm, to all other sides at least 3 cm. The total lead/bismuth block was cuboid-shaped with a length of 16 cm, a width of 10 cm and a height of 15 cm. It was built of six lead and two bismuth elements, as visible in figure 3-29.

Calculations have been carried out using the Monte Carlo code FLUKA. As described in the previous chapter 3.1, the source description of Ziegner et al. [Ziegner et al., 2014] was adapted for FLUKA using the "SOURCE" user routine. Also the modelled geometry was analogue, including mainly the graphite of the thermal column. For photon simulations also surrounding concrete was considered. All parts of each experimental setup were modelled in detail, including the bismuth shield, irradiation box, phantoms, alanine detectors, and activation foils. With the organic tissue some simplifications were made from the complex appearance visible in figure 3-30 d). Composition and density of materials were obtained from literature or the manufacturer. In total the simulated geometry comprised several cubic metres.

The default settings for hadron therapy "HADROTHE" have been used, with "USRBIN" scoring to calculate dose and particle propagation. The user-routine "COMSCW" was modified in a way that every energy deposition of a particle i is multiplied with a factor RE_i derived from the Hansen and Olsen model leading to the weighted alanine response [Bassler et al., 2008]. Comparing results of the routine and those of "USRBIN"-scoring of physical dose, RE can be calculated according to equation (42). Single components of the weighted and non-weighted dose were scored similarly by assigning a factor 1 or 0 respectively to the relevant components. By comparing these calculated values of response and absorbed dose components the RE values of equation (85) could be determined. This way all parts of the equation were identified.

Since the photon dose D_γ not only contains contributions of primary photons, but also from (n,γ)-reactions, and primary photons and neutrons are calculated separately, the component is the sum out of dose from both calculations. Associated uncertainties are calculated using equation (86). Calculations were carried out until the uncertainties of dose and components were below 2%. Uncertainties associated with RE values were calculated using error propagation analogous to equation (86).

$$\mathrm{u}_{D_{total}} = \sqrt{\left(\frac{\partial D_{total}}{\partial D_1}\mathrm{u}_1\right)^2 + \left(\frac{\partial D_{total}}{\partial \mathrm{D}_2}\mathrm{u}_2\right)^2} \qquad (86)$$

3.2.1.2 Alanine comparison study

Besides the alanine detectors from Harwell Dosimeters Limited described above, detectors from two other manufacturers, were irradiated at the TRIGA Mainz. Within cooperations also the read-out was carried out in different institutions, namely the University of Oslo (UO) and the University of Palermo (UP). Tables 3-7 and 3-8 summarise details regarding the three different dosimeters. The additional dosimeters were also cylindrical, but differ in several other properties. In the case of #2 pellets had no slanted edges. Besides, all types slightly vary in the cylinder dimensions. Variation in mass is not only a function of size, but also of the pellet composition, which differs through the use of individual binders. The uncertainty of the read-out procedures was calculate similar to those of the NPL and determined to be around 3%.

With the two additional detector series the PMMA experiment, described in the previous subsection, was repeated with little aberrations. The pellet position within the phantom was slightly varied, but the same phantom and irradiation setup was used. In all experiments the neutron fluence was monitored, analogue as before.

FLUKA calculations were also carried out analogue to those for the NPL experiments, with adjusted dosimeter positions and in particular pellet compositions. For pellets purchased from Synergy Health binder was assumed to contain carbon, hydrogen and oxygen in similar fractions as the other pellet types. Density of the binder was calculated from the weight fraction of the binder.

Table 3-7. Dimensions of the alanine detectors

#	Read-out institution	Cylindrical pellets Mass / mg	 Diameter / mm	 Height / mm
1	National Physical Laboratory (NPL) United Kingdom	55.0	5.0	2.2
2	University of Oslo (UO) Norway	64.5	5.0	3.0
3	University of Palermo (UP) Italy	68.0	4.8	3.0

Table 3-8. Manufacturer and read-out details of the alanine detectors

#	Read-out institution	Spectrometer	Manufacturer	Pellet composition
1	NPL	Bruker X-band spectrometer	Harwell Dosimeters Limited	90.9% L-α-alanine 9.1% paraffin wax
2	UO	Bruker EMX-micro spectrometer	Bruker BioSpin Corporation	96% L-α-alanine 4% polyethylene
3	UP	Bruker ECS 106 spectrometer	Synergy Health	96% L-α-alanine 4% binder*

* composition not specified by the producer

3.2.1.3 Alanine doped with Gadolinium

The solid state dosimeters were produced by the University of Palermo. In a first step 5$\%_{wt}$ of gadolinium(III) oxide, Gd_2O_3, were mixed with 95$\%_{wt}$ L-α-alanine (Fluka, Buchs, Switzerland). The oxide was used in form of nanoparticles with a diameter of 35 µm to 70 µm, with a mean size of 50 µm. Due to the relatively low amount of gadolinium the elemental composition of the dosimeters is not largely affected. To the alanine-gadolinium mixture 20$\%_{wt}$ paraffin wax were added as a binder. Finally pellets were pressed in cylindrical shape with a diameter of 4 mm and a height of 7 mm. For direct comparison pellets without gadolinium were produced analogue with the same amount of binder. To protect the dosimeters they were packed in groups of three inside PE cylinders for transport and irradiation. Cylinders (diameter 2.4 cm, height 2.0 cm) are shown in figure 3-31. The minimum distance between dosimeters is 6.3 mm, minimum thickness of PE towards the outside is 3.0 mm. Read-out was again performed at the University of Palermo, where a Bruker ECS 106 spectrometer was used. The general procedure was analogue to measurements described before, although the baseline needed to be adjusted due to presence of gadolinium [Marrale et al., 2007 and 2014b]. For dose estimation again the peak-to-peak amplitude of the alanine spectrum was normalized to the pellet mass.

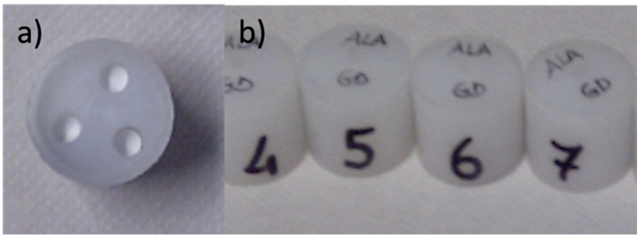

Figure 3-31. Photographs of PE cylinders: a) opened from above, b) exterior view

Dosimeters were exposed to the field of the thermal column of the TRIGA Mainz in two different experimental setups. To cover a broad range of neutron fluence, the PE cylinders (containing three dosimeters each) were irradiated separately in identical positions, but with varying reactor power and duration. A summary of irradiations carried out can be found in table 3-9. In these experiments again the cubic PMMA phantom (15 cm side length) was used. PE cylinders were located in a central position inside the phantom. In the second setup the boric acid neutron shield was used. PE cylinders were positioned on the central length axis in a depth of 14 cm, with at least 5 cm shielding in each direction. Detailed descriptions of the phantoms can be found in previous sections. Routinely all experiments were accompanied by neutron flux measurements using gold foil activation.

Table 3-9. Irradiations carried out with alanine and gadolinium doped alanine. Each X indicates a separate irradiation with three detectors inside a PE container.

Irradiation parameters		**Experimental setup**			
Reactor power / kW	**Duration / min**	**PMMA phantom**		**Boric acid shield**	
		Gd-Alanine	**Alanine**	**Gd-Alanine**	**Alanine**
2.5	17	X		X	
5.0	17	X	X	X	X
25	17	X		X	
50	17	X	X	X	X
100	45	X	X	X	X
	90	X		X	

For interpretation calculations using the FLUKA code were carried out. The same basic model of the TRIGA Mainz was used as before. Again absorbed dose and dose components (weighted and un-weighted) were calculated as main result. Simplifications were made for the gadolinium containing detector. A detailed model ought to consist of the alanine-paraffin mixture containing innumerable Gd_2O_3-nanoparticle spheres of different sizes. Such model not only appears to be impracticable, but also fails due to limitations of the FLUKA code. Therefore, detectors were modelled as homogenous mixtures of organic elements and gadolinium.

Dose, deposited due to the gadolinium neutron capture, is mostly (≈99%) deposited by photons, minor fractions by internal conversion and Auger electrons. In the FLUKA code though, none of the secondary particles are transported. The complete Q energy contributes to the kerma. Photons, being long range particles, deposit energy in the nanoparticles and the alanine-paraffin mass, but beyond also outside of the dosimeter. In contrast the electrons deposit energy mostly inside the nanoparticles. Spectra of the emitted particles can be found in literature [Ali et al., 1994, Schultz et al., 2010, Sakurai and Kobayashi, 2014]. In FLUKA though, the dose of all particles is deposited at the location of the neutron capture. The calculated dose is hence overestimated. It contains fractions which are in the experiment deposited in the nanoparticle spheres (not existing in calculations), as well as outside the detector. In both cases no contribution to the measureable detector response can be expected. The calculation of dose components, given in equation (85), and following also of the absorbed dose, has to lead to an inevitably overestimation.

In auxiliary simulations the gadolinium dose was identified by assigning alternative cross sections, i.e. of carbon or oxygen, to the gadolinium atoms. These atoms have very small cross sections and account for large weight fractions in the alanine- paraffin mass. Such process was necessary, since, due to the code limitations, it was not possible to assign weighting factors, i.e. using a “COMSCW” user-file with the gadolinium particles. Uncertainties of results were in the same range below 5% as in experiments described earlier.

3.2.2 Epithermal neutron fields

As for the main investigations at the TRIGA pellets were obtained and read-out by Harwell Dosimeters Limited and the NPL. Details about the manufacturing and ESR measurements can be found in the previous section 3.2.1.

The characteristics of the alanine detector in epithermal fields were investigated at two different facilities. The FiR 1 research reactor in Espoo, Finland, and the THOR research reactor in HsinChu, Taiwan ROC. Both have been used or are still used for clinical trials in BNCT. While at the TRIGA pellets were irradiated in an isotropic field, at the two other facilities collimated beams have been utilised. Detailed descriptions of the facilities can be found in literature [Auterinen et al., 2001, Liu et al., 2011], while they will be only briefly introduced here.

The FiR 1 is also a TRIGA reactor build by General Atomics. However, for clearness reasons, the term TRIGA here only refers to the reactor in Mainz. The FiR 1 has a maximum power of 250 kW_{th} in the steady state mode, can be pulsed like the reactor in Mainz, and has analogue irradiation positions. However it has been completely re-built for BNCT treatments. The thermal column has been replaced by a beam shaping assembly and a treatment room. A horizontal cut of the reactor is shown in figure 3-32. The moderator is made of Fluental™, a material mostly containing aluminium and fluorine. After 63 cm of Fluental™ the design is completed by a 9 cm layer of bismuth followed by a collimator also made out of bismuth and in addition a lithium polymer, which is in part enriched with lithium-6. The circular beam exit in the treatment room is located 173.1 cm from the reactor core and has an opening radius of 7.0 cm. A neutron beam with predominantly epithermal energies is provided, contaminated only with a small fraction of photons produced in reactor structure materials and the beam shaping assembly. Energy spectra as used in the calculations can be found in appendix F. Two alanine detectors have been irradiated one after the other free in air in the centre of the beam exit fixed with tape. Eight pellets have been irradiated on the central, longitudinal axis of a cylindrical PMMA phantom also positioned on the central beam axis with contact to the wall. The phantom had a radius of 10.0 cm and a length of 24.0 cm. In this beam, dose rates are smaller than at TRIGA, due to the lower neutron flux and the lower photon contamination. Therefore pellets free in air have been irradiated for about 7.5 hours and in phantom for about 5.5 hours. Neutron fluence was measured using gold foils only during the phantom experiment.

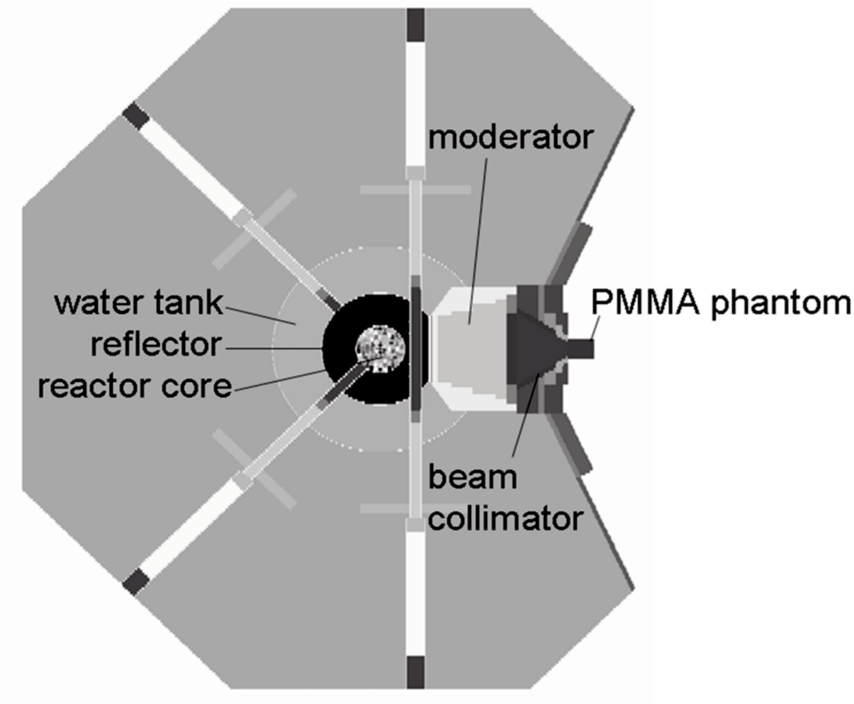

Figure 3-32. Schematic drawing of the research reactor FiR 1 with the respective irradiation position [Schmitz et al., 2015].

THOR in Taiwan is the biggest of the three reactor facilities. In steady state it reaches a power of 1.2 MW. In addition it has several more horizontal beam tubes, as figure 3-33 suggests. As at the FiR 1, also at THOR the BNCT beam line is a re-built thermal column. The beam shaping assembly consist out of layers of

Fluental™ and aluminium for moderation, a layer of bismuth for photon shielding, and a collimator, made out of bismuth and lithium carbonate. To filter thermal neutrons the moderator is in addition equipped with two sheets of cadmium. The wall towards the treatment room is made out of lead. The beam exit is circular (7.0 cm radius), located 226 cm form the reactor core and provides a predominantly epithermal field, similar to FiR 1. Spectra can as well be found in appendix F. The neutron flux at maximum power is only slightly higher than at FiR 1. Fifteen alanine pellets have been irradiated on the central, longitudinal axis of a cubic PMMA phantom with 21 cm lateral length for 1 hour. Thereby the phantom was positioned central in front of the beam exit with contact to the wall. One more pellet has been fixed in the centre of the beam exit and irradiated free in air for 4.5 hours.

Experiments in both facilities are illustrated by the photographs in figure 3-34. Parts a) to c) in the upper row refer to FiR 1 and parts d) to f) in the lower row refer to THOR. Table 3-10 summarises data of the three reactor facilities used in this work.

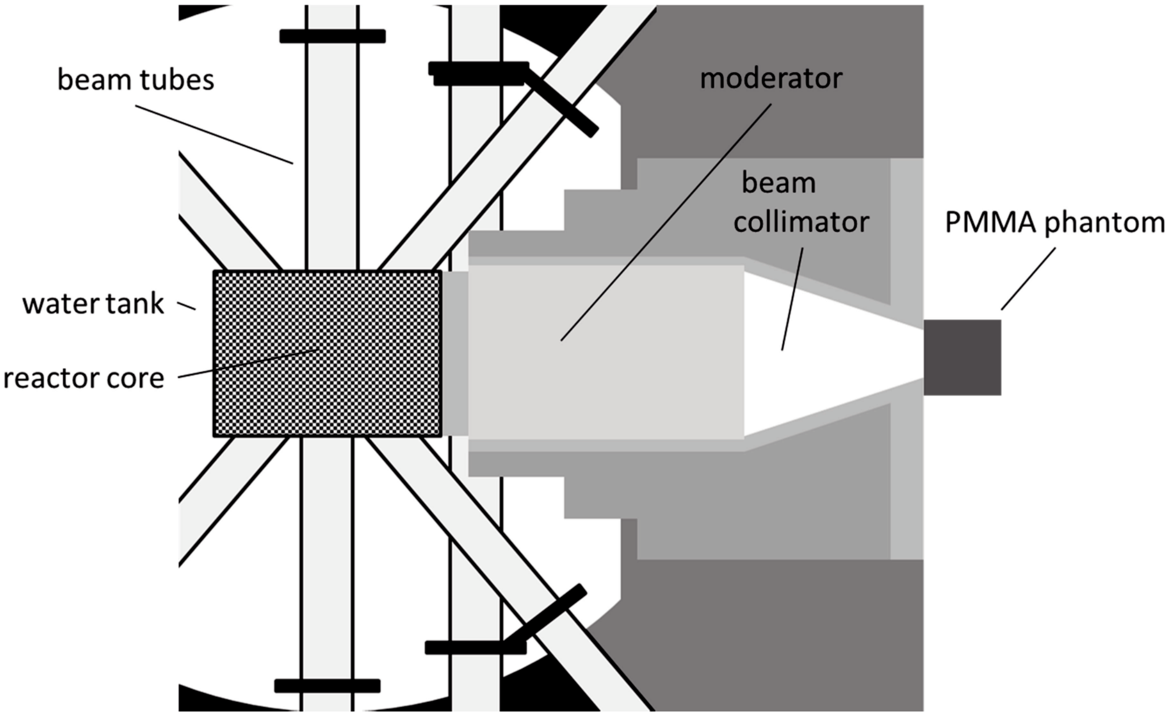

Figure 3-33. Schematic drawing of the research reactor THOR with the respective irradiation position [Schmitz et al., 2015].

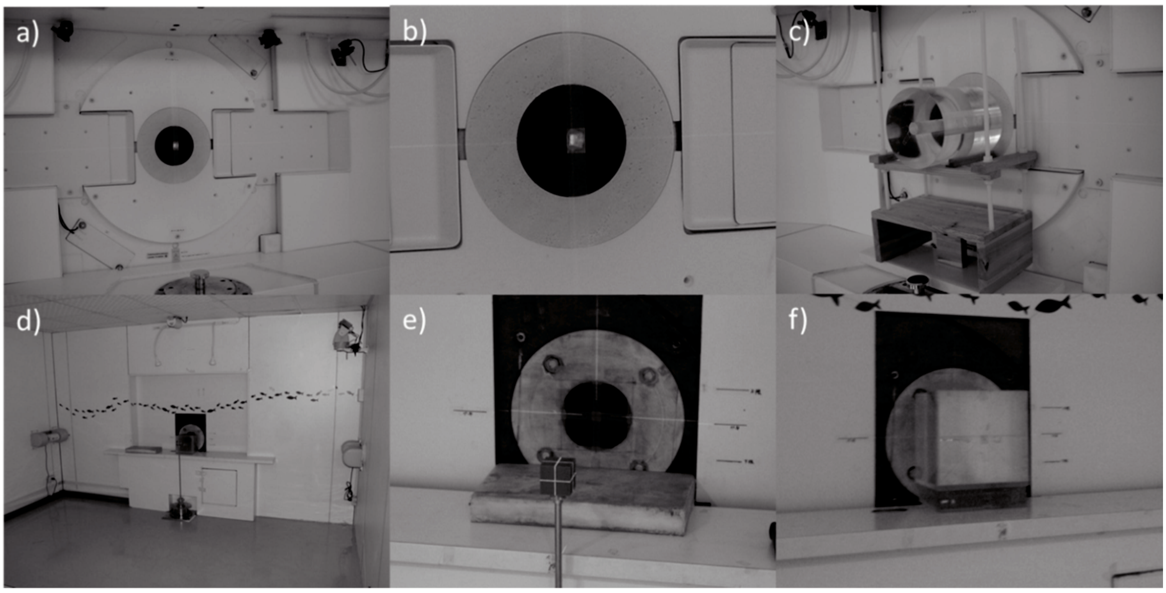

Figure 3-34. Photographs of experiments in epithermal fields: a) FiR 1 beam exit, b) FiR 1 free in air pellets, c) FiR 1 PMMA phantom, d) THOR beam exit, b) THOR free in air pellets (with cube for position control in front of the beam exit), c) THOR PMMA phantom.

Table 3-10. Characteristics of irradiation facilities used in the present work

	TRIGA, Mainz	FiR 1, Helsinki	THOR, HsinChu
Reactor power	0.1	0.25	1.2
Irradiation position	Thermal column	BNCT facility	BNCT facility
Irradiation field	Isotropic field	Collimated beam	Collimated beam
Main neutron energy	Thermal	Epithermal	Epithermal
Neutron fluence rate* / $s^{-1}cm^{-2}$	$3.0 * 10^{10}$	$1.2 * 10^{9}$	$1.3 * 10^{9}$
Experimental setups	PMMA phantom Teflon phantom Neutron shield Photon shield	PMMA phantom Free in air	PMMA phantom Free in air

* For mentioned reactor power at the most forefront irradiation position of the TRIGA and at the beam exits of FiR 1 and THOR.

Calculations have been again carried out using the Monte Carlo code FLUKA. Simulations had an analogue conceptual design as those described in the previous section 3.2.1. The descriptions of the source planes of each facility were provided by the cooperation partners and are regularly used with MCNP. Therefore they needed to be adapted for FLUKA in the form of a “SOURCE” user routine. Compared to the TRIGA model several major modifications arouse from the difference in beam design. The distance between the experimental setup and the source plane is in the case of the TRIGA around 35 cm. At FiR the distance is reduced to 5 cm, at the THOR the source plane is in contact to the phantom (0 cm). Such on the one hand the modelled geometry can be reduced; on the other hand the source description needs to be much more detailed. Both planes are defined circular with a radius of 11.0 cm. While at the TRIGA two independent parameters (energy and position) were sampled for each particle emitted, at the two other facilities three parameters (energy, positon, and polar angle) are used. In addition between these parameters dependencies had to be considered. Therefore, for example the polar angle distribution is a function of the position on the source plane, or the emission energy. Again both types of primary particles are simulated separately. In addition at THOR, the neutron spectrum is further divided in a thermal, epithermal and fast part, each one processed in an independent calculation. Uncertainty calculations of the combination of single parts of each dose component are made analogue to equation (86). To verify the source definition in FLUKA an evaluation has been made by comparison to MCNP data, from which the source was adapted. The modelled geometry was in both cases reduced to about 0.25 m^3, mainly containing dry air. Each experimental setup was modelled in detail, including the beam exit, phantom, alanine detectors, and activation foils. Composition and density of the materials were obtained from literature or manufacturers. Analogue default settings and “USRBIN” scoring have been used. An identical user-routine “COMSCW” was employed. Calculations were finished when uncertainties of dose and components were below 2%. Uncertainties associated with RE values were again calculated using error propagation analogue to equation (86).

3.2.3 Results

3.2.3.1 Response in thermal neutron fields

This first sub-section summarises the results of experiments in the radiation field of the thermal column of the TRIGA Mainz, including the phantom study carried out with the NPL, the alanine comparison study and the experiments using the gadolinium doped alanine. For easier comparability all values of detector response and absorbed dose are normalised with the irradiation time and shown as rates in Gy/min. Since all experiments are affected by the RE, considerations towards them are prepended.

Phantom and shielding study

According to equations (42) and (85) a total RE as well as three component REs (RE_γ, RE_p, RE_n) have to be determined for each pellet. Although the calibration photon spectrum differs from those in the experiments RE_γ is defined to be unity. As already described previously (sub-section 1.5.2.2) this assumption is supported by literature [Bermann et al., 1971, Regulla and Deffner, 1982, Anton et al., 2008]. Hence regarding primary and secondary photons detector response equals absorbed dose. Values different from unity were shown earlier for photon energies below 100 keV. However, calculations of the photon spectra showed that the great majority of the photon dose is deposited by higher energy photons and such RE values do not have to be taken into account.

RE values reported in the following text were solely calculated using results of the MC code FLUKA and the implemented comscw user-routine, which is containing results of the Hansen and Olsen model.

With a weight fraction of about 15% of nitrogen alanine contains about five times the nitrogen in tissue. Consequently, the proton dose D_p plays an important role in the interpretation of the response. Emitted particles have a range on the micrometre scale and constant emission-energy. Therefore identical proton slowing down spectra were expected in all alanine pellets. Indeed in MC calculations such spectrum was observed, independent of pellet position or surroundings. RE_p was therefore expected to have a fixed value. It was determined to be 0.56 ± 0.01 and has been found in the calculations of all experiments at all facilities.

For the weighting factor for the fast neutron dose, $\mathrm{RE_n}$, such considerations are not valid. The kinetic energy distribution of the recoiling protons is a function of the neutron spectrum. Since the neutron spectrum changes between facilities, with the irradiated material and with depth in phantom, the proton spectrum is also changing and so does $\mathrm{RE_n}$. However, in the thermal field of the TRIGA Mainz no fast neutron was observed, and $\mathrm{RE_n}$ is not considered.

With all phantom and shielding experiments gold foils were irradiated. Resulting neutron fluxes were determined as thermal equivalent as described in section 3.1.2 and are shown in figure 3-35 as a function of depth in the thermal column. Experiments are differentiated by colour. Were multiple irradiations were made, the data points are average values of all measurements. Variations between values at the same position in the same experiment differed only within the measurement uncertainty. It can be seen, that the neutron flux is mainly a function of depth, deviations are the result of differences in the lateral shift from the central axis of the thermal column. Only materials with very different macroscopic cross sections show big deviations in the figure. Accordingly, the neutron flux in the photon shield is slightly higher, while it is clearly lower with the neutron shield.

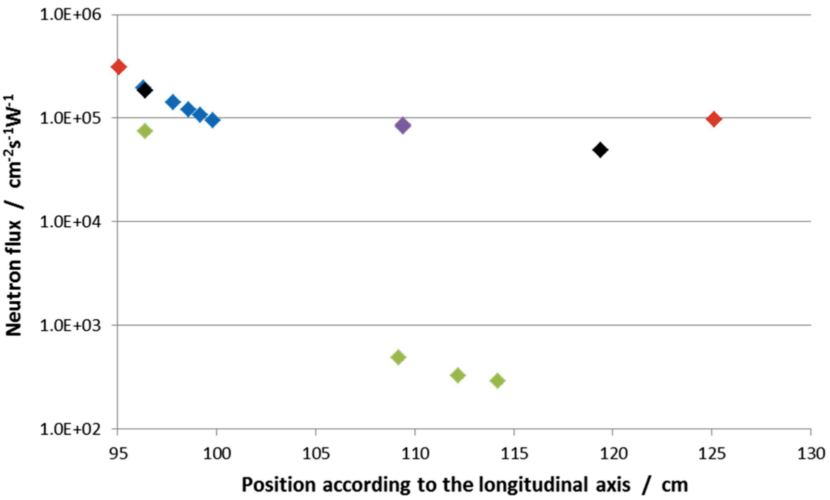

Figure 3-35. Average thermal equivalent neutron flux measured using gold foil activation: PMMA phantom (black), Teflon phantom (red), liver tissue (blue); neutron shield (green), and photon shield (purple). All values have uncertainties between 3% and 4%.

The measured alanine detector response, D_{ref}, for the phantom and shielding study is indicated in black in figure 3-36 a) to e). Except for the values measured for detectors in photon shielding, all results are shown as dots and as a function of depth in the phantom. With the photon shielding values are indicated by columns.

On 20 cm length in the PMMA phantom values decrease, similar to the neutron flux (compare also figure 3-14), exponentially from 1.72 ± 0.04 Gy/min to 0.72 ± 0.02 Gy/min. The response rate in the Teflon phantom is lower, decreasing over 29 cm from 1.50 ± 0.04 Gy/min to 0.56 ± 0.01 Gy/min. Due to the dimension of the boric acid container, with the neutron shielding the foremost pellet is located further back. As a result, much lower response rate of about 0.6 Gy/min is observed. In addition only a slight decrease is observed depending on the longitudinal position. In the lead and bismuth photon shielding pellets were irradiated side by side. The measured response rate is 0.47 ± 0.01 Gy/min for both pellets. The distance to the core was 109 cm, as indicated in the figure.

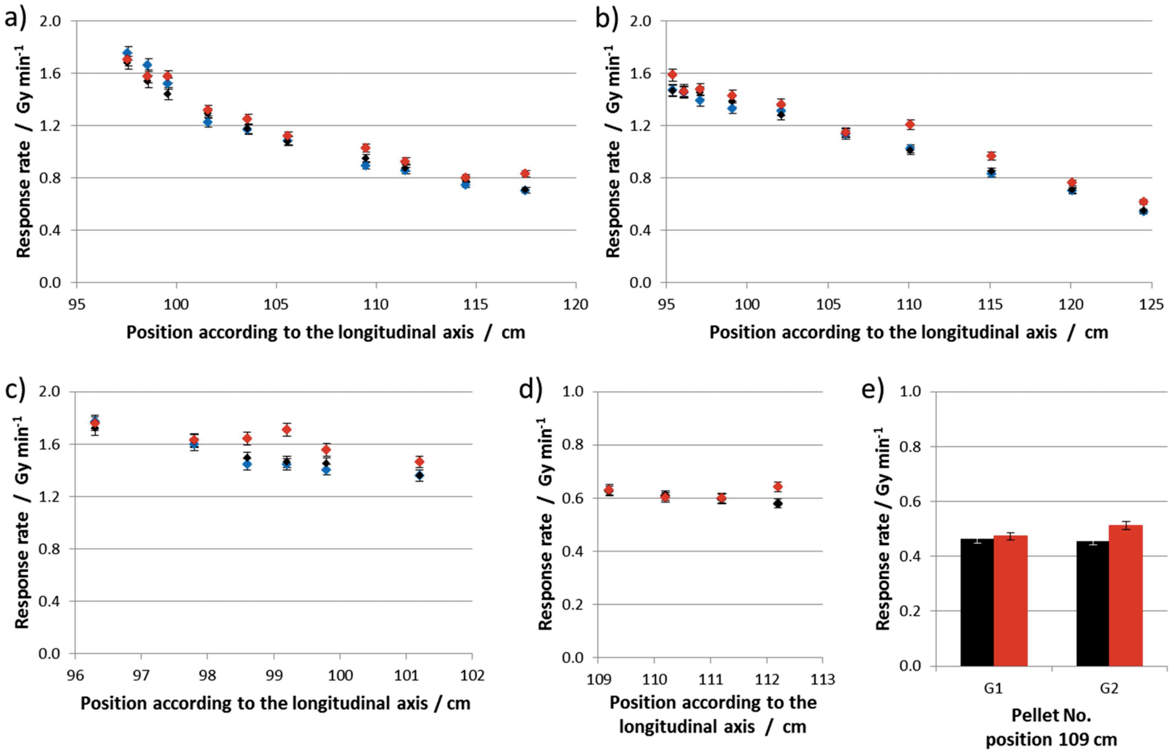

Figure 3-36. Measured (black) and calculated (FLUKA - red, MCNP - blue) alanine response D_{ref} for the TRIGA in the PMMA phantom (a), Teflon phantom (b), liver tissue (c); neutron shield (d), and Photon shield (e).

Within the same figure measured values are compared to FLUKA calculations, shown in red. The agreement between the values is good. The largest difference between measured values and those calculated with FLUKA is 15%, the mean value over 32 pellets is 3%. For comparison, were available, also values calculated with MCNP are shown. They were calculated by M. Ziegner for the same experiments [Ziegner et al., 2014]. The general strategy in using MCNP was the adoption of the FLUKA component REs to MCNP absorbed doses. Particularly in figure 3-36 b) and c) FLUKA superimposes a fluctuation over the monotonically decreasing NPL readouts, which is a result of the statistical uncertainty in calculations. MCNP values show an average difference of 2.5% as well as a monotonically decreasing trend without fluctuations.

Response components have been calculated with the RE values described above. As already mentioned there the fast neutron dose D_n was found to be negligible. Depending on the actual position, the fast neutron component was two to four orders of magnitude smaller than the nitrogen proton dose. The total RE is a result of the single REs and the dose composition in each pellet according to equation (85). The separation in components is shown for all experiments in figure 3-37 a) to e) as calculated by FLUKA. Pellets are numbered according to their longitudinal position. The dose composition depends strongly on the surrounding phantom material or shielding. In liver tissue as well as in PMMA similar responses have been observed. The secondary photon dose is dominated by 2.23 MeV hydrogen photons, the total RE values, shown in figure 3-38, are varying between 0.84 ± 0.01 and 0.93 ± 0.01, whereby on average they are slightly higher in PMMA. Figure 3-38 also shows the total RE values of the other experiments. In Teflon the composition of the secondary photon dose is different. Teflon does not consist of any hydrogen hence the only hydrogen photons are generated in the pellets themselves. The most relevant photons are generated by the fluorine in Teflon and the carbon, also in Teflon but mainly from the surrounding graphite. Resulting total REs are significantly lower with values between 0.69 ± 0.01 and 0.73 ± 0.01, due to the relatively higher contribution of nitrogen protons. Comparing the absolute value of the nitrogen proton dose rate in Teflon and PMMA, similar values are observed, when correcting for the higher neutron flux in Teflon. In boric acid the proton dose is suppressed. Therefore only primary and secondary photons remain and the total RE is unity. Secondary photon dose is

again dominated by 2.23 MeV photons from hydrogen, but also from 0.48 MeV from boron. With the photon shield the primary photons make no contribution. Since lead and bismuth have no reasonable (n,γ) cross-sections, the secondary photons are also reduced. This results in RE values of 0.68 ± 0.01, which are hence similar to those in Teflon, although the exact dose composition is different.
Comparing the total RE values of figure 3-38, in the three phantom experiments (tissue, PMMA and Teflon) a slight increase with depth can be observed, which is most obvious with the blue data points of the detectors irradiated in liver tissue. This observation corresponds to a trend in figure 3-37, where in comparison doses generated by neutrons decrease more with depth than those generated by photons. Since the only dose component with an RE smaller than one is the proton dose, the total RE might be also used as measure of the relevance of this component. A summary of component RE values can be found in section 3.3 in table 3-11.

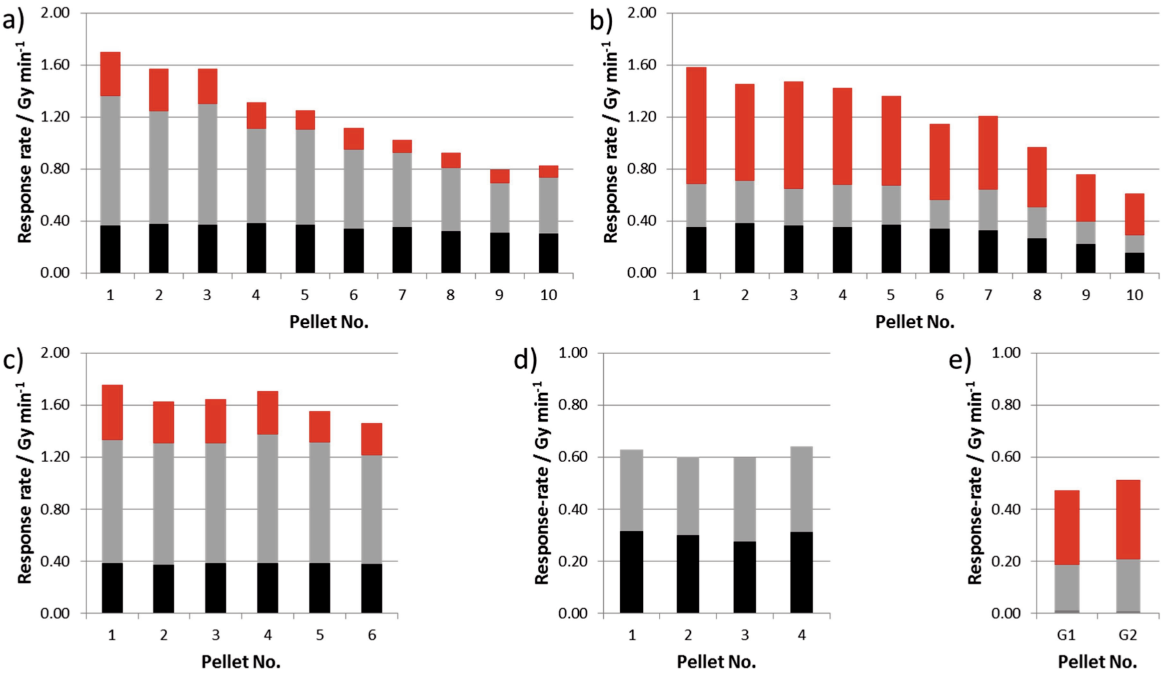

Figure 3-37. Components of the alanine response D_{ref} calculated with FLUKA for the TRIGA; Primary photon response (black), secondary photon response (grey) and proton response (red); PMMA phantom (a), Teflon phantom (b), liver tissue (c); neutron shield (d), and Photon shield (e). All values have a statistical uncertainty between 2% and 3%.

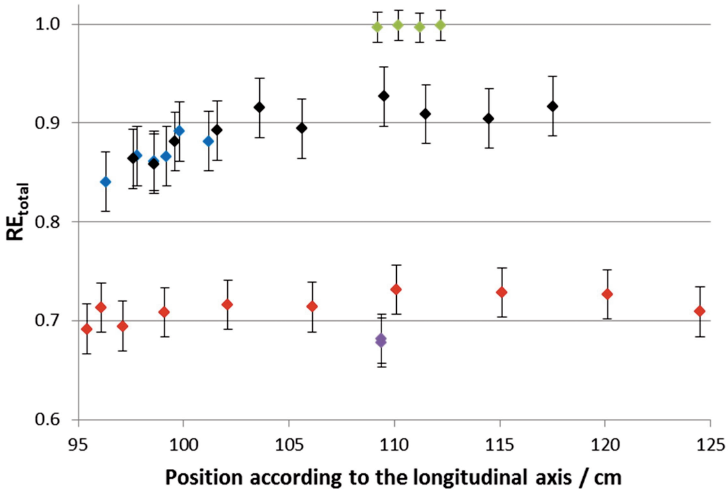

Figure 3-38. Values of the total RE according to FLUKA calculations in the PMMA phantom (black), Teflon phantom (red), liver tissue (blue); neutron shield (green), and Photon shield (purple).

Comparison study

In further experiments with the alanine detector, different blends from three manufacturers were compared by irradiation in the PMMA phantom. In particular this comparison shows the influence of the binder on the response.

Data series of the NPL was already presented in figure 3-36 a) and is again plotted with black filled diamonds in figure 3-39. Within the figure NPL series is compared to those measured by the University of Oslo (UO) and the University of Palermo (UP), plotted with red, respectively blue filled diamonds. As above, data is shown as a function of depth in the thermal column. In both cases the measured response is higher; in the case of UO by about 15% and in case of UP by about 8% relative to the NPL response. Gold foil measurements were in agreement for all experiments. Differences in response are hence not a consequence of differences in neutron fluence. The general course, following an exponential-like decrease, is the same for all three blends. Calculations are shown for each series in the same colour, but with unfilled dots. The reached agreement between calculations and measurement is again good, with a mean deviation of 3% for both data sets. Maximum deviation of 9% was found for the foremost pellet of UP. In all series no systematic shift between measurement and calculation was observed.

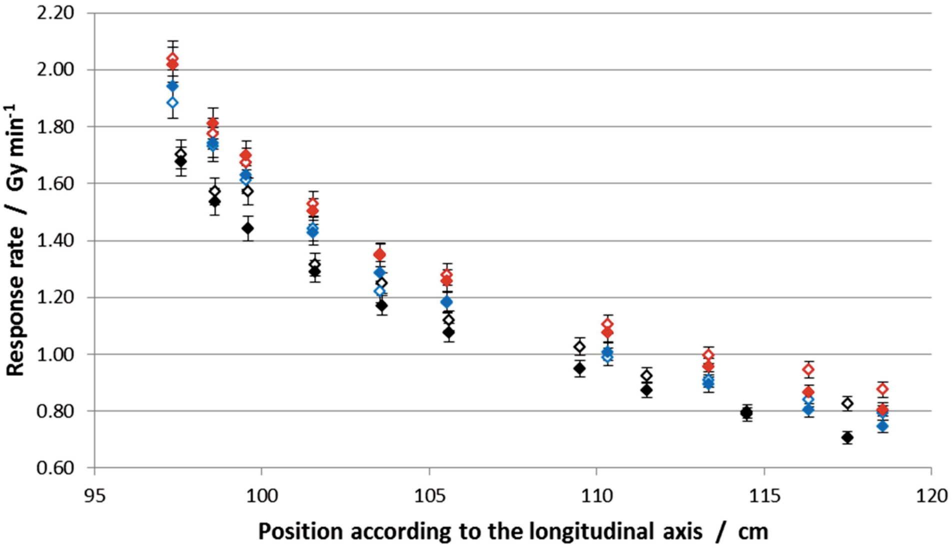

Figure 3-39. Measured (filled) and calculated (unfilled) alanine response D_{ref} for the TRIGA in the PMMA phantom with three different sets of alanine pellets: NPL (black), UO (red), and UP (blue).

As illustrated by the dose composition in figure 3-40, increase in dose is not uniform in all components. For better visibility in the figure data points are connected, using different types of lines for each series. The response due to primary photons is shown in black. Within uncertainties, calculated response is almost even at same depth for all three blends. NPL data is only slightly higher. Observation is different for the two other components, which seem to be responsible for the higher total dose response in the UO and UP dosimeters. Especially for the secondary photon dose (grey) response of the NPL pellets is significantly lower. Also the relative amount of proton dose in the NPL detectors is slightly lower. Hence in turn the total REs of the NPL pellets are higher, as visible by comparison to UO and UP REs in figure 3-41. Regarding component REs identical values as before were found.

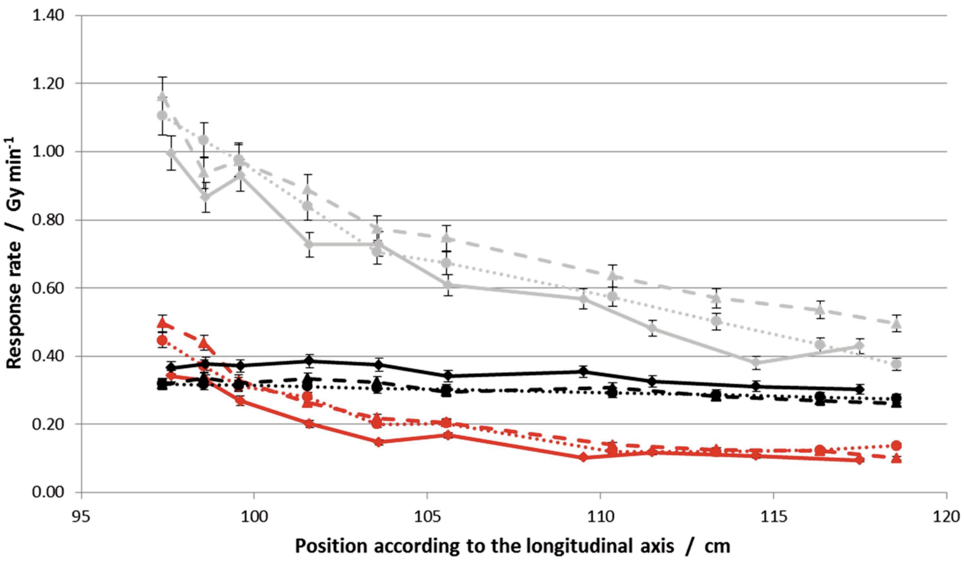

Figure 3-40. Components of the alanine response D_{ref} calculated with FLUKA for the pellets read-out at NPL (diamonds – solid line), UO (triangles – dashed line), and UP (circles – dotted line) with primary photon response (black), secondary photon response (grey) and proton response (red).

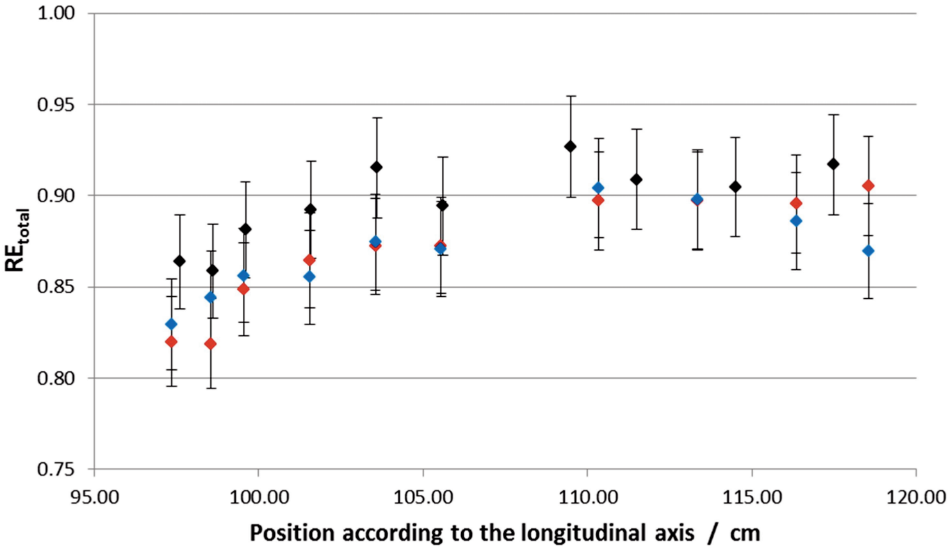

Figure 3-41. Values of the total RE according to FLUKA calculations for the pellets read-out at NPL (black), UO (red), and UP (blue).

Experiments using Gadolinium doped alanine

As mentioned previously, experiments with the gadolinium oxide-alanine mixtures were carried out with broad range of reactor powers and irradiation times, but without measuring a depth dose curve in phantom. Detector response is therefore displayed as a function of neutron fluence instead of depth. Neutron fluence was calculated from the activation of gold foils. Measured results for detectors irradiated in the PMMA phantom are shown in part a), for those irradiated in the boric acid neutron shield in part b) of figure 3-42.

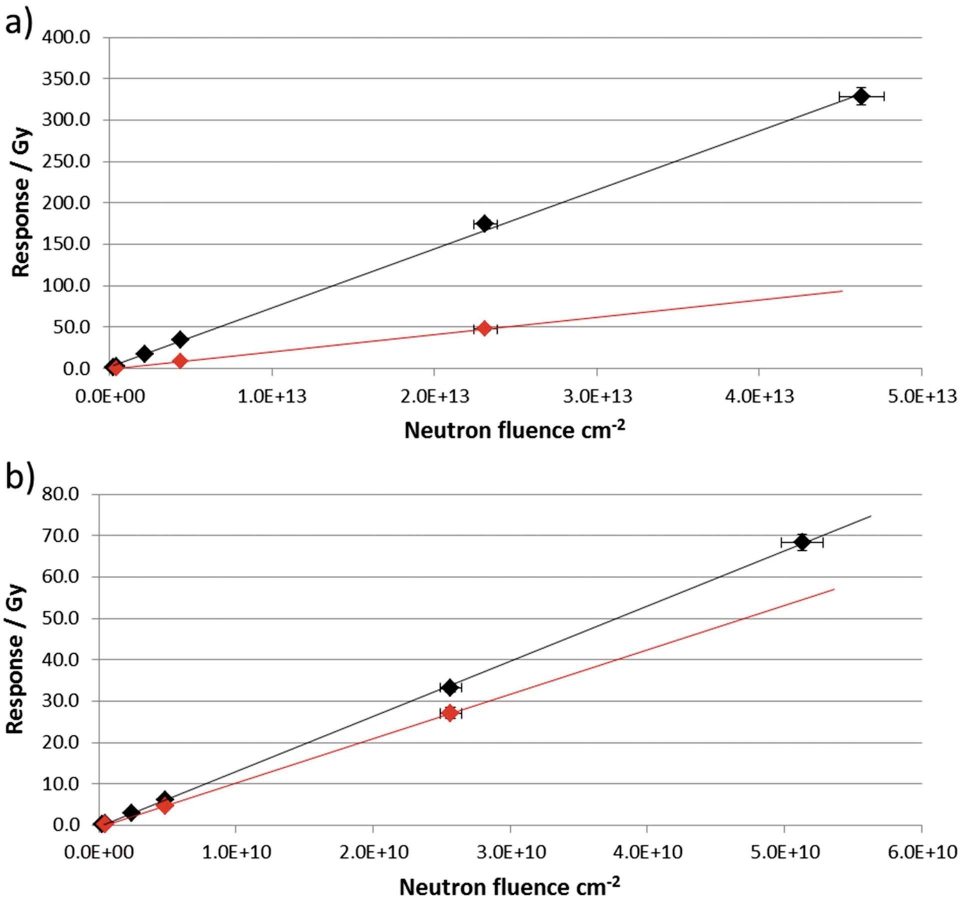

Figure 3-42. Measured response as a function of neutron fluence for dosimeters containing gadolinium (black) and dosimeters lacking gadolinium (red) as measured in the PMMA phantom (a) and in the boric acid neutron shield (b).

Detectors containing gadolinium are indicated black, those without gadolinium are indicated red. The highest response of 329 ± 8 Gy has been measured after irradiation with 100 kW_{th} for 45 min in the PMMA phantom. In each experiment the correlation between response and neutron fluence is linear for both detector types.

For illustration in the figure lines in the accordant colour are added. As expected the response of detectors containing gadolinium is increased compared to those consisting only of alanine and binder. The increase is with a factor of 3.52 larger in the PMMA experiment, than in the boric acid experiment, where it only accounts for 1.26. Compared to earlier experiments the change in the alanine response between the two setups is identical with respect to the change in elemental composition, due to the enlarged amount of binder (20%).

Detector response and response composition were again calculated with the FLUKA code. Results are compared with measurements in figure 3-43. The ESR response is given as averaged value of all measurements (extrapolated for 100 kW_{th} reactor power) in black columns. The corresponding FLUKA response is shown in red columns. In case of the alanine detectors without gadolinium the agreement is good. The calculated response of the gadolinium-alanine shows the expected, significant overestimation. In a third column the response composition out of components is given. For gadolinium-free pellets it was found to be analogue to the composition found in earlier experiments. The relative fractions of different components remain similar, as the total response does. In the pellets containing gadolinium photon components are increased, the proton component is only present in the PMMA phantom and slightly reduced. The additional gadolinium dose is indicated in blue. In the PMMA experiment the component represents 73.7% of the total dose. In the boric acid shielding fraction is reduced to 3.6%. The reduction corresponds to the measured and calculated decrease in neutron flux due to the shielding. However, especially form the composition in part b) it is obvious that the gadolinium component as calculated cannot be responsible for the complete overestimation, also the photon components seem to be overestimated.

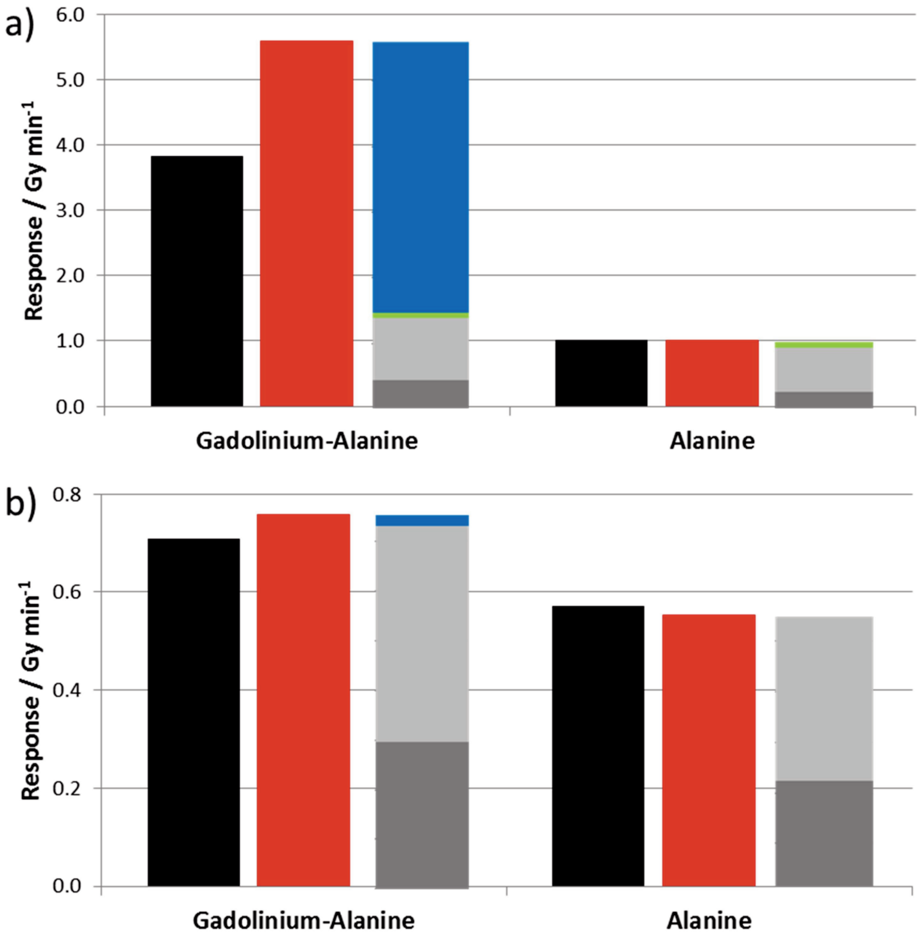

Figure 3-43. Comparison of measured response (black), response calculated with FLUKA (red), and differentiation of response components (primary photon response - dark grey, secondary photon response - light grey, and proton response - green, and gadolinium dose - blue) in the PMMA phantom (a) and in the boric acid neutron shield (b). All values are for a reactor power of 100 kW$_{th}$.

3.2.3.2 Response in epithermal neutron fields

Results of experiments in epithermal fields were again gathered in cooperation with the NPL. Also the same set of RE values, as defined in equation (85), was used. Different to thermal fields, in epithermal fields in addition the fast neutron RE, $\mathrm{RE_n}$, has to be considered. Descriptions of the other component RE were given in the previous section. Values ($\mathrm{RE}_\gamma \overset{\text{def}}{=} 1.00$, $\mathrm{RE_p} = 0.56 \pm 0.01$) were found to be also valid in epithermal fields. As expected the weighting factor for the fast neutron dose $\mathrm{RE_n}$ is the only one which was not found to be constant. It depends on the neutron spectrum and hence on facility, irradiated material, and positon within the experimental setup. Due to all these parameters the energy spectrum of recoiling protons is changing and so does $\mathrm{RE_n}$. Values between 0.71 ± 0.03 and 0.58 ± 0.09 have been observed in calculations at FiR 1 and THOR.

Results as measured in PMMA phantoms are illustrated in figure 3-44 a) and b) in black. On the horizontal axis, the position on the longitudinal axis is shown in terms of distance to the beam exit. The distance from the beam exit to the reactor core is larger by 173.1 cm in the case of FiR 1 and 226 cm in the case of THOR. Figure 3-45 a) and b) illustrates the free in air measurements. Compared to the TRIGA neutron field dose rates are lower. Therefore results are shown in units of Gy/h. Also compared to TRIGA a build-up effect is observed in the depth dose profiles. At FiR 1, shown in part a) in each figure, response rate increases in PMMA from 5.5 ± 0.1 Gy/h to 9.5 ± 0.2 Gy/h before it decreases nearly exponentially to 0.97 ± 0.02 Gy/h. Results indicate a maximum at a depth of 2.0 cm. In the epithermal beam at THOR the build-up region has been examined in more detail. Due to differences in the neutron energy spectrum the course is slightly different from that at FiR 1. The maximum response is reached in the pellet at a depth of 2.3 cm in the PMMA phantom. Six values have been measured in front of the maximum, eight behind it. Response rates increase from 8.9 ± 0.2 Gy/h to 11.5 ± 0.3 Gy/h before they decrease to 0.67 ± 0.02 Gy/h at a depth of 18 cm. Figure 3-46 shows the build-up region in detail.

The pellet irradiated free in air at FiR 1 shows a much lower response rate compared to the pellet at the same position inside the phantom (0.89 ± 0.02 Gy/h). Correlation at THOR is similar (1.84 ± 0.05 Gy/h), although in general dose rate is higher but not doubled.

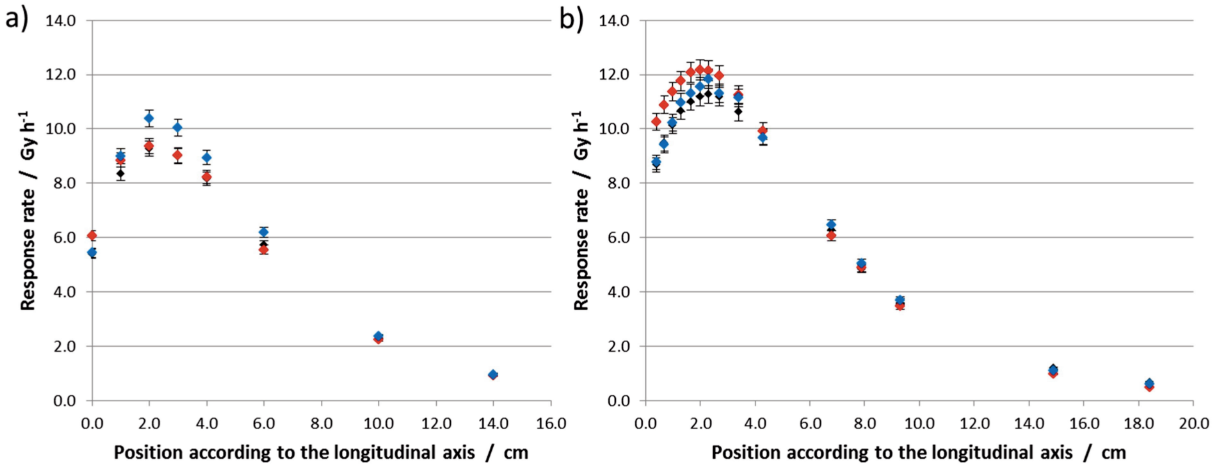

Figure 3-44. Alanine response D_{ref} in PMMA phantoms (measured – black; FLUKA – red; MCNP – blue) for a) FiR 1 and b) THOR.

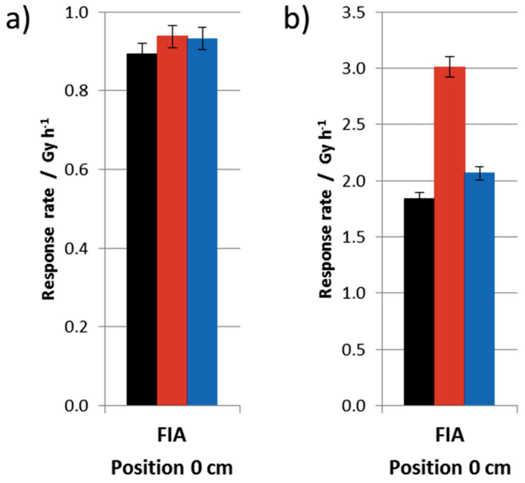

Figure 3-45. Alanine response D_{ref} free in air (measured – black; FLUKA – red; MCNP – blue) for a) FiR 1 and b) THOR.

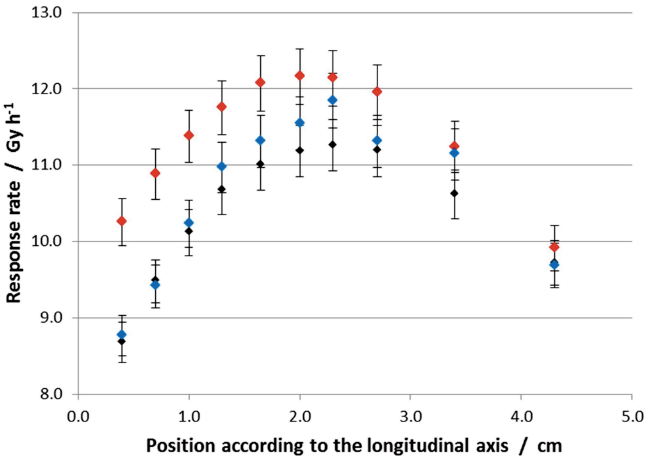

Figure 3-46. Detailed build-up region at THOR: Measured (black) and calculated (FLUKA – red, MCNP – blue) alanine response D_{ref} in PMMA phantom.

In figure 3-44 again measured values are compared to calculations using FLUKA, indicated in red, and again for comparison reasons MCNP, indicated in blue. In both cases MCNP calculations were carried out by partners at the local facilities. In a first step during the FLUKA calculations the source file had to be evaluated. In its final form, as used for the calculations displayed in figure 3-44, agreement between MCNP and FLUKA concerning fluence and energy spectra in several build-ups were tested and found to be matching within 2% at both facilities. Thus also agreement achieved regarding the alanine response is good at both facilities. Analogue to the approach at the TRIGA, component RE values were adopted from FLUKA and applied on absorbed doses calculated by MNCP.

However, the MCNP data series shown for THOR in figure 3-44 b) is not calculated with the regular MCNP plane source model. Due to better agreement with the measurement, a more sophisticated two-step model was used, which is starting from the reactor core instead of using a source plane. Especially for areas close to the beam exit this model provides higher accuracy. Since this source definition is not applicable to FLUKA, compared MC calculations at THOR are based on different source definitions.

At FiR 1 differences between FLUKA and the measurements have a mean value of 5%. Absolute differences are biggest for the first two data points. Values taken from MCNP are deviating between1% and 7%. Between the two codes the mean difference for total and component values is 2% with a maximum value of 19%. Similar agreement like at FiR 1 is only reached for depth from 3 cm onwards at THOR. From the surface to 3 cm, an overestimation decreasing with depth was found. In the free in air experiment the measured value is overestimated by FLUKA by 1.2 Gy/h, hence nearly 64%. In the PMMA phantom differences between FLUKA and the measurements have a mean value of 6%. Values obtained by MCNP deviate about 1% from the measurements. Between the two codes differences up to 16% can be observed at lowest depth with an average value of 6%. Free in air deviation between codes is 48%. The deviations between both codes are mainly due to different source definitions.

Four dose components have been observed in both epithermal fields. The relative values are similar at FiR 1 and THOR, and so are the REs. The response composition, as calculated by FLUKA is shown in figure 3-47 a) and b) for both reactors, figure 3-48 shows the MCNP results for THOR. RE values are displayed in figure 3-49 a) and b), according to FLUKA, and again for both facilities. At FiR 1 total RE values are between 0.74 ± 0.01 and 0.91 ± 0.01. Analogue values at THOR vary between 0.71 ± 0.01 and 0.92 ± 0.01. Compared to the PMMA phantom at TRIGA, total REs are lower. As with the TRIGA results photon dose is shown in two parts, although the primary photon dose is much lower. For RE_{γ} and RE_{p} identical values have been observed. With the epithermal beam the fast neutron component contributes more substantially and is relatively biggest in the free in air pellets. At FiR 1 RE_{n} varies between 0.71 ± 0.03 and 0.58 ± 0.09. The value is highest for the foremost pellet in the PMMA phantom and then decreases. Free in air 0.69 ± 0.03 has been calculated. At THOR value RE_{n} is varying between 0.64 ± 0.05 and 0.68 ± 0.07 in phantom and has a value of 0.65 ± 0.06 free in air. A summary of component RE values found in epithermal and thermal fields can be found in section 3.3 in table 3-11.

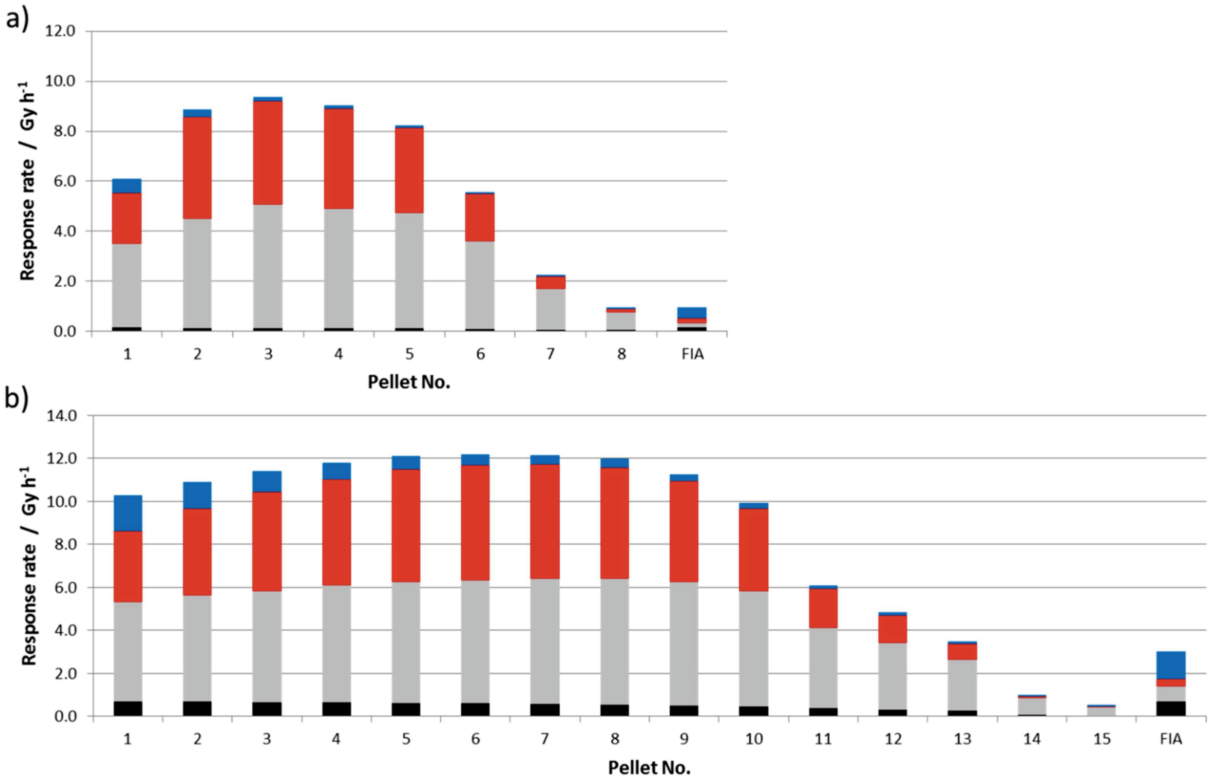

Figure 3-47. Components of the alanine response D_{ref} calculated with FLUKA for a) FiR 1 and b) THOR: Primary photon response (black), secondary photon response (grey), proton response (red) and fast neutron dose (blue) in the PMMA phantom and free in air (FIA). Fast neutron dose values have a statistical uncertainty between 6% and 12%, other values between 2% and 3%.

Figure 3-48 shows the components as calculated by MCNP, weighted with the REs of FLUKA. Since with the sophisticated MCNP model no separated photon and neutron source is used only a total photon dose is shown. Comparison of figures 3-47 b) and 3-48 shows the origin of the deviation in figure 3-46. A similar relative overestimation of FLUKA towards MCNP is observed for photon and proton response, decreasing with depth. The different absolute values of the alanine response are a result of these two components. Deviations of the fast neutron response follow a different course. For low depth both codes agree within the statistical uncertainty. Large relative differences from 7% up to 30% are only found for depth bigger than 6 cm, but with small absolute differences below 0.1 Gy/h.

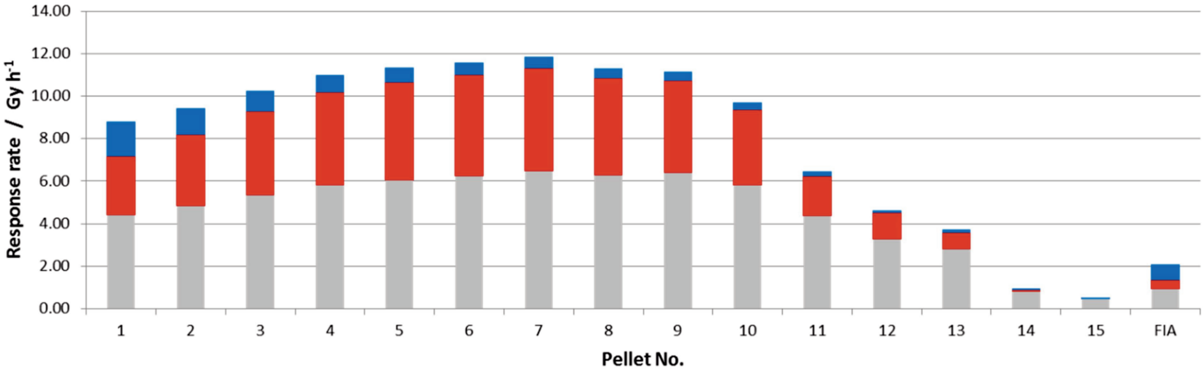

Figure 3-48. Components of the alanine response D_{ref} calculated with MCNP at THOR: Photon response (grey), proton response (red) and fast neutron dose (blue) in the PMMA phantom. Fast neutron dose values have a statistical uncertainty between 8% and 12%, other values between 2% and 3%.

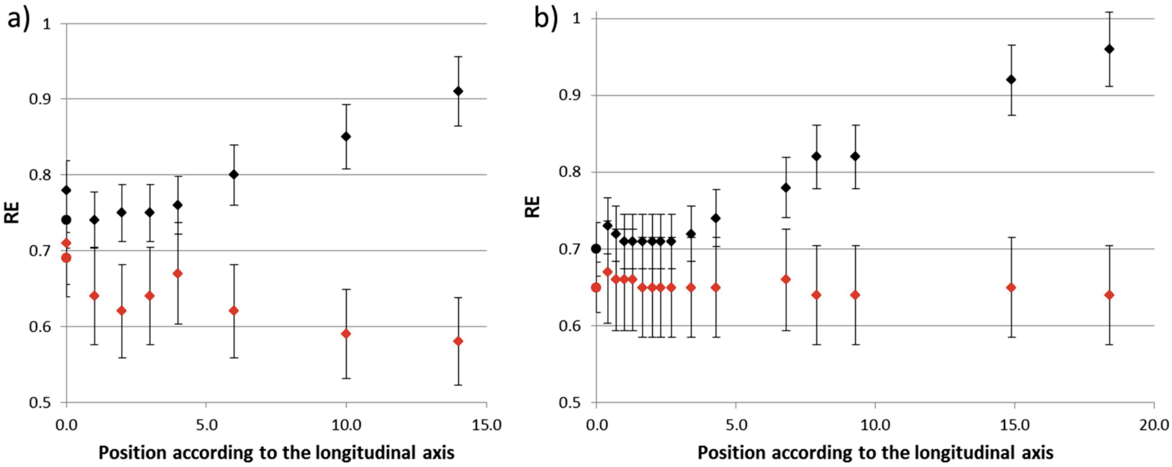

Figure 3-49. Values of the total RE (black) and fast neutron RE (red) at FiR 1 (a) and THOR (b) according to FLUKA calculations in the PMMA phantom (diamonds) and free in air (circles).

3.3 The lithium formate detector

Formate detectors were mentioned in section 1.5.3. Compared to alanine they are similar in their elemental composition and consequently also regarding most dose components, as evident in equation (87). However, the big difference is the presence of an element with a notifiable higher neutron capture cross section, with big impact on the dose composition. The corresponding equation (85) in the previous alanine chapter needs to be modified only slightly for the use with lithium formate. Due to the absence of nitrogen, the proton dose is not relevant. Instead the lithium dose $\mathrm{D_L}$ has to be considered. In photon fields, but also towards charged particles, the parameters of lithium formate are similar to those of the alanine. The response behaviour is linear up to high doses, and fading is negligible for low doses [Waldeland et al., 2011]. The ESR spectrum only consists of a single line, as a consequence the detector was found more sensitive [Vestad et al., 2003].

$$D_{ref} = RE_{\gamma}D_{\gamma} + RE_{N}D_{N} + RE_{L}D_{L} \qquad (87)$$

In turn the lithium dose component is in many ways comparable to the BNCT boron dose. The underlying nuclear reaction can be written as an (n,α)-reaction and in both cases an isotope with minor abundance reacts. As already mentioned in section 3.1.4 lithium-6 has a natural abundance of 7.4%. With 940 barn the thermal neutron capture cross section of the reaction is lower than the one of the boron-10 reaction, but still one of the highest among light elements. Different to the reaction of boron-10, the residual nuclei is a tritium particle. The reaction was displayed previously in section 3.1.4 in equation (84). Resulting particles have high LETs and low ranges in the micrometre scale, although their energy is higher than those of the particles of the boron reaction. Both particles relevant for the lithium dose are of similar energy. Therefore, the component $\mathrm{D_L}$ can be also written as sum of an alpha component $\mathrm{D_A}$ and a tritium component $\mathrm{D_T}$, both afflicted to an individual RE. In the experiments described here the response of lithium formate is examined in a PMMA phantom and inside boron neutron shielding. Experiments were conducted analogue to those in the alanine studies. Also the general methodology is similar.

The main purpose in the investigation of the lithium detector arouse from the lack of a sufficient boron containing detector. Due to the analogies, lithium formate is an ideal candidate to study the applicability of the system, consisting of MC simulations and ESR measurements, on detectors containing elements with high cross sections.

3.3.1 Material and methods of the characterisation in thermal neutron fields

Lithium formate monohydrate was obtained from Sigma-Aldrich and pressed without any further binder. Pellets were cylindrically shaped, with a diameter of 5 mm and a height of 2.5 mm. The average mass was 65 mg. The manufacturing and read-out process was again carried out in cooperation with the University of Oslo (UO), Norway. Read-out of the ESR dosimeters has been performed with an EMX-micro ESR spectrometer. A detailed description of the read-out can be found in literature [Waldeland et al., 2011]. Calibration was made using ^{60}Co photons. Twelve detectors of each material have been irradiated with four different photon dose values between 7 Gy and 28 Gy. Detector response was again recorded from the peak-to-peak amplitude of the ESR-signal. As a second quantity, the peak width (from maximum to minimum) was determined. The uncertainty of the read-out procedure was calculated as for the alanine detectors in the comparison study to be around 3%.

Irradiations have been carried out in the thermal column of the TRIGA Mainz. As before the 20 × 20 cm^2 channel has been used, which was equipped with the 5 cm bismuth shield at the reactor-near end. Inside the channel experiments were placed in the standard PE-box. Two build-ups of the alanine study have been re-used. In the cuboid shaped PMMA phantom (10 × 10 × 23 cm^3) ten pellets were positioned on the central length axis. In a second build-up the cylindrically shaped neutron shield has been used. Eight lithium formate pellets were irradiated inside. Phantom and shield are described in detail in section 3.2.1. Both setups were irradiated twice and accompanied by gold foil measurements. In order to achieve a comparable absolute dose response in all experiments the maximum power of 100 kW$_{th}$ had to be adjusted to 1.0 kW$_{th}$ for the experiment with lithium formate in the PMMA phantom. Detectors in the PMMA phantom were irradiated for

20 minutes, detectors in boric acid for 10 minutes.

Absorbed dose and dose composition have been calculated for each dosimeter using the Monte Carlo code FLUKA (2011-2b). The used reactor model has been described previously (compare sub-section 3.1.1.2). Again default settings for hadron therapy “HADROTHE” were equipped, with “USRBIN” scoring to calculate the absorbed dose and dose response. Multiple “USRBIN” scoring cards were combined with a “COMSCW” user-routine, assigning weighting factors to every dose deposited. The routine contains particle and energy specific RE values. Different to the work with alanine, the necessary values were derived from track structure theory of Katz and Butts with the help of the cooperation partner [Waldeland et al., 2010b]. A description of the theory can be found in sub-section 1.6.6.2. “USRBIN” scoring cards gave weighted response as well as absorbed dose for the dedicated particle species. By comparison RE factors were determined according to equation (87). The LET of various particles was determined employing “USRYIELD” cards. In general simulations were carried out until uncertainties below 3% were reached for the observed resulting values. However, dose components with relative fractions below 2% resulted in uncertainties up to 11%, values in the LET spectra with similar relative size had uncertainties up to 16%.

3.3.2 Results

3.3.2.1 ESR spectra

As expected a linear dose dependence of the peak-to-peak-height has been observed in the calibration range. Notably two different line widths were observed with the lithium formate. Pellets irradiated in the photon reference field and in the boric acid shielding had a width of 1.49 ± 0.01 mT, while in the PMMA phantom broadening to 1.58 ± 0.02 mT was observed. Figure 3-50 shows two exemplary first derivative spectra of lithium formate with indicated line width. Comparable four line spectra of alanine, as for example observed in the experiments described in section 3.2.1.2, had a mean line width of 0.664 mT without a significant difference between neutron and photon irradiation. A comparison to ESR spectra of other materials can be found in figure 3-55.

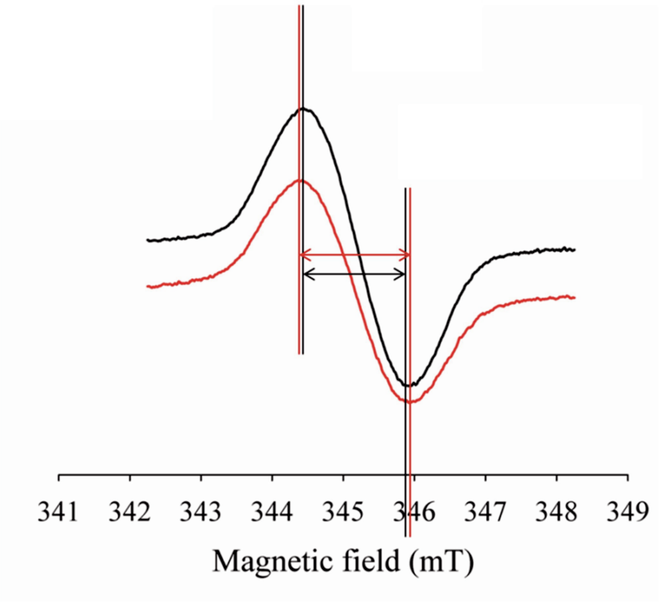

Figure 3-50. ESR spectra of lithium formate dosimeters irradiated with photons (black) and neutrons (red).

3.3.2.2 Absorbed dose and detector response

The measured depth dose curve in the PMMA phantom shows a different behaviour as observed before with the alanine detector. Detector response is shown in figure 3-51. Measured dose response is indicated in black. All values are again normalised with irradiation time for better comparison. While for alanine a continuous, nearly exponential decrease was observed, the course in the formate experiment differs. The initial decrease is steeper and the curve ends in a slight increase. It starts at 1.12 ± 0.03 Gy/min, reaches a minimum at a depth of 19.2 cm and 0.35 ± 0.01 Gy/min and ends at 0.44 ± 0.01 Gy/min. The course is rather comparable to the corresponding gold foil measurements shown in figure 3-16, than to the alanine. The reactor power was chosen 1.0 kW_{th}, the normalised response of the detector is, hence, about 70 times higher relative to alanine.

The measured values are compared to those calculated by FLUKA. In figure 3-51 response D_{ref}, weighted by RE, is indicated in red, un-weighted absorbed dose is shown in blue. Between measurement and calculation a slight underestimation of about 10% can be observed. The RE value found by the comscw file for lithium formate has an almost constant value of 0.36 ± 0.02. The comparable value of alanine was much higher and increasing with depth (from 0.82 to 0.91)

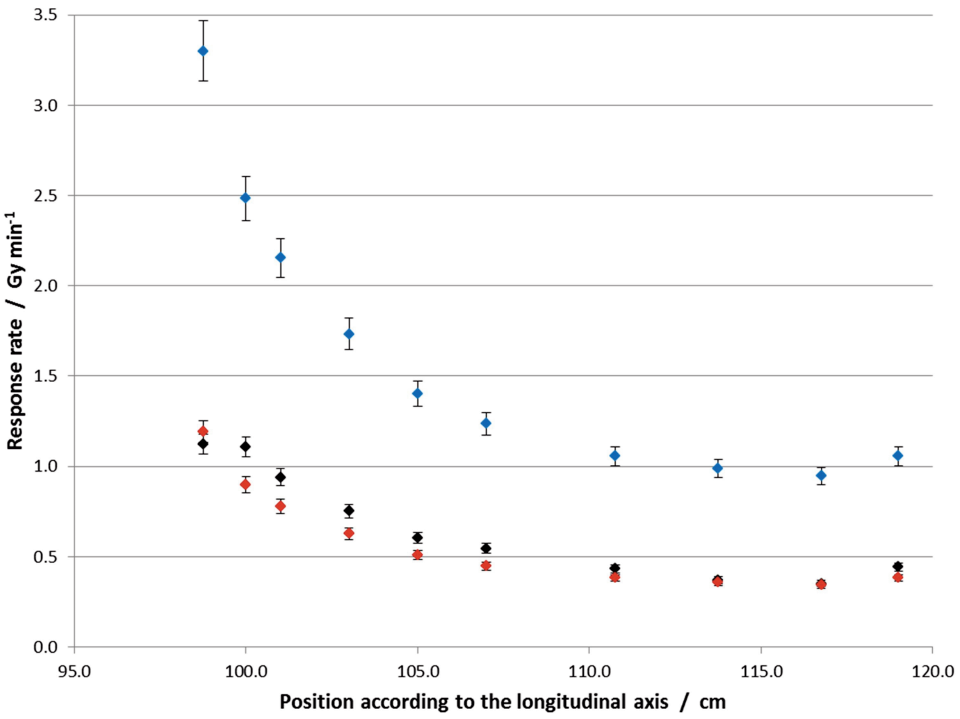

Figure 3-51. Depth dose curve in the PMMA phantom for the lithium formate detector: Measured response (black), calculated response (red) and calculated absorbed dose (blue).

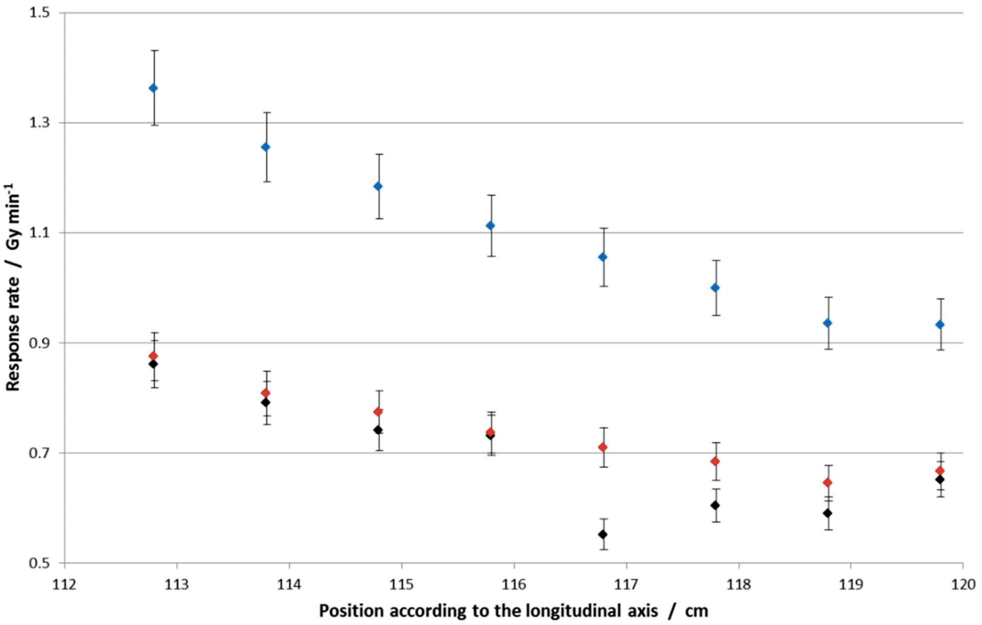

Figure 3-52. Depth dose curve in the boric acid neutron shield for the lithium formate detector: Measured response (black), calculated response (red) and calculated absorbed dose (blue).

Also with the boric acid shielding different depth dose behaviour as before was observed. Figure 3-52 shows the lithium formate result with a decrease from 0.86 ± 0.03 Gy/min to 0.65 ± 0.02 Gy/min with the lowest value at 0.55 ± 0.02 Gy/min. The RE is increasing from 0.70 ± 0.03 to 0.78 ± 0.03. Calculations, again shown in blue for absorbed dose and red for response, show a fair agreement. The mean deviation averages to 8%. Excluding the fifth pellet, an outlier deviating by 29%, mean deviation is reduced to 5%. Alanine showed a nearly constant response at all depth, and, hence, a different course, although the position within the shield was a little different, as can be seen by the position on the horizontal axis in figure 3-36 d). The RE, found to be one with the alanine, indicates the reason for the different depth dose behaviour. Smaller than one, calculations suggest that the lithium dose has not been completely suppressed.

In the calculations the response has been fragmented into the described components. In figure 3-53 the decomposition of dose is shown for the PMMA phantom. High LET particles emitted after the neutron capture of lithium-6 are dominating, generating between 98.9% and 99.3% of the dose in all detectors. In the figure the dose is separated into an alpha and tritium part. According to simulations, in all pellets 68% of the lithium dose was generated by tritium, 32% by alpha particles respectively. Within the calculations component RE values of 0.43 and 0.26 for tritium and alpha particles were found. In absorbed dose therefore only 57% are due to the tritium. The value corresponds to the value expected theoretically from the reaction data indicated in equation (84). For better visibility primary and secondary photon dose are not separated in the figure.

The dose composition of the lithium formate irradiated in the neutron shield is shown in figure 3-54. Primary and secondary photon dose (here separated again) have a comparable contribution as in the alanine experiments. The two photon components make about half of the total photon dose each, decreasing from 0.57 Gy/min to 0.47 Gy/min, with a slight increase to 0.51 Gy/min in the very back position. The major difference compared to earlier findings, occurs though the additional lithium dose in the formate. In absorbed dose a fraction of up to 55% has been calculated for the foremost pellet, giving a fraction of about 30% in response. Smallest fraction was calculated for the most distant pellet with values of 40% in absorbed dose and 20% in response. As could be expected the same RE values have been determined for the alpha and tritium particles as in the

PMMA experiment. Also the relative fractions of both particles are the same. The varying increasing total RE is a result of the decreasing fraction of the lithium dose with depth. Table 3-11 summarises all component REs, also including those of the alanine dosimeter described in the previous section. Similar to the nitrogen proton RE also the lithium RE, and the RE of its two particles were found to be constant. In general the decrease in lithium dose between the two experiments corresponds to the decrease in neutron flux, as also observed with the gadolinium-alanine. For such detectors, where the ratio of dose per neutron and dose per photon is significantly increased, the boric acid shield is insufficient regarding a complete shielding.

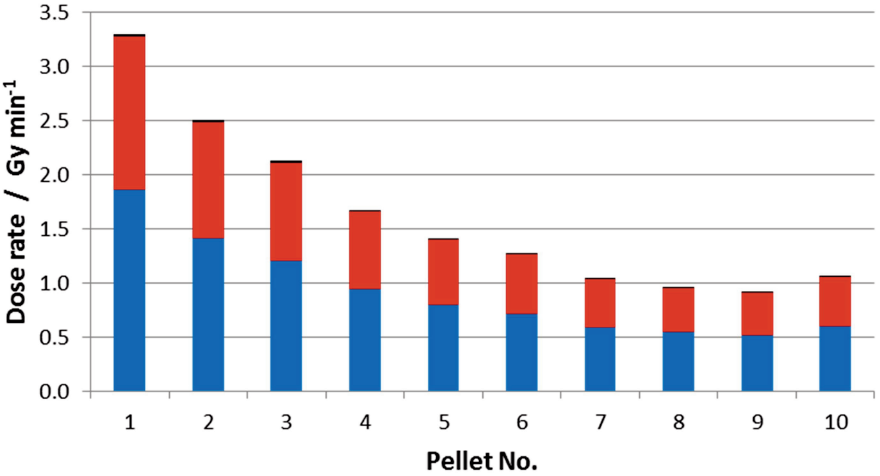

Figure 3-53. Components of absorbed dose in lithium formate in the PMMA phantom: Photon dose (black), alpha part of lithium dose (red), tritium part of lithium dose (blue).

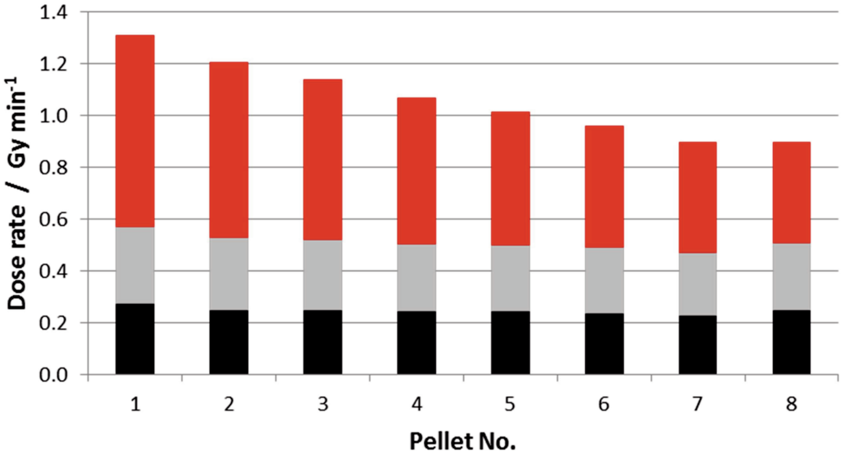

Figure 3-54. Components of absorbed dose in lithium formate in the boric acid neutron shield: Primary photon dose (black), secondary photon dose (grey), lithium dose (red).

Table 3-11. Component RE values in the alanine and lithium formate detector

Dose component	RE		
	Lithium formate	Alanine	
	thermal field	thermal field	epithermal field
Photon dose	1.00	1.00	1.00
Nitrogen dose	*n.o.**	0.56	0.56
Fast neutron dose	*n.d.**	*n.d.**	0.58 - 0.71**
Lithium dose	0.36	*n.o.**	*n.o.**
Alpha dose	0.26	*n.o.**	*n.o.**
Tritium dose	0.43	*n.o.**	*n.o.**

* n.o. – not occurring; n.d. – not determined

** depending on field, position in field, and surrounding materials

3.4 Other ESR detectors

Besides alanine (section 3.2), and lithium formate (section 3.3) various other materials were irradiated in the thermal column of the TRIGA research reactor in order to investigate their possible role in the intended dosimeter set. Most of them were chosen because of their chemical relation to one of the two other substances. Phenylalanine was selected as a precursor for experiments with BPA (compare figure 1-2). Since the boron compound is analogue to amino acids, of which several are having favourably parameters in ESR dosimetry, the idea was to introduce BPA as boron containing ESR dosimeter. However, after phenylalanine was found to be insufficient, experiments with BPA were reduced to a minimum. In these limited tests no ESR response was found. Results are not included in this thesis.

Formate salts were chosen regarding the expected dose components. To introduce optionally the nitrogen proton dose or to reduce the response to photons only, the positive ion to the formate anion was exchanged. This series includes also calcium carbonate, representing a detector without any elements having neutron capture cross sections which are sufficient to generate a neutron dose component.

Equation (88) shows absorbed dose D as the sum of possible dose components $\mathrm{D_i}$ (γ – photon dose, N – fast neutron dose, P – proton dose) in the described compounds. Table 3-12 summarises dose components, as expected during neutron irradiation, for each material. Due to the similarity in nuclear interactions possible REs are expected constant, as in former experiments.

$$D_{abs} = D_{\gamma} + D_N + D_P \tag{88}$$

Table 3-12. Expected dose components in the examined detector materials as deposited during neutron irradiation

Material	**Photon dose**	**Fast neutron dose**	**Proton dose**
Phenylalanine	X	X	X
Ammonium formate	X	X	X
Calcium formate	X	X	
Calcium carbonate	X		

As mentioned in the introduction (compare section 1.5.3) these materials were already at least roughly examined in photon fields [Grün, 1989; Callens et al., 1998; Gancheva et al., 2006]. Especially regarding the formates extensive ESR studies were carried out [Vestad et al., 2003; Gustafsson et al., 2004]. Since such studies are going beyond the scope of this work, the results in these publications were only checked pointwise and adapted to the ESR machine used here. To reveal the ESR signal dependence towards microwave power and modulation amplitude for example Vestad and co-workers collected 480 ESR spectra for each material. As will be shown in the next section this has been impracticable during the present work. The characterisation of the ESR signals therefore was done only fragmentary and solely used to confirm earlier findings.

3.4.1 Material and methods of the characterisation in thermal neutron fields

Substances examined were phenylalanine, ammonium formate, calcium formate, and calcium carbonate. All compounds were obtained in analytical grade from Sigma Aldrich, St Louis, United States. The complete procedure of pellets manufacturing, irradiation and read-out was done on the campus of the University of Mainz or the University Medical Center. Due to this, transport could be limited to a minimum and pellets were used without any binder, such as paraffin wax, although pellets are more brittle this way. The shape of the pellets was chosen analogue to those in previous experiments: Cylindrical, with a height of 2.5 mm and a diameter of 5.0 mm. With an uncertainty of 5%, the pressed pellets of phenylalanine, ammonium formate, calcium formate, and calcium carbonate had weights of 60 mg, 74 mg, 99 mg, and 134 mg, respectively.

Pellets were read-out in the ESR laboratory of the May Planck Institute for Polymer Research, Mainz. Spectra were recorded as first derivative using a Mini Scope MS 200 ESR-spectrometer from Magnettech, Berlin, Germany. Due to the limited size of the sample cavity it was not possible to measure entire pellets. Therefore, materials were pestled after irradiation and only a fraction was inserted into a quartz tube, used as sample holder. Tubes were manufactured by the glassblower of the Institute of Nuclear Chemistry and had a length of 15 cm. Their outer diameter was 3.0 mm, with an inner diameter of 2.0 mm and a wall thickness of 0.5 mm. Tubes were open at both ends, but sealed with Critoseal® (VWR International, Randor, United States), a vinyl plastic compound, after the substance was inserted. Both, tube and sealing material, did not contribute to the ESR signal. Each tube was filled to a level of 1.0 cm, and exactly weighed.

Where not mentioned differently ESR parameters were chosen constantly during all measurements. Due to the machine heating, temperature in the sample cavity was 37 °C. The microwave power was 0.50 mW. Scan width and modulation amplitude were 4.0 mT and 0.3 mT, respectively. Sweep time for each scan was 60 s. With each sample 60 scans were conducted, after first half of scans samples were rotated by 180°. Although reproducibility of spectra was found to be sufficient, a Mn/MgO reference standard was used.

As mentioned above work on the characterisation of signals was limited. Due to the duration of the recording of single spectra a detailed analysis of optimal ESR parameters was found impracticable. In part parameter settings given in literature, for example those leading to highest intensities, or those close to microwave saturation, could not be used due to limitations of the ESR machine. Hence adaption in this work was difficult. However, comparison of signal intensities of the materials was made following the publications of Vestad and Gustafsson [Vestad et al., 2003; Gustafsson et al., 2004]. They investigated the ESR signal intensity as function of spectrometer parameters, mainly microwave power and modulation amplitude. For direct comparison they chose individual spectrometer settings for each material aiming to reach about 52% of the maximum signal intensity achievable. These intensities were then compared between materials at certain values of absorbed dose. The range of parameters they used could not be applied to the ESR machine used here. Validation of the optimal parameters they determined was hence possible only to a limited extent. However, during this limited validation their findings could not be refuted. Intensity comparison between materials was therefore conducted with the individual parameters given in table 3-13. In addition signal intensities after neutron and photon irradiation were compared for each material. Single samples of all materials were measured again at later times to investigate fading effects.

Table 3-13. Individual settings of microwave power and modulation amplitude (MA)), as used during comparison of signal intensities, and time between end of irradiation and start of spectrum recording.

Material	Power / mW	MA / mT	Time / h	Reference
Alanine	6.33	0.990	20	[Vestad et al., 2003]
Lithium formate	39.9	1.25	21	[Vestad et al., 2003]
Ammonium formate	15.8	0.7	23	[Gustafsson et al., 2004]
Calcium formate	15.9	0.990	22	[Vestad et al., 2003]
Calcium carbonate	50.0	1.6	24	[Borgonove et al., 2007]

During analysis of the spectra three quantities, peak-to-peak amplitude, line width (from maximum to minimum), and area under the peaks, were determined. For reliable analysis some spectra were fitted using polynomials. This was necessary especially with weak signals. Following the publication of Waldeland [Waldeland et al., 2010b] ninth order polynomials were used. In addition, correction was made for signal fading. Partially a massive effect was observed. To quantify intraday fading single samples were re-measured during a day. Combined uncertainty of read-out and manufacturing procedure was calculated to be around 8%. For doses below 10 Gy which are in afflicted to fading, uncertainties up to 20% have been calculated.

Calibration was made in the 6 MV photon field of a Siemens Oncor LINAC located in the Clinic and Policlinic for Radio Oncology and Radiotherapy at the University Medical Center Mainz. Ten detectors of each material have been irradiated with ten different photon dose values between 4.0 Gy and 68.4 Gy. Dose was deposited with a rate of 3 Gy/min with a dose plan including 20 segments using beam from 90° and 270°.

Neutron irradiations were again carried out in the thermal column of the TRIGA Mainz, using the 20×20 cm^2 channel. The channel was regularly equipped with the 5 cm bismuth shield at the reactor-near end. Analogue to before two setups were used, both placed inside the standard PE-box. In the cuboid shaped PMMA phantom ($10 \times 10 \times 23$ cm^3) and in the cylindrically shaped neutron shield ten respectively eight pellets were positioned on the central length axis. Phantom and shield are described in detail in section 3.2.1. Irradiations in both setups were carried out three times with each material. All irradiations were accompanied by gold foil measurements.

The Mini Scope MS 200 ESR machine has a lower sensitivity than the other spectrometers in this work. As a consequence the duration of all irradiations was enlarged. Experiments were conducted with the maximum power of 100 kW$_{th}$ for 60 minutes each, in PMMA as well as in boric acid. For the ESR signal intensity comparison two additional irradiations were carried out in each setup. In these experiments the ten sample positons were filled with two pellets of each material (excluding phenylalanine, but including alanine and lithium formate). Irradiation parameters were chosen identical.

Absorbed dose and dose composition have been calculated for each dosimeter and material using the Monte Carlo code FLUKA (2011-2b). Reactor model, default settings for hadron therapy “HADROTHE”, and “USRBIN” scoring were used as described before. Thereby “USRBIN” scoring cards were combined with “COMSCW” user-routines, depending on the actual detector material and the expected dose components. A model assigning RE weighting factors was not used, since such model was not available for the described compounds. Consequently MC calculations were limited to the determination of absorbed dose and its components. A summary of the expected components for each material was given in table 3-12. Absorbed dose is the sum of these components. Since at the TRIGA the fast neutron dose is negligible in Calcium formate and carbonate response and absorbed dose are expected to be equal. Dose components with relative fractions below 2% resulted in calculation uncertainties up to 10%, values in the LET spectra with similar relative size had uncertainties up to 16%. Statistical uncertainties afflicted to all other values were below 3%.

3.4.2 Results

3.4.2.1 Phenylalanine

In the dose range absorbed within the experiments no quantifiable ESR-spectra could be recorded. Very weak signals, only marginally different from the baseline have been observed after prolongation of irradiation time to six hours (instead of one hour). Comparison to spectra, as for example published by Gancheva and co-workers [Gancheva et al., 2006], however, could not confirm the radical species. Patterns of the spectra were overlaid by noise, so that it cannot be excluded that the signal might even originate from impurities, although the amnio acid was obtained in analytical grade. Therefore, in particular no correlation of peak area or peak-to-peak amplitude with the expected dose values could be revealed. Results remain similar also with longer recording times.

3.4.2.2 Formate Detectors

With the formates a linear dose dependence of the peak-to-peak-height has been observed in the calibration range. Different to the observation made with lithium formate, neither with ammonium formate nor with calcium formate line broadening was found in the spectra. However, as visible in figure 3-55, each formate shows a characteristic line shape, whereby the identical radical ($\mathrm{CO_2}^-$) is dominating according to literature [Vestad et al., 2003]. For comparison also the spectra of alanine, lithium formate, and calcium carbonate are shown in the figure. All spectra were recorded with the same spectrometer using the identical parameters, given in the previous section. For the figure spectra were scaled to the same amplitudes. Spectra of alanine and lithium formate were already presented earlier (compare figures 1-9 and 3-50). Among formate spectra calcium formate exhibits a narrower line shape and a characteristic doublet-like pattern. Similar pattern can be observed with the carbonate. The shape of the ammonium formate spectrum is comparable to the lithium formate, but exhibits a narrower pattern, too.

Signal intensities, which are normalised in figure 3-55, exhibit big differences between materials and were investigated in two ways. First differences between photon and neutron irradiation for an identical absorbed dose were examined. As stated above no change was observed in line width for any of the materials. However, ammonium formate showed a difference in signal intensity, and hence in peak-to-peak amplitude and area below spectra, between the irradiation in the PMMA phantom and the two other irradiations (calibration and boric acid neutron shied). Calcium formate shows no such difference.

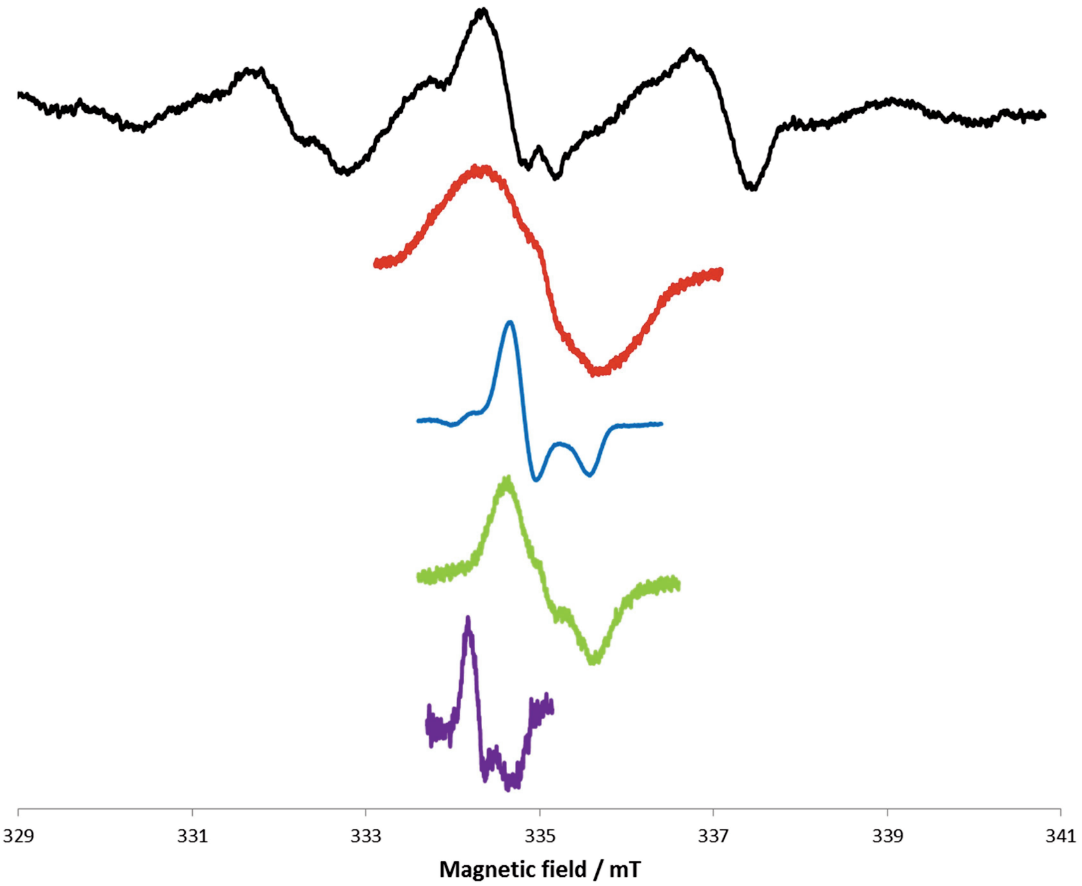

Figure 3-55. Comparison of ESR spectra of five different materials: Alanine (black), lithium formate (red), calcium formate (blue), ammonium formate (green), and calcium carbonate (purple). All spectra were recorded using identical parameters and were scaled to identical amplitudes.

Different to calcium formate ammonium formate response has a non-photon dose component. The concept of RE applies, and the change in intensity corresponds to the RE-value. Due to the lack of a specific ammonium formate model, RE-values were determined by matching measurement and calculated absorbed dose. Analogue to before such process had to start from the examination of dose components. Table 3-12 reveals that three components had to be considered. RE factors assigned to photon dose components are unity by definition. In consequence only the proton dose can be used for the modification. In addition the RE-factor is expected to be constant. And indeed applying a factor $\mathrm{RE_p}$ of 0.25 leads to an agreement, in which deviations between modified response and measurements add up to zero.

Further comparison of ESR signal intensities was made between materials. As stated in the previous section, this was done only roughly and consecutive to the more extensive work of other groups. The intensity differences found during this work are listed in table 3-14, together with literature values. Analogue to most publications intensities thereby are given relative to the alanine signal. In general the presented values are in adequate agreement with earlier findings. Bigger deviation can only be observed for ammonium formate, which is described to be more sensitive in literature.

Table 3-14. ESR signal intensities of formates relative to alanine

Material	This work	Literature	
	Relative intensity	Relative intensity	Reference
Alanine	1.0*	1.0*	-
Lithium formate	4.0 ± 0.4	5.5**	[Vestad et al., 2003]
Ammonium formate	1.5 ± 0.2	7.0	[Gustafsson et al., 2004]
Calcium formate	4.4 ± 0.5	4.4**	[Vestad et al., 2003]

* All intensities normalised to the alanine signal

**Value extracted from figures

In this context also signal fading is an important parameter. Signals of lithium formate and alanine are described to be constant over a long period. Measurements carried out in the ESR laboratory of the May Planck Institute confirmed these findings. In contrast ammonium formate and calcium formate showed significant signal fading, as illustrated in figure 3-56.Thereby no difference has been observed between neutron and photon irradiated pellets. Also neither the total dose nor the dose rate seems to exert influence on the amount of fading. The decrease is uniform among the analysed spectral quantities, and shown for the peak-to-peak amplitude in the figure. For both compounds the intensity of the initial spectrum, recorded one day after the irradiation, was taken for 100%. The signal of calcium formate drops about 9% on the first day after the initial measurement and decreases to about 20% in the next 100 days. The course of the intensity is similar for ammonium formate. Here decrease reaches nearly 30% on the first day after the initial measurement. After more than 100 days signal intensity is only about 17% of the first record. With recording times of one hour for each sample, series were measured over whole days. To account for the intraday fading single detectors were re-measured several times during such series and used to correct for the effect.

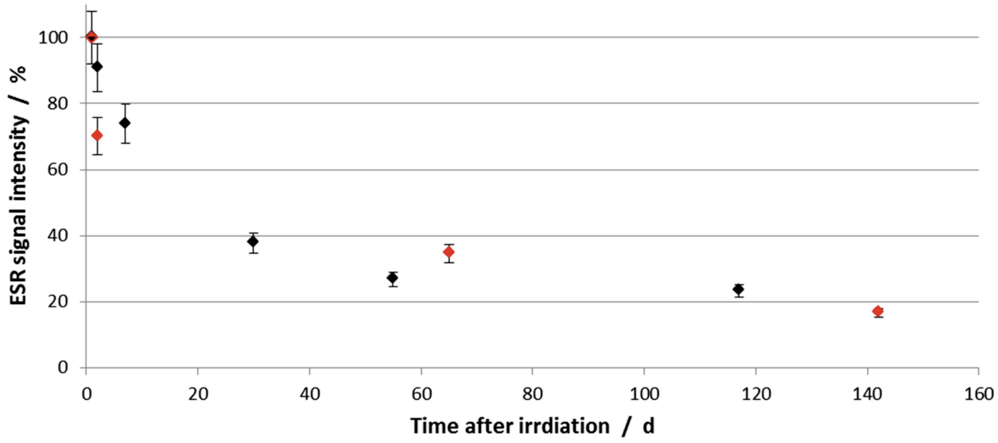

Figure 3-56. ESR signal intensity of calcium formate (black) and ammonium formate (red) as a function of time. Intensity of the initial spectrum (one day after the irradiation) for both compounds was set to 100%.

The manufacturing, read-out and correction procedure was carried out as planned during all experiments. Depth dose curves, measured for detectors irradiated inside the PMMA phantom are shown for both formates in figure 3-57. As before the measured response is indicated in black. Each data point represents the average of three detectors. For each detector the response has been determined and corrected individually as described and averaged afterwards. Compared to experiments described earlier, depth dose curves are more fluctuating. In the case of calcium formate, shown in part a), the highest response was measured for the third depth with a value of 1.68 ± 0.14 Gy/min. The lowest value of 0.84 ± 0.07 Gy/min was determined for the backmost dosimeter. A function, detector responses would follow, cannot be confidently recognised from the measured data. Also a build-up, as observed in epithermal fields, is not evident. Similar observations are made for ammonium formate, shown in part b), although highest response was measured for the first depth (1.50 ± 0.13 Gy/min). With 0.38 ± 0.03 Gy/min the lowest value was again determined in the rearmost position.

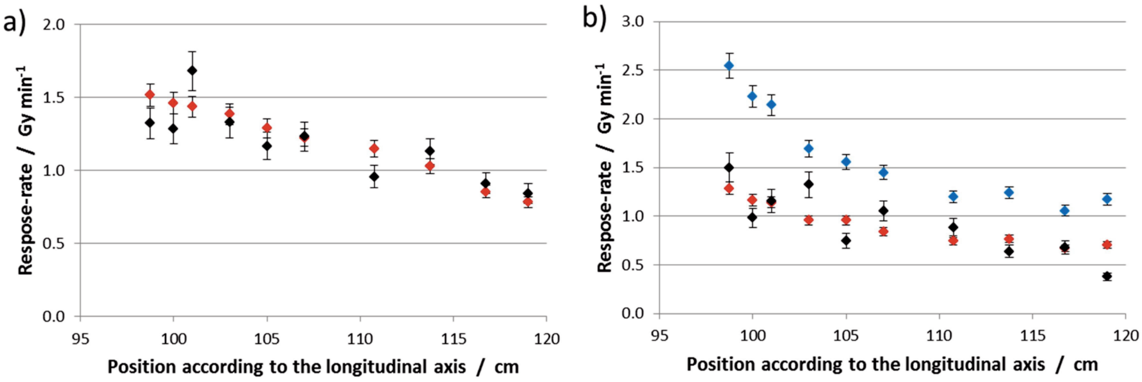

Figure 3-57. Depth dose curve in the PMMA phantom for a) calcium formate and b) ammonium formate: Measured response (black), calculated response (red) and calculated absorbed dose (blue). In the case of calcium formate response equals dose.

Among calculated results response is shown in red, absorbed dose in blue. As expected, in the case of calcium formate response and absorbed dose are equal, due to the described RE of one for photon doses. Calculated values are decreasing with depth form 1.51 ± 0.05 Gy/min to 0.78 ± 0.04 Gy/min. Decrease appears rather linear than exponential. However, accompanying calculations with enlarged range of depth revealed the expected exponential relation, but it decreases slowly. With the ammonium formate the exponential decrease is more obvious, especially in the blue curve. Here values decrease with depth from 2.55 ± 0.08 Gy/min to 1.17 ± 0.06 Gy/min. Transition from absorbed dose to response was different to before not done using a comscw user-file. It was calculated by simply weighting the dose components as described above. The proton RE was scaled in a way to achieve the best possible accordance, with an average deviation of zero. Calculated response decreases from 1.28 ± 0.07 Gy/min to 0.70 ± 0.06 Gy/min. The component RE leads to total RE increasing with depth from 0.50 to 0.64. With both detectors agreement between response and measurement is adequate. However, significance of the result for ammonium formate is limited to the agreement in the course of the curve, since values were scaled. Deviations range from 1% to 87%. Averaging the absolute values leads to a mean deviation of 16%. Corresponding values of calcium formate deviate between 20% and 1% with an average of 9%.

Calculated dose components are shown in figure 3-58. Again part a) represents values calculated for calcium formate, part b) values for ammonium formate. Primary photon dose plays a similar role in both detectors. On average primary photon dose makes about 40% of the total dose in the case of calcium formate. Thereby the relative values increases from 34% to 47%. In the case of ammonium formate, the mean value is 52% and increases from 27% to 47%. Analogue to earlier experiments the component decreases slowly with increasing depth. Secondary photon dose decrease exponentially, but also with a small negative slope. Only proton dose values, calculated for the ammonium formate, exhibit a steeper decrease. Their relative fraction declines from 32% to 19%.

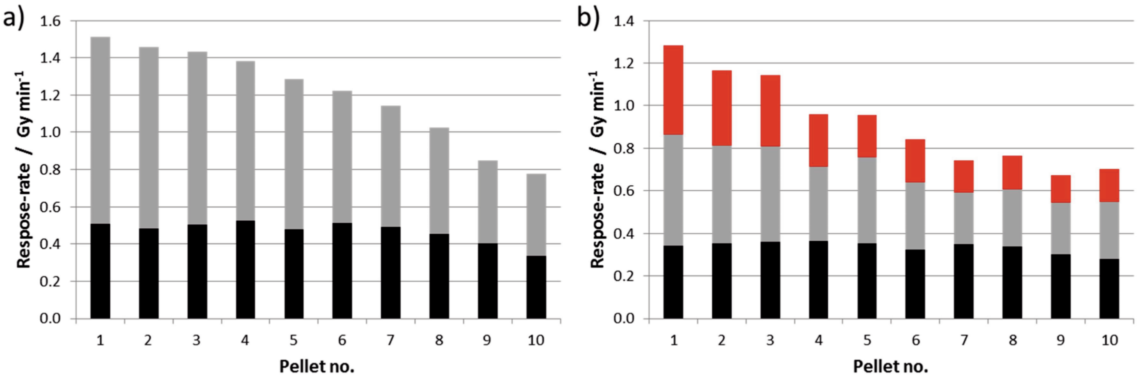

Figure 3-58. Components of absorbed dose in a) calcium formate and b) ammonium formate in the PMMA phantom: Primary photon dose (black), secondary photon dose (grey), proton dose (red).

Analogue figures for experiments conducted inside the boric acid neutron shield are shown in figures 3-59 and 3-60. Again parts a) display data for calcium formate, parts b) data for ammonium formate. Measured response is repeatedly plotted in black. For calcium formate it decreases from 0.84 ± 0.07 Gy/min to

0.66 ± 0.05 Gy/min. In the case of ammonium formate fluctuations are bigger and no decrease can be observed. Values vary between 0.51 ± 0.06 Gy/min and 0.68 ± 0.08 Gy/min.

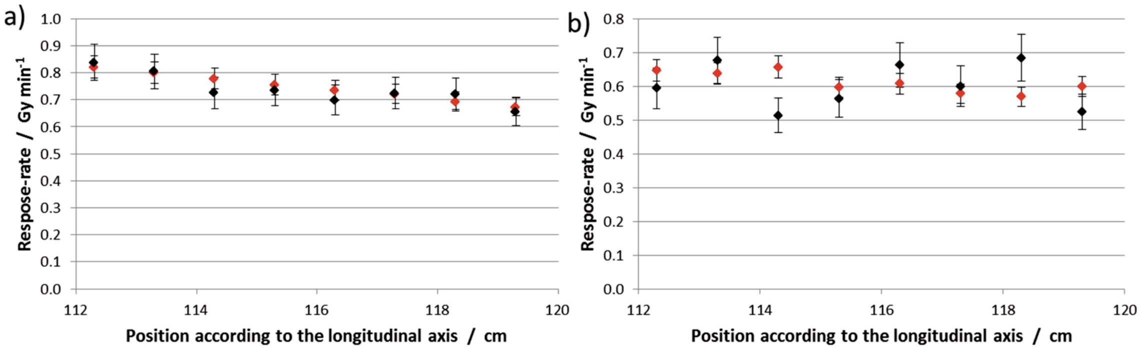

Figure 3-59. Depth dose curve in the boric acid neutron shield for a) calcium formate and b) ammonium formate: Measured response (black), calculated response (red). In both cases response and absorbed dose equal.

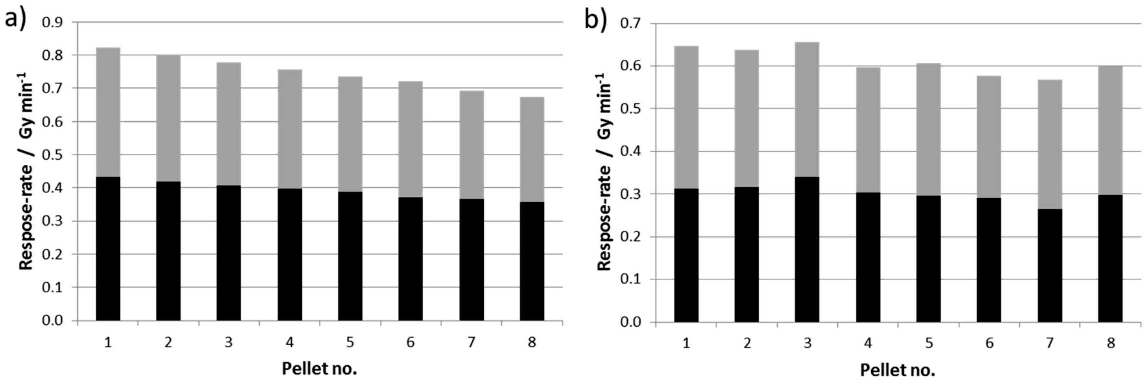

Figure 3-60. Components of absorbed dose in a) calcium formate and b) ammonium formate in the boric acid neutron shield: Primary photon dose (black), secondary photon dose (grey), proton dose (red).

As obvious from figure 3-60 no other than photon doses contribute to the response. In agreement with the expectations, hence, in figure 3-59 the calculated response shown in red is equal to the absorbed dose. For calcium formate good agreement has been achieved. Deviations range from less than 1% to 7%, with a mean value of 3%. The calculated response closely follows the measured response. In contrast deviations of ammonium formate are bigger. Values between 4% and 28% were observed, leading to a mean deviation of 12%.

Dose components were mentioned before and are shown in detail in figure 3-60. In both detector materials only two components are present. The proton dose, observed for ammonium formate in the PMMA phantom, is fully suppressed. For both materials the course of primary photon dose is quantitatively similar as in the PMMA phantom. Absolute values of the secondary photon dose are lowered, but still decreasing exponentially.

3.4.2.3 Calcium carbonate

The calcium carbonate ESR line shape was presented in figure 3-55. Similar as calcium formate, it exhibits a doublet-like pattern although the line is narrower. Comparing spectra recorded after neutron and photon irradiation neither line broadening nor change in intensity per unit of absorbed dose has been observed. In literature the $\mathrm{CO_2}^-$-radical is identified as dominant species [Jacobs et al., 1989], even though other radical species might be generated as mentioned in subsection 1.5.3 in the introduction. As likely from the noise in figure 3-55, signal intensity is low. Relative to the alanine signal an intensity of 0.51 ± 0.06 was determined in this work. From the work of Borgonove et al. [Borgonove et al., 2007] a value of 0.43 ± 0.05 can be extracted, although the authors refrain from this comparison. No significant signal fading was observed during the first 100 days.

The depth dose curve, plotted in figure 3-61 for the experiment in the PMMA phantom, exhibits a more explicit exponential decrease than the formates in the previous subsection. The measured black dots decrease from 1.49 ± 0.15 Gy/min to 0.91 ± 0.09 Gy/min. Calculated results again shown in red are in good agreement. Values drop from 1.52 ± 0.07 Gy/min to 0.78 ± 0.04 Gy/min. The largest deviation can be observed at a depth of 110.75 cm with 16%, on average both series differ by 6.4%.

Figure 3-62 shows the corresponding dose composition. Response is dominated by the secondary photons, and as expected primary photon dose is the only other contributor. The relative fraction of the primary photon dose increases with depth from 25% to 35%, due to the slower absolute decrease with depth. Since in both cases RE is unity, response is equal to absorbed dose.

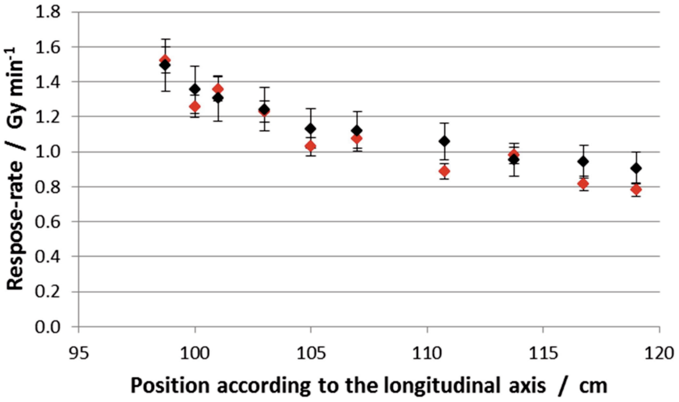

Figure 3-61. Depth dose curve in the PMMA phantom for calcium carbonate: Measured response (black), calculated response/absorbed dose (red).

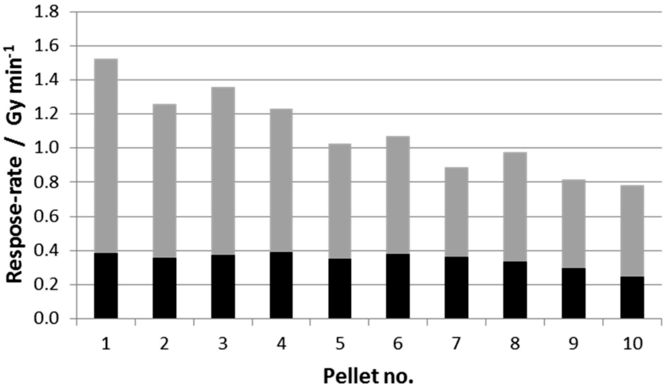

Figure 3-62. Components of absorbed dose in calcium carbonate in the PMMA phantom: Primary photon dose (black), secondary photon dose (grey).

Inside the boric acid neutron shield similar observations have been made. The depth dose curve in figure 3-63 shows a decrease in measured values from 0.70 ± 0.07 Gy/min to 0.49 ± 0.6 Gy/min at the most backward point. However, after the first half of the curve values seem to reach a plateau, visible slightly above 0.5 Gy/min. In contrast calculated data shows a continuous decrease (0.64 ± 0.03 Gy/min to 0.58 ± 0.03 Gy/min). Curve is considerably flatter and seems on the one hand to overestimate the measured values and not to reproduce the initial decrease on the other hand.

Inspection of the dose composition, given in figure 3-64, reveals that the primary photon dose remains on the level also observed in the PMMA phantom experiment. The secondary photon dose though is again reduced. Primary photon dose has an almost constant relative fraction of 55% of the total dose.

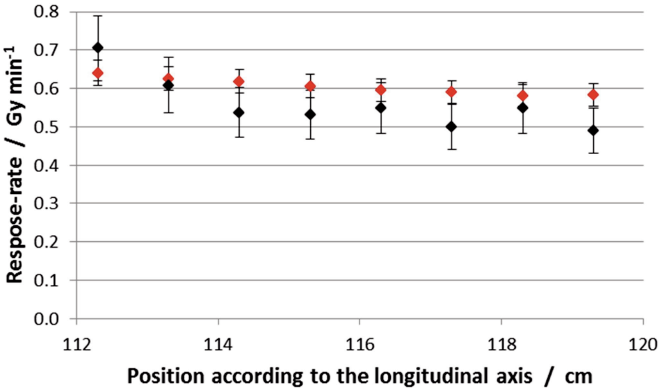

Figure 3-63. Depth dose curve in the boric acid neutron shield for calcium carbonate: Measured response (black), calculated response/absorbed dose (red).

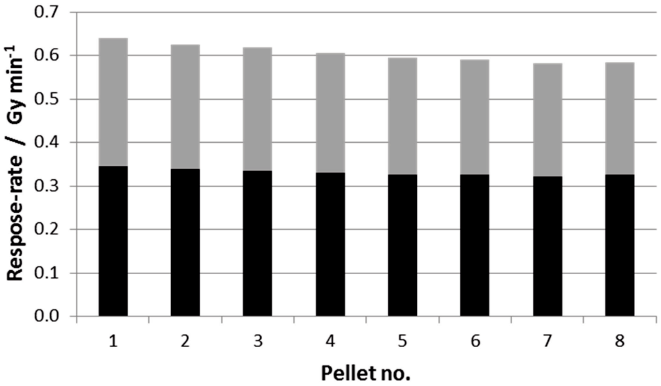

Figure 3-64. Components of absorbed dose in calcium carbonate in the boric acid neutron shield: Primary photon dose (black), secondary photon dose (grey).

4. Discussion

4.1 The TRIGA Mainz model

Due to its detailed input the model developed by Ziegner et al [Ziegner et al., 2014] is the most sophisticated model available for the TRIGA research reactor in Mainz. The evaluation carried out as part of this work showed that it enables precise predictions regarding particles fluxes and dosimetry. In this chapter the results of the activation foil measurements, described in section 3.1.4, are discussed. Discussion of the dosimetric evaluation, carried out with the alanine detector, can be found in the next chapter. However, due to its great relevance for the complete work, first the experiment preconditions for activation foil measurements are addressed.

4.1.1 Experiment preconditions

To determine absolute neutron flux or neutron fluence values, a precise determination of the metal foil activation is required. In this context the detector efficiency is an important parameter with great influence on the resulting value. Geometry and distribution of activity are relevant as well as the environment of the activity. The regular calibration standard at the TRIGA Mainz is QCY48 solution, provided by PTB. Routinely 500 µL of it are used in a capillary tube. In this case activity is distributed in a three dimensional cylinder and aqueous environment. In contrast in foils the activity can be considered as homogeneously distributed in a more or less two dimensional plane. Another difference arises from the PMMA holder. Between foil and detector window is merely air. Looking on figure 3-7 it can be seen that the emitted gammas in case of the 500 µL standard in addition besides air also have to pass through PMMA. Due to these differences the 500 µL standard is unsuitable when calibrating the detector for activation foils. As an alternative calibration foils were prepared by evaporation of QCY standard. Figure 3-11 compares both types of calibration standards at a certain energy as a function of distance to the detector window, behind which the detector crystal is located. The small deviation between the three foils prepared indicates the little influence of statistical processes during the evaporation procedure. As expected the difference between both types is decreasing as the distance towards the detector increases and geometry is losing its relevance. One possible problem is the loss of activity during the evaporation. In this case the amount of radioactivity would have been overestimated and therefore the efficiency would be underestimated. But since efficiency is equal from a certain distance onwards it is ensured that the correct amount of radioisotopes has been taken into account and no relevant fraction was lost.

Differences in figure 3-11 between the curves are visible for small distances. In case of the liquid standard, more dense material is between standard and detector, hence gamma-rays are more scattered and efficiency is lower. At bigger distances the few millimetre of the PMMA layer, which need to be passed, are of smaller relevance. In addition at higher distance both standards appear to be point-shaped towards the detector.

In general, a higher efficiency is preferred to reduce measurement times, but on the other hand the influence of geometry increases. Even between the calibration foil and activated metal foils differences are present, for example due to inexact positioning on the PMMA element or due to the distribution of activity on the calibration foil after evaporation. During the process radioisotopes tend to be collected in the outer ring of the pipetted drop. At small differences in addition in the spectra summation effects would have to be taken into account. For measurements in this work therefore as a compromise a position 7 cm in front of the detection window has been chosen.

A second parameter important when measuring absolute fluxes is the self-absorption. This effect has been investigated in the pile experiment; results are shown in figures 3-12 and 3-13. In case of a strong self-absorption a foil behind another foil should observe a reasonable lower neutron flux. As can be seen in figure 3-13 this is the case for most foils but the effect is small. Averaging the relative value for every first, second, third foil and including the single fourth foil leads to figure 4-1. Due decreasing number of foils in the third and especially fourth position the uncertainty increases, but however the decrease in relative neutron flux is evident. Averaging over all steps between foils located behind each other leads to a decrease in flux of 1.4 ± 0.6 %.

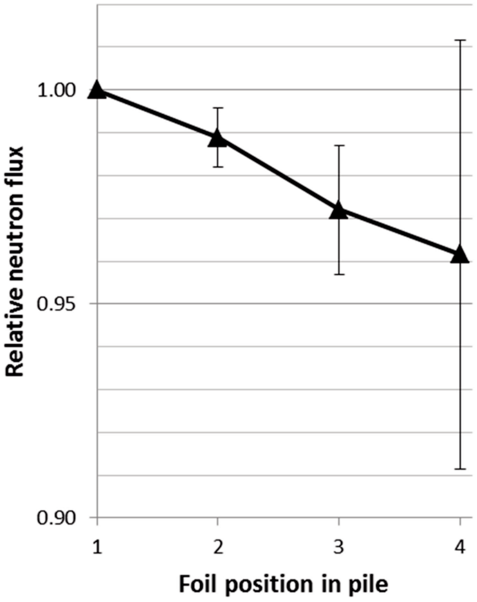

Figure 4-1. Relative thermal neutron equivalent flux as a function of position averaged over all piles

The self-absorption was neglected in any further experiment. Since foils are positioned behind each other and flux is decreasing with distance to the reactor core, the change in the figure partially originates from there. Calculations with FLUKA showed that in air the flux drops on the space occupied by two foils and their packing (tape and label) in the same positon by 0.36%. Following about 1% of neutron flux is lost in the foil behind due to the fore foil. Extrapolation shows that the self-shielding within in each foil leads to decrease in the observed flux of 0.5 ± 0.3 %. Compared to the relevance of the positioning, as well relative to the core as lateral (compare figure 3-12), the effect of self-absorption is negligible. Alternative, theoretical determination methods, using formulas assuming a unidirectional homogenous field of thermal neutrons, lead to comparable results, but seem to be less reliable due to the rather complex field in the thermal column. Another argument for the negligibility is the observed difference between measurements and calculations for example in figure 3-14. If the effect would be perceivable, a systematic shift should be observed between measurement and calculation, but only statistical fluctuation is recognised.

4.1.2 Neutron field characterisation

With the knowledge of basic tests and characterisations the evaluation of the TRIGA model was carried out. Regarding neutrons it was done with respect to the flux distribution throughout the modelled geometry, and the energy spectrum in two setups.

4.1.2.1 Neutron flux distribution

Measurements and calculations regarding the flux distribution have been compared in three experimental setups. The biggest extent was reached with the free in air experiment in the central 10 × 10 cm^2 channel, where a range of more than 1 m has been examined. As expected, the flux decreases exponentially and therefore appears linear in the logarithmic plot. Over the whole distance the flux drops by almost two orders of magnitude, as visible in figure 3-14, and in good agreement with modelled values over the complete range. Inside the reactor near front as well as in the back in addition no trend was observed in the differences. Hence the model is valid over the whole length axis, without decline of exactness towards the borders.

As the phantom experiments suggest, the model is also valid alongside the central length axis in the 20 × 20 cm^2 channel. Things are, in addition, more complicated in these experiments, since more materials with different elemental compositions and densities had to be recognised. However, between the measured and calculated values again good agreement was achieved (figure 3-16). Compared to the free in air experiment along the central axis of the phantom exponential decrease in flux can only be found on the first two thirds. In the last third, the curve flattens, reaches a minimum and slightly increases towards the back of the phantom. The result appears as a consequence of the isotropy of the neutron field in the thermal column and the raised macroscopic cross section of the phantom compared to most of the surroundings. Due to omnipresent scattering, noticeable fractions of the flux are not unidirectional from the front, but also from other angles, even from the opposite direction. Such considerations are also supported by the second phantom experiment. In a unidirectional beam a foil rotated by 90° should by less activated. As can be seen in figure 3-17 this is not the case. Compared to the values in figure 3-16 at corresponding depths almost identical fluxes where observed. Furthermore figure 3-17 illustrates the asymmetry in the 20 × 20 cm^2 channel, since on the left side fluxes are higher. When combining figures 3-16 and 3-17 the minimum of the neutron flux seems to be near the central length axis in a depth of about 18 cm. This is confirmed by FLUKA simulations and demonstrates that the phantom is penetrated by neutrons from all sides, although the strength is not uniform from all directions. In FLUKA the angular distribution of the flux can be investigated using USRBDX cards. Simulations with USRBDX cards have been carried out for the gold foil positions in the experiment shown in figure 3-17. At the position of the gold foils planes where inserted and neutrons where counted, which were passing them from either side. At the centrum of the forefront of the phantom the ratio between neutrons going into the phantom and those leaving the phantom is 1.06 ± 0.05. Hence the amount of neutrons in either direction is almost equal. The value for the central position in the back of the phantom is similar (1.04 ± 0.05). In the three positions on the left side with an average of 13% (1.18 ± 0.05) more neutrons are entering the phantom than leaving it, on the other side this value is reduced to 7% (1.07 ± 0.05).

4.1.2.2 Neutron spectrometry

Besides the neutron flux distribution, also the neutron spectra in the thermal column have been investigated. Measurements carried out inside the thermal column were compared to measurements made in the PTS, located in the periphery of the reactor core, to experiments described in literature [Protti et al., 2012], and to data modelled with the FLUKA code.

A typical neutron spectrum, as represented by the source spectrum for the thermal column in the TRIGA model, is given in figure 4-2. Different to previous figures, in this work the spectrum is not given in neutrons per energy bin, but neutrons per MeV. However, the spectrum in the figure is identical with the spectra shown in figure 3-5. It can be divided in three sections: Neutrons are released during fission with energies in the MeV region. In the figure the green line represents a possible fission spectrum. Obviously most of these fission neutrons are already moderated when reaching the location of the source plane, because the black dots are just poorly following the green line. In collisions with moderating elements (at the TRIGA mainly the zirconium hydride, water and graphite) the fission neutrons are slowed down. A result is the epithermal $1/E$-region, shown in blue. The thermal region (red line) is described by a Maxwell-Boltzmann distribution around the temperature of 293.6 K, corresponding to a neutron energy of 0.025 eV.

The relation of these three regions can be revealed by spectral indices. For the indices in figure 3-18 each resonance activation rate is divided by the thermal activation rate of gold. All resonance energies are part of the $1/E$-region, as visible in figure 4-2, where energies of the first resonance in the corresponding cross section of each element is indicated in orange. Accordingly, such indices illustrate the proportion of thermal and epithermal region. In the phantom density of moderating atoms around the foils was highest, hence the values for the corresponding indices are lowest. With foils irradiated free in air less moderation occurs and the index values are rising. The same effect was observed when reducing the distance to the centre of the core, by using the PTS. Neutrons travelled through less moderating material to reach the activation foils. As a consequence, the fraction of already thermalized neutrons is smaller. Another consequence is the decrease in values with increasing resonance energy, as also visible in figure 3-18.

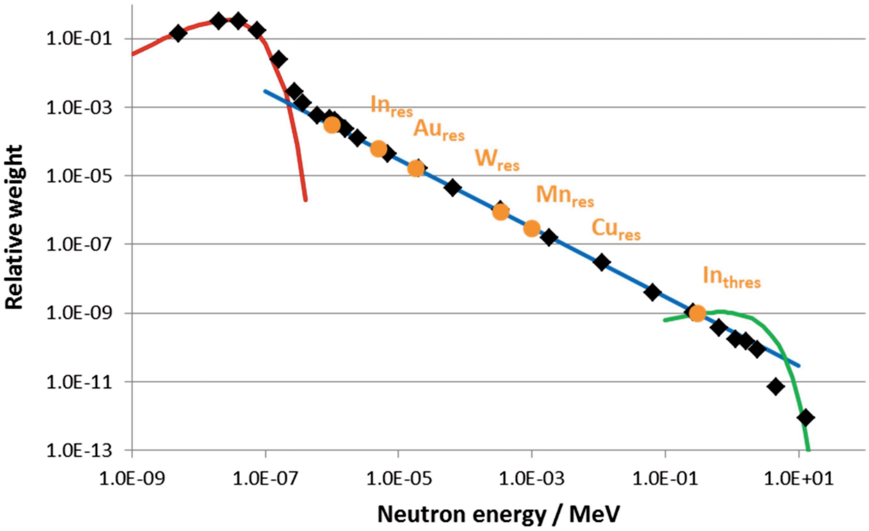

Figure 4-2. Illustration of the composition of a thermal neutron spectrum (black dots; represented by the thermal column source spectrum, derived from the TRIGA model), out of a thermal region (red line), an epithermal region (blue line) and a fast region (green line). In Addition energies of the first resonance in cross sections, respectively threshold energy for the indium-115 reaction, of the activation foil elements are given (orange). Values of the spectrum are given in neutrons per MeV.

The (n,n')-reaction of indium has a threshold located in the fission area. For the PTS index of the corresponding activation rate increase compared to the thermal column values is bigger than for the other indices. It therefore indicates that the fraction of fission neutrons is notable in the PTS. This could be expected, since the PTS is located in the outer ring of the reactor core with fuel elements only centimetres away. In contrast, as indicated by the source spectrum in figure 4-2, in the thermal column moderation occurs more prominently. Also, spectra in figures 3-20 and 3-21 suggest that only a minor fraction of neutrons is present in energy range of fission. Indeed, the corresponding indices in figure 3-18 a) are the lowest, of those determined. Cadmium ratios, defined reversely, are shown in figure 3-19. Consequently a reverse trend can be seen. The value is highest in the thermal column with the moderating phantom, while it is substantially decreased in the PTS.

All facilities compared in part b) of figure 3-18 have in common that their neutron spectra are predominately thermal. The LENA reactor in Pavia, Italy, is also a TRIGA Mark II and values presented in figures 3-18 and 3-19 are as well collected in a thermal column. Although the reactor has a maximum power of 250 kW_{th} and the column has been modified differently, the values of the indices are very similar to those determined for the TRIGA Mainz, especially those of the phantom experiment. Also the values of MURR are similar. Only the RA3 has substantially lower values.

In the SAND II algorithm, the measured data series for the thermal column were matched with the modeled data in form of input spectra. The algorithm regularly adjusts such spectra in iterations. However, the input spectra, derived from the model using the FLUKA code, were found to be sufficient solutions of the measured foil activations (figure 3-21 and 3-22). Therefore, besides the neutron distribution the model is also able to correctly predict neutron energy spectra, and can be therefore seen as validated regarding its neutron part.

4.1.2.3 Online neutron monitoring

Another issue is described in section 3.1.4. Activation foils are helpful tools regarding the determination of neutron fluence, flux, and spectrum. However, when using such foils for quality assurance during regular experiments, fluence cannot be adjusted according their properties and high activation may be the result. In order to perform reliable measurements, with reasonable dead times of the gamma detector, a decay of several half-life periods may has to be awaited. In the case of gold with half-life of almost three days, this waiting time can easily reach some weeks. Therefore, in most cases alternative detectors are used for neutron monitoring. As an example in this work a pin diode, augmented with a conversion foil, has been tested in the field of the TRIGA.

The presented build-up in the low-flux end of the thermal column was selected due to several advantages. In the position the cable between detector and preamplifier is shortest, providing narrow peaks and low background. The detector itself was chosen relatively small (≈1 mm^2). Combined with the aluminium foil, covered with the 42 $\mu g/cm^2$ lithium fluoride, the detector could be operated at all reactor powers between 1 kW_{th} and 100 kW_{th}. The correlation of the detector output with the neutron flux is linear for all powers, as obvious from figures 3-25 to 3-28. These advantages also compensate the arising difficulty, which is also apparent in figures 3-26 to 3-28. Due to the small distance to the boral liner, the isotropy of the neutron field is disturbed. A shift of 3.0 cm, as done during a single irradiation, significantly changes the correlation of detector counts and flux. Hence high accuracy in positioning has to be assured for comparable results. However, with a holder, different from the phantom used here, this should be simple to realise. This way the detector would be also easy to remove, since it requires no permanent installation. Since also in long-term irradiations the signal was stable, the pin-diode detector is a simple and reliable instrument for online monitoring, especially suitable for the thermal column due to its size and flexibility.

For application in a certain experiment positions of interest will have to be calibrated against the detector position in pre-tests first. However since the correlation is linear for all powers, calibration can be performed with low fluence, providing easy activation foil read-out, even if the later experiment requires a high fluence. A further simplification can be made concerning the electronic components. The multi channel analyser delivers a spectrum (compare figure 3-24), containing unnecessary information, and requires evaluation afterwards. For mere flux monitoring a single channel analyser, with a window adjusted on the tritium peak, directly delivering a count rate, might be more expedient. This way the desired count rate, necessary for flux correlation, would be preserved instantly. Maybe with some software modifications, also the neutron flux would be directly accessible.

4.2 ESR detectors in neutron fields

Within this thesis the alanine detector is the dosimeter which was investigated most detailed. Ongoing from these results various other detectors were examined. Therefore, the first section in this chapter is dedicated to the alanine detector, further detectors, also the alanine-gadolinium dosimeters are discussed in the following section 4.2.2. Parts of especially the alanine discussion are already published [Schmitz et al. 2014].

Based on the knowledge gained, the possibilities of the detectors towards a detector set, as intended in the motivation, are discussed in the next chapter (4.3).

4.2.1 The alanine detector

The results of the alanine detector enable a detailed analysis of the alanine response in thermal and epithermal neutron fields. Experiments were pursuing two central objectives. Both were in parts connected and coped with together. Although previous work [Schmitz, 2010] proofed the general applicability of the alanine detector in mixed neutron and photon fields, it was a central issue to fully understand the response behaviour in the present work. In the same step, the TRIGA Mainz model (developed by Ziegner et al [Ziegner et al., 2014]) was examined regarding dose predictions. In the previous chapter the model was already found to be valid regarding neutron field calculations. However, calculations of energy deposition include also photon transport and, hence, testing is more comprehensive.

In general results, given in section 3.2.3, show good agreement between the measured ESR response and the calculated dose response in all experiments. As obvious with the comparison study, the model stays valid also when the pellet composition changes. Besides the question about the general applicability of calculations including the Hansen and Olsen model, it also had to be shown that the FLUKA code is capable of advanced neutron simulations. As stated before

FLUKA is a high energy physics code, in which routines regarding thermal neutron transport were added subsequently. In this work therefore central calculations were accompanied by calculations with MCNP, a routinely used code in neutron transport. FLUKA and MCNP led to comparable results regarding absorbed dose and dose components. Due to the fact that the FLUKA weighting factors have been applied in MCNP calculations, the agreement in dose response is similar. Especially the experiments in epithermal fields proofed that FLUKA is capable of complex source definitions, although it appears to be limited to either simple geometries. It might be possible to model complex source structures, as for instance reactor cores, but only with extensive effort. Furthermore it remains unclear if the FLUKA neutron transport is sufficient for such problems. Within this work limitations occurred for instance with the calculations for the gadolinium-alanine. Details are given in the corresponding subsection 4.2.2.1. Also differences observed between the codes are commented along with the specific experiments.

4.2.1.1 Relative Effectiveness (RE)

The total RE of the pellets varies between 0.69 and unity as a function of the dose composition and the single component REs.

RE_γ was set to unity. Not using a special RE for low energy photons has been experimentally confirmed with the results at TRIGA in boric acid. All dose has been deposited by photons in similar energy range as in the other experiments. The measured response was found to be equal to the unweighted (i.e. RE = 1) absorbed dose from the MC calculations. Possible deviations, as described in subsection 1.5.2.2 of the introduction, would have not been revealed due to the connected uncertainties, but seem to be negligible in this context.

RE_p and RE_n are both a function of proton energy. The nitrogen protons are emitted with a definite energy and have a short range. Therefore RE_p is constant. The value has been found in all experiments and is consistent with all results at TRIGA, where no other RE smaller than unity had to be taken into account. The value seems to be also independent form the actual pellet composition, since it was also found for the detectors in the comparison study. RE_n was not found to be constant. As described in chapter 1.7 the recoiling proton energy is a function of the incident neutron energy. Due to moderation neutron energies decrease and so do the resulting proton energies. As described in the publication of Bassler [Bassler et al., 2008] in the discussed proton energy range RE decreases with decreasing energy. This can be observed in the values shown in figure 3-49. $\mathrm{RE_n}$ is decreasing with phantom depth in both cases, although the decrease may be not significant for THOR in part b), as a result of the relatively high uncertainties.

4.2.1.2 Thermal neutron fields

Thermal neutrons fields, as present in the thermal column of TRIGA, have no fast neutron fraction and lead to a response only consisting of two dose components: photon and proton dose.

Photons have a long range and they are only shielded by heavy elements, as seen with the lead and bismuth shielding. Their propagation is almost undisturbed by light elements as constituents of the phantoms. The primary photon dose generated outside the simulated geometry stays at a constant level in tissue and only slowly decreases in PMMA, Teflon and boric acid. The decrease is very slow and a function of distance to the core. Slight differences can be explained by variations in the lateral position. Only the photon shield, containing heavy elements, leads to the expected decrease in primary photon dose.

The secondary photon dose is in addition a function of the element species and density present in the experiment. The carbon of the graphite in the thermal column has thermal neutron capture cross sections for (n,γ)-reactions of 3.9×10^{-3} b. Only the large amount of more than two tons of graphite leads to a contribution which becomes relevant when other elements are absent as for example in the Teflon or photon shield experiment. This also confirms earlier findings [Blaickner et al., 2012]. In Teflon an additional contribution is generated by the fluorine. Fluorine and carbon contributions become both less important if hydrogen is present as in the three other experiments. Therefore the secondary photon dose is low in Teflon and the photon shielding and similarly high in PMMA, tissue and the boric acid neutron shield. In these cases the secondary photon dose is mainly a function of the hydrogen present. In the boric acid, the 478 keV photons from excited lithium, resulting from the 94% boron neutron capture, play a similar role. Due to the lower hydrogen content (5 % weight fraction compared to 8 % weight fraction in PMMA) the dose rate nevertheless stays similar.

As mentioned before the protons of the nitrogen interaction are of very short range. The nitrogen concentration outside the pellet is therefore of no interest for the dose inside the pellet. The nitrogen dose only depends on the thermal neutron fluence-rate in the pellet. Due to this the proton dose is a function of distance to the core. Only when the propagation is disturbed by absorbing materials, such as boric acid, the dose component changes significantly. These considerations are confirmed by the linear correlation of measured neutron fluxes in figure 3-35 and proton response components in figure 3-37, shown in figure 4-3. The neutron fluxes had to be estimated from the gold activation foil data by exponential fitting, to gain values regarding the flux inside the pellets. As indicated by figure 3-16 this is not totally correct and might explain deviations from linear behaviour obvious in figure 4-3. Furthermore, some of the pellets differed in lateral position from the axis of gold foils. This is the case especially in the experiment with liver tissue and can lead to significant over- respectively underestimation as suggested by figure 3-17. However the linear trend is obvious. Besides the neutron flux a second parameter has an influence on the proton response rate. It becomes obvious from the comparison study and figure 3-40. With the change in pellet composition, density, and fraction of binder, the amount of nitrogen atoms varies, and hence also the number of reactions and amount of energy deposited changes.

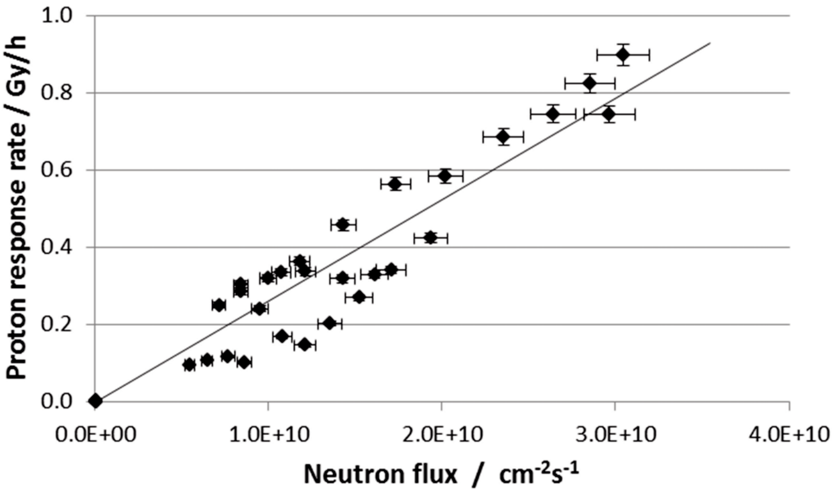

Figure 4-3. Proton response rate as a function of neutron flux in the pellet. Response as calculated, flux values were estimated from gold foils accompanying the alanine irradiations.

4.2.1.3 Epithermal neutron fields

As indicated earlier, most neutron interactions resulting in dose depositions occur at thermal energies. Fast or epithermal neutrons have to be moderated to become energies before the interactions become relevant. This can be easily seen with the free in air results at FiR 1 and THOR. Moderation happens with light elements and as a function of density. In air neutrons are less moderated and therefore the thermal neutron interactions are fewer. Photon and proton doses are reduced while dose resulting from fast neutrons is higher than for any measured position in phantom. Overall the total dose is lower in air.

Similar observations can be made in phantom. Due to moderation, the relative fraction of thermal neutrons increases with phantom depth. At the same time the absolute value of the neutron flux decreases. These opposing trends result in the observed build-up in secondary photon and proton response shown in figures 3-44 and 3-46. Also due to moderation the fast neutron fraction decreases with phantom depth and so does the fast neutron response.

At TRIGA no build-up has been observed. Although distances are bigger compared to the other facilities, calculations show that at no point in the thermal column neutron moderation compensates for the decrease in neutron flux in such a way that a build-up would occur. This can be explained by the fact that the neutrons entering the thermal column are already thermalized.

In general the dose composition is very different from the one observed in the PMMA experiment at TRIGA. Both facilities FiR 1 and THOR fulfil the requirements of the IAEA Tecdoc 1223 [IAEA Tecdoc 1223, 2001] for BNCT treatment facilities regarding fast neutron or photon contamination. In comparison to TRIGA primary photon dose fraction is much lower. The absolute doses are lower also because of the lower neutron fluence-rates (see table 3-10). But due to the similar element compositions in the experiments the relative size of secondary photon and proton dose is comparable.

Differences between measured and calculated results, but also between FLUKA and MCNP, are especially observed in figures 3-44 b) and 3-46, both showing the same data. These deviations are a result of different source definitions. The sophisticated MCNP model leads to a better agreement than the FLUKA plane source. The high complexity of the source designed for MCNP, limits the transferability into a FLUKA source routine.

4.2.2 Other detector materials

As explained within the Motivation (chapter 2) a combination of detectors with varying particle sensitivities would be fortunate for field characterisation. In similar manner different activation foil materials were combined for neutron spectrometry. Experience in handling and modelling of the alanine detector in neutron fields and knowledge about other detectors gained in literature were the basis for the selection of materials. Those finally used are discussed in the next three subsections. The first subsection is dedicated to the alanine detector doped with gadolinium; also lithium formate has an own subsection, since it exhibited special characteristics which were augmented by extended modelling. Further compounds are collected in the final subsection. There also further attempts towards a boron containing dosimeter are described.

4.2.2.1 Alanine doped with gadolinium

The aim of the work carried out in cooperation with M. Marrale from the University of Palermo, Italy, was the investigation of dosimeters with higher neutron to photon sensitivity ratio. As mentioned before, gadolinium was found superior to boron to serve as dopant, since emitted particles are of longer range. The gadolinium is added as the oxide in the form of nanoparticles with diameters between 30 µm to 70µm, with a mean value of 50 µm. However, the modelling succeeded only partially. A lack in detailed understanding remains.

Two detector types, alanine pellets containing gadolinium and pellets without the additional element, were compared in two experimental setups, inside a PMMA phantom and boric acid neutron shielding. Different to before no depth dose curve was recorded, but response as a function of neutron fluence. Linear increase in response was observed in all experiments. Since dose rate effects are not known for alanine, the observed linearity in figure 3-42 is similar to the one shown in figure 1-12 in the introduction. Also with the additive, radicals are still detected only from the alanine. Therefore a change in the linearity would have been surprising.

In case of the alanine the response could be reproduced by modelling, and confirmed earlier findings. Although besides the used materials and the facility the experimental setup was entirely different, analogies with experiments described before are obvious. In PMMA again three response components are separated, while in the boric acid the proton dose is reduced to a negligible value. Comparing to the PMMA phantom in the boric acid neutron shield response rate is expectable reduced.

The trend is comparable in experiments conducted with the gadolinium containing detector. Towards gadolinium free detectors though, values are increased in both setups. The addition of gadolinium oxide significantly improves the sensitivity, especially in the PMMA experiment, as visible in figure 3-42. The factor, with which the response is increasing, is almost three times bigger in the PMMA experiment than inside boric acid shielding. Anyhow, increase is not limited to neutrons in the first place. Gadolinium is also known as radioenhancer in photon radiotherapy. High Z elements have the ability to interact with photons, finally resulting in emission of Auger or internal conversion electrons. The energy deposition though is higher with the neutron interactions, due to the enormous capture cross section. Indeed simulations with the FLUKA code have shown increase in neutron, but also photon response components, as shown in figure 3-43. The increase leads to an overestimation explainable by the simplified model of the detector that was used for the simulations. The necessity for these simplifications was explained earlier. Most important is the fact that the Q energy of the gadolinium interactions is contributing directly to the kerma in the code, without secondary particles being transported.

The boric acid shield reduces the neutron flux by two orders of magnitude according to simulations and measurements (compare figure 3-35). This factor can be also found between the gadolinium doses in the two setups. The shielding did, hence, not suppress the gadolinium neutron dose to a negligible value. Compared to the detectors in the PMMA phantom about 1% of the gadolinium dose component remained. However, if the overestimation has the same relative size in both experiments, it is obvious from figure 3-43 that the overestimation cannot be limited to the gadolinium neutron dose. Consequently in both experiments overestimations towards neutron and as well photon interactions with gadolinium need to be considered. The experiments with the gadolinium free detectors suggest that the “regular” alanine dose components were calculated correctly.

From the calculated data quantification of these overestimations is afflicted to substantial uncertainties. An attempt using additional calculations did not lead to reliable results. In these single or multiple gadolinium oxide nanoparticle spheres, with varying diameters between 30 µm and 70 µm, were located in a volume of alanine surrounded by PMMA. The nano-spheres were programmed as homogenous particle sources of either electrons or photons. Necessary energy spectra were taken from literature [Ali et al., 1994, Schultz et al., 2010, Sakurai and Kobayashi, 2014]. By mainly USRBIN scoring the amount of energy deposited in either of the materials, gadolinium oxide, alanine, and PMMA, was compared. Factors derived from these simulations were intended to be used for weighting of the calculated detector response.

Photon simulations indicated that most of the energy is deposited outside nanospheres and alanine, leaving less than 5% of energy in the alanine. In contrast the electrons have a very limited range and deposit energy solely in the oxide and the alanine. However the ratio between both is a function of nanosphere diameter and electron energy. Already small changes in both parameters lead to big deviations in the result. Due to the fact that the detailed diameter distribution is unknown and also the spherical surface is only an approximation, results are uncertain, even though in some parameter sets the weighing factor corrects the original calculation in an acceptable way. However, since these results are of an either arbitrary character, they are not shown here. The combination of a first step dose calculation with the primary particles and a second step dose distribution estimation with the secondary particles could in principle be used to reproduce the response of the gadolinium-alanine dosimeter, if all necessary data is available. Furthermore other codes than FLUKA might be more rewarding and enable calculation in one step.

4.2.2.2 The lithium formate detector

The lithium formate detector was examined in the thermal neutron field using the previously validated model of the TRIGA Mainz. Experiments were conducted similar to those with the alanine detector and, hence, discussion here is possible by comparison to results gained there. The key point in understanding of the detector response is again the RE concept. As expected many analogies have been found between the RE of the lithium reaction in the formate and the RE of the nitrogen reaction in the alanine. In both reactions two particles are generated. While with the nitrogen the bigger carbon ion is of minor interest, with the lithium two particles of comparable mass are produced. However, the range of these particles is limited and the stoichiometry of the reaction is fixed. Hence the same arguments as before allow assuming a fixed RE value for reaction and product particles. And indeed, fixed values for the reaction and each product particle were found and listed in table 3-11. The agreement with the measured data is less compelling as discussed later in comparison with the alanine, but evaluation of the modelled data is, in addition, accessible by a second quantity.

The characteristic ESR spectrum was observed. $\bullet CO_2^-$ is the dominant radical species in lithium formate. The line broadening of the lithium formate in the PMMA phantom experiment has been previously observed and explained in detail with fast neutrons [Malinen et al., 2006]. Malinen and co-workers stated that the general line shape is not a result of the presence of different radical species, but of inhomogeneous line broadening due to lower spin-spin relaxation rates (compare explanation regarding the T_2 relaxation time in section 1.5.1) In order to quantify the differences in line broadening between different particle species Waldeland proposed a phenomenological approach, in which a Pseudo-Voigt profile is employed [Waldeland et al, 2010b]. Voigt profiles are commonly used in spectroscopy and result from the concurrence of two broadening mechanisms, described by the convolution of a Gaussian and a Lorentzian profile. In the discussed approach the Gaussian profile accounts for the mentioned inhomogeneous line broadening, and the Lorentzian profile for single radical spins and homogeneous broadening. One parameter determining the width of the Lorentzian part is the spin-spin relaxation rate, which in turn depends on the amount of dipolar spin-spin interactions. As can be seen in figure 3-53 nearly all dose is deposited by particles with high LET. The mean LET of alpha and tritium particles from the lithium reaction have a calculated value of 223.7 keV/µm and 65.7 keV/µm respectively. The dose weighted, combined LET of both particles amounts to 133.5 keV/µm. In space surrounding the tracks of these particles two effects have to be considered. As the RE values smaller one suggest the radical yield is reduced, simultaneously the radical density is increased compared to photon irradiation. The higher density causes a higher magnitude of intratrack, dipolar spin-spin interactions, which are according to Waldeland et al. are responsible for the increased broadening.

The Pseudo-Voigt profile used in their approach is described by equation (89), where B represents the magnetic field strength, B' the integrand, B_0 the magnetic field strength of the Gaussian part maximum, and Σ_G and Σ_L the half width at half maximum of Gaussian and Lorentzian shaped functions. The Lorentzian width is furthermore defined according to equation (90). Assuming that the radical yield is proportional to the product of LET and RE, the Lorentzian line width is increasing linearly with the constant b (per keV/µm) from an offset Σ_L^0, representing the Lorentzian line width for radiation with an LET of or close to zero.

$$g(B) \propto \int_{-\infty}^{\infty} \frac{\exp\left(-ln(2)\left[\left(B'-B_0\right)^2/\Sigma_G^2\right]\right)}{\Sigma_L^2+(B-B\prime)^2} dB' \qquad (89)$$

$$\Sigma_L = \Sigma_L^0 + b * RE * LET \qquad (90)$$

Waldeland and co-workers determined the values of Σ_G, Σ_L^0, and b in an iterative process. Values of RE and LET were determined similar as in the present thesis. Using parts of their values and own calculations of RE and LET a line width of 1.60 mT is predicted for the particles obtained with thermal neutrons. Hence the modelled value is within the uncertainty of the width of 1.58 ± 0.02 mT, which has been determined from the spectra. The line width determined here is bigger than the line width obtained previously with fast neutrons (measured as well as modelled) [Malinen et al., 2006]. However, in fast neutron fields recoiling protons have to be considered leading to a lower mean LET. The value determined here is also consistent with the data measured for protons and nitrogen ions interpreted with the same model [Waldeland et al, 2010b].

Although the result is not contributing anything new to the existing explanations for the line broadening, it shows that measurements are consistent with earlier findings. Line broadening and considerations towards the RE suggest that the response of lithium formate in the PMMA phantom can be treated as if the pellet would have been homogenously irradiated with alpha and tritium particles of the described energies.

The clearest depiction of the lithium formate depth dose curves in the two experiments can be made by comparison to the analogue alanine experiments. Due to the big difference in the macroscopic cross section towards thermal neutrons of the two materials, the response measured in the depth dose curve in the PMMA phantom differs by a factor of 70. Furthermore, as a result of the totally different dose composition, the curves show a different behaviour. While in alanine the majority of the dose is deposited by long range photons, in the formate almost all dose is deposited by high LET short range particles. The response in lithium formate appears to be a direct function of the neutron flux, as obvious when comparing to the accompanying gold foil measurements. However, considering gold foil measurements in the same phantom without detectors, presented in figure 3-16, it can be seen that the lithium formate has an additional shielding effect, which is also confirmed by the simulations. Due to this shielding effect decrease in detector response with depth is steeper. The increase observed at the rear side of the phantom, however, is similar to the increase observed in figure 3-16.

Also in the boric acid neutron shield the obtained dose rate is bigger than in the comparable alanine experiment. Dose composition suggests that again neutron dose was not fully suppressed, as observed similar with the gadolinium containing detectors. For an entire shielding of these response components the factor of 100 in reduction of the thermal neutron flux appears to be insufficient, as a consequence of the high macroscopic cross section. Different to the alanine experiment, where a constant response at all depth in the shielding was observed, with the lithium formate a decrease was measured. However a similar explanation as for the PMMA experiment applies. The dose is in part a function of the neutron flux, which qualitatively is following the course of the response curve, as confirmed via gold foil measurements. Indicated by the line broadening though, the lithium dose seems to play a minor role. Only an insignificant mean broadening of 0.005 mT was observed between spectra from calibration and shielding.

As expected the calculated absorbed dose overestimates the detector response in all experiments. With the weighing factors derived from track structure theory adequate agreement has been found between measurement and simulation, although differences are bigger as those found with the Hansen and Olsen model using alanine. Values are underestimating the measurements, indicating that the modelled RE is slightly too low. This is especially immanent in the PMMA experiment, where the lithium dose is dominant.

The dose from the lithium reaction is a function of the neutron flux in the detector position. The nuclear reaction has a Q-value of 4.78 MeV. Particles are emitted with a kinetic energy of $E_\alpha = 2055\,keV$ and $E_t = 2728\,keV$. The ratio of both energies can be found in the simulations looking on the ratio of absorbed dose afflicted to the two particles. For all pellets in both experiments (D_α/D_t) gives 0.75 and equals to (E_α/E_t). The described component RE values, summarized in table 3-11, are fixed as mentioned earlier. Comparison to literature findings is difficult, since so far no data exists for this specific reaction in lithium formate. Due to experimental reasons data for alpha and tritium particles in the specific energy range observed here are not accessible with external particle irradiation, as a consequence of their range. However, the order of magnitude of the described values is probable. Experiments with heavier particles of similar LET gave values in the same range for comparable materials. Waldeland et al [Waldeland et al., 2010b] reported a RE of about 0.6 for 164 keV/µm nitrogen ions in lithium formate and Olsson et al [Olsson et al., 2000] found a value of about 0.45 for 200 keV/µm neon ions in ammonium tartrate. For alanine Olsen and Hansen measured and calculated various REs below 0.4 for heavy ions as oxygen or argon [Olsen and Hansen, 1990].

The photon dose rate behaviour is similar as with the alanine detector. This becomes obvious when comparing figure 3-37 to figures 3-53 and 3-54. Calculation results confirm once more that the primary photon dose rate is only a function of depth in the thermal column, while the secondary photon dose also depends on the experimental build-up. Due to the presence of hydrogen in the detectors as well as in PMMA and boric acid the 2.22 MeV hydrogen photon is dominating. Due to the big amount of graphite also (n,γ) reactions of carbon occur. The 0.48 MeV photon of boron (emitted in 94% of cases by lithium after the boron neutron capture) has to be taken into account only for the shielding experiments.

Lithium formate monohydrate appears suitable for application in neutron fields. The high sensitivity enables application even in weak neutron fields or for minor neutron components in a mixed field. Thereby the amount of line broadening can give information about the amount of high LET dose depositing particles. All measurements could be simulated using FLUKA in combination with track structure theory. The agreement is sufficient but might be improvable, as the more accurate results of alanine suggest. The application of the Hansen and Olsen response model, which is an improvement of track structure theory in many aspects, may lead to better results.

Furthermore, the described experiments suggest that the modelling approach could be easily transferred to a boron containing detector, once it is discovered. Underlying nuclear reactions are similar, and so is sensitivity. From the modelling point of view, the step from alanine to lithium formate was bigger, than the step from lithium formate to a boron containing, organic compound would be. Also the FLUKA code could be used, since particles emitted after the boron neutron capture are transported.

4.2.2.3 Further compounds

Four more materials were examined closely, using the established experiment designs. Among them were two formates, calcium formate and ammonium formate, a carbonate, having the advantage to lack of hydrogen, and the amino acid phenylalanine.

The compound mentioned last was found insufficient. The non-observation of a quantifiable ESR-signal has different reasons. A general concern affecting all experiments in chapter 3.4 is about the ESR machine. The big advantage of the Miniscope MS 200 of magnettech is easy handling and the bench-top design. The choice was made with a view on possible later clinical applications. In general the machine can be used without any further ESR infrastructure. However, due to the reduced sensitivity, for example compared to the spectrometer used at NPL, and especially due to the limited cavity, requiring additional sample preparation, adjustments had to be made. Spectra recording times were much longer and the absolute dose deposited during irradiations was raised. Still, nevertheless, there are limits when it comes to materials with relatively small sensitivity towards radiation.

Obviously such limit was reached in the case of phenylalanine. In literature sensitivity relative to alanine of about 5% can be found [Gancheva et al., 2006]. In addition the authors in this study found massive fading of 25% in the first five days. After 55 days signal is decreased to 30% of the initial intensity. For their investigation they were using absorbed doses above 5 kGy, which are infeasible for clinical application.

Due to these facts adversities might have been expectable, but, however, experiments were conducted as preliminary tests for irradiations of BPA, which could have served as a boron-containing dosimeter. As explained before, despite of the phenylalanine results, very limited tests with BPA were carried out nonetheless, but results were not improved compared to the phenylalanine.

In cooperation with Steve Bottle from the Queensland University of Technology in Brisbane, Australia, a further attempt towards a boron containing material was made. The intension was the development of a molecule analogue to the one shown in figure 4-4. The idea behind such molecule was the generation of stable nitroxide radicals during irradiation. The material would have to form crystals and be stable over a wide temperature range. Due to hyperfine coupling with hydrogen the ESR signal of the displayed compound would be rather complex. Therefore a molecule containing less hydrogen was preferred. After synthesis in Brisbane, the compound should have been tested at the TRIGA Mainz. However, no such compound could be realized so far and, hence, no experiments were conducted.

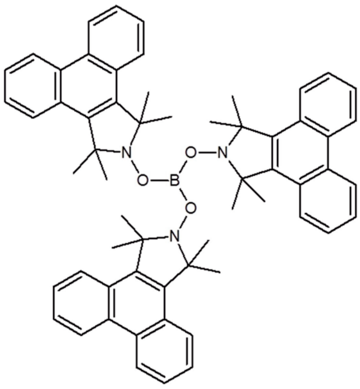

Figure 4-4. Molecule structure of a simple boron containing nitroxide.

Spectra recorded for the remaining compounds comply with those reported in literature. As in this work though, also in literature no change in spectra was observed in comparable dose compositions. Line broadening effects similar to those observed with lithium formate are indeed expected with all formates [Lund et al., 2002], and should as well occur in neutron fields when protons or heavier particles deposit dose. But as with the lithium formate, to cause an effect the fraction of the particular dose component needs to be high. With the lithium formate line broadening was observed in the PMMA phantom, but not in boric acid, where photon dose components were not minor anymore. Analogue in all irradiations with materials discussed here the photon dose components were dominating. Therefore, line broadening could not be expected. Different line shapes are a consequence of different crystal structures and resulting differences in dipolar spin-spin interactions, but also of hyperfine coupling with the cation, which is not being resolved due to the modulation amplitude.

In the previous sections the concept of RE was decisive, while it is a minor important part here. Among the three detectors, which are discussed hereinafter, only one detector has a single dose component, requiring a factor different from one. This is the nitrogen proton dose of ammonium formate. During irradiations in epithermal or fast neutron fields both calcium as well as ammonium formate are expected to have an additional fast neutron dose component from recoiling hydrogen protons. These would be afflicted to RE, similar as observed during the alanine studies. In this context specific track structure models for these compounds would be advantageous. Generally therefore several quantities as for example the D_{37}-dose (compare section 1.6.2) need to be determined. To proof reliability specified models then would have to be tested in various fields. However, this would have exceeded the possibilities of this work. Considerations how these RE factors can be determined without track structure modelling are discussed below in connection with the dose composition.

Due to the predominance of photon doses in most cases the response complies with the absorbed dose and RE is not necessary for verification of calculation correctness. The quality of agreement in depth dose curves between measurements and simulations is promising. Improvement is certainly possible with a spectrometer enabling measurements of whole pellets or bigger sample masses. Besides the quality of the spectrum this would also simplify sample processing, which is certainly not optimal for routine use as it has been presented here. For easier handling the admixture of a binder might be fortunate. However, fluctuations observed in measurements presented in figures 3-57 to 3-63 are mainly a consequence of the ability of the spectrometer as discussed earlier in this subsection. Slight improvement though might be possible by further prolonging of recording times, but simultaneously this would increase uncertainties in fading corrections, which are immanent for the formates as visible in figure 3-56.

Depth dose curves recorded for the two formates and the carbonate followed the expectations and confirmed conclusions drawn formerly. Measured response of ammonium formate is following the course of the calculated data, but is also showing rather large statistical deviations from this course. These variations are not only a consequence of signal fading and corresponding correction, but also of the hygroscopicity of the substance. To avoid major impact handling of the material sealed or in dry air it has been recommend [Gustafsson et al., 2004]. After sample processing, during storage and measurement this was achieved in the sealed quartz tubes. During irradiations, mandatory decay time and processing, though, radicals in pellets were exposed to normal humidity. To counteract the effect, silica gel was used when possible, but not during irradiations due to the high volume. The general signal loss should hence be minor, however, it cannot be ruled out that some pellets were more impaired than others.

The different decrease in neutron and photon field with depth was already apparent in calculations belonging to the alanine study. Comparison of figures 3-57 and 3-51, showing calcium formate and lithium formate in the same experiment, illustrates the subject. While in the first case the dominant short-range neutron doses show a rapid decrease, with the calcium formate the slope of the underlying exponential function is reduced in a way that it appears linear. To reveal the exponential decrease experimentally the depth investigated would have to be enlarged. Already introducing an additional dose component, increasing the relative neutron dose fraction, makes decrease more characteristic again as visible in figure 3-57 b).

The only deviation, which seems to be systematic, can be observed in figure 3-63, showing the depth dose curve of calcium carbonate observed in the PMMA phantom. Two problems are obvious. In the first part the calculations are not following the course of the measured curve and at higher depth values are overestimated. Multiple reasons have to be considered. The first problem might originate from the measurement. Although statistical uncertainty seems to be reduced compared to the ammonium formate, the overall uncertainty remains high. Due to low sensitivity absolute signal areas were quite low. Assuming the first value is overestimating, the decrease in the first data points disappears. Weather this is the case or not, the decrease is not significant. However, there is a general systematic deviation by a certain factor. Only unlikely it is related to the concept of RE, since in no comparable experiment and in particular in the calcium carbonate PMMA phantom experiment such was found. The agreement in the

PMMA experiment also makes a fundamental problem in calculations unlikely. Furthermore, fading or fading correction is not a problem since the signal was found stable over time and is described this way also in literature [Grün, 1989]. Most probable the issue is the positioning. Inside the shield the neutron field changes rapidly. Hence if the position in the experiment was different as in simulations a deviation would be the logical consequence. The shield is completely filled with boric acid powder, which has to be partially removed, when inserting the detectors. An imperfection during the refilling cannot be fully excluded, which would cause an analogue deviation between experiment and calculation as imprecise positioning.

Dose composition in the experiments matches expectations formulated in the introduction of chapter 3.4. The general response behaviour is similar to detectors discussed before, including the relative fraction of certain dose components. Furthermore, no additional dose component needed to be introduced. Detectors mainly combine components which were addressed before.

Comparison of the different detector responses enables verification of the calculated primary photon dose by employing a further method. Primary photon dose components should be conform to each other when normalised with mass energy absorption coefficient ratios (compare subsection 1.3.2.1). To test this, compound coefficients have been calculated from the element data in NIST publications [NIST] as a function of energy and folded with the photon spectrum of the thermal column. For ratios of calcium formate to ammonium formate and to lithium formate values of 1.36 and 1.33 respectively were determined. Indeed these ratios match within uncertainties with the average ratios of FLUKA primary photon dose components, which are corresponding to 1.39 ± 0.06 and 1.35 ± 0.06. Difference is a consequence of the adoption of a single photon spectrum for all pellets.

Similar calculation is not possible with the secondary neutron dose. As discussed earlier, the component depends on the neutron flux, which in turn is much more disturbed by the detectors than the photon flux. In addition parts of it are generated inside the detector itself and therefore depend on the element cross sections.

The proton dose recognised with the ammonium formate is the only dose component, among detectors discussed here, requiring application of a RE factor for transformation of response into absorbed dose and vice versa. For lack of a specific RE model for the detector the factor was extracted from the available data. Consequently the factor, found to be 0.25, has not been verified as the previous ones were. Their calculation and measurement were nearly independent from each other. The discussion of boric acid experiments, though, manages without RE values and good agreement (compare figure 3-59) demonstrates that the photon dose components (primary and secondary) have been calculated correctly also with the ammonium formate. Since towards the PMMA phantom simulation only minor parts of the geometry changed, it is no exaggeration to assume that photon doses were calculated properly also there. As shown before in figure 4-3, dose deposited by nitrogen protons is a function of neutron fluence. In the PMMA experiment neutrons fluence was monitored using gold activation foils. Their results were in agreement with the corresponding results of the FLUKA calculation. Therefore also proton dose can be assumed to be calculated in the correct way. The biggest source of uncertainty regarding the RE factor is due to the measurement, which exhibits the already discussed fluctuations. The RE factor of 0.25 has hence not been verified using track structure modelling, but was successfully tested by accompanying calculations, as the flux monitoring and the photon component only experiment in boric acid.

The two formates as well as the carbonate, discussed in this subsection, were showed to have good potential as neutron dosimeters. The two containing calcium might be even less tissue equivalent than alanine and lithium formate, but in a detector set, as intended in the motivation, they are helpful supplements. Before possible application, methods should be refined. The use of a benchtop spectrometer has not proven successful, especially with low doses in therapeutic range and materials generating rather few radicals per unit of absorbed dose. Also the experimental design should be adjusted to enable the use of sealed ammonium formate pellets. The fading effects, observed with the two formates in figure 3-56, are manageable, when storage times are kept short and photon calibration and neutron irradiation happen close to simultaneously.

In general it could be shown that the various ESR detectors in neutron fields are as flexible to use as in photon fields and that their response parameters are nearly independent of the dose depositing particles.

4.3 Possibilities of application

Future BNCT neutron sources will be predominantly accelerators. All BNCT facilities planned or under construction are accelerator based. Afflicted advantages were discussed in the introduction (compare chapter 1.2). There are research reactors establishing new BNCT facilities, but these exist and are modified only. Accelerators, as for example the build in Kyoto, though, provide even more epithermal fields than most actual reactor based facilities [Tanaka et al. 2009]. Therefore any possible application mandatorily needs to consider epithermal dose deposition. In respect thereof table 4-1 expands table 3-12 (section 3.4) to the relevant materials.

Table 4-1. Expected dose components in the examined detector materials as deposited during neutron irradiation.

Material	**Dose components**			
	Photon dose	**Fast neutron dose**	**Proton dose**	**Lithium dose**
Alanine	X	X	X	
Ammonium formate	X	X	X	
Calcium formate	X	X		
Calcium carbonate	X			
Lithium formate	X	X		X

In the first step in ESR dosimetry in this work dose components were analysed using four different experimental setups with the alanine detector. By combining the detectors shown in the table it is possible to check calculation of dose components in one single experiment. Calcium carbonate contains no hydrogen. Even in epithermal fields response will only consist out of photon components. Neutron scattering with subsequent recoiling occurs not only with hydrogen, but also with carbon or heavier atoms. However, corresponding cross sections are small and not leading to significant dose components with the considered neutron energies. In organic substances neutron dose is mainly generated by two elements, hydrogen and nitrogen. Calcium formate excludes the nitrogen dose, and would generate a fast neutron dose if used in an epithermal field. Alanine and ammonium formate exhibit the same components including the nitrogen dose and fast neutron dose. Although ammonium formate leads to some difficulties it remains important, since it combines the dose components in different relative fractions. The detector, hence, provides additional verification similar to the experiments in PMMA and Teflon phantoms during the alanine study. In lithium formate nitrogen dose is replaced by a lithium dose. Due to the dominance of this component in the response the detector provides only small additional information. However, the dosimeter could be a good tool to check and investigate the function of shielding, as for example used for eye balls during irradiations of the head.

For application, though, some modifications to the experimental setups which were presented here are needed, as mentioned in the previous section. Work with the benchtop machine showed that the ESR measurement has to stay dedicated to specialised labs in the case of clinical use. Some institutions also provide manufacturing and calibration, but mostly such service is limited to alanine. A suitable phantom should enable irradiation of several sets of all five detectors. THereby all detectors of one set should share the same depth, to avoid corrections for the change in field when comparing the responses. This could be achieved by arranging detectors on rings around the axis of interest, for example (as in most experiments in this work) the central axis. Space between detectors needs to be large enough to exclude mutual interference. In the experiments with lithium formate a shielding effect was obvious. On the other hand fields as present in the thermal column exhibit lateral asymmetries. The competing effects need to be balanced.

Obviously recurring adaption and modification is necessary, depending on the actual facility. However, it was proven that ESR dosimetry has the potential to be a serviceable tool in BNCT dosimetry.

5. Summary and suggestions for future research

The purpose of this work was the investigation of ESR detectors in neutron fields as an alternative or supplemental method to existing systems in Boron Neutron Capture Therapy (BNCT). Ionising radiation passing through matter generates radicals. Using Electron Spin Resonance (ESR) spectrometry these radicals can be detected. Using proper materials and adequate calibration, the detector response can be correlated to absorbed dose. Analogue to the established BNCT methods the work was aiming to combine several ESR detector materials in a set, enabling dosimetric characterisation and model validation in a few simple or even a single irradiation.

Among ESR dosimeters the alanine detector is best known. It has been exposed to the biggest variety of particles, starting from photons, ending with exotic beams of antiprotons, and has been subject of many modelling attempts. Such it was logic to start studying the possibilities of ESR dosimetry in BNCT with the alanine detector. First tests in the field of the TRIGA Mainz were conducted prior to this thesis [Schmitz, 2010]. However, in this work the alanine study has been continued and expanded. Data for alanine in neutron field was limited before and mainly focussed on response in fast neutron fields. In this work the detector has been irradiated in various phantoms and also in fields of other reactor facilities. The response was modelled with the FLUKA code, having results of the Hansen and Olsen model implemented. It has been shown within this work that it is possible to fully understand and decompose the response of the alanine detector in thermal and epithermal neutron fields. For the first time the response of the alanine detector in neutron fields was fractionised in four dose components, each assigned an individual factor accounting for the Relative Effectiveness (RE).

The basis of such modelling though is the simulated geometry and the programmed source. Therefore an essential part of this work was dedicated to the validation of the latest TRIGA Mainz model, developed in cooperation with the Austrian Institute of Technology in Vienna, Austria [Ziegner et al., 2014]. For the validation extensive neutron distribution and spectrometry experiments were conducted, using metal foil activation. Data gained in those experiments was compared to model predictions. It was shown that the TRIGA Mainz model is consistent with all neutron distribution and spectrometry experiments. Due to the results of the alanine study, the same conclusion can be drawn regarding photons. Both are the two primary particles necessary to consider in neutron fields.

Knowledge gained with the alanine and the validated TRIGA Mainz model enabled comprehensive studies on further ESR detector materials. As for the alanine, also for these materials data on the neutron response was either few or lacking. Knowing the expectable dose components, the main objective was the investigation of modelling possibilities and response behaviour.

A central issue in this part of the work was the identification of a boron containing material, enabling assessment of the boron dose. Numerous publications exist, where alanine was mixed with boron compounds. Due to the short range of boron particles after neutron capture, grain size is of big importance and limits the possibilities of modelling. The use of alanine mixed with gadolinium oxide was found more promising, due to the different secondary particles. However, again because of the insecurities in the size of the gadolinium nanoparticles, but also because of limitations of the FLUKA code, modelling approaches partially failed. A detector, including the boron atom in the molecular structure would eliminate such difficulties, but a proper material has not been found so far. Boron-phenylalanine, chosen because of its similarity to alanine and the relation to BNCT, was found insufficient, as also phenylalanine, the basic compound. Another attempt was made in cooperation with the Queensland University of Technology in Brisbane, Australia. But also here, no success could be achieved.

Similar to the neutron capture of boron-10 is the neutron capture of lithium-6. Lithium formate was therefore investigated as an analogue to a boron containing detector. As an additional parameter, lithium formate enables the estimation of the neutron dose fraction from the line shape. The more high LET particles deposit dose, the larger is the effect of line broadening. It has been shown in this work that the effect with neutrons is empirically explainable and consistent with findings in other particle fields. The general response behaviour of lithium formate could be reproduced similar to the alanine, although a less advanced model has been used. Future research regarding the detector in neutron fields should be focussed on the application of the Hansen and Olsen Model (studies on protons and heavier ions exist [Herrmann, 2012]) and investigate the response behaviour in epithermal neutron fields to include fast neutron dose components, i.e. deposited for example by recoiling protons.

Further compounds examined were calcium formate, ammonium formate and calcium carbonate. The response of the two calcium compounds consists only of photon dose components in thermal neutron fields. The measured and calculated responses are, hence, equal to absorbed dose. In epithermal fields only the calcium formate is expected to have a fast neutron response. However, experimental confirmation is still lacking. In thermal fields though both detector responses could be reproduced, again including dose component separation. Ammonium formate exhibits an additional proton dose response from the nitrogen neutron capture. In the absence of a dedicated response model the afflicted RE has been determined experimentally. Through experiment comparison, it could be shown that photon responses were again calculated correctly. Occurring experimental difficulties with the substance can be avoided in future with the recommendations in this work and in literature as discussed earlier. As with the lithium formate future research should focus on modelling and epithermal fields. In thermal fields though, the ammonium formate has proven applicability, as the other materials.

Five materials (alanine, ammonium, calcium, and lithium formate, as well as calcium carbonate) were found suitable for a dosimeter set for the characterisation of thermal and epithermal BNCT neutron fields. Each of these detectors shows a different behaviour and dose composition. Their irradiation can be a helpful tool in field characterisation and model validation. Due to the same reasons, in some areas ESR detectors are superior to the currently predominant ionisation chambers. How far both types of detectors can be complementary or even synergistic will have to be part of future research.

Because of the often described flexibility and fortunate features of ESR dosimeters, various applications in neutron fields outside BNCT appear interesting. In cosmic radiation neutrons are the largest fraction (depending on altitude between 35% and 50%), but occur in conjunction with protons, electrons, muons and pions. Besides monitoring on earth, application is also important in aviation or astronautics. Accelerator based neutron beams are used for material testing and determination of radiation hardness or soft errors. Neutron fields are also generated in nuclear power plants. Due to possible demands for deconstruction or damages in shielding by corrosion or accident, neutron dosimetry is crucial. Therefore, in these areas the use of ESR detectors might be similar rewarding as in BNCT.

6. References

[ABTA, 2012] ABTA, Glioblastoma and malignant Astrocytoma, A.B.T. Association, Editor 2012, American Brain Tumor Association: http://www.abta.org/secure/glioblastoma-brochure.pdf

[Ali et al., 1994] M.A. Ali, V.A. Khitrov, Y.V. Kholnov, A.M. Sukhovoj, and A.V. Vojnov, Properties of the ^{158}Gd compound state gamma-decay cascades, *Journal of Physics G: Nuclear and Particle Physics* **20**, 1943-1953 (1994).

[Anton et al., 2008] M. Anton, R.P. Kapsch, M. Krystek, and F.Renner, Response of the alanine/ESR dosimetry system to MV x-rays relative to ^{60}Co radiation, *Physics in Medicine and Biology* **53**, 2753-2770 (2008).

[Atherton, 1993] N.M. Atherton, Principles of electron spin resonance, Ellis Horwood Ltd, New York (1993).

[Attix, 1986] F.H. Attix, Introduction to radiological physics and radiation dosimetry, A Wiley Interscience publication, New York (1986).

[Auterinen et al., 2001] I. Auterinen, P. Hiismäki, P. Kotiluoto, R. Rosenberg, S. Salmenhaara, T. Seppälä, T. Serén, V. Tanner, C. Aschan, M. Kortesniemi, A. Kosunen, J. Lampinen, S. Savolainen, M. Toivonen, and P. Välimäki, Metamorphosis of a 35 year-old Triga reactor into a modern BNCT facility, in: Frontiers in Neutron Capture Therapy, edited by M.F. Hawthorne, K. Shelly, R.J. Wiersema, Vol. 1 Plenum Press, New York, 267–275 (2001).

[Barth et al., 2012] R.F. Barth, M. Graca, H Vicente, O.K. Harling, W.S. Kiger III, K.J. Riley, P.J. Binns, F.M. Wagner, M. Suzuki, T. Aihara, I. Kato, and S. Kawabata, Current status of boron neutron capture therapy of high grade gliomas and recurrent head and neck cancer, *Radiation Oncology* **7**, 146-167 (2012).

[Bartolotta et al., 1999] A. Bartolotta, M. Brai, V. Caputo, V. De Caro, L.I. Giannola, R. Rap, and G. Teri, ESR Solid State Dosimetry: Behaviour of Various Amino Acids and Blend Preparation Procedures, *Radiation Protection Dosimetry* **84**, 2093-296 (1999).

[Baran et al, 2006] M.P. Baran, O.A. Bugay, S.P. Kolesnik, V.M. Maksimenko, V.V. Teslenko, T.L. Petrenko, and M.F. Desrosiers, Barium Dithionate as an EPR Dosimeter, *Radiation Protection Dosimetry* **120**, 202-204 (2006).

[Bassler et al., 2008] N. Bassler, J.W. Hansen, H. Palmans, M.H. Holzscheiter, S. Kovacevic, and the AD-4/ACE collaboration, The Antiproton Depth Dose Curve Measured with Alanine Detectors, *Nuclear Instruments and Methods B* **266**, 929–936 (2008).

[Bassler and Holzscheiter, 2009] N. Bassler and M. Holzscheiter, Calculated LET spectrum from antiproton beams stopping in water, *Acta Oncologica* **48**, 223-226 (2009).

[Battistoni et al, 2007] G. Battistoni, S. Muraro, P.R. Sala, F. Cerutti, A. Ferrari, S. Roesler, A. Fasso`, and J. Ranft, The FLUKA code: Description and benchmarking, Proceedings of the Hadronic Shower Simulation Workshop 2006, Fermilab, 6-8 September 2006, edited by M. Albrow, and R. Raja, *AIP Conference Proceeding* **896**, 31-49, (2007).

[Bermann et al., 1971] F. Bermann, H. de Choudens, and S. Descours, Application a la Dosimetriede la Mesure par Resonance Paramagnetique Electronique des Radicaux Libres Crees dans les Acides Amines, in: Advances in Physical and Biolgical Radiation Detectors STI/PUB/269, p. 311, IAEA, Vienna (1971).

[Berman, 1978] Adaptation of a free radial dosimeter to the intercomparison of fast neutron beams. IAEA contract No. 1542/R2/RB, Final report (1978).

[Bernier et al, 2004] J. Bernier, E.J. Hall, and A. Giaccia, Radiation oncology: a century of achievements, *Nature Reviews Cancer* **4**, 737-747 (2004).

[Bittner et al., 2014] M.I. Bittner, A.L.Grosu, N. Wiedenmann, and J.J. Wilkens, A systematic review of antiproton radiotherapy, *Frontiers in Physics* **1**, 1-8 (2014).

[Blaickner et al., 2012] M. Blaickner, J.V. Kratz, S. Minoucher, G. Otto, H. Schmidberger, C. Schütz, L. Vogtländer, B. Wortmann, and G. Hampel, Dosimetric feasibility study for an extracorporal BNCT application on liver metastases at the TRIGA Mainz, *Applied Radiation and Isotopes* **70**, 139-143 (2012).

[Borgonove et al., 2007] A.F. Borgonove, A. Kinoshita, F. Chen, P. Nicolucci, and O. Baffa, Energy dependence of different materials in ESR dosimetry for clinical X-ray 10MVbeam, *Radiation Measurements* **42**, 1227-1232 (2007).

[Bradshaw et al., 1962] W.W. Bradshaw, D.G. Cadena, G.W. Crawford, and H.A.W. Spetzler, The Use of Alanine as a Solid Dosimeter, *Radiation Research* **17**, 11-21 (1962).

[Brahme, 1984] Brahme, A., Dosimetric precision requirements in radiation therapy. *Acta Oncologica* **23**, 379-391 (1984).

[Butts and Katz, 1967] J.J. Butts, and R. Katz, Theory of RBE for Heavy Ion Bombardment of Dry Enzymes and Viruses, *Radiation Research* **30**, 855-871 (1967).

[Callens et al, 1998] F. Callens, G. Vanhaelewyn, P. Matthys, and E. Boesman EPR of Carbonate Derived Radicals: Applications in Dosimetry, Dating and Detection of Irradiated Food, *Applied Magnetic Resonance* **14**, 235-254 (1998).

[Caswell et al., 1980] R.S. Caswell, J.J. Coyne, and M.L. Randolph, Kerma Factors for Neutron Energies below 30 MeV, *Radiation Research* **83**, 217-254 (1980).

[Chadwick, 1932] J. Chadwick, The existence of a neutron, *Proceedings of the Royal Society of London A* **136**, 692-708 (1932).

[Chappell and Fowler, 1994] R. Chappell, and J. Fowler, Steepness of dose-response curve for larynx cancer. *Radiotherapy and Oncology* **30**, 90.

[Ciesielski and Wielopolski, 1994] B. Ciesielski and L. Wielopolski, The Effects of Dose and Radiation Quality on the Shape and Power Saturation of the EPR Signal in Alanine, *Radiation Research* **140**, 105-111 (1994).

[Ciesielski and Wielopolski, 1995] B. Ciesielski and L. Wielopolski, The Effects of Boron on the Electron Paramagnetic Resonance Spectra of Alaine Irradiated with Thermal Neutrons, *Radiation Research* **144**, 59-63 (1995).

[Coderre and Morris, 1999] J.A. Coderre, and G.M. Morris, The Radiation Biology of Boron Neutron Capture Therapy, *Radiation Research* **151**, 1-18 (1999).

[Croff, 1980] A.G. Croff, A User's Manual for the ORIGEN2 Computer Code, Oak Ridge National Laboratory, Oak Ridge, TN, United States (1980).

[Cuttone et al., 1999] G. Cuttone, L .Raffaele, L. Barone Tonghi, A. Rovelli, M.G. Sabini, E. Egger, A. Kacperek, M. Brai, A. Bartolotta, G. Teri, et al., First dosimetry intercomparison results for the CATANA project, Phys. Medica, (1999).

[Delaney et al., 2005] G. Delaney, S. Jacob, C. Featherstone, and M. Barton, The Role of Radiotherapy in Cancer Treatment, *Cancer* **104**, 1129-1137 (2005).

[Dertinger and Jung, 1969] H. Dertinger, and H. Jung, Molekulare Strahlenbiologie, Springer- Verlag, Berlin (1969).

[D'Errico et al., 1996] F. d'Errico, P. Fattibene, S. Onori, and M Pantaloni, Criticality Accident Dosimetry with ESR Spectroscopy, *Applied Radiation and Isotopes* **47**, 1335-1339 (1996).

[Dodd et al., 1985] N.J.F. Dodd, A.J. Swallow, and F.J. Ley, Use of ESR to identify irradiated food, *Radiation Physics and Chemistry* **26**, 451-453 (1985).

[Eberhardt and Kronenberg, 2000] K. Eberhardt and A. Kronenberg, The research reactor TRIGA Mainz : A neutron source for versatile applications in research and education, *Kerntechnik* **65**, 269-274 (2000).

[Ebert et al., 1965] P.J. Ebert, K.a. Hardy, and D.G. Cadena, Energy Dependance of Free Radical Production in Alanine, *Radiation Research* **26**, 178-197 (1965).

[ENDF] National Nuclear Data Center, Brookhaven National Laboratory (BNL), Evaluated Nuclear Data File (ENDF) Retrieval & Plotting: http://www.nndc.bnl.gov/sigma/index.jsp

[Fattibene et al., 2002] P. Fattibene, C. De Angelis, S. Onori, and R. Cherubini, Alanine Response to Proton Beams in the 1.6-6.1 MeV Energy Range, *Radiation Protection Dosimetry* **101**, 465-468 (2002).

[Fattibene and Callens, 2010] P. Fattibene and F. Callens, EPR dosimetry with tooth enamel: A review, *Applied Radiation and Isotopes* **68**, 2033-2116 (2010).

[Ferlay et al., 2013] J. Ferlay, E. Steliarova-Foucher, J. Lortet-Tieulent, S. Rosso, J.W.W. Coebergh, H. Comber, D. Forman, and F. Bray, Cancer incidence and mortality patterns in Europe: Estimates for 40 countries in 2012, *European Journal of Cancer* **49**, 1374-1403 (2013).

[Ferrari et al., 2005] A. Ferrari, P.R. Sala, A. Fasso`, and J. Ranft, FLUKA: a multi-particle transport code, CERN-2005-10, INFN/TC_05/11, SLAC-R-773 (2005).

[Fukuda et al., 2003] H. Fukuda, J. Hiratsuka, T. Kobayashi, Y. Sakurai, K. Yoshino, H. Karashima, K. Turu, K. Araki, Y. Mishima , and M. Ichihashi, Boron neutron capture therapy (BNCT) for malignant melanoma with special reference to absorbed doses to the normal skin and tumor. *Australasian Physical and Engineering Science in Medicine* **26**, 97-103 (2003).

[Galindo and Ureña-Nuñez, 1993] S. Galindo, and F. Ureña-Nuñez, EPR Signal Enhancement of Alanine Irradiated with Thermal Neutrons, *Radiation Research* **133**, 387-389 (1993).

[Gancheva et al., 2006] V. Gancheva, E. Sagstuen, and N.D. Yordanov, Study on the EPR/dosimetric properties of some substituted alanines, *Radiation Physics and Chemistry* **75**, 329-335 (2006).

[Gerson and Huber, 2003] F. Gerson and W. Huber, Electron spin resonance spectroscopy of organic radicals, Wiley-VCH, Weinheim (2003).

[Gerstenberg et al., 1990] H.M. Gerstenberg, J.W. Hansen, J.J. Coyne, and J. Zoetelief, Calculations of the Relative Effectiveness of Alaine for Neutrons with energies up to 17.1 MeV, *Radiation Protection Dosimetry* **31**, 85-89 (1990).

[González and Santa Cruz, 2012] S.J. González and G.A. Santa Cruz, The Photon-Isoeffective Dose in Boron Neutron Capture Therapy, *Radiation Research* **178**, 609-621 (2012).

[Griffin et al., 1994] P.J. Griffin, J.G. Kelley, and J.W. VanDenburg, User's Manual for SNL-SAND-II Code, *RSICC Peripheral Shielding Routine Collection, SAND93-3957* (1994).

[Grün, 1989] R. Grün, Electron Spin Resonance (ESR) Dating, *Quaternary International* **1**, 65-109 (1989).

[Gustafsson et al., 2004] H. Gustafsson, S. Olsson, A. Lund, and E. Lund, Ammonium Formate, a Compound for Sensitive EPR Dosimetry, *Radiation Research* **161**, 464-470 (2004).

[Hampel et al., 2009] G. Hampel, B. Wortmann, M. Blaickner, J. Knorr, J.V. Kratz, A. Lizón Aguilar, S. Minouchehr, S. Nagels, G. Otto, H. Schmidberger, C. Schütz, and L. Vogtländer, Irradiation facility at the TRIGA Mainz for treatment of liver metastases, *Applied Radiation and Isotopes* **67**, 238–241 (2009).

[Hansen, 1984] J.W. Hansen, Experimental Investigation of the Suitability of the Track Structure Theory in Describing the Relative effectiveness of High-LET Irradiation of Physical Radiation Detectors, PhD-Thesis, Risø National Laboratory, Roskilde, Denmark (1984).

[Hansen and Olsen, 1984] J.W. Hansen and K.J Olsen, Experimental and Calculated Response of a Radiochromic Dye Film Dosimeter to High-LET Radiations, *Radiation Research* **97**, 1-15 (1984).

[Hansen and Olsen, 1985] J.W. Hansen and K.J Olsen, Theoretical and Experimental Radiation Effectiveness of the Free Radical Dosimeter Alanine to Irradiation with Heavy Charged Particles, *Radiation Research* **104**, 15-27 (1985).

[Hansen and Olsen, 1989] J.W. Hansen and K.J. Olsen, Predicting Decay in Free-radical Concentration in L-α-Alanine Following High-LET Radiation Exposures, *Applied Radiation and Isotopes* **40**, 935-939 (1989).

[Hansen et al., 1987] J.W. Hansen, K.J. Olsen, and M. Wille, The Alaine Radiation Detector for High and Low LET Dosimetry, *Radiation Protection Dosimetry* **19**, 43-47 (1987).

[Hansen et al., 1989] J.W. Hansen, M.P.R. Waligórski, and E. Byrski, Intercomparison of Gamma Ray, X Ray, and Fast Neutron Dosimetry using Alanine Detectors, *Radiation Protection Dosimetry* **27**, 85-92 (1989).

[Henriksen, 1966] T. Henriksen, Free Radicals in Solid Biological Substances by Heavy Ions, *Radiation Research* **27**, 676-693 (1966).

[Haapaniemi et al., 2014] A. Haapaniemi, L. Kankaanranta, H. Koivunoro, K. Saarilahti, A. Mäkitie, T. Atula, and H. Joensuu, Boron Neutron Capture Therapy (BNCT) in the Management of Recurrent Laryngeal Cancer, in: 16th International Congress of Neutron Capture Therpay, edited by the International Society of Neutron capture Therapy, Helsinki (2014), p. 59.

[Herrmann and Baumann 1997] Herrmann T., and Baumann M., Strahlenbiologie: kurz und bündig. Vol.3, Gustav Fischer Verlag, Jena (1997), p.19.

[Herrmann et al., 2011] R. Herrmann, O. Jäkel, P. Sharpe, H. Palmans, and N. Bassler, Dose response of alanine detectors irradiated with carbon ion beams, *Medical Physics* **38**, 1859-1866 (2011).

[Herrmann, 2012] R. Herrmann, Prediction of the Response Behaviour of One-Hit Detectors in Particle Beams, PhD-Thesis, Department of Physics and Astronomy, Faculty of Science and Technology, Aarhus University, Denmark (2012).

[Hopewell et al., 2012] J.W. Hopewell, G.M. Morris, A.E. Schwint, and J.A. Coderre, Boron Neutron Capture Therapy: Application of Radiobiological Principles, in: Neutron Capture Therapy, edited by W.A.G. Sauerwein, A. Wittig, R. Moss, and Y. Nakagawa, Springer, Berlin (2012), p. 329.

[Hoskin, 1986] P. Hoskin (Editor), Radiotherpy in Practice: Radioisotope Therapy, Oxford University Press, New York (2007).

[IAEA Tecdoc 1223, 2001] International Atomic Energy Agency (IAEA), Current Status of Neutron Capture Therapy (IAEA-TECDOC-1223), IAEA, Vienna, (2001).

[ICRU Report 45, 1989] ICRU Report No. 45, Clinical neutron dosimetry. Part I: Determination of absorbed dose in a patient treated by external beams of fast neutrons, International Commission on Radiation Units and Measurements, Bethesda, MD (1989), Chapter 3.

[ICRU Report 60, 1998] ICRU Report No. 60, Fundamental Quantities and Units for Ionizing Radiation, International Commission on Radiation Units and Measurements, Bethesda, MD (1998).

[Jacobs et al., 1989] C. Jacobs, P. de Cannière, R. Debuyst, F. Dejehet, and D. Apers, ESR Study of Gamma-ray Irradiated Synthetic Calcium Carbonates, *Applied Radiation and Isotopes* **40**, 1147-1152 (1989).

[Jansen et al., 1997] J.T.M. Jansen, C.P.J. Raaijmakers, B.J. Mijnheer, and J. Zoetelief, Realtive Neutron Sensitivity of Tissue-Equivalent Ionisation Chambers in an Epithermal Neutron Beam for Boron Neutron Capture Therapy, *Radiation Protection Dosimetry* **70**, 27-32 (1997).

[Jones and Wambersie, 2007] D.T.L. Jones and A. Wambersie, Radiation therapy with fast neutrons: A review, *Nuclear Instruments and Methods in Physics Research A* **580**, 522-525 (2007).

[Kankaanranta et al., 2011] L. Kankaanranta, T. Seppälä, H. Koivunoro, P. Välimä, A. Beule, J. Collan, M. Kortesniemi, J. Uusi-Simola, P. Kotiluoto, I. Auterinen, T.Serèn, A. Paetau, K. Saarilahti, S. Savolainen, and H. Joensuu, L-Boronophenylalanine-Mediated Boron Neutron Capture Therapy for Malignant Glioma Progressing after External Beam Radiation Therapy: A Phase I Study, *International Journal of Radiation Oncology in Biology and Physics* **80**, 369-376 (2011).

[Kankaanranta et al., 2012] L. Kankaanranta, T. Seppälä, H. Koivunoro, K. Saarilahti, T. Atula, J. Collan, E. Salli, M. Kortesniemi, J. Uusi-Simola, P. Välimäki, A. Mäkitie, M. Seppänen, H. Minn, H. Revitzer, M. Kouri, P. Kotiluoto, T.Serèn, I. Auterinen, S. Savolainen, and H. Joensuu, Boron Neutron Capture Therapy in the Treatment of Locally Recurred Head-and-Neck Cancer: Final Analysis of a Phase I/II Trial, *International Journal of Radiation Oncology in Biology and Physics* **82**, 67-75 (2012).

[Karger and Jäkel, 2007] C.P. Karger and O. Jäkel, Current Status and New Developments in Ion Therapy, *Strahlentherapie und Onkologie* **183**, 295-300 (2007).

[Kato et al., 2004] I. Kato, K. Ono, Y. Sakurai, M. Ohmae, A. Maruhashi, Y. Imahori, M. Kirihata, M. Nakazawa, and Y. Yura, Effectiveness of BNCT for recurrent head and neck malignancies, *Applied Radiation and Isotopes* **61**, 1069-1073 (2004).

[Kato et al., 2009] I. Kato, Y. Fujita, A. Maruhashi, H. Kumada, M. Ohmae, M. Kirihata, Y. Imahori, M. Suzuki, Y. Sakrai, T. Sumi, S. Iwai, M. Nakazawa, I. Murata, H. Miyamaru, and K. Ono, Effectiveness of boron neutron capture therapy for recurrent head and neck malignancies, *Applied Radiation and Isotopes* **67**, 37-42 (2009).

[Katz, 1993] R. Katz, Relative Effectiveness of Mixed Radiation Fields, *Radiation Research* **133**, 390 (1993).

[Katz et al., 1972] R. Katz, S.C. Sharma, and M. Homayoonfar, Detection f Energetic Heavy Ions,

[Katz, 1978] R. Katz, Track Structure Theory in Radiobiology and in Radiation Detection, *Nuclear Track Detection* **2**, 1-28 (1978).

[Khan et al., 2010] R. Khan, S. Karimzadeh, and H. Böck, TRIGA fuel burn-up calculations and its confirmation, *Nuclear Engineering and Design* **240**, 1043-1049 (2010).

[Koivunoro et al., 2014] H. Koivunoro, T. Schmitz, E. Hippeläinen, Y-H. Liu, T. Serén, P. Kotiluoto, I. Auterinen, and S. Savolainen, The FiR 1 photon beam model adjustment according to in-air spectrum measurements with the Mg(Ar) ionization chamber, *Applied Radiation and Isotopes* **88**, 134-138 (2014).

[Kosunen et al., 1999] A. Kosunen, M M. Kortesniemi, H. Ylä-Mella, T. Seppälä, J. Lampinen, T. Serén, I. Auterinen, H. Järvinen, and S. Savolainen, Twin Ionisation Chambers for Dose Determinations in Phantom in an Epithermal Neutron Beam, *Radiation Protection Dosimetry* **81**, 187-194 (1999).

[Koukourakis et al., 2009] G. Koukourakis, N. Kelekis, V. Armonis, and V. Kouloulias, Brachytherapy for Prostate Cancer: A systematic review, *Advances in Urology,* 1-11 (2009).

[Kraft et al., 1992] G. Kraft, M. Krämer, and M. Scholz, LET, trackstructure, and models, *Radiation and Environmental Biophysics* **31**, 161-180 (1992).

[Králík and Turek, 2004] M. Králík, and K. Turek, Characterisation of neutron fields around high-energy x-ray radiotherapy machines, *Radiation Protection Dosimetry* **110**, 503-507 (2004).

[Kreiner et al., 2014] A.J. Kreiner, J. Bergueiro, Daniel Cartelli, M. Baldoa, W. Castella, J. Gomez Asoia, J. Padulo, J. Sandín, M. Igarzabal, J. Erhardt, D. Mercuri, A.A. Valda, D.M. Minsky, M.E. Debray, H.R. Somacal, M.E. Capoulat, M.S. Herrera, M.F. del Grosso, L. Gagetti, M. Suarez Anzorena, N. Canepa, N. Real, M. Gun, H. Tacca, Present status of Accelerator-Based BNCT, *Reports of Practical Oncology and Radiotherapy*, in press (2014).

[Lin et al., 2011] Y.C. Lin, Y.H. Liu, S.H. Jiang, H.M. Liu, and W.T. Chou, The refinement of dose assessment of the THOR BNCT beam, *Applied Radiation and isotopes* **69**, 1834-1837 (2011).

[Liu et al., 2011] Y.H. Liu, P.E. Tsai, H.T. Yu, Y.C. Lin, Y.S. Huang, C.K. Huang, Y.W.H. Liu, H.M. Liu, and S.H. Jiang, Performance evaluation of the source description of the THOR BNCT epithermal neutron beam, *Applied Radiation Isotopes* **69**, 1892–1896 (2011).

[Locher, 1936] G. Locher, Biological effects and therapeutic possibilities of neutrons, *American Journal of Roentgenology* **36**,1-13 (1936).

[Lund et al., 2002] A. Lund, S. Olsson, M. Bonora, E. Lund, and H. Gustafsson, New materials for ESR dosimetry, *Spectrochimica Acta Part A* **58**, 1301-1311 (2002).

[Lund et al., 2005] E. Lund, H. Gustafsson, M. Danilczuk, M.D. Sastry, A. Lund, T.A. Vestad, E. Malinen, E.O. Holec, and E. Sagstuen, Formates and dithionates: sensitive EPR-dosimeter materials for radiation therapy, *Applied Radiation and Isotopes* **62**, 317-324 (2005).

[Lyons, 1996] R.G. Lyons, Back to basics: Qualitative spectral analysis as an investigatory tool, using calcite as a case study, *Applied Radiation and Isotopes* **47**, 1385-1391 (1996).

[Macey et al., 2001] D.J. Macey, L.E. Williams, H.B. Breitz, A. Liu, T.K. Johnson, P.B. Zanzonico, AAPM Report No. 71: A Primer for Radioimmunotherapy and Radionuclide Therapy, Report of Task Group #7, AAPM Nuclear Medicine Committee, Medical Physics Publishing, Madison, United States (2001).

[Malinen et al., 2003] E. Malinen, E.A. Hult, E.O. Hole, and E. Sagstuen, Alanine Radicals, Part 4: Relative Amounts of Radical Species in Alanine Dosimeters after Exposure to 6-19 MeV Electrons and 10 kV-15 MV Photons, *Radiation Research* **159**, 149-153 (2003).

[Malinen et al., 2004] E. Malinen, T.A. Vestad, E.A. Hult, E.O. Hole, E. Sagstuen, Estimation of X-ray beam quality by electron paramagnetic resonance (EPR) spectroscopy, *Applied Radiation and Isotopes* **60** 929-937 (2004).

[Malinen et al., 2006] E. Malinen, E. Waldeland, E. O. Hole, and E. Sagstuen, LET effects following neutron irradiation of lithium formate EPR dosimeters, *Spectrochimica Acta A* **63**, 861–869 (2006).

[Marrale et al., 2007] M. Marrale, M. Brai, G. Gennaro, A. Triolo, A Bartolotta, M.C. D'Oca, and G. Rosi, Alanine Blends for ESR Measurements of Thermal Neutron Flence in a Mixed Radiation Field, *Radiation Protection Dosimetry* **126**, 631-635 (2007).

[Marrale et al., 2008] M. Marrale, G. Gennaro, M. Brai, S. Basile, A. Bartolotta, and M.C. D'Oca, Exposure of Gd_2O_3-alanine and Gd_2O_3-ammonium tartrate ESR dosimeters to thermal neutrons: Experiments and Monte Carlo simulations, *Radiation Measurements* **43**, 471-475 (2008).

[Marrale et al., 2014a] M. Marrale, M. Brai, A. Longo, S. Panzeca, L. Tranchina, E. Tomarchio, A. Parlato, A. Buttafava, and D. Dondi, Neutron ESR dosimetry through ammonium tartrate with low Gd content, *Radiation protection dosimetry* **159**, 233-236 (2014).

[Marrale et al., 2014b] M. Marrale, M. Brai, A. Longo, S. Panzeca, A. Carlino, L. Tranchina, E. Tomarchio, A. Parlato, A. Buttafava, D. Dondi, and A. Zeffiro, EPR/alanine pellets with low Gd content for neutron dosimetry, *Radiation protection dosimetry* **161**, 383-386 (2013).

[Marrale et al., 2015] M. Marrale, T. Schmitz, S. Gallo, G. Hampel, A. Longo, S.Panzeca, and L. Tranchina, Comparison of EPR response of alanine and Gd2O3-alanine dosimeters exposed to TRIGA Mainz reactor, *Applied Radiation and Isotopes* **106**, 116-120 (2015).

[Matsuda et al., 2009] M. Matsuda, T. Yamamoto, H. Kumada, K. Nakai, M. Shirakawa, T. Tsurubuchi, and A. Matsumura, Dose distribution and clinical response of glioblastoma treated with boron neutron capture therapy. 13th International Congress on Neutron Capture Therapy BNCT: a new option against cancer, *Applied Radiation and Isotopes* **67**, 19-21 (2009).

[Mele et al., 1990] I. Mele, S. Slavic, M. Ravnik, and V. Dimic, TRIGA database for ORIGEN2, in: 11th TRIGA User Conference, European Nuclear Society, Heidelberg, Germany (1990).

[Menendéz et al., 2009] P.R. Menéndez, B.M.C. Roth, M.D. Pereira, M.R. Casal, S.J. González, D.B. Feld, G.A. Santa-Cruz, J. Kessler, J. Longhino, H. Blaumann, R. Jiménez Rebagliati, O.A. Calzetta Larrieu, C. Fernández, S.I. Nievas, and S.J. Liberman, BNCT for skin melanoma in extremities: Updated Argentine clinical results. *Applied Radiation and Isotopes* **67**, 50-53 (2009).

[Mishima et al., 1989] Y. Mishima, M. Ichihashi, S. Hatta, C. Honda, K. Yamamura, and T. Nakagawa, New Thermal Neutron Capture Therapy for Malignant Melanoma: Melanogenesis-Seeking ^{10}B Molecule-Melanoma Cell Interaction From In Vitro to First clinical Trial, *Pigment Cell Research* **2**, 226-234 (1989).

[Morita et al., 2006] N. Morita, J. Hiratsuka, C. Kuwabara, T. Aihara, K. Ono, H. Fukuda, H. Kumada, T. Harada, and Y. Imajo, Successful BNCT for Patients with Cutaneous and Mucosal Melanomas: Report of 4 Cases, in: 12th International Congress on Neutron Capture Therapy - From the Past to the Future, edited by the International Society for Neutron Capture Therapy, Neutrino OSAKA Inc., Osaka (2006), p. 18.

[Moss, 2014] R.L. Moss, Critical review, with an optimistic outlook, on Boron Neutron Capture Therapy (BNCT), *Applied Radiation and Isotopes* **88**, 2-11 (2014).

[Munck af Rosenschöld, 2012] P. Munck af Rosenschöld, The Clinical Commissioning of Beams for Neutron Capture Therapy, in: Neutron Capture Therapy, edited by W.A.G. Sauerwein, A. Wittig, R. Moss, and Y. Nakagawa, Springer, Berlin (2012), p. 259.

[Nakagawa and Hatanaka, 1997] Y. Nakagawa and H. Hatanaka, Boron neutron capture therapy, Journal of Neuro-Oncology **33**, 105-115 (1997).

[New York Times, 1901] X-Rays Used as a Remedy for Cancer, New York Times, 2. Nov. 1901.

[Nigg, 2012] D.W. Nigg, Physical Dosimetry and Spectral Characterization of Neutron Sources for Neutron Capture Therapy, in: Neutron Capture Therapy, edited by W.A.G. Sauerwein, A. Wittig, R. Moss, and Y. Nakagawa, Springer, Berlin (2012), p. 227.

[NIST] National Institue of Standards and Technology, Physical Reference Data, J. H. Hubbell and S.M. Seltzer. Tables of X-Ray Mass Attenuation Coefficient and Mass Energy-Absorption Coefficients from 1 keV to 20 MeV for Elements Z = 1 to 92 and 48 Additional Substances of Dosimetric Interest. http://www.nist.gov/pml/data/xraycoef/index.cfm (2014).

[Ohno et al., 2001] S. Ohno, K. Furukawab, M. Taguchi, T. Kojima, and H. Watanabe, An ion-track structure model based on experimental measurements and its application to calculate radiolysis yields, *Radiation Physics and Chemistry* **60**, 259-262 (2001).

[Olko, 1999] P. Olko, Calculation of the Relative Effectiveness of Alanine Detectors to X rays and Heavy Charged Particles using Microdosimetric One-Hit Detector Model, *Radiation Protection Dosimetry* **84**, 63-66 (1999).

[Olko, 2002] P. Olko, The microdosimetric one-hit detector model for calculating the response of solid state detectors, *Radiation Measurements* **35**, 255-267 (2002).

[Olsen and Hansen, 1990] K.J. Olsen and J.W. Hansen, The Response of the Alanine Dosimeter to Low Energy Protons and High Energy Heavy Charged Particles, *Radiation Protection Dosimetry* **31**, 81-84 (1990).

[Olsson et al., 2000] S.K. Olsson, E. Lund and A. Lund, Development of ammonium tartrate as an ESR dosimeter material for clinical purposes, *Applied Radiation and Isotopes* **52**, 1235-1241 (2000).

[Onori et al., 1996] S. Onori, M. Pantaloni, S. Baccaro, and P.G. Fuochi, Influencing factors on ESR bone dosimetry, *Applied Radiation and Iostopes* **47**, 1637-1640 (1996).

[Onori et al., 1999] S. Onori, F. d'Errico, C. De Angelis, E. Egger, P. Fattibene, and I. Janovsky, Alanine dosimetry of proton therapy beams, *Medical Physics* **24**, 447-453 (1999).

[Palmans, 2003] H. Palmans, Effect of Alanine Energy Response and Phantom Material on Depth Dose Measurements in Ocular Proton Beams, Technology in *Cancer Research and Treatment* **2**, 579-586 (2003).

[Papanikolaou et al., 2004] N. Papanikolaou, J. Battista, A. Boyer, C. Kappas, E. Klein, T. Mackie, M. Sharpe, and J. Van Dyk, Tissue inhomogeneity corrections for megavoltage photon beams, Technical Report 85, AAPM Task Group (2004).

[Pelowitz, 2008] D. Pelowitz, "MCNPX™ User's Manual" LA-CP-07-1473, Los Alamos National Laboratory (2008).

[Pihet et al., 1990] P. Pihet, H.G. Menzel, R. Schmidt, M. Beauduin, and A. Wambersie, Biological Weighting Function for RBE Specification of Neutron Therapy Beams. Intercomparison of 9 European Centres, *Radiation Protection Dosimetry* **31**, 437-442 (1990).

[Protti et al., 2012] N. Protti, S. Bortolussi, M. Prata, P. Bruschi, S. Altieri, and D. Nigg, Physical neutron dosimetry for the university of pavia thermal neutron source for BNCT research, 15th International Congress on Neutron Capture Therapy Conference Proceedings, 148 (2012).

[PTCOG, 2014] Martin Jermann, PTCOG Secretary, Particle Therapy Patient Statistics (per end of 2013): http://www.ptcog.ch/index.php/ptcog-patient-statistics (2014).

[Raaijmakers et al., 2000] C.P.J. Raajimakers, E.L. Nottelmann, and B.J. Mijnheer, Phantom materials for boron neutron capture therapy, *Physics in Medicine and Biology* **45**, 2353-2361 (2000).

[Regulla and Deffner, 1982] D.F. Regulla, and U. Deffner, Dosimetry by ESR Spectroscopy of Alanine, *Applied Radiation and Isotopes* **33**, 1101-1114 (1982).

[Rogers et al., 2005] D.W.O. Rogers, I. Kawrakow, J.P. Seuntjens, B.R.B. Walters, and E. Mainegra-Hing, NRC user codes for EGSnrc, Ionizing Radiation Standards National Research Council of Canada Ottawa, NRCC Report PIRS-702, Rev B (2005).

[Rogus et al., 1994] R.D. Rogus, O.K. Harling, and J.C. Yanch, Mixed field dosimetry of epithermal neutron beams for boron neutron capture therapy at the MITR-II research reactor, *Medical Physics* **21**, 1611-1625 (1994).

[Rutherford, 1920] E. Rutherford, Nuclear constitution of atoms, *Proceedings of the Royal Society of London A* **97**, 374-400 (1920).

[Ryynänen et al., 2002] P. Ryynänen, A. Kangasmäki, P. Hiismäki, J. Coderre, A.Z. Diaz, M. Kallio, J. Laakso, M. Kulvik, and S. Savolainen, Non-linear model for the kinetics of 10B in blood after BPA–fructose complex infusion, *Physics in Medicine and Biology* **47**, 737-745 (2002).

[Sakurai and Kobayashi, 2014] Y. Sakurai, and T. Kobayashi, Experimental Verification of the Nuclear Data of Gadolinium for Neutron Capture Therapy, *Journal of Nuclear Science and Technology* **39**, 1294-1297 (2014).

[Salt et al., 2004] C. Salt, A.J. Lennox, M. Takagaki, J.A. Maguire, and N.S. Hosmane, Boron and gadolinium neutron capture therapy, *Russian Chemical Bulletin, International Edition* **53**, 1871-1888 (2004).

[Seppälä et al., 1999] T. Seppälä, J. Vähätalo, I. Auterinen, A. Kosunen, D.W. Nigg, F.J. Wheeler, and S. Savolainen, Modelling of brain tissue substitutes for phantom materials in neutron capture therapy (NCT) dosimetry, *Radiation Physics and Chemistry* **55**, 239-246 (1999).

[Schmitz, 2010] T. Schmitz, Bestimmung und Simulation der Neutronen- und Gammadosis in der thermischen Säule des TRIGA Reaktors Mainz und Borbestimmung in Blut- und Gewebeproben mittels Prompt-Gamma-Aktivierungsanalyse im Rahmen der Bor-Neutronen-Einfangtherapie, Diploma-Thesis, Insititut für Kernchemie, Johannes Gutenberg-Universität Mainz, Germany (2010).

[Schmitz et al., 2010] T. Schmitz, M. Blaickner, C. Schütz, N. Wiehl, J.V. Kratz, N. Bassler, M.H. Holzscheiter, H. Palmans, P. Sharpe, G. Otto, and G. Hampel, Dose calculation in biological samples in a mixed neutron-gamma field at the TRIGA reactor of the University of Mainz, *Acta Oncologica* **49**, 1165-1169 (2010).

[Schmitz et al., 2011] T. Schmitz, M. Blaickner, M. Ziegner, N. Bassler, C. Gunewald, J.V. Kratz, C. Schütz, P. Langguth, P. Sharpe, H. Palmans, M.H. Holzscheiter, G. Otto, and G. Hampel, Dose determination using alanine detectors in a mixed neutron and gamma field for boron neutron capture therapy of liver malignancies, *Acta Oncologica* **50**, 817-822 (2011).

[Schmitz et al., 2015] T. Schmitz, N. Bassler, M. Blaickner, M. Ziegner, M.C. Hsiao, Y.H. Liu, H. Koivunoro, I. Auterinen, T. Serén, P. Kotiluoto, H. Palmans, P. Sharpe, P. Langguth, and G. Hampel, The alanine detector in BNCT dosimetry: Dose response in thermal and epithermal neutron fields, *Medical Physics* **42**, 400-412 (2015).

[Schramm and Rossi, 1996] D.U. Schramm and A.M. Rossi, Electron spin resonance (ESR), electron nuclear double resonance (ENDOR) and general triple resonance of irradiated biocarbonates, *Applied Radiation and Isotopes* **47**, 1443-1455 (1996).

[Schraube et al., 1989] H. Schraube, E. Weitzenegger, A. Wieser, and D.F. Regulla, Fast Neutron Response of Alanine Probes, *Applied Radiation and Isotopes* **40**, 941-944 (1989).

[Schütz et al., 2011] C. Schütz, C. Brochhausen, S. Altieri, K. Bartholomew, S. Bortolussi, F. Enzmann, D. Gabel, G. Hampel, C. J. Kirkpatrick, J. V. Kratz, S. Minouchehr, H. Schmidberger, and G. Otto, Boron Determination in Liver Tissue by Combining Quantitative Neutron Capture Radiography (QNCR) and Histological Analysis for BNCT Treatment Planning at the TRIGA Mainz, *Radiation Research* **176**, 388-396 (2011).

[Schultz et al., 2010] D. Schultz, B. Blasy, J.C. Santana, C. Young, J.C. Petrosky, J.W. McClory, D. LaGraffe, J.I. Brand, J. Tang, W. Wang, N. Schemm, S. Balkir, M. Bauer, I. Ketsman, R.W. Fairchild, Y.B. Losovyj, and P.A. Dowben, The K-shell Auger electron spectrum of gadolinium obtained using neutron capture in a solid state device, *Journal of Physics D: Applied Physics* **43**, 075502 (2010).

[Serén et al., 2001] T. Serén, I. Auterinen, P. Kotiluoto, and T. Seppälä, Neutron Beam Characterization at the Finnish BNCT Facility – Measurements and Calculations, in: Reactor dosimetry: Radiation Metrology and Assessment, edited by J.G. Williams, D.W. Vehar, F.H. Ruddy, and D.M. Gilliam, American Society for Testing and Materials, Philadelphia (2001), p. 175.

[Sharpe and Septhon, 1999] P.H.G. Sharpe, and J.P. Septhon, Alanine Dosimetry at NPL - the Development of a Mailed Reference Dosimetry Service at Radiotherapy Dose Levels, Technical report, IAEA-SM-356/65 (1999).

[Slater, 2006] J.M. Slater, Considerations in Indentifying Optimal Particles for Radiation Medicine, *Technology in Cancer Research and Treatment* **5**, 73-79 (2006).

[Slatkin, 1991] D.N. Slatkin, A History of Boron Neutron Capture Therapy of Brain Tumours, *Brain* **114**, 1609-1629 (1991).

[Snyder et al., 1958] H.R. Snyder, A.J. Reedy, W.J. Lennarj, Synthesis of aromatic boronic acids, Aldehyde boronic acids and a boronic acid analog of tyrosine, *Journal of the American Chemical Society* **80**, 835-838 (1958).

[Soloway et al., 1967] A.H. Soloway, H. Hatanaka, and M.A. Davis, Penetration of brain and brain tumour VII. Tumour binding sulfhydryl boron compounds, *Journal of Medicinal Chemistry* **10**, 714-717 (1967).

[Sørensen et al., 2011] B.S. Sørensen, J. Overgaard, and N. Bassler, In vitro RBE-LET dependence for multiple particle types, *Acta Oncologica* 50, 757-762 (2011).

[Staffurth, 2010] J. Staffurth, A Review of the Clinical Evidence for Intensity-modulated Radiotherapy, *Clinical Oncology* **22**, 643-657 (2010).

[Stuglik and Sadlo, 1996] Z Stuglik and J. Sadlo, A Response of L-α-alanine and Standard Bone Powder on 3.4 MeV/amu ^{59}Co Ion Beams, *applied Radiation and Isotopes* **47**, 1219-1222 (1996).

[Tanaka et al. 2009] H. Tanakaa, Y. Sakurai, M. Suzuki, T. Takata, S. Masunaga, Y. Kinashi, G. Kashino, Y. Liu, T. Mitsumoto, S. Yajima, H. Tsutsui, M. Takada, A. Maruhashi, and K. Ono, Improvement of dose distribution in phantom by using epithermal neutron source based on the Be(p,n) reaction using a 30 MeV proton cyclotron accelerator, *Applied Radiation and Isotopes* **67**, 258-261 (2009).

[Thomas et al., 2002] D.J. Thomas, A.G. Bardell, and E.M. Macaulay, Characterisation of a gold foil-based Bonner sphere set and measurements of neutron spectra at a medical accelerator, *Nuclear Instruments and Methods A* **476**, 31-35 (2002).

[Trompier et al., 2004] F. Trompier, P. Fattibene, D. Tikunov, A. Bartolotta, A. Carosi, and M. C. Doca, EPR Dosimetry in a Mixed Neutron and Gamma Radiation Field, *Radiation Protection Dosimetry* **110**, 437-442 (2004).

[Vestad et al., 2003] T.A. Vestad,E. Malinen, A. Lund, E.O. Hole, and E. Sagstuen, PR dosimetric properties of formates, *Applied Radiation and Isotopes* **59**, 181-188 (2003).
[Waldeland et al., 2010a] E. Waldeland, E.O. Hole, E. Sagstuen, and E. Malinen, The energy dependence of lithium formate and alanine EPR dosimeters for medium energy x-rays, *Medical Physics* **37**, 3569-3575 (2010).

[Waldeland et al., 2010b] E. Waldeland, E. O. Hole, B. Stenerlöw, E. Grusell, E. Sagstuen, and E. Malinen, Radical Formation in Lithium Formate EPR Dosimeters after Irradiation with Protons and Nitrogen Ions, *Radiation Research* **174**, 251–257 (2010).

[Waldeland et al., 2011] E. Waldeland, J.H. Hansen, and E. Malinen, Characterization of lithium formate EPR dosimeters for high doe applications – Comparison with alanine, *Radiation Measurments* **46**, 213-218 (2011).

[Waligórski et al., 1986] M.P.R. Waligórski, R.N. Hamm, and R. Katz, The Radial Distribution of Dose around the path of a Heavy Ion in Liquid Water, *Nuclear Tracks and Radiation Measurements* **11**, 309-319 (1986).

[Waligórski et al., 1989] M.P.R. Waligórski, G. Danialy, K.S. Loh, and R. Katz, The Response of the Alanine Detector After Charged-Particle and Neutron Irradiations, *Applied Radiation and Isotopes* **40**, 923-933 (1989).

[Waterman et al., 1979] F.M. Waterman, F.T. Kuchnir, and L.S. Skaggs, Energy Dependence of the neutron sensitivity of C-CO_2, Mg-Ar and TE-TE ionization chambers, *Physics in Medicine and Biology* **24**, 721-733 (1979).

[Weinberg and Wigner, 1958] A.M. Weinberg and E. P. Wigner, The Physical Theory of Neutron Chain Reactors, The University of Chicago Press, Chicago (1958).

[Wilkens and Oelfke, 2004] J. Wilkens and U. Oelfke, A phenomenological model for the relative biological effectiveness in therapeutic proton beams, *Physics in Medicine and Biology* **49**, 2811 (2004).

[Wittig et al., 2008] A. Wittig, J. Michel, R.L. Moss, F. Stecher-Rasmussen, H.F. Arlinghaus, P. Bendel, P.L. Mauri, S. Altieri, R. Hilger, P.A. Salvadori, et al., Boron analysis and boron imaging in biological materials for Boron Neutron Capture Therapy (BNCT), *Critical Reviews in Oncology/Hematology* **68**, 66-90 (2008).

[Wortmann, 2008] B. Wortmann, Auslegung und Optimierung einer Bestrahlungseinrichtung für die Bor-Neutroneneinfangtherapie an autotransplantierten Organen, PhD-Thesis, Fakultät Maschinenwesen, Technical University Dresden, Germany (2008).

[X-5 Monte Carlo Team, 2003] X-5 Monte Carlo Team, MCNP: A General Monte Carlo N-Particle Transport Code, Version 5, LA-UR-03-1987, Los Alamos National Laboratory (2003).

[Yoshimoto et al, 2013] M. Yoshimoto, H. Kurihara, N. Honda, K. Kawai, K. Ohe, H. Fujii, J. Itami, and Y. Arai, Predominant contribution of L-type amino acid transporter to 4-borono-2-18 F-fluoro-phenylalanine uptake in human glioblastoma cells, *Nuclear Medicine and Biology* **40**, 625-629 (2013).

[Zacharatou Jarlskog and Paganetti, 2008] C. Zacharatou Jarlskog and H. Paganetti, Risk of Developing Second Cancer from Neutron Dose in Proton Therapy as Function of Field Characteristics, Organ, and Patient Age, *International Journal of Radiation Onkology in Biology and Physics* **72**, 228-235 (2008).

[ZfKD, 2014] German Centre for Cancer Registry Data, Contributions to Federal Health Reporting: Cancer in Germany 2009/2010, *brochure*, Robert Koch Institute, Berlin, 2014.

[Ziegner et al., 2014] M. Ziegner, T. Schmitz, R. Khan, M. Blaickner, H. Palmans, P. Sharpe, G. Hampel, and H. Böck, Confirmation of a realistic reactor model for BNCT dosimetry at the TRIGA Mainz, *Medical Phyics* **41**, 111706 (2014).

[Zonta et al., 2006] A. Zonta, U. Prati, L. Roveda, C. Ferrari, S. Zonta, A.M. Clerici, C. Zonta, T. Pinelli, F. Fossati, S. Altieri, S. Bortolussi, P. Bruschi, R. Nano, S. Barni, P. Chiari, and G. Mazzini, Clinical lessons from the first applications of BNCT on unresectable liver metastases, *Journal of Physics: Conference Series* **41**, 484-495 (2006).

7. Appendices

Appendix A – Collection of RE values in literature

Taken from different references, RE values are differentiated by particle type and energy. A “c” in the last column “crossing” states that the particle was crossing the pellet and hence did not stop in it.

Reference	Particle		RE	ΔRE	crossing
	Type	Energy / MeV/u			
Bradshaw_1962	proton	14	0,71	0,14	
Ebert_1965	proton	7,7	0,48	0,14	
		10,2	0,62	0,13	
		12,6	0,59	0,12	
		14,5	0,71	0,14	
		15,8	0,68	0,14	
Fattibene_2002	proton	1,63	0,61	0,04	
		2,85	0,61	0,04	
		3,97	0,63	0,04	
		5,05	0,65	0,05	
		6,1	0,62	0,06	
Cuttone_1999 (from Herrmann PhD)	proton	40	1,02	0,05	c
		60	0,99	0,05	c
Bartolotta_1999	proton	23,6	0,96	0,03	c
		13,7	0,92	0,03	c
Onori_1999	proton	62	0,97	0,02	c
Herrmann_PhD_2012	proton	104,5	0,98	0,02	c
		106,4	0,98	0,02	c
		114,7	0,97	0,02	c
		116,4	0,97	0,02	c
		125,5	1,01	0,03	c
		127,1	1,00	0,03	c
		135,7	0,99	0,04	c
		137,2	0,99	0,04	c
		145,9	1,02	0,03	c
		147,4	1,02	0,03	c
		156,3	0,99	0,04	c
		157,1	1,02	0,03	c
		166	1,00	0,03	c
		167,3	0,99	0,03	c
		176,6	0,99	0,02	c
		177,8	0,99	0,02	c

(continued)

Reference	Particle		RE	ΔRE	crossing
	Type	Energy / MeV/u			
Herrmann_PhD_2012	proton	186,7	1,02	0,03	c
		187,9	1,02	0,02	c
		196,4	1,01	0,02	c
		197,6	1,01	0,02	c
		206	0,98	0,02	c
		207,7	0,98	0,02	c
		217,7	1,00	0,02	c
		218,8	0,99	0,02	c
	14-N	9,3	0,36	0,05	
	56-Fe	5,8	0,18	0,03	
		9,3	0,30	0,04	
	82-Kr	5	0,31	0,04	
		9,3	0,27	0,03	
	131-Xe	9,3	0,31	0,04	
Bermann_1978 (from Waligorski 1989)	proton	160	1,00		c
	4-He	162,5	1,00		c
		58,6	1,00		c
Hansen&Olsen_1990	proton	16	1,00	0,03	
		6	0,86	0,03	
		3	0,74	0,07	
		2	0,65	0,02	
		1	0,54	0,04	
	16-O	4	0,32	0,02	
	40-Ar	18,5	0,37	0,02	
	58-Ni	15,4	0,35	0,07	
	238-U	15	0,33	0,06	
		5,9	0,27	0,03	
	208-Pb	13,8	0,25	0,05	
Hansen&Olsen_1985	4-He	5	0,58	0,04	
	7-Li	3	0,37	0,04	
	32-S	2,5	0,25	0,04	
Henriksen_1966	4-He	10,4	0,99	0,04	c
	7-Li	10,4	0,88	0,04	c
	11-B	10,4	0,61	0,04	c
	12-C	10,4	0,55	0,04	c
	16-O	10,4	0,41	0,04	
	19-F	10,4	0,42	0,04	
	20-Ne	10,4	0,37	0,04	
	28-Si	10,4	0,35	0,04	
	40-Ar	10,4	0,31	0,04	

(continued)

Reference	Particle		RE	ΔRE	crossing
	Type	Energy / MeV/u			
Herrmann_2011	12-C	68,94	0,84	0,03	c
		76,22	0,85	0,03	c
		88,16	0,86	0,03	c
		94,33	0,87	0,03	c
		109,3	0,89	0,03	c
		114,6	0,89	0,03	c
		147,8	0,91	0,03	c
		152,1	0,92	0,03	c
		200,7	0,93	0,03	c
		204,3	0,93	0,03	c
		291,8	0,96	0,03	c
		294,3	0,95	0,03	c
		393,5	0,96	0,03	c
		395,9	0,95	0,03	c

Appendix B – Dimensions of the TRIGA Mark II research reactor Mainz, Germany

Values are taken from constructional drawings of the reactor and were used for MC modelling.

Description	Shape and Material	Physical Dimension
Tank	cylindrical / aluminium	
Outer diameter		200 cm
Height		625 cm
Total fluid lever		610 cm
Fluid lever above core		≈490 cm
Thickness		6 mm
Water temperature		32 – 38 °C

(continued)

Description	Shape and Material	Physical Dimension
Shielding	octagon / concrete	
Height		820 cm
Min. radial thickness		230 cm
Height above ground		655 cm
Lower part		
Height		370 cm
Width		655 cm
Upper part		
Height		287 cm
Width		381 cm
Reflector	cylindrical / graphite	
Radial thickness		30.5 cm
Outer diameter		109 cm
Outer height		58 cm
Height above tank ground		61 cm
Inner diameter		45.7 cm
Inner height		55.9 cm
Cover	aluminium	
Thermal column	cuboid / grahite	
Cover	aluminium	
Width/Heigth		122 cm
Length		168 cm
Thickness		12.7 mm
Liner	boral	
Thickness		3.2 mm
Concreate Gate	box-shaperd / concrete	
Thickness		106.7 cm
Liner	boral	
Thickness		3.2 mm

Appendix C – Height profiles of the neutron flux in the irradiation positions of the PTS

Height profiles were measured using wire out of aluminium-gold alloy. Wires were fixed perpendicular in the irradiation capsule with the help of a Teflon holder. Irradaition was carried out twice in each PTS.

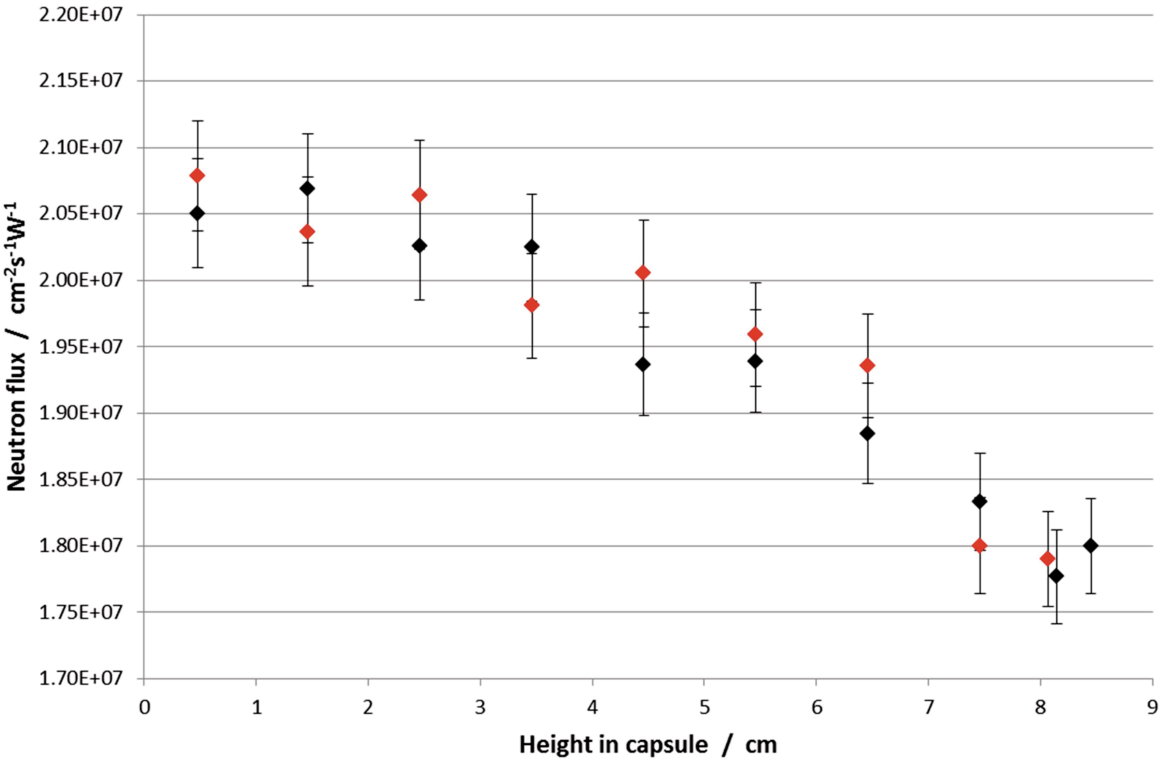

Figure 7-1. Thermal equivalent neutron flux in the two PTS as a function of height in irradiation capsule: PTS 1 (black) ending in the central laboratory and PTS 2 (red) ending in the reactor hall.

Appendix D – Gamma spectrometer efficiency curves

Curves are always defined by two functions, a low and a high energy part. The border between both is the line in the calibration spectrum at 166 keV (compare table 3-3). Curves are for positions one to ten in the PMMA holder. The corresponding distance of the calibration foil to the detector window in cm is $(2n-2)$, of the 500 µL standard $(2n-1)$, with n number of the position.

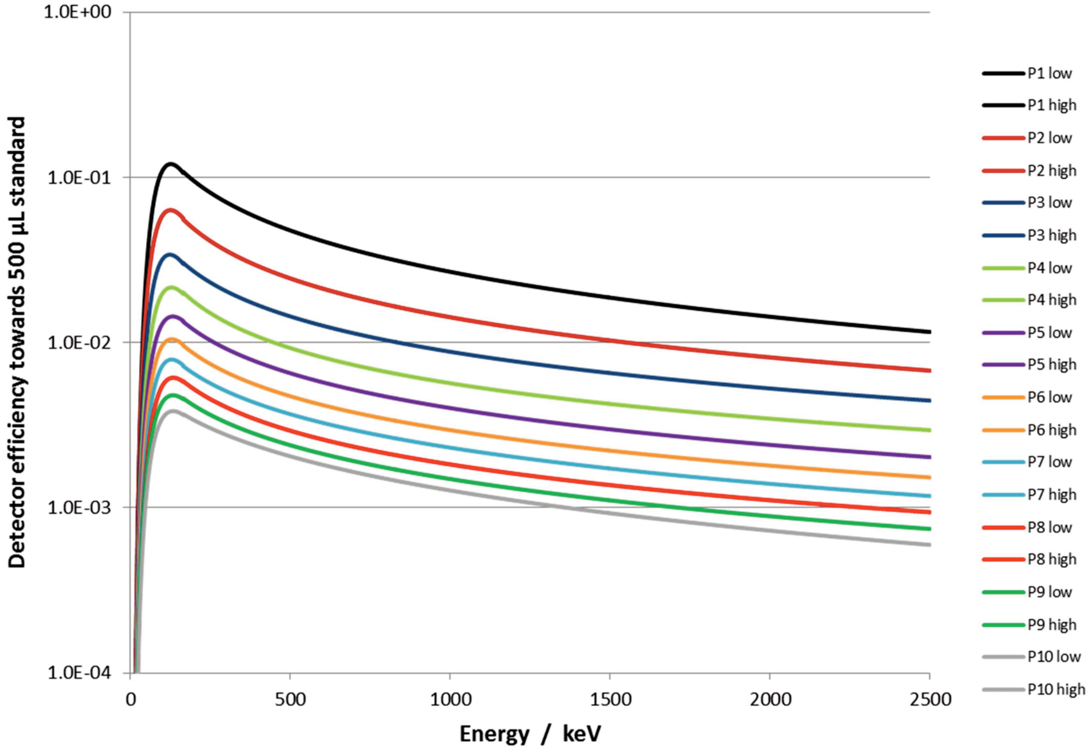

Figure 7-2. Detector efficiency as a function of energy, as determined with the 500 µL liquid standard

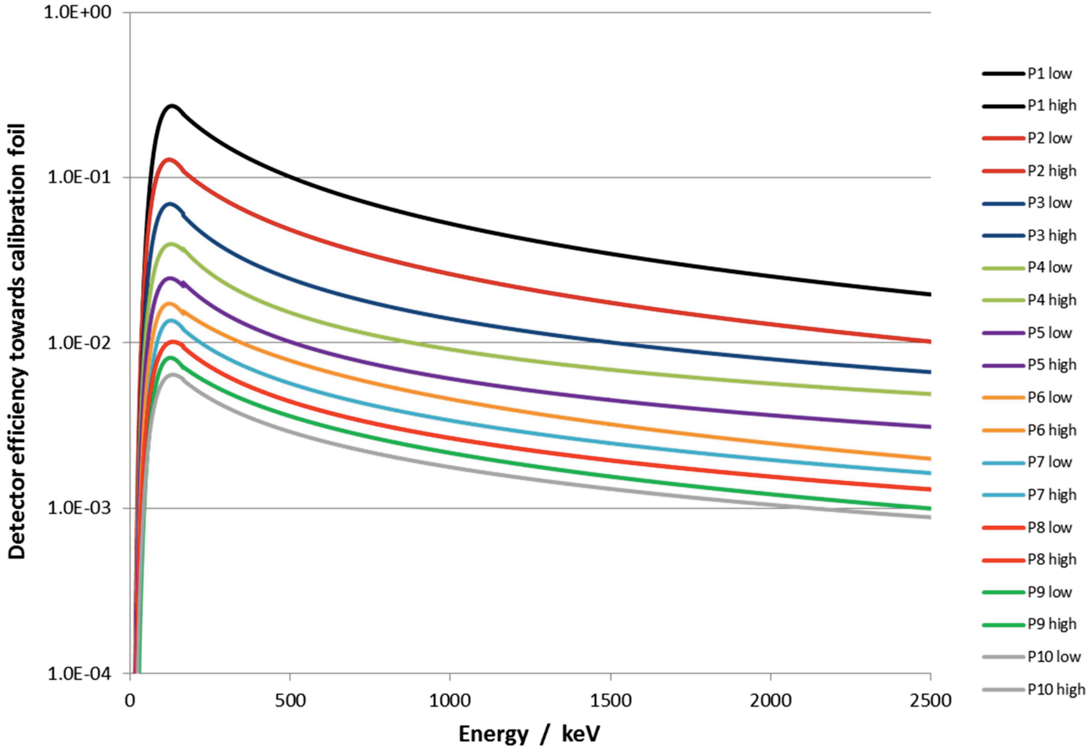

Figure 7-3. Detector efficiency as a function of energy, as determined with the calibrations foils.

Appendix E – Reaction rates for different foil materials in various positions at the TRIGA Mainz

Table 7-1. Reaction rates for activation foils used in the thermal column and in the PTS. For each foil thermal and epithermal rate is shown.

Foil material and type of interaction		Reaction rates / cm^{-2}s^{-1}W^{-1}					
		thermal column				in-core position	
		free in air		on phantom		PTS	
		th	res	th	res	th	res
Cu	**(n,γ)**	7.62E-19	1.33E-21	9.59E-19	2.54E-21	7.63E-17	6.38E-18
Mn	**(n,γ)**	1.91E-18	3.73E-21	1.60E-18	6.91E-21	1.62E-16	1.23E-17
W	**(n,γ)**	4.72E-18	7.77E-20	2.36E-18	1.53E-19	5.01E-16	3.14E-16
Au	**(n,γ)**	1.73E-17	2.87E-19	5.27E-18	5.42E-19	1.34E-15	7.60E-16
In	**(n,γ)**	2.45E-17	5.07E-19	3.15E-17	9.25E-19	n.d.	9.99E-16
In	**(n,n')**		4.65E-23		1.43E-22		1.68E-18

Appendix F – Energy spectra of the primary particles at FiR1 in Espoo, Finland, and at THOR in Hsinchu, Taiwan

For the simulations of the two reactor facilities, analogue to simulations at the TRIGA Mainz, two primary particles were used. The following figures show the corresponding energy spectra, which were normalised to an area of one below the curves. Spatial and angular distribution of the source definitions are not addressed in the figures.

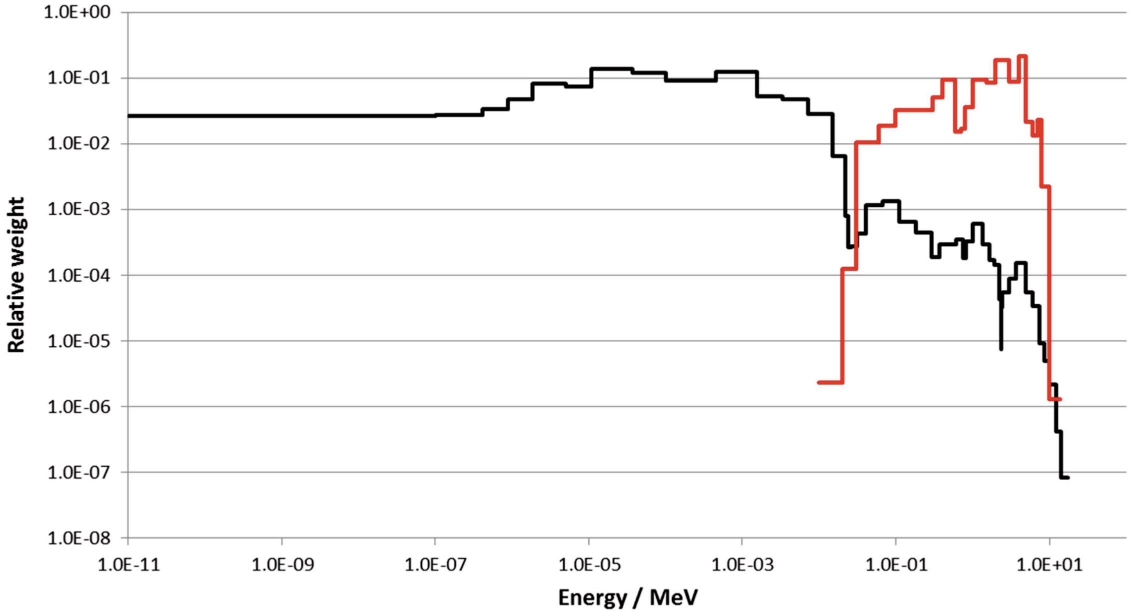

Figure 7-4. Neutron (blue) and photon (red) spectra of the FiR1 research reactor in Espoo, Finland, as used in simulations.

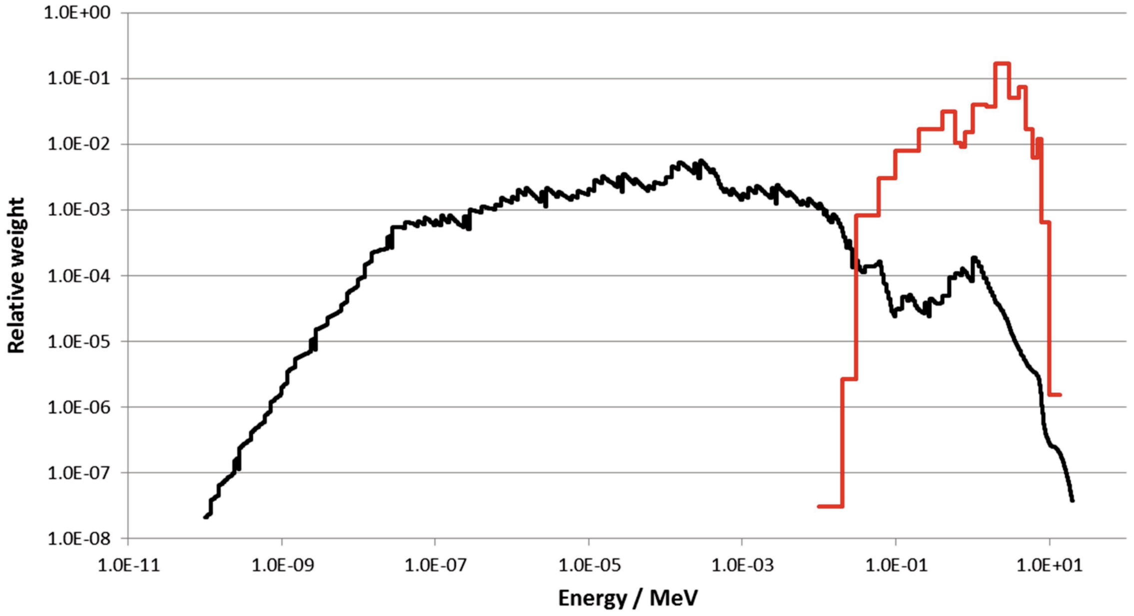

Figure 7-5. Neutron (blue) and photon (red) spectra of the THOR research reactor in Hsinchu, Taiwan, as used in simulations.